UNIVERSITÀ DEGLI STUDI DI GENOVA

SCUOLA POLITECNICA

DIME

Dipartimento di Ingegneria Meccanica, Energetica, Gestionale e dei Trasporti

Tesi di Dottorato

in

Ingegneria delle machine e dei sistemi per l'energia, l'ambiente e la propulsione

Analisi e modellazione di sistemi a celle a combustibile di tipo PEM

Relatore:

Chiar.ma Prof. Ing. Loredana Magistri

Candidato:

Marco De Campo

Aprile 2019

UNIVERSITY OF GENOA

POLYTECHNIC SCHOOL

DIME

Department of Mechanical Engineering, Energy, Management and Transports

P.h.D Thesis

in

Engineering of machines and systems for the energy, the environment and the propulsion

Analysis and modeling of PEM fuel cell systems

Supervisor:

Chiar.ma Prof. Ing. Loredana Magistri

Candidate:

Marco De Campo

April 2019

Abstract

The purpose of this thesis is to create a transient model of a PEM fuel cell system, based on Matlab Simulink, as general, flexible and adaptable as possible, in order to be easily set on different type of systems. The object of the study is the development of the simulation tool, and its validation against literature and experimental data. An important aim of the developed dynamic semi-empirical model is to try to adopt a theoretical physics-based approach whenever possible, in order to have an accurate scientific correlation between experimental output and theoretical laws, without neglecting the accuracy that could be provided by empirical equations.

The major work is focused on the fuel cell stack modeling and involves also a large review of literature analysis concerning the simulation of PEM-FCs. In order to guarantee the adaptability of the model, taking inspiration from the latest studies in this field, a differential evolution algorithm is developed to realize the fitting process of the modeled polarization curve, by means of the stack voltage model, on experimental data. This algorithm has a strategic importance for the choice and the setting of the stack voltage equations on the real static performance of the PEM fuel cell system analyzed, with a proved error of about 2-3%.

The transient behaviors captured in the model includes flow characteristics, inertia dynamics, lumped-volume manifold filling dynamics, time evolving-homogeneous reactant pressure or mole fraction, membrane humidity and thermal response of fuel cell and cooling system.

From one side, the validation against literature data of Section 4 is realized after the development of a general dynamic PEM-FC system model described in Section 2 and 3, comprising all the components normally present in these systems. The comprehensive dynamic model proposed, usually not presented in literature, perform very well respect to the experimental data, comprising the thermic data and the hydration of the membrane, the most important operative parameters but also the most complex ones to simulate.

On the other side, the HI-SEA Joint Laboratory, between Fincantieri S.p.A. and the University of Genoa, allows to study a PEM fuel cell system of 8 stacks sized 33 kW each for a total maximum power of 260 kW. The adaptation and the simplification of the dynamic model to this plant layout helps to study a bigger and more complex PEM-FC system and to validate the model to the experimental data. The simplification of the dynamic model starts form the necessity to set the equations only by the commercially available data, usually limited to the datasheet information. This limitation makes the HI-SEA model less detailed but, at the same time, simpler and able to provide different important results, as the stack and cooling system thermal balances, starting from few easily obtainable data.

Index

Index of Figures

List of Symbols

A	area, m^2
A_{cs}	cross-sectional area, m^2
A_E	effective area of the flow restriction, m^2
$A_{ext,FC}$	external surface of the fuel cell stack, m^2
A_{FC}	cell active area, cm^2
A_R	minimum cross-sectional area, m^2
A_T	cross-sectional area of the throat, m^2
C_D	discharge coefficient
c_i	concentration of specie i, mol/cm^3
$c_{p,i}$	heat capacity at constant pressure of species i, J/(kg·K)
D	diffusion coefficient of reacting species
D_w	diffusion coefficient of water in the membrane, cm^2/s
E	Nernst potential, V
E^o	standard state reference potential or Open Circuit Voltage OCV, V
E_0^o	SAPT state reference potential, V
e^-	electrones
F	Faraday's number, equal to 96485 C/mol
ΔF_c	standard state free energy of chemisorption from the gas state, J/mol
ΔF_e	standard state free energy of activation for the reaction, J/mol
ΔF_{ec}	standard state free energy of activation for the chemisorption, J/mol
h_{FC}	heat transfer coefficient of the fuel cell stack, $W/(m^2 \cdot K)$
ΔH_c	hydrogen lower heating value, J/kg
i_{st}	stack current, A
i_{lim}	stack limit current, A
i_0	exchange current, A
j_{st}	stack current density, A/cm^2
k	nozzle mass flow constant
k^0	intrinsic rate constant
M	Mach number
M_i	molar mass of species i, kg/mol
m_i	mass of species i, kg
m_{conc}	empirical coefficient for concentration loss, V
$M_{m,dry}$	membrane dry equivalent weight, kg/mol
N	number of moles of the gas
$N_{v,osmotic}$	net water flux caused by electro-osmotic drag, $mol/(s \cdot cm^2)$
$N_{v,diff}$	net water flux caused by back-diffusion, $mol/(s \cdot cm^2)$
n	number of electrons involved in the chemical reaction, 2
n_{conc}	empirical coefficient for concentration loss, cm^2/A

n_d	electro-osmotic drag coefficient
n_{FC}	number of cells
p	pressure, Pa (unless stated otherwise)
p_s	stagnation pressure, Pa
p_T	pressure at the throat, Pa
R	universal gas constant, 8.3145 J/(mol·K)
R_i	gas constant of the species i, J/(kg·K)
$R_{ohm}^{electronic}$	Ohmic electronic resistance, Ω·cm^2
R_{ohm}^{proton}	Ohmic proton resistance, Ω·cm^2
ΔS^o	standard state entropy change, kJ/mol
ΔS_0^o	SAPT state entropy change, kJ/mol
T	temperature, K
T_s	stagnation temperature, K
T_{st}	stack temperature, K
T_0	standard state temperature, 298.15 K
t_m	membrane thickness, cm
V	volume, m^3 (unless stated otherwise)
V_{AN}	anode volume, m^3
V_{CA}	cathode volume, m^3
V_{FC}	cell voltage, V
V_{st}	stack voltage, V
v	velocity, m/s
W_i	mass flow rate of species i, kg/s
x_i	mole fraction of species i
y_i	mass fraction of species i
$y_{O_2,amb}$	atmospheric oxygen mass fraction, 0.233
W_i	mass flow of species or components i, kg/s

Greek

α	charge transfer coefficient
α_c	cathode transfer coefficient
γ	heat capacity ratio
δ_{gdl}	gas diffusion layer thickness, cm
ε_{FC}	effectiveness of the fuel cell cooling system
η	overvoltage, V
η_{act}	overvoltage due to activation, V
η_{ohm}	overvoltage due to ohmic resistance, V
η_{conc}	overvoltage due to concentration, V
λ_m	membrane water content
λ_{O_2}	oxygen excess ratio
ρ	density, kg/m^3

$\rho_{m,dry}$	membrane dry density, kg/cm^3
$\sigma_{30°C}$	membrane conductivity at 30°C, (Ω·cm)$^{-1}$
σ_m	membrane conductivity, (Ω·cm)$^{-1}$
Φ_i	relative humidity of species i
ω_i	humidity ratio of species i

Subscripts

a	air
AN	anode
amb	ambient
atm	atmospheric conditions
avg	average
br	branch
CA	cathode
$cool$	coolant
cp	compressor
cr	critic or choking
des	desired
dry	dry flow
ds	downstream
exc	exchange
ext	external
FC	fuel cell
HE	heat exchanger
ht	stack heater
in	inlet
inj	injected water
man	manifold
out	outlet
rm	return manifold
s	stagnation
sm	supply manifold
st	fuel cell stack
T	throat
v	vapor
w	water

Superscripts

o	standard state
0	initial conditions
$*$	value at liquid/gas interface

List of Acronyms

BoP	Balance of Plant
DAQ	Data AcQuisition System
DE	Differential Evolution
DNV-GL	Det Norske Veritas Germanischer Lloyd
ECAs	Emission Control Areas
EMSA	European Maritime Safety Agency
EU	European Commission
FAT	Factory Acceptance Test
FC	Fuel Cell
FCS	Fuel Cell Systems
GHGs	GreeenHouse Gasses
GUI	Graphics User Interface
HHV	High Heat Value
HI-SEA	Hydrogen Initiative for Sustainable Energy Application Laboratory
IES	Innovative Energy Systems Laboratory
ICE	Internal Combustion Engines
IMO	International Maritime Organization
JRC	Joint Research Centre of the EU
LHV	Low Heat Value
MEA	Membrane Electrode Assembly
MFC	Mass Flow Controller
NIST	National Institute of Standards and Technology
NTU	Number of Transfer Units
OCV	Open Circuit Voltage
PEM-FC	Polymer Electrolyte Membrane Fuel Cell
PID	Proportional Integral Derivative controller
SAPT	Standard Ambient Pressure and Temperature
SOA	State Of the Art
UNIGE	UNIversity of GEnoa

Index of Tables

1 Background and Introduction

The purpose of this thesis is to create a PEM-FC system model as complete and flexible as possible. To properly explain the developed model, the thermodynamics review together with the orifice equations review is presented, since widely used in different occasions. Them, a brief dissertation of the hydrogen properties and of the fuel cells technologies are presented. The introduction to the dynamic models developed, explaining the logic scheme, all the modeled components and the two application to different PEM-FC systems follows. Finally, the literature review is reported, in which the state of the art of the PEM fuel cell modeling is analysed. In the same Section is also provided a description of the used approaches for modeling the individual components.

1.1 Review of the Thermodynamics of Gas Mixture

This paragraph describes the basic thermodynamic properties of gas mixtures, with a focus on the mixtures involving gases and water vapor, extensively used in the PEM fuel cell model. The fundamental assumption at the basis of this discussion is to consider gas mixtures as ideal gases. Specifically, each component of the mixture is independent by the presence of other components and can be treated individually as an ideal gas. The ideal gas law is:

$$pV = NRT = mR_iT \tag{1.1}$$

where p is the gas pressure, V is the gas volume, N is the number of moles of the gas, m is the mass of the gas, R is the universal gas constant, R_i is the gas constant and T is the gas temperature. Analysing a mixture of gas A and B, the total number of moles of the mixture is equal to the sum of the number of moles of each component as follows:

$$N = N_A + N_B \tag{1.2}$$

Considering each component as an ideal gas, the ideal gas law holds:

$$\begin{aligned} p_AV &= N_ART \\ p_BV &= N_BRT \end{aligned} \tag{1.3}$$

where p_A and p_B are the partial pressures of gases A and B. Replacing Equation (1.1) and (1.3) in the Equation (1.2), results:

$$p = p_A + p_B \tag{1.4}$$

Thus, for a mixture of ideal gases, the pressure of the mixture is the sum of the partial pressures of the individual components.

Mixtures involving dry air and water vapor can be described by different quantities. The humidity ratio ω is defined as the ratio of the water vapor mass m_v to the dry air mass m_a as follows:

$$\omega = \frac{m_v}{m_a} \tag{1.5}$$

However, the humidity ratio does not give a good representation of the humidity of the mixture because the maximum amount of water vapor that the air can hold (saturation) depends on the temperature and pressure of the air.
The relative humidity, which represents the amount of water in the air relative to the maximum possible amount, is therefore more widely used. The relative humidity Φ is defined in Equation (1.6) as the ratio of the partial pressure of water vapor to the equilibrium vapor pressure of water at the same temperature.

$$\Phi = \frac{p_v}{p_{sat}} \tag{1.6}$$

The next equation is obtained by applying the ideal gas law to the humidity ratio definition, presented in Equation (1.5).

$$\omega = \frac{m_v}{m_a} = \frac{p_v V / R_v T}{p_a V / R_a T} = \frac{R_a p_v}{R_v p_a} = \frac{M_v p_v}{M_a p_a} \tag{1.7}$$

The relation between the humidity ratio and the relative humidity can be now derived as follows:

$$\Phi = \omega \frac{M_a p_a}{M_v p_{sat}} \tag{1.8}$$

The saturation pressure p_{sat} depends on the temperature and is easily obtained from a common thermodynamic table of vapor. In the PEM fuel cell model, for the best achievable results, it has been chosen to calculate the saturation pressure by means of a set of four polynomial equations, obtained from a data regression using the Matlab functions dedicated. The result is the following Matlab code, ready to be used inside any Matlab model.

```
% ***** Saturation Pressure *****
if T<333.15
    p_sat_H2O = 6.724136297056386e-07*T^4 - 7.275490810279587e-04*T^3 +
2.969881912941677e-01*T^2 - 5.416844321033899e+01*T +
3.722403620916549e+03;
elseif T<433.15
    p_sat_H2O = 1.495713685503351e-06*T^4 - 1.825218311834390e-03*T^3 +
8.470901653233313e-01*T^2 - 1.769873593224579e+02*T +
1.402983842744454e+04;
elseif T<533.15
    p_sat_H2O = 1.343667935291511e-06*T^4 - 1.548939938649714e-03*T^3 +
6.591871124810556e-01*T^2 - 1.202790615323854e+02*T +
7.620604639994208e+03;
else
    p_sat_H2O = 1.006814469908304e-05*T^4 - 2.136003536986599e-02*T^3 +
1.752662850090859e+01*T^2 - 6.501866475112054e+03*T +
9.128176354446471e+05;
end
p_sat_H2O = p_sat_H2O*1000;
```

1.2 Review of the Orifice Equation

In many parts of the fuel cell system, fluids flows through a conduct restriction that gives a flow area reduction. As explained in the previous Section, in this model all the gaseous flows are considered as ideal flows, also called equivalent ideal flows. The equivalent ideal flow is the steady adiabatic reversible (frictionless) flow of an ideal fluid through a duct of identical geometry and dimensions [1]. For a real fluid flow, the departures from the ideal assumptions are taken into account by introducing a flow coefficient or discharge coefficient C_D defined in terms of an effective cross-sectional area of the duct and a reference area, as reported in Equation (1.9) [1]. The reference area A_R is usually taken as the minimum cross-sectional area. The effective area of the flow restriction A_E is then the cross-sectional area of the throat of a frictionless nozzle which would pass the measured mass flow between a large upstream reservoir at the upstream stagnation pressure and a large downstream reservoir at the downstream measured static pressure [1].

$$C_D = \frac{A_E}{A_R} \tag{1.9}$$

Consider the flow of an ideal gas with constant specific heats through the duct shown in Figure 1.1.

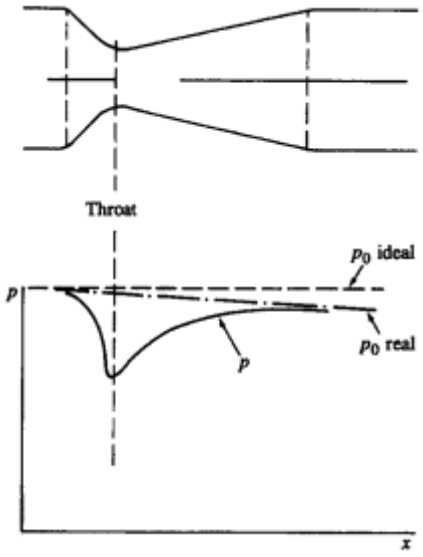

Figure 1.1 – Pressure distribution for gas flow through a nozzle [1]

For the ideal flow, the stagnation temperature and pressure, T_s e p_s, are related to the conditions at other locations in the duct by the steady flow energy equation and isentropic relation below [1].

$$T_s = T + \frac{v^2}{2c_p} \tag{1.10}$$

$$\frac{T}{T_s} = \left(\frac{p}{p_s}\right)^{\frac{\gamma-1}{\gamma}} \tag{1.11}$$

By introducing the Mach number, the following equations are obtained:

$$\frac{T_s}{T} = 1 + \frac{\gamma - 1}{2} M^2 \tag{1.12}$$

$$\frac{p_s}{p} = \left(1 + \frac{\gamma - 1}{2} M^2\right)^{\frac{\gamma}{\gamma-1}} \tag{1.13}$$

where Mach number M is:

$$M = \frac{v}{\sqrt{\gamma RT}} \tag{1.14}$$

The mass flow rater W is:

$$W = \rho A v \tag{1.15}$$

With the ideal gas law and the above equations for p and T, the mass flow rate can be rearranged as follows:

$$\frac{W_{ideal}\sqrt{\gamma RT_s}}{Ap_s} = \gamma M \left(1 + \frac{\gamma - 1}{2} M^2\right)^{\frac{-(\gamma+1)}{2(\gamma-1)}} \tag{1.16}$$

$$\frac{W_{ideal}\sqrt{\gamma RT_s}}{Ap_s} = \gamma \left(\frac{p}{p_s}\right)^{\frac{1}{\gamma}} \left\{\frac{2}{\gamma - 1}\left[1 - \left(\frac{p}{p_s}\right)^{\frac{\gamma-1}{\gamma}}\right]\right\}^{\frac{1}{2}} \tag{1.17}$$

For given value of p_s and T_s, the maximum mass flow occurs when the velocity at the minimum area of throat equals the velocity of sound. This condition is called choked or critical flow. When the flow is choked the Mach number at the throat is equal to 1, thus the pressure at the throat p_T is related to the stagnation pressure p_s as follows:

$$\left(\frac{p_T}{p_s}\right)_{cr} = \left(\frac{2}{\gamma + 1}\right)^{\frac{\gamma}{\gamma-1}} \tag{1.18}$$

This ratio is called the critical pressure ratio and is equal to 0.528 for γ=1.4 and 0.546 for γ=1.3.

For a real gas flow, the discharge coefficient is introduced. Then, for subcritical flow, the real mass flow rate is given in terms of conditions at the minimum area of throat by:

$$W_{real} = \frac{C_D A_T p_s}{\sqrt{RT_s}} \left(\frac{p_T}{p_s}\right)^{\frac{1}{\gamma}} \left\{\frac{2\gamma}{\gamma - 1}\left[1 - \left(\frac{p_T}{p_s}\right)^{\frac{\gamma-1}{\gamma}}\right]\right\}^{\frac{1}{2}} \tag{1.19}$$

For a choked flow, by substituting Equation (1.18) into Equation (1.19), the real mass flow is given by equation below.

$$W_{real} = \frac{C_D A_T p_s}{\sqrt{RT_s}} \gamma^{\frac{1}{2}} \left(\frac{2}{\gamma+1}\right)^{\frac{\gamma+1}{2(\gamma-1)}} \tag{1.20}$$

Flow coefficient are determined experimentally and are a function of the shape of the passage, the Reynolds number and Mach number of the flow, and the gas properties [1]. For a Mach number at the throat less than about 0.7 and for passages of similar shape, the flow coefficient is essentially a function of Reynolds number only [1].

For flow rates less than about 60 percent of the choked flow, the effects of compressibility on the mass flow are less than 5 percent [1]. Therefore, if the difference between upstream and downstream pressure is small and always falls into sub-critical flow region, the flow rate can be calculated by a linearized form of the sub-critical real flow equation (1.19) as follows [2]:

$$W = k\left(p_{upstream} - p_{downstream}\right) \tag{1.21}$$

where k is the nozzle constant, obtainable from an experimental measurement, carried out in stationary conditions, of real mass flow rate, upstream and downstream pressure of each components characterized by orifice equation.

1.3 Hydrogen Properties

Hydrogen is a chemical element with symbol H and atomic number 1. With a standard atomic weight of 1.008, hydrogen is the lightest element on the periodic table. Its monatomic form (H) is the most abundant chemical substance in the Universe, constituting roughly 75% of all baryonic mass. The most common isotope of hydrogen is Protium (name rarely used, symbol ^{1}H) composed by one proton and no neutrons, and the other isotopes are Deuterium (^{2}H) and Tritium (^{3}H). All the isotopes of hydrogen form covalent molecules like H_2, D_2 and T_2, because of the single electron in the atom. At standard temperature and pressure, hydrogen is a colourless, odourless, tasteless, non-toxic, non-metallic, highly combustible diatomic gas with the molecular formula H_2. Hydrogen has an ambivalent behaviour towards other elements, occurring as an anion (H^-) or cation (H^+) in ionic compounds, forming covalent bonds, e.g. with carbon, or even behaving like a metal to form alloys or intermetallic compounds at ambient temperature.

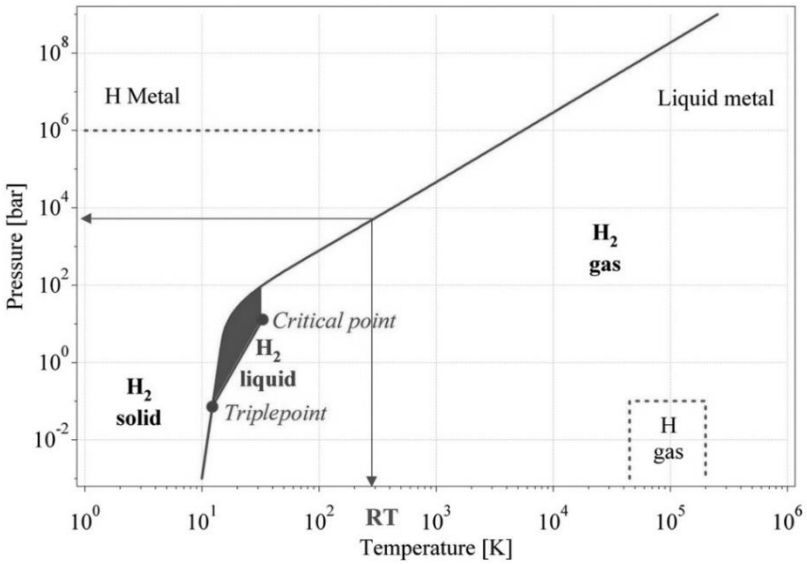

Figure 1.2 – Primitive phase diagram for hydrogen [3] [4]

The primitive phase diagram of the hydrogen molecule H_2 is shown in Figure 1.2. At low temperatures, hydrogen is a solid with a density of 70.6 kg/m^3 at -262°C, and a gas at higher temperatures with a density of 0.089886 kg/m^3 at 0°C and a pressure of 1 bar. Hydrogen is a liquid in a small zone between the triple and critical points with a density of 70.8 kg/m3 at -253°C. At ambient temperature (298.15 K), hydrogen gas is described by the Van der Waals equation:

$$p(V) = \frac{n \cdot R \cdot T}{V - n \cdot b} - a \cdot \frac{n^2}{V^2} \tag{1.22}$$

where p is the gas pressure, V the volume, T the absolute temperature, n the number of moles, R the gas constant, a is the dipole interaction or repulsion constant and b is the

volume occupied by the hydrogen molecules [5]. The strong repulsive interaction between hydrogen is responsible for the low critical temperature (T_c = 33 K) of the gas.
In relation to the hydrogen phase diagram presented in Figure 1.2, Figure 1.3 shows the trend of the density as a function of the hydrogen pressure. In the figure is also visible the regression curve expressed as a third-degree polynomial.

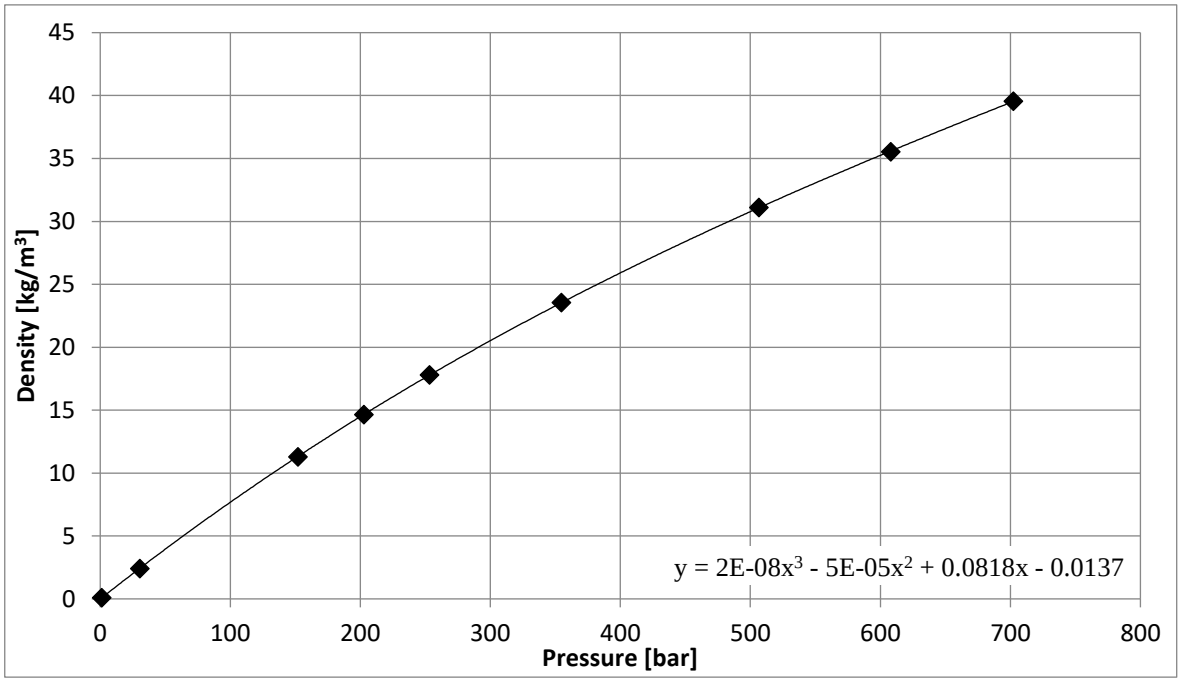

Figure 1.3 – Hydrogen Density as function of pressure (Data from NIST)

When hydrogen reacts with oxygen, H_2O is formed and energy is released. This amount of energy when normalised with the quantity of hydrogen reacted represents the energy density of hydrogen which is distinguished between the low heat value (LHV) and the high heat value (HHV). The differentiation between HHV and LHV is based upon the state of the H_2O products of the reaction. If the H_2O is in the vapour phase the normalised energy released is called the LHV (or net calorific value). On the other hand, if the H_2O is in the form of liquid water then the normalised energy released is called the HHV (or gross calorific value) that is higher than the LHV by about 10% accounting also for the heat of condensation of water vapour into liquid. In most applications, such as high temperature fuel cells, H_2O is produced as steam, therefore the LHV represents more accurately the energy available to do external work. However, in certain applications, such as proton exchange membrane fuel cells, H_2O is produced in liquid form (water); in such a case the use of the HHV of hydrogen is more appropriate.
The energy density of hydrogen can be expressed either on a weight basis (mass energy density) or on a volume basis (volumetric energy density) and it can easily be calculated based on basic thermodynamic principles as described in [6]. The energy released during the "combustion" of hydrogen, i.e. the heat of formation of H_2O, is given by the following equations [5]:

$$H_{2(g)} + {}^{1}/_{2}\, O_{2(g)} \leftrightarrow H_2O_{(g)} \qquad \Delta H_{298.15\,K} = -242\frac{kJ}{mol} \tag{1.23}$$

$$H_{2(g)} + {}^{1}/_{2}\, O_{2(g)} \leftrightarrow H_2O_{(l)} \qquad \Delta H_{298.15\,K} = -286\frac{kJ}{mol} \tag{1.24}$$

Equation (1.23) is applicable when H_2O is produced in a form of vapour and can be used for the calculation of the LHV of hydrogen, while Equation (1.24) is applicable when H_2O is formed as liquid, thus this heat of formation can be used to calculate the HHV of hydrogen [6]. The mass energy density of hydrogen at 298.15 K or 25°C is simply the division between the above-mentioned heats of formation and the molecular weight of hydrogen (i.e. $2.016 \cdot 10^{-3}$ kg). Therefore, the mass energy densities of hydrogen at 25°C are 119.716 MJ/kg (LHV) and 141.500 MJ/kg (HHV) while at 0°C the mass energy densities of hydrogen are 120.131 MJ/kg (LHV) and 141.686 MJ/kg (HHV) [6].

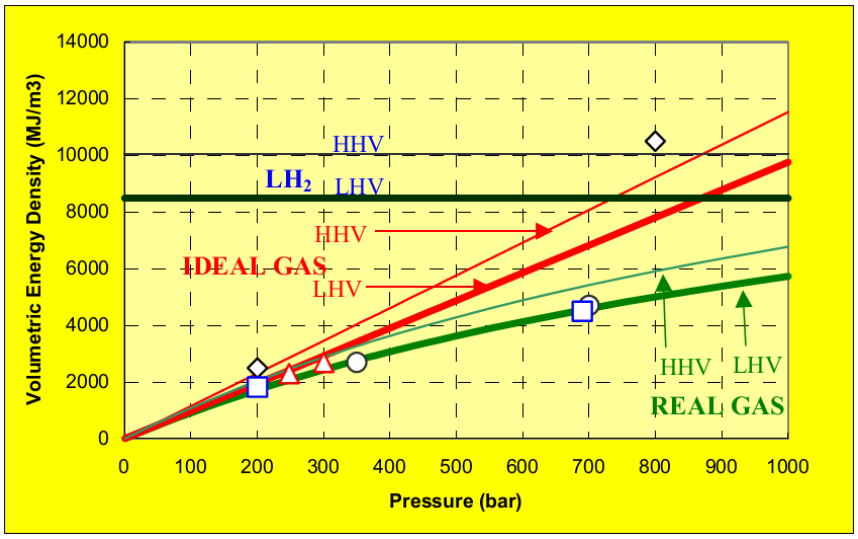

Figure 1.4 – Calculated values for the volumetric energy density of hydrogen against reported values [6]***. LH_2 stands for liquid hydrogen***

Although the discrepancies between the reported values of the volumetric energy density of hydrogen at low pressures are insignificant, reported values at high pressures may vary significantly. Figure 1.4 shows the calculated values (at 20°C) plotted against values reported in the literature [6]. It is clear that the volumetric energy density of compressed hydrogen (LHV) cannot reach the energy density of liquid hydrogen (LH_2) within the practically acceptable storage pressures. Furthermore, the assumption of ideal gas behaviour leads to significant errors in estimating the volumetric energy density of hydrogen.

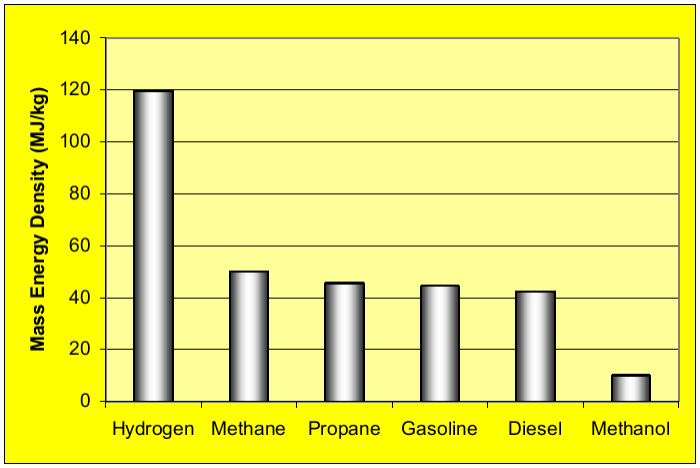

Figure 1.5 – Mass energy density of fuels (LHV) [6]

Compared to other conventional fuels, hydrogen has the highest mass energy density, almost 2.5 times the energy released during the combustion of conventional hydrocarbon fuels (Figure 1.5). Therefore, on a weight basis, the amount of fuel required to deliver a given amount of energy is significantly reduced when hydrogen is utilised. More importantly, hydrogen has the lowest volumetric energy density when compared with conventional fuels, as highlighted by Figure 1.6.

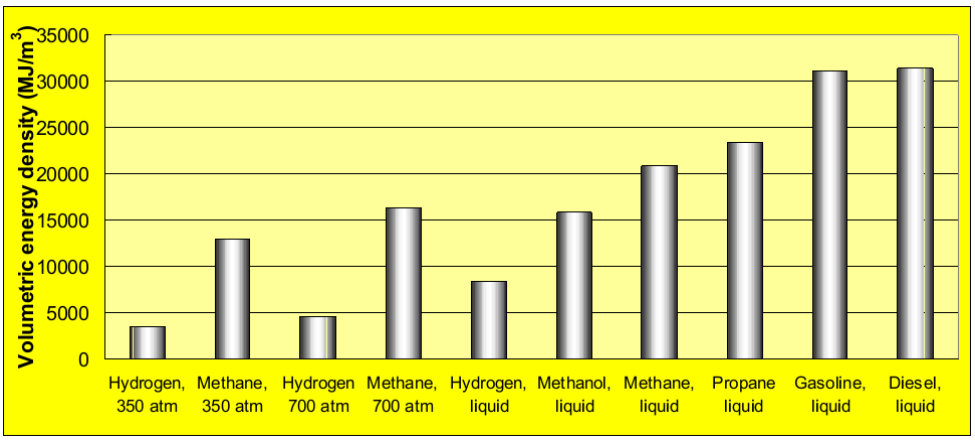

Figure 1.6 – Volumetric energy density of typical types of fuel (LHV) [6]

Hydrogen is a flammable gas and can feed a fire or an explosion under specific conditions, such as mixed with oxygen in certain composition ranges with a concurrent presence of an ignition source. The concentration range in air in which hydrogen is capable of supporting a self-propagating flame when ignited is called the flammability range. Under ambient conditions, hydrogen is flammable over a wide range of concentrations (4-75%) and explosive in a narrower range (15-59%) [6]. The flammability ranges for a number of conventional fuels is shown in Figure 1.7. The upper flammability range of hydrogen, i.e. the highest concentration of hydrogen in air (75- 85% depending on the temperature, as highlighted by Figure 1.8) has important consequences for hydrogen storage: it becomes

evident that hydrogen is not flammable when stored (due to the lack of oxygen). Hydrogen becomes flammable only in the peripheral areas of a leak, where the mixing of hydrogen with air is within its flammability range. Given that hydrogen diffuses very fast, increased chances for a fire and explosion may be encountered when leakage is in an enclosed environment.

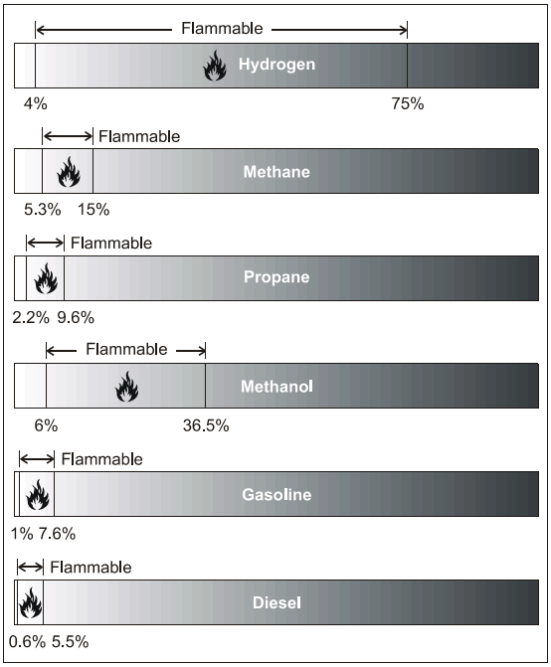

Figure 1.7 – Flammability limits of conventional fuels [6]

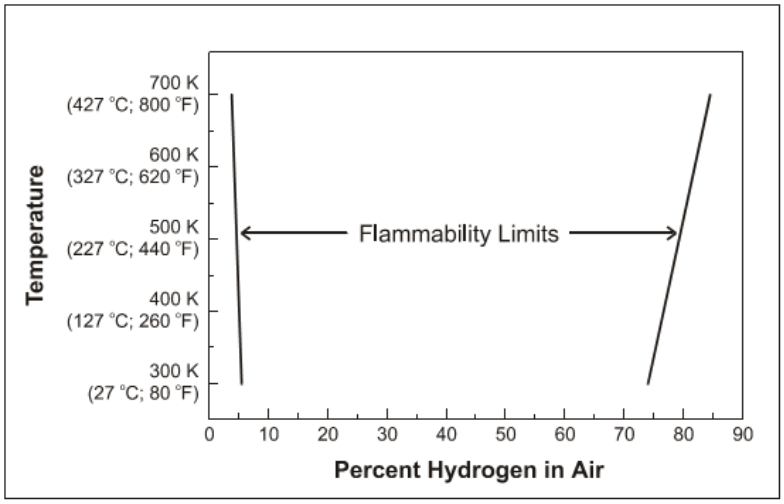

Figure 1.8 – Hydrogen flammability limits as a function of the temperature [7]

Another important property of hydrogen is the auto-ignition temperature, i.e. the minimum temperature required to initiate self-sustained combustion in a combustible fuel mixture in the absence of an ignition source. This temperature for hydrogen is 585°C, higher than any other conventional fuel such as methane (540°C) and gasoline (230-480°C). In the absence of such a high temperature, an appropriate hydrogen mixture can be combusted only by an ignition source such as a flame or a spark. However, the minimum energy required to initiate

combustion (the ignition energy) is 0.03 mJ, almost an order of magnitude lower than that of conventional fuels. Therefore, hydrogen can ignite more easily than other fuels. It is claimed that the energy generated by static electricity discharge or even by the agitation of compressed or liquid hydrogen may generate enough energy to cause ignition [6].

1.4 Introduction to Fuel Cells

Fuel cells are electrochemical devices that convert the chemical energy of a reaction directly into electrical energy. The fuel cell principle was discovered in 1839 by William R. Grove, a Welsh judge and physical scientist. The basic physical structure or building block of a fuel cell consists of an electrolyte layer in contact with a porous anode and cathode on either side [8]. In a typical fuel cell, gaseous fuels are fed continuously to the anode (negative electrode) compartment and an oxidant (i.e., oxygen from air) is fed continuously to the cathode (positive electrode) compartment; the electrochemical reactions take place at the electrodes to produce an electric current [8].

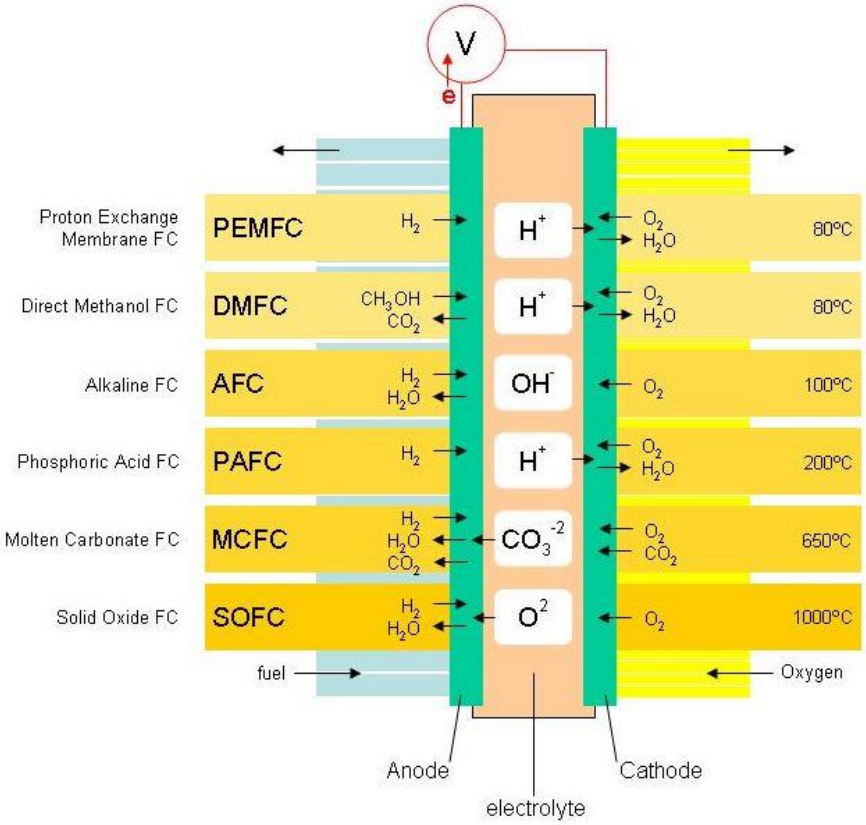

Figure 1.9 – Different fuel cell chemical processes [9]

Some schematic representations of different fuel cell types, with the reactant/product gases and the ion conduction flow directions through the cell, are shown in Figure 1.9. Note that the ion specie (positive or negative) and its transport direction can differ, influencing the site of water production and removal.
In this thesis, the Polymer Electrolyte Membrane Fuel Cell (PEM-FC) has been considered, powered by hydrogen and air. The overall reaction of this fuel cell type is:

$$H_2 + \frac{1}{2} O_2 \Rightarrow H_2O \tag{1.25}$$

In detail, hydrogen gas reacts on the anode electrode, with the help of a platinum catalyst, separating into electrons and hydrogen protons as follows:

$$H_2 \Rightarrow 2H^+ + 2e^- \tag{1.26}$$

The hydrogen electrons flow through an external circuit creating electric current, while hydrogen protons pass through the electrolyte to the cathode electrode and combine with oxygen molecules provided by cathode air mass flow producing water, according to the following equation.

$$\frac{1}{2} O_2 + 2H^+ + 2e^- \Rightarrow H_2O \tag{1.27}$$

The process of direct conversion of chemical fuel energy into electrical energy allows fuel cells to obtain a major energy efficiency with respect to the traditional processes of energy conversion as, for example, internal combustion engines (ICE). In ICE, fuel chemical energy is firstly converted into thermal energy by combustion, and only later is transformed into mechanical energy. Since thermal energy is involved, the efficiency of the process is limited by the Carnot cycle, a limitation that does not apply to fuel cells. Furthermore, if pure hydrogen is used as fuel into a fuel cell, the outcome is composed only by electric current, water and heat, without typical pollutants usually present in ICE emissions as unburned hydrocarbons, carbon dioxide and monoxide, nitrogen oxide or sulphur oxide.

1.4.1 Fuel Cell Composition

Figure 1.10 shows the chemical reactions and the structure of typical PEM-FCs. This kind of fuel cells has good performance related to: high power density, a polymeric electrolyte with good mechanical resistance, long life as well as low corrosion. PEM fuel cells operate in the temperature range of 50÷100°C that allows safe operation and reduces the need of thermal insulation.

Standard electrolyte material currently used in PEM-FCs is composed by fluorinated Teflon-based material originally produced by E.I. DuPont de Nemours for NASA space application in the mid-1960s. The DuPont electrolytes usually make use of special Teflon support know with the brand name Nafion. The most used electrolyte membrane for PEM-FCs is the Nafion 117 [8]. The Nafion membranes, which are fully fluorinated polymers, exhibit exceptionally high chemical and thermal stability and are stable against chemical attack in strong bases, strong oxidizing and reducing acids, H_2O_2, Cl_2, H_2, and O_2 at temperatures up to 125°C [8]. Nafion consists of a fluoropolymer backbone, similar to Teflon, upon which sulfonic acid groups $SO_3^-H^+$ are chemically bonded. When the membrane is hydrated, the hydrogen ions H^+ in the sulfonic groups are mobile. DuPont fluorinated electrolytes have achieved over 50,000 hours of operation [8].

The electrolyte membrane is sandwiched between anode and cathode electrodes usually composed by carbon nanoparticles and a small amount of platinum applied to increase the rate of chemical reaction (Figure 1.10). The three components (electrolyte membrane, anode and cathode electrodes) are sealed together to form a single Membrane Electrode Assembly MEA.

Most PEFCs currently use machined graphite plates for current collection and distribution, gas distribution and thermal management [8] while others still use metallic plates. Sometimes these plates are schematized in two different layers: anode or cathode channel and corresponding gas diffusion layers (Figure 1.10). Cooling is accomplished by using a heat transfer fluid, usually water, which is pumped through integrated coolers within the stack. The temperature rise across the cell is kept to less than 10°C [8]. Water-cooling and humidification are in series, which results in a need for high quality water.

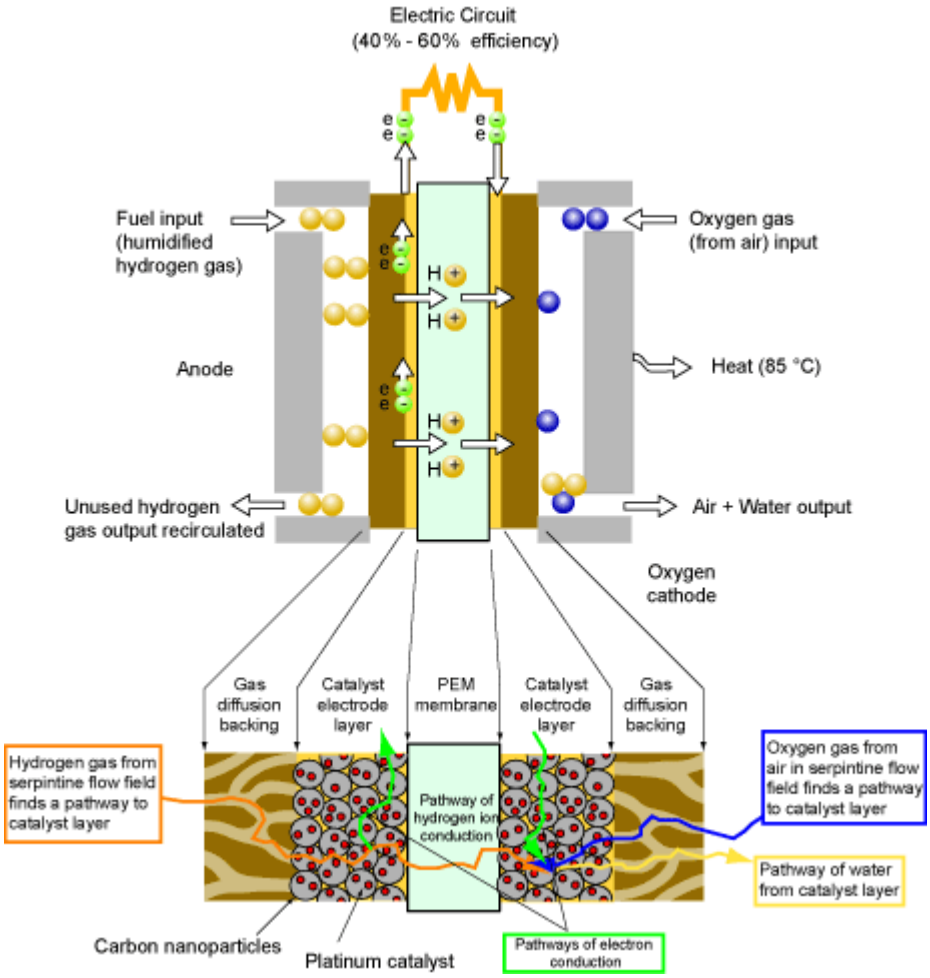

Figure 1.10 – PEM fuel cell structure [10]

The performance of a fuel cell is normally represented by a polarization curve, which is a plot of cell voltage versus cell current density (current per unit cell active area, A/cm^2).

The operative voltage produced by one cell is in general between 0 and 1 volts, depending mainly on fuel cell typology and operating conditions. An average value of PEM fuel cell

voltage can be considered equal to 0.7 volts. To get higher voltage, many cells are stacked in series. Therefore, the total stack voltage is the sum of all cell voltages that can be approximated by the average voltage multiplied by the number of cells. The maximum value of cell current density is a characteristic of the considered fuel cell type is normally between $0 \div 2$ A/cm^2.
Figure 1.11 shows a generalized polarization curve, presented in [11], where the regions of influence of the voltage losses are also visible.

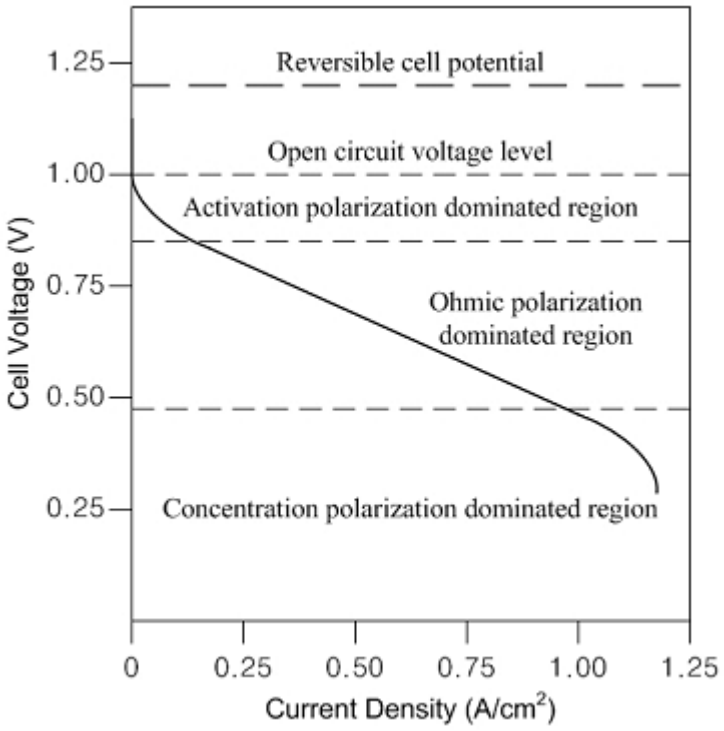

Figure 1.11 – Generalized polarization curve of a fuel cell [11]

1.5 PEM-FC Models Introduction and Overview

The first purpose of this thesis is to create a dynamic model able to simulate electrochemical, dynamic and thermal effects, while other effects, such as spatial variation of parameters, are lumped and included in ordinary differential equations or different equation forms. Another important target of this model is to be more general, adaptable and flexible as possible, in order to be easily set on different type of PEM fuel cell systems.
Being interested in the development of a dynamic model, it is important to analyse the orders of magnitude of the simulated phenomena, to justify the choices made in the following. The relevant time constant for a PEM-FC system are summarized as follows [2]:

- Electrochemistry O (10^{-19} s)
- Hydrogen & manifolds O (10^{-1} s)
- Membrane water content O (unclear)
- Flow control/supercharging devices O (10^{0} s)

- Cell and stack temperature O (10^2 s)

where O stands for the order of magnitude. The extremely fast transient phenomena of both electrochemical reactions and electrode electrical dynamics have minimal effects on the PEM fuel cell global dynamics and hence can be ignored. The transient behaviours due to manifold filling dynamics, membrane water content, supply devices and temperature control may impact the behaviour of the PEM-FC, and thus, are included in the model [2]. Interactions between processes, when appropriate, are also included. However, with relatively slow responses, the stack temperature may be viewed as a separate control system which is equipped with a separate controller [2].
The block diagram of a typical PEM-FC system, showing the subsystem blocks along with input/output signals, is visible in Figure 1.12.

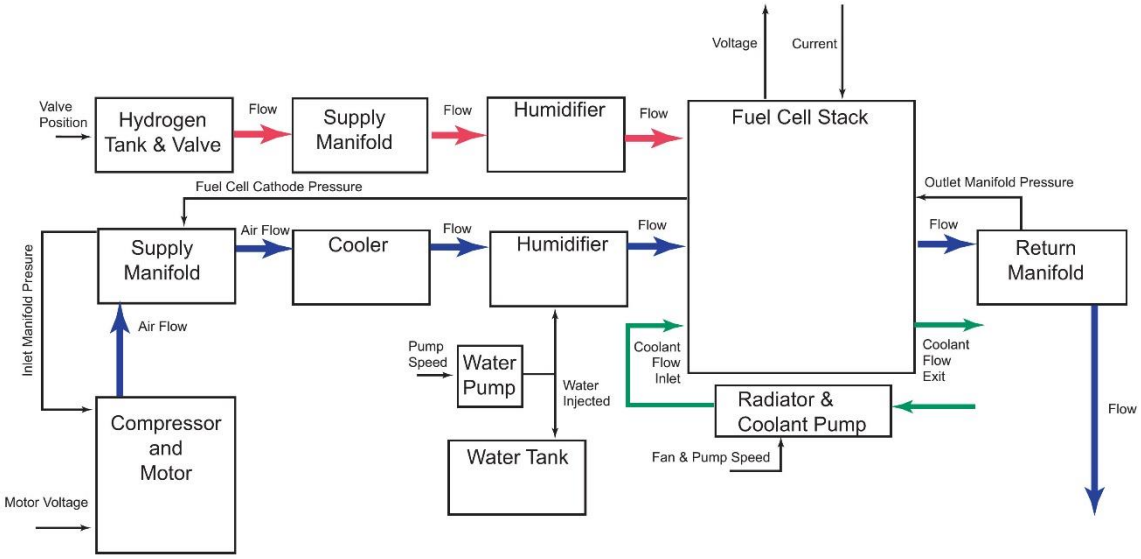

Figure 1.12 – System block diagram [2]

The development of a dynamic model of a fuel cell reactant supply subsystem is explained in Sections 2 and 3. The model incorporates the transient behaviours that are important for integrated control design and analysis. Models of the auxiliary components, namely a hydrogen supply valve, a compressor, manifolds, humidifiers and the temperature control are presented in Section 3. The compressor model is an ideal model with appropriate delays to simulate the dynamic behaviour. The manifold dynamic models are based on lumped-volume filling dynamics [2]. Static models of the humidifiers are developed using thermodynamics.
The fuel cell stack model in Section 2 is composed of four interacting sub-models, namely stack voltage, cathode flow, anode flow, and membrane hydration models [2]. The stack voltage is calculated in Section 2.1 based on the Nernst potential, activation, Ohmic and concentration losses. Flow equations, mass continuity, and electrochemical relations are used to create lumped-parameter dynamic models of the flow in the anode and cathode in Sections 2.3 and 2.4 [2]. Mass transport of water across the fuel cell membrane is calculated

in the membrane hydration model in Section 2.2 [2] and the stack thermal balance considered is presented in Section 2.5.
An ideal control of air supply from the compressor, a perfect control of hydrogen and air humidifiers and an ideal control of the hydrogen supply valve are integrated into the model.
In Section 4 are presented the stack voltage validation and the PEM-FC system validation, performed with experimental data measured by Laurencelle et al. in [12] using a Ballard MK5-E 4 kW PEM-FC system. The model predicts transient behaviour similar to that reported in the literature. Despite the impossibility to perform the thermal model validation against literature data referred to the PEM fuel cell taken from [12], in Section 4.3 some thermal simulations, with relative observations, are presented.
Appendix A shows the differential evolution algorithm developed for the regression of the experimental polarization curves. This algorithm results very effective, fast and flexible and is able to set the model of the polarization curve on the experimental data, obtaining all the unknown or desired stack voltage model parameters, summarized in Section 2.1.5. This algorithm is used to obtain the parameters of the stack voltage models both for the Ballard MK5-E PEM-FC system in Section 4.1 and for the Nuvera Orion Stacks in Section 6.1, despite the different approach used to represent the polarization curves of these stacks.
In fact, in Section 6, the dynamic model of the HI-SEA laboratory PEM-FC system is introduced. The HI-SEA laboratory is composed by two cooling and electrical branches with 4 PEM-FC stacks Nuvera Orion of 30 kW each. For these kind of fuel cells, detailed information about, for example, the characteristic geometrical dimensions and chemical composition of the polymeric membrane are not available. Moreover, the balance of plant is very impacting especially in fluid dynamics and thermal terms. Therefore, the dynamic model developed is a simplification of the general model developed and exposed in Section 2 and 3, with the aim to realize the most possible detailed model based on the characteristic PEM-FC data normally available in the market, with a special focus on the cooling circuit that strongly influences the performance and dynamic response of the stacks and for which most of the data necessary for the dynamic model can be obtained directly and manually from the plant.

1.6 Literature Review and Model Analysis

The models developed in the literature can be classified into three main categories, namely, fuel cell performance models, steady-state fuel cell system models, and dynamic fuel cell system models [13]. Another important classification divides the models in fully theoretical models, fully empirical or semi-empirical models. When many data are available, and the purpose of a dynamic model is to represent to the best the behaviour of a fuel cell, a fully empirical model or a semi-empirical model are used. Theoretical models, instead, well represent all the involved phenomena but usually are less precise. Therefore, in order to create a dynamic model more adaptable as possible, a semi-empirical model is developed to unite the general validity of the theoretical approach and the accuracy of the results guaranteed by an empirical model.

Most of the publications referred to fuel cell modeling have targeted the fuel cell performance prediction. Models in this category are mostly steady-state. They are developed at the cell level and include spatial variations of the fuel cell parameters. Complex electrochemical, thermodynamic and fluid mechanics principles are used to develop these models. The performance or efficiency of the fuel cell under different steady-state operating conditions can be determined using this type of model [13]. The main purposes of these models are to design the fuel cell components and to choose the fuel cell operating points. While these models are not suitable for dynamics studies, they establish the fundamental effects of operating parameters, such as pressure and temperature, on the fuel cell voltage. Many studies ([14]–[19] and [12], [20]–[22]) presented the formulation of fuel cell resistances which is used to predict fuel cell polarization characteristics at different operating conditions. Mass transport of gas and water was also included in several publications ([15], [14] and [23]) with one-dimensional models. Springer et al. [23] presented a model predicting net water flow per proton through the membrane and the increase in membrane resistance due to the membrane water content. Many publications addressed the water and thermal management of the fuel cell. Nguyen and White [24] developed a model investigating the effectiveness of various humidification designs. Fuller and Newman [25] developed a two-dimensional mass transport model of membrane electrode assembly to examine the water, thermal and reactant utilization of the fuel cell. A three-dimensional numerical model that predicts the mass flow between the cathode and anode channels was presented in [26]. A model predicting transient responses of the fuel cell stack was given in [27]. The heat transfer transient phenomena were incorporated into this model. All the papers in the above category used a combination of experiments and physical laws to derive their models.

Laurencelle et al. [12] presented experimental results of fuel cell stack responses during load transitions. The transient behaviour of stack voltage during positive and negative load switching was observed in the experiment.

Steady-state system models are typically used for component sizing, static trade-off analysis, and cumulative fuel consumption or hybridization studies [13]. The models in this category represent each component such as the compressors, heat exchangers, and fuel cell stack voltage as a static performance or efficiency map [13].

Several studies concern the membrane hydration. Springer et al. in [23] developed the one-dimensional polymer electrolyte model still more used, measuring in laboratory, at 30°C, water diffusion coefficient, electro-osmotic drag coefficient and membrane conductivities of a Nafion 117 membrane, as function of the membrane water content. Similar approaches have been proposed by Dutta et al. in [26], Nguyen and White [24] in and Motupally et al. in [28] for Nafion 115. A quasi-3D water transport model for PEM fuel cell was developed by Kulikovsky in [29]. Wu et al. in [30] used the Kulikovsky approach to create a non-isothermal transient model of water transport for PEM fuel cell. Recent studies, conducted by Ge et al. in [31] and [32], suggest a new approach on the basis of their measurements of absorption, desorption, transport of water and electro-osmotic drag coefficient in polymer electrolyte membranes at different temperatures.

Several dynamic fuel cell system models exist in the literature. Different levels of dynamic behaviour were incorporated into each of the models. The thermal dynamics are considered to be the slowest dynamics in the fuel cell system. Therefore, several publications have included only the temperature dynamic in their models and ignored the other dynamics such as air supply and humidity, but neither modeling details nor simulation results were given in these papers [13].

Probably the most complete model in the literature is the comprehensive control-oriented model developed by Pukrushpan in [13], even if the thermal dynamic was neglected due to the target of automotive applications, with dynamic responses faster than thermal dynamic.

Therefore, the model developed in this thesis is completely based on the work explained in [13]. However, despite the logical framework appears very similar, the model is also very different because it has been developed with different purposes. This model was developed to create a dynamic model able to simulate all the dynamic effects, including thermal transients, and also to be more general, adaptable and flexible as possible, in order to be easily set on different type of PEM fuel cell systems. For this reason, the presented model uses a more theoretical approach to simulate the fuel cell performance, i.e. the polarization curve of the PEM-FC, and a simpler approach to simulate the other auxiliary components of the PEM-FC system. All the sub-models are developed to be easily adaptable as possible.

In particular the stack voltage model is developed on the basis of the Nernst voltage, activation loss model described by Amphlett et al. in [15] or by Mert at al. in [22], Ohmic loss model related to the membrane hydration model, explained by Springer et al. in [23] or by Mann et al. in [21], and the generic concentration loss model presented in [8]. Therefore, the stack voltage model can be represented by two different set of equations, to better adapt to different types of stack. The flexibility of this stack voltage model is assured by the differential evolution algorithm, developed based on the works presented in [33], [34] and [35], and able to calculate all the stack parameters desired using at limit one polarization curve. Obviously, with more polarization curves available, the model is more accurate.

The anode and cathode mass flow models take into account all the hydrogen, air, vapor and liquid water mass flows into the fuel cell. Thus, the mass flow models are able to simulate the condensation of the liquid water inside the fuel cell channels. In this thesis a dead-end fuel cell has been considered, but the anode flow model already includes a tool able to simulate the anode timed purge, for a future development concerning the nitrogen diffusion through the membrane and its consequent purge.

After a detailed comparison of the models available and developed in the last years, the membrane hydration model is based on the Springer et al. approach reported in [23]. This approach allows to calculate the water content of the membrane reported at 30°C and then, with thermal correction factors, to obtain the net water flow across the membrane and the membrane conductivity.

The manifolds, humidifiers and air compressor models are similar to those developed by Pukrushpan in [13], while the hydrogen supply model is an ideal and simplified model to make the complete model easily adaptable to different PEM-FC systems.

At last, the stack thermal model is developed based on the thermal balance of the fuel cell, considering also the heat supplied or removed by the inlet and outlet mass flows.

2 PEM-FC Model: Fuel Cell Stack

The fuel cell stack model, developed starting from the model presented in [2], contains four interacting sub-models which are the stack voltage, the anode mass flow, the cathode mass flow, the membrane hydration and the stack thermal models. A block diagram of the PEM fuel cell stack model is shown in Figure 2.1.

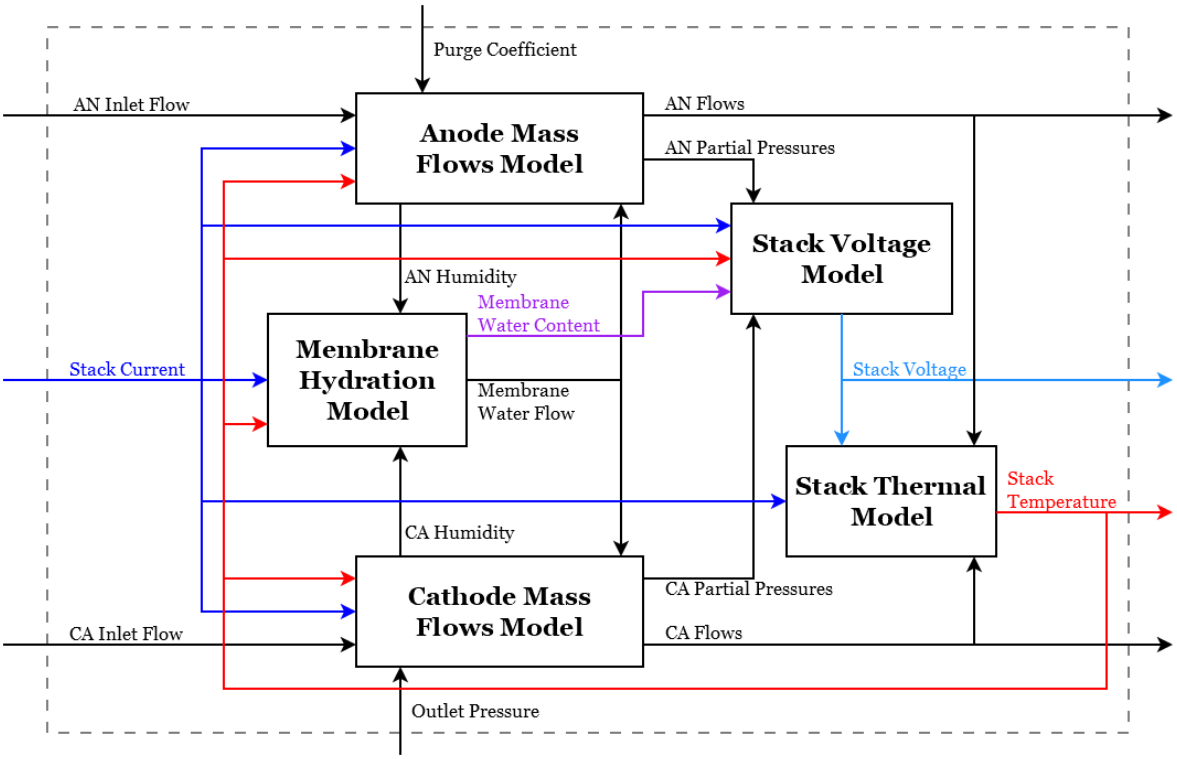

Figure 2.1 – Block diagram of fuel cell stack model

In the stack voltage model, a set of operating conditions such as reactant gas partial pressures, cathode pressure, stack temperature, stack current and membrane humidity are used to calculate the stack voltage. The cathode and anode flow models use mass conservation along with thermodynamic properties to calculate the pressure and the relative humidity of the reactant gas flows inside the stack flow channels [2]. The membrane hydration model uses stack current and the anode and cathode humidity to calculate the humidity of the membrane and the net water flow across the membrane. The stack thermal model performs the energy balance of the PEM fuel cell to obtain the stack temperature, assumed to be uniform over the whole stack. In this section, these five sub-models are presented and, for the stack voltage and the membrane hydration models, different modeling approaches are introduced, identifying the best sets of equations.

2.1 Stack Voltage Model

In this Section, the fuel cell stack voltage model is discussed. The inputs and the outputs of this model are schematized in Figure 2.2.

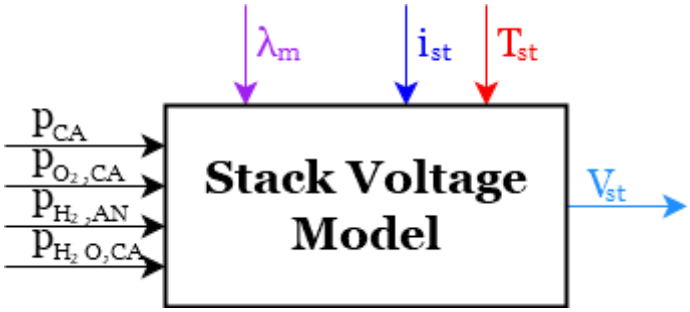

Figure 2.2 – Block diagram of stack voltage model

In the first sub-section, the chemical energy released from the fuel cell is calculated from the Gibbs free energy of the reactants. The available energy to produce external work is calculated from Gibbs free energy and corrected in terms of temperature, pressure and concentration, obtaining the Nernst equation.
The real stack voltage is less than the Nernst voltage due to three irreversible losses: activation, Ohmic and concentration loss, discussed in the related sub-sections. Different approaches for every loss are available in literature and, in the next sections, the most widespread ones are presented. The activation loss model is developed on the basis of the semi-empirical model developed by Amphlett et al. in [14] and [15], recently used in [36] [37] [38], or alternatively on the basis of the Mert et al. work [22], adopted in recent work [39] [40] [41] [42]. The Ohmic loss model is developed on the basis of the empirical model proposed by Springer et al. in [23], directly related to the membrane hydration model exposed in Section 2.2, or alternatively on the basis of the Mann et al. model [21]. For concentration loss a theoretical model and an entirely empirical model are proposed as reported in [8], even if for practical applications the empirical model is recommended, for its better adaptability and precision to the real performance of the fuel cell systems.

2.1.1 Nernst Equation

The fuel cell directly converts the chemical energy of the fuel into electrical energy. The chemical energy released from the fuel cell can be calculated from the change in Gibbs free energy, which is the difference between the Gibbs free energy of the product (liquid water) and the Gibbs free energy of the inputs or reactants (hydrogen and oxygen). For the hydrogen/oxygen fuel cell, the basic chemical reaction is:

$$H_2 + \frac{1}{2}O_2 \leftrightarrows H_2O \tag{2.1}$$

The change in the Gibbs free energy, referring to standard state (pressure = 1 bar), is:

$$\Delta g_f^o = \left(g_f^o\right)_{H_2O} - \left(g_f^o\right)_{H_2} - \left(g_f^o\right)_{O_2} \tag{2.2}$$

The change in the Gibbs free energy Δg_f varies with both temperature and pressure and it is calculate as follows:

$$\Delta g_f = \Delta g_f^o - \frac{RT_{st}}{nF} \ln \left[\frac{p_{H_2} \left(p_{O_2}\right)^{0.5}}{p_{H_2O}} \right] \tag{2.3}$$

where Δg_f^o is the change in Gibbs free energy at standard pressure (1 bar) and at ambient temperature (25°C) calculated using Equation (2.2). The change in the Gibbs free energy Δg_f depends on temperature of the fuel cell T_{st} and on the partial pressure terms, commonly referred to the partial pressure at the anode and cathode channels.

If the fuel cell process was "reversible", all the Gibbs free energy would be converted to electrical energy, which corresponds to the electrical work used to drive the electrical charge through the external circuit. For each mole of hydrogen two moles of electrons pass in the external circuit (n = 2), therefore the electrical work done (charge · voltage) is:

$$Electrical\ work\ done = -nFE \tag{2.4}$$

The electrical work could be equal to the change in Gibbs free energy if the system is considered reversible:

$$\Delta g_f = -nFE \tag{2.5}$$

Therefore, using Equation (2.3), the reversible voltage of the fuel cell is expressed by the following equation, also called Nernst equation:

$$E = E^o - \frac{RT_{st}}{nF} \ln \left[\frac{p_{H_2} \left(p_{O_2}\right)^{0.5}}{p_{H_2O}} \right] \tag{2.6}$$

where the partial pressures are normally referred to the anode and cathode channels and E^o is the standard state reference potential, also called Open Circuit Voltage OCV, and varies with the temperature of the fuel cell.

A more detailed approach, proposed by Amphlett et al. in [15], considers the partial pressure terms (in atm) correspond to the concentration $c_{H_2}^*$ and $c_{O_2}^*$ at the interface of the gas diffusion layer (anode and cathode) and the water film surrounding the catalyst sites. With this hypothesis and considering that PEM fuel cells always work at low temperature (less than 100°C), the water produced at the cathode site is considered in liquid form, therefore the liquid water partial pressure at gas/liquid interface is equal to one and the Nernst equation becomes [15]:

$$E = E^o - \frac{RT_{st}}{nF} \ln \left[p_{H_2}^* \left(p_{O_2}^*\right)^{0.5} \right] \tag{2.7}$$

The Standard Atmosphere Pressure and Temperature state (SAPT), equal to 298.15 K and 1 atm, permits to define a SAPT reference potential E_0^o equal to 1.229 V. Therefore, the standard state reference potential E^o varies from the SAPT state reference in accordance with temperature as presented in the following equation, where T_0 is the standard state temperature equal to 298.15 K [15].

$$E^o = E_0^o + (T_{st} - T_0)\frac{\Delta S^o}{nF} \tag{2.8}$$

The entropy change of a given reaction is approximately constant (the variation in specific heat with the expected changes in temperature is minimal) and can be set to the standard state value [15]. Thus the OCV varies directly with temperature as follows [15]:

$$E^o = 1.229 - 298.15\frac{\Delta S_0^o}{nF} + \frac{\Delta S_0^o}{nF}T_{st} \tag{2.9}$$

Using literature values for the standard state entropy change, the value of $\Delta S_0^o/nF$ in this equation is calculated to be -0.85·10^{-3} V/K [15]. Therefore, Equation (2.7) can be written as follows:

$$E = 1.229 - 0.85 \cdot 10^{-3}(T_{st} - 298.15) + \frac{RT_{st}}{nF}\ln\left[p_{H_2}^*\left(p_{O_2}^*\right)^{0.5}\right] \tag{2.10}$$

Differently from the approach adopted by Amphlett et al. in [15], the hydrogen and oxygen partial pressures can considered at the anode and cathode channels, offsetting this simplification with the introduction of the concentration loss, not considered in the Amphlett model, to take account of the mass transport and diffusion along the gas diffusion layer. This approach is commonly adopted [14]-[21] and , thus the Equation (2.10) can be expressed as follows:

$$E = 1.229 - 0.85 \cdot 10^{-3}(T_{st} - 298.15) + \frac{RT_{st}}{nF}\left[\ln\left(p_{H_2}\right) + \frac{1}{2}\ln\left(p_{O_2}\right)\right] \tag{2.11}$$

2.1.2 Activation Loss

The activation loss or activation overvoltage depends on the energy losses related to electron transfer and to continuous breaking and forming of chemical bonds at the anode and cathode. Part of the available energy is lost in driving the chemical reaction that transfer the electrons to and from the electrodes [43].

2.1.2.1 Amphlett et al. [14]

In the solid polymer fuel cell models available in literature, the kinetics of hydrogen oxidation on platinum have been considered very rapid. Consequently, the voltage drop due to activation can be predominantly attributed to the cathode reaction [14].
When mass transfer effects are negligible, reaction kinetics can be described by the Butler-Volmer equation [14]:

$$i_{st} = i_0 \left[e^{\frac{-\alpha n F \eta_{act}}{RT_{st}}} - e^{\frac{(1-\alpha) n F \eta_{act}}{RT_{st}}} \right] \tag{2.12}$$

Considering the general electrode process of Equation (2.13), the exchange current i_0 is provided by Equation (2.14).

$$aA + ne^- \leftrightarrows bB \tag{2.13}$$

$$i_0 = nFA_{cs}k^0 \left[e^{\frac{-\Delta F_e}{RT_{st}}} \cdot (c_A^*)^{a(1-\alpha)} \cdot (c_B^*)^{b\alpha} \right] \tag{2.14}$$

where:

- n is the number of electrons involved per mole of electrolyzed component in the rate controlling step;
- a and b represent the appropriate reaction orders of the rate controlling step with respect to the reactant and product;
- A_{cs} is the cross-sectional surface area over which the reaction is occurring;
- k^0 is the intrinsic rate constant;
- ΔF_e is the standard free energy of activation for the reaction [14].

The constant α is called the charge transfer coefficient and is the proportion of the electrical energy applied that is harnessed in changing the rate of an electrochemical reaction [43]. Its value depends on the reaction involved and on the material the electrode is made from, but it must be in the range 0 to 1.0. For the hydrogen electrode, its value is about 0.5 for a great variety of electrode materials [43]. At the oxygen electrode, the charge transfer coefficient shows more variation, but is still between about 0.1 and 0.5 in most circumstances [43]. Thus α is usually considered equal to 0.5 for cathode and anode electrodes.
For large values of η_{act}, the second exponential in Equation (2.12) is negligible, yielding the cathode Tafel expression below:

$$\eta_{act\_CA} = -\frac{RT_{st}}{\alpha nF} \ln\left(\frac{i_{st}}{i_0}\right) \tag{2.15}$$

Given the relatively high overvoltage of the cathode reaction, its kinetics can be described as following. Thus the cathode activation overvoltage can be expressed as [14]:

$$\eta_{act\_CA} = \frac{RT_{st}}{\alpha_c nF} \left\{ \ln\left[nFA_{cs}k^0 e^{\frac{-\Delta F_e}{RT_{st}}} \left(c_{O_2}^*\right)^{(1-\alpha_c)} \left(c_{H^+}^*\right)^{(1-\alpha_c)} \left(c_{H_2O}^*\right)^{\alpha_c} \right] - \ln(i_{st}) \right\} \tag{2.16}$$

where α_c represents the cathode transfer coefficient.
Given the assumption of constant water concentration at the membrane/cathode interface, the proton concentration in Equation (2.16) is constant, as the terms k^0, A, n, F, R, ΔF_e and α_c [14]. The only remaining variables are the concentration of oxygen at the reaction sites, the current and the temperature.
The activation overvoltage of the hydrogen oxidation reaction can be defined by anode Tafel expression, obtainable from the Equation (2.12) neglecting the first exponential:

$$\eta_{act\_AN} = -\frac{RT_{st}}{2F}\ln\left(\frac{i_{st}}{i_0}\right) \tag{2.17}$$

As the rate controlling step at the anode is likely to be chemisorption of hydrogen, Berger suggests that the exchange current can be defined as [14]:

$$i_{0\,AN} = 4FA_{cs}k^0 \cdot e^{\frac{-(\Delta F_{ec}-0.5\Delta F_c)}{RT_{st}}} \cdot c^*_{H_2} \cdot e^{\frac{-0.5\Delta F_c}{RT_{st}}} \tag{2.18}$$

where ΔF_{ec} is the standard state free energy of activation for chemisorption and ΔF_c is the standard state free energy of chemisorption from the gas state. Thus the activation overvoltage at the anode can be defined as [14]:

$$\eta_{act\_AN} = \frac{RT_{st}}{2F}\left\{\ln\left[4FA_{cs}k^0 \cdot e^{\frac{-(\Delta F_{ec}-0.5\Delta F_c)}{RT_{st}}} \cdot c^*_{H_2} \cdot e^{\frac{-0.5\Delta F_c}{RT_{st}}}\right] - \ln(i_{st})\right\} \tag{2.19}$$

The variation in hydrogen concentration in the inlet fuel flow for most low pressure fuel cell applications is expected to be relatively small ($x_{H_2} > 0.75$, 2atm < p < 4atm), thus the resulting change in activation overvoltage is less than 0.010 V [14]. Therefore, for most empirical modeling applications, the hydrogen concentration term in Equation (2.19) can be approximated as a constant [14].

The total activation overvoltage for a fuel cell is the sum of the anode and cathode overvoltages. The following equation represents the total activation overvoltage in parametric form [14]:

$$\eta_{act} = \xi_1 + \xi_2 T_{st} + \xi_3 T_{st}\ln\left(c^*_{O_2}\right) + \xi_4 T_{st}\ln(i_{st}) \tag{2.20}$$

Where the constant parametric coefficients are:

$$\xi_1 = \left(\frac{-\Delta F_e}{\alpha_c nF}\right) + \left(\frac{-\Delta F_{ec}}{2F}\right) \tag{2.21}$$

$$\xi_2 = \frac{R}{\alpha_c nF}\ln\left[nFA_{cs}k^0\left(c^*_{H^+}\right)^{(1-\alpha_c)}\left(c^*_{H_2O}\right)^{\alpha_c}\right] + \frac{R}{2F}\ln\left(4FA_{cs}k^0 c^*_{H_2}\right) \tag{2.22}$$

$$\xi_3 = \frac{R}{\alpha_c nF}(1-\alpha_c) \tag{2.23}$$

$$\xi_4 = -\left(\frac{R}{\alpha_c nF} + \frac{R}{2F}\right) \tag{2.24}$$

The concentration of dissolved oxygen at the gas/liquid interface can be defined by a Henry's law expression reported in Equation (2.24), where the Henry's law constant in the denominator is derived from readily available solubility data [14].

$$c^*_{O_2} = \frac{p^*_{O_2}}{5.08 \cdot 10^6 \cdot e^{\left(\frac{-498}{T_{st}}\right)}} \tag{2.25}$$

Reference [14] also gives Equation (2.25) to calculate oxygen pressure at the gas/liquid interface from the water saturation pressure and log mean average mole fraction of water into the cathode channel.

$$p_{O_2}^{*} = p_{H_2O}^{sat}\left[\frac{1}{exp\left(\frac{4.192 \cdot j_{st}}{T_{st}^{\ 1.334}}\right) \cdot x_{H_2O}^{channel}} - 1\right] \tag{2.26}$$

where j_{st} [A/cm^2] is the stack current density defined in the next equation as stack current (equal to cell current) per cell active area:

$$j_{st} = \frac{i_{st}}{A_{FC}} \tag{2.27}$$

2.1.2.2 Mert et al. in [22]

Another possible approach, presented by Mert et al. in [22], suggests to use a simplified formulation for the activation loss, always starting from the Tafel Equation (2.28).

$$\eta_{act} = \frac{RT_{st}}{\alpha_{AN} nF} \ln\left(\frac{j_{st}}{j_0}\right) \tag{2.28}$$

Usually Tafel equation provides unreliable results in terms of temperature response, since the exchange current density j_0 is assumed to be constant, thus the resulting activation loss is proportional to the operative temperature of the fuel cell. In reality, as commonly known, the activation loss decreases with stack temperature increase. Therefore, to solve this trouble, Berning in [44] propose the following equation that provides the value of the exchange current density as function of the stack temperature:

$$j_0 = 1.08 \cdot 10^{-17} \cdot exp(0.086 \cdot T_{st}) \tag{2.29}$$

This formulation results simpler than the Amphlett et al. one because, instead of four parameters, it is sufficient to find the constant value of the anode charge transfer coefficient α_{AN}, which is characteristic of the fuel cell type considered and its value must be between 0 and 1.

2.1.3 Ohmic Loss

The Ohmic loss is due to the electrical resistance of the membrane electrode assembly MEA, composed by the resistance of the polymer membrane to the transfer of proton H^+ and the resistance of the graphite electrodes and graphite collector plates to the transfer of electrons. This could be expressed using Ohm's Law equation below:

$$\eta_{ohm} = \eta_{ohm}^{electronic} + \eta_{ohm}^{proton} = j_{st}\left(R_{ohm}^{electronic} + R_{ohm}^{proton}\right) \tag{2.30}$$

Resistance to electron flow should be approximately constant over the relatively narrow temperature range of PEM fuel cell operation and it is also negligible in comparison with

the proton resistance. Therefore, the size of the voltage drop due to the Ohmic loss is proportional to the current density as follows:

$$\eta_{ohm} = j_{st} R_{ohm}^{proton} \tag{2.31}$$

where R_{ohm} [$\Omega \cdot cm^2$] is the internal electrical resistance. The resistance depends strongly on the membrane humidity [12] and the fuel cell temperature [15]. The study realized by Springer et al. in [23] shows that the Ohmic resistance is a function of the membrane conductivity σ_m as follows:

$$R_{ohm}^{proton} = \frac{t_m}{\sigma_m} \tag{2.32}$$

where t_m [cm] is the thickness of the membrane and the membrane conductivity σ_m [$(\Omega \cdot cm)^{-1}$] is a function of membrane water content λ_m and stack temperature T_{st}.

The membrane of the Nafion type is a registered trademark of Dupont and broadly used in PEM-FC. Dupont uses the following product designations to denote the thickness of the Nafion membranes [21] [45]:

- Nafion 117: 7 mil (t_m = 0.0178 cm)
- Nafion 115: 5 mil (t_m = 0.0127 cm)
- Nafion 112: 2 mil (t_m = 0.0051 cm)
- Nafion 211: t_m = 0.00254 cm
- Nafion 212: t_m = 0.00508 cm

2.1.3.1 Springer et al. [23]

The value of the membrane water content λ_m, at stack temperature equal to 30°C, varies between 0 and 14, which is equivalent to the relative humidity of 0% and 100% respectively [23]. The equation used to calculate the membrane water content is the Equation (2.56). The influence of membrane water content on the membrane conductivity can be noted in Equation (2.33), while the exponential term of the Equation (2.34) is the activation energy term and allow the correction based on the stack temperature, if the fuel cell is not at 30°C.

$$\begin{cases} \sigma_{30°C} = (0.005139\lambda_m - 0.00326) & \lambda_m \geq 1 \\ \sigma_{30°C} = 0 & \lambda_m < 1 \end{cases} \tag{2.33}$$

$$\sigma_m = \sigma_{30°C} \cdot exp\left[1268\left(\frac{1}{303} - \frac{1}{T_{st}}\right)\right] \tag{2.34}$$

This approach is commonly used in PEM fuel cell modeling, as evidenced by several recent publications

2.1.3.2 Kulikovsky [29]

A similar formulation to Equation (2.33) for the membrane conductivity is proposed by Kulikovsky in [29] and reported in the follow equation:

$$\begin{cases} \sigma_m = (0.5738\lambda_m - 0.7192) & \lambda_m \geq 1.253 \\ \sigma_m = 0 & \lambda_m < 1.253 \end{cases} \tag{2.35}$$

where the membrane water content λ_m is defined by a different equation, visible in Table 2.1. This formulation results independent by the stack temperature and for this reason not considered as a valid alternative to the Springer et al. model proposed.

2.1.3.3 Mann et al. [21]

Mann et al. in [21] propose the Equation (2.36) to define the resistivity of Nafion membranes. The membrane resistivity r_m is defined as the inverse of the membrane conductivity σ_m as visible in Equation (2.37). The membrane resistivity results a function of the current density j_{st}, the stack temperature T_{st} and the membrane water content λ_m.

$$r_m = \frac{181.6 \cdot \left(1 + 0.03 \cdot j_{st} + 0.062 \left(\frac{T_{st}}{303}\right)^2 (j_{st})^{2.5}\right)}{[\lambda_m - 0.634 - 3 \cdot j_{st}] \cdot exp\left[1268 \left(\frac{1}{303} - \frac{1}{T_{st}}\right)\right]} \tag{2.36}$$

$$\sigma_m = \frac{1}{r_m} \tag{2.37}$$

The Figure 2.3 shows the comparison between these three different approaches presented, where the ohmic overvoltages are calculated at fixed membrane water content ($\lambda_m = 14$) and stack temperature ($T_{st} = 50°C$).

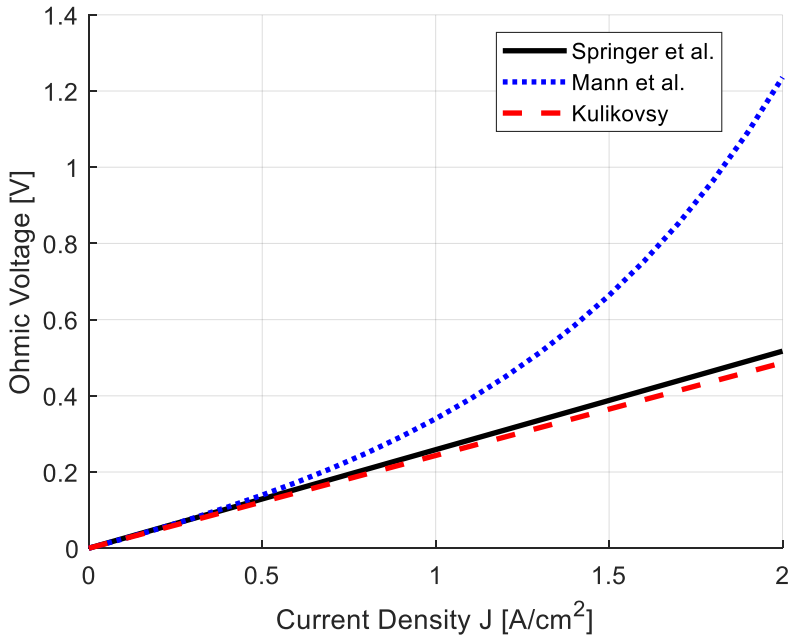

Figure 2.3 – Comparison of different approaches for ohmic voltages (λ = 14 and T_{st} = 50°C)

Springer et al. formulation provides quite similar results to the Kulikovsky one, while Mann et al. is different in term of linearity of the results. In fact, even if the reference work [21] is not specified, this approach seems to include the concentration losses, which become predominant at high current density values, as explained in the following section. Therefore, the non-linearity of the Mann et al. approach respect to the others can be explained by the fact that it already includes the diffusive losses. This approach is commonly used in PEM fuel cell modeling, as evidenced by several recent publications [36], [38], [40], [41], while the Springer et al. formulation is recently used in [46].

2.1.4 Mass Transport and Concentration Losses

If the oxygen at the cathode of the fuel cell is supplied in the form of air, then it is self-evident that during fuel cell operation there is a slight reduction in the concentration of the oxygen in the region of the electrode, as the oxygen is extracted. The extent of this change in concentration depends on the current being taken from the fuel cell and on physical factors relating to how well the air around the cathode can circulate and how quickly the oxygen can be replenished [47].
Similarly, if the anode of a fuel cell is supplied with hydrogen, there is a reduction in hydrogen concentration that depends on the electric current generated by the fuel cell (and hence H_2 consumption) and the physical characteristic of the hydrogen supply system [47].
In both cases, the reduction in gas concentration results in a reduction in voltage, especially at high current density. However, it is generally agreed among fuel cell researchers that there is no analytical solution to the problem of modeling the changes in voltage that works satisfactorily in all cases [48].
One approach that does yield an equation that has some value and use is to see the effect of this reduction in concentration (or partial pressure) by revisiting Equation (2.6). The rate of mass transport to an electrode surface in many cases can be described by Fick's first law of diffusion [8]:

$$i_{st} = -\frac{nFD}{\delta_{gdl}}(c_B - c_S) \tag{2.38}$$

where D is the diffusion coefficient of the reacting species, c_B is its bulk concentration, c_S is its surface concentration, and δ_{gdl} is the thickness of the diffusion layer. The limiting current i_{lim} is a measure of the maximum rate at which a reactant can be supplied to an electrode, and occurs when $c_S = 0$, i.e. [8]:

$$i_{lim} = -\frac{nFD}{\delta_{gdl}}c_B \tag{2.39}$$

The following equation is obtained by appropriate manipulation of Equations (2.38) and (2.39).

$$\frac{c_S}{c_B} = 1 - \frac{i_{st}}{i_{lim}} \tag{2.40}$$

The Nernst equation for the reactant species at equilibrium conditions, or when no current is flowing, is [8]:

$$E_{i=0} = E^o - \frac{RT_{st}}{nF}\ln(c_B) \tag{2.41}$$

When current is flowing, the surface concentration becomes less than the bulk concentration, and the Nernst equation becomes [8]:

$$E = E^o - \frac{RT_{st}}{nF}\ln(c_S) \tag{2.42}$$

The potential difference ($\Delta E = \eta_{conc}$) produced by a concentration change at the electrode is called the concentration polarization [8]:

$$\eta_{conc} = -\frac{RT_{st}}{nF}\ln\left(\frac{c_S}{c_B}\right) \tag{2.43}$$

Upon substituting Equations (2.40) in (2.56), the concentration polarization is given by the equation:

$$\eta_{conc} = -\frac{RT_{st}}{nF}\ln\left(1 - \frac{i_{st}}{i_{lim}}\right) \tag{2.44}$$

In this analysis of concentration polarization, the activation polarization is assumed negligible. The charge transfer reaction has such a high exchange current density that the activation polarization is negligible in comparison with the concentration polarization (most appropriate for the high temperature cells) [8].
However, this theoretical approach has many weaknesses, especially in the case of fuel cells supplied with air rather than pure oxygen, which is the vast majority [47]. There are also problems with lower-temperature cells, and those supplied with hydrogen mixed with other gases such as carbon dioxide for the fuel [47]. No account is taken for the production and removal of reaction products, such as water, and neither is any account taken of the build-up of nitrogen in air systems [47].

Another approach that has no claim for a theoretical basis, but is entirely empirical, has become more favoured lately, and yields an equation that fits the results very well [12], [48]. This approach uses Equation (2.58) because it gives a very good fit to the results, if the constants m_{conc} and n_{conc} are chosen properly, and also appears to be quite widely used in the fuel cell community [47].

$$\eta_{conc} = m_{conc} \cdot exp(n_{conc} \cdot j_{st}) \tag{2.45}$$

The value of m_{conc} is typically about $3 \cdot 10^{-5}$ V, and n_{conc} about 8 cm^2/A [47]. Although the Equations (2.57) and (2.58) look very different, if the constants are chosen carefully the results can be quite similar.

The mass transport or concentration overvoltage is particularly important in following cases:

- The air supplied to the cathode is not well circulated.
- The nitrogen, that is left behind after the oxygen is consumed, can cause a mass transport problem at high currents (it effectively blocks the oxygen supply).
- In proton exchange membrane fuel cells (PEM-FCs), the removal of water can also be a cause of mass transport or concentration overvoltage.

2.1.5 Stack Voltage

In general, combining all the voltage drops associated with the losses explained in the previous sections, the fuel cell operating voltage results:

$$V_{FC} = E - \eta_{act} - \eta_{ohm} - \eta_{conc} \tag{2.46}$$

where the Nernst voltage is calculated always by the Equation (2.11). Different approaches have been presented for each loss parameter and, based on the literature review realized, two possible combinations have been selected to better describe different PEM fuel cell systems.

2.1.5.1 Amphlett-Springer

The first set of equations to calculate the PEM fuel cell operating voltage uses the Amphlett et al. [14] approach for the activation loss and the Springer et al. [23] formulation for Ohmic loss, explained in details in the previous sections and summarized below:

$$\begin{gathered} \eta_{act} = \xi_1 + \xi_2 T_{st} + \xi_3 T_{st} \ln\left(c_{O_2}^*\right) + \xi_4 T_{st} \ln(i_{st}) \\ \eta_{ohm} = j_{st} R_{ohm} = j_{st} \frac{t_m}{(0.005139\lambda_m - 0.00326) exp\left[1268\left(\frac{1}{303} - \frac{1}{T_{st}}\right)\right]} \\ \eta_{conc} = m_{conc} \cdot exp(n_{conc} \cdot j_{st}) \end{gathered} \tag{2.47}$$

2.1.5.2 Mert-Mann

The second set of equations uses the Mert et al. [22] approach for the activation loss and the Mann et al. [21] formulation for Ohmic loss, as summarized below:

$$\begin{gathered} \eta_{act} = \frac{R T_{st}}{\alpha_{AN} n F} \ln\left(\frac{j_{st}}{1.08 \cdot 10^{-17} \cdot exp(0.086 \cdot T_{st})}\right) \\ \eta_{ohm} = j_{st} R_{ohm} = j_{st} t_m \frac{181.6 \cdot \left(1 + 0.03 \cdot j_{st} + 0.062\left(\frac{T_{st}}{303}\right)^2 (j_{st})^{2.5}\right)}{[\lambda_m - 0.634 - 3 \cdot j_{st}] \cdot exp\left[1268\left(\frac{1}{303} - \frac{1}{T_{st}}\right)\right]} \end{gathered} \tag{2.48}$$

The calculated voltage V_{FC} represents the voltage of a single cell. Since individual cells are stacked up in series to form a fuel cell stack with higher voltage, the total voltage of the stack can be approximated considering the same voltage for all the cells, by multiplying the single cell voltage for the total number of cells as follows:

$$V_{st} = V_{FC} \cdot n_{FC} \tag{2.49}$$

Therefore, the electric power generated by the fuel cell is calculated by the following equation:

$$P_{el} = V_{st} \cdot i_{st} \tag{2.50}$$

In Section 4 the complete validation of this stack voltage model is performed using experimental data available in literature.

2.2 Membrane Hydration Model

The membrane hydration model allows to calculate the characterizing parameters of the membrane, i.e. the water content and the mass flow rate of water across the membrane, both assumed uniform over its surface area. The membrane water content influences ohmic loss as described in Section 2.1.3 and membrane water flow is used in anode and cathode mass balances in Sections 2.3 and 2.4. Input and output parameters are shown schematically in Figure 2.4.

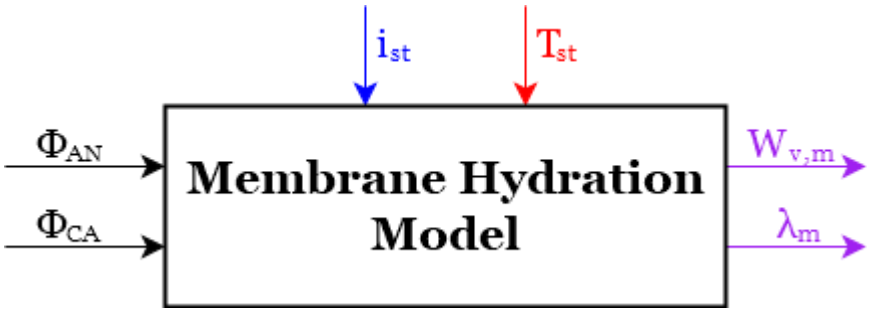

Figure 2.4 – Block diagram of membrane hydration model

In general, the water transport across the membrane is characterized by two distinct phenomena:

- Water molecules are dragged across the membrane from anode to cathode by the hydrogen proton. This phenomenon is called ***electro-osmotic drag***. The amount of water transported is represented by the electro-osmotic drag coefficient n_d, which is defined as the number of water molecules dragged per H^+ ion through the membrane. Equation (2.51) shows the net water flux from anode to cathode of one cell caused by electro-osmotic drag $N_{v,osmotic}$ where j_{st} [A/cm^2] is the stack current density defined in Equation (2.27) and F is the Faraday's number.

$$N_{v,osmotic} = n_d \frac{j_{st}}{F} \tag{2.51}$$

- ***Back-diffusion*** of water from cathode to anode, which lessens the concentration gradient along the membrane. Equation (2.52) shows the net water flux from cathode to anode of one cell caused by back-diffusion $N_{v,diff}$. Furthermore, D_w [cm^2/s] is the diffusion coefficient of water in the membrane defined in Equation (2.59), c_v [mol/cm^3] is the water concentration defined in Equation (2.63) and z is the distance in the direction normal to the membrane.

$$N_{v,diff} = D_w \frac{dc_v}{dz} \tag{2.52}$$

Combining these two water transport phenomena and approximating the water concentration gradient in the membrane to be linear over the membrane thickness, the water flow across the membrane can be written as (assuming positive values in the direction from anode to cathode):

$$N_{v,membr} = N_{v,osmotic} - N_{v,diff} = n_d \frac{j_{st}}{F} - D_w \frac{\left(c_{v,CA} - c_{v,AN}\right)}{t_m} \tag{2.53}$$

Where $N_{v,membr}$ [mol/(s·cm^2)] is the water flow rate per unit area in one cell and t_m [cm] is the thickness of the membrane (see Section 2.1.3).
Total stack water mass flow rate across the membrane $W_{v,membr}$ can be calculated by equation below, where A_{FC} [cm^2] is the cell active area and n_{FC} is the number of cells in the stack.

$$W_{v,membr} = N_{v,membr} \cdot M_v \cdot A_{FC} \cdot n_{FC} \tag{2.54}$$

The production of water by the oxygen reduction reaction at the cathode and humidification conditions of the inlet gas streams also influence the spatial variations of water content within the polymeric electrolyte, but they have already been considered in Sections 2.3 and 2.4 for the calculation of anode and cathode relative humidity.

2.2.1.1 Springer et al. [23]

In order to determine the water mass flow rate across the membrane, it is still necessary to define the electro-osmotic drag coefficient n_d, the back-diffusion coefficient D_w and the water concentration at the membrane surface on the anode and cathode sides $c_{v,AN}$ and $c_{v,CA}$. All these parameters are functions of a parameter introduced by Springer et al. in [23], the membrane water content λ that can have a value as high as 14 under ideal, 100% relative humidity conditions and has had reported values as high as 22 [23] and 23 [21] under supersaturated conditions. In literature, there are different approaches and models, resulting from several studies and experiments on fuel cell membranes. However, the theoretical approach and experimental results exposed by Springer et al. in [23] are globally recognized as the basis of the membrane hydration modeling. Springer et al. developed an isothermal

and one-dimensional hydration model for a complete polymer electrolyte fuel cell with a 117 Nafion membrane, using the same approach described by the previous equations.
Springer et al. measured the membrane water content at 30°C and defined it $\lambda_{i,30°C}$ as the ratio of the number of water molecules to the number of charge sites. Furthermore $\lambda_{i,30°C}$ is presented in [23] and reported in Equation (2.56) as a function of water activity a_i, which, in the case of gas, is equivalent to the relative humidity Φ_i, as shown in Equation (2.55).

$$a_i = \frac{x_{v,i} p_i}{p_{sat,i}} = \frac{p_{v,i}}{p_{sat,i}} = \Phi_i \tag{2.55}$$

$$\lambda_{i,30°C} = \begin{cases} 0.043 + 17.81 a_i - 39.85 {a_i}^2 + 36 {a_i}^3 & if \quad 0 < a_i \leq 1 \\ 14 + 1.4(a_i - 1) & if \quad 1 < a_i \leq 3 \end{cases} \tag{2.56}$$

$$a_m = \frac{a_{AN} + a_{CA}}{2} \tag{2.57}$$

where the subscript i represents anode (AN), cathode (CA) or membrane (m).
Figure 2.5 shows the plot of the average membrane water content $\lambda_{m,30°C}$ versus the average water activity a_m, calculated by Equation (2.57). The value of $\lambda_{m,30°C}$, calculated as the average between $\lambda_{AN,30°C}$ and $\lambda_{CA,30°C}$ as proposed in [49], is used to represents the average water content in the membrane.

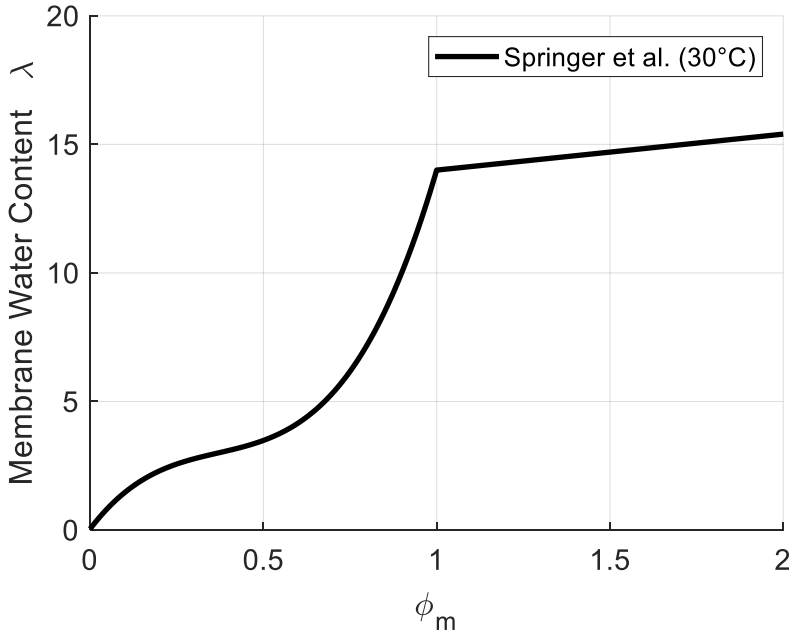

Figure 2.5 – Membrane water content λ Vs membrane relative humidity Φ_m

A more conservative approach, exposed in [26], uses water content in the anode flow, because the membrane water content tends to be lower on the anode side. In fact, at high current density, water transport from anode to cathode by electro-osmotic drag exceeds the water back-diffusion from cathode to anode.

Springer et al. present in [23] the following formulation for electro-osmotic drag coefficient n_d, obtained from an experiment conducted at 80°C.

$$n_d = \frac{2.5}{22}\lambda_{AN} \tag{2.58}$$

Equations (2.59) e (2.60) show the expression provided in [23] to calculate the water diffusion coefficient D_w as function of the average membrane water content and stack temperature, by means of the activation energy term of the equation (2.59).

$$D_w = D_\lambda exp\left[2416\left(\frac{1}{303} - \frac{1}{T_{st}}\right)\right] \tag{2.59}$$

$$D_\lambda = \begin{cases} 0.89 \cdot 10^{-6} & if\ \ \lambda_m < 2 \\ (-3.25 + 2.05\lambda_m) \cdot 10^{-6} & if\ \ 2 \leq \lambda_m < 3 \\ (6.65 + 1.25\lambda_m) \cdot 10^{-6} & if\ \ 3 \leq \lambda_m < 4 \\ \left(2.563\lambda_m + 0.0264{\lambda_m}^2 - 0.00067{\lambda_m}^3\right) \cdot 10^{-6} & if\ \ \lambda_m \geq 4 \end{cases} \tag{2.60}$$

The water concentrations at the membrane surfaces on the anode and cathode sides, used in Equation (2.53), are functions of the membrane water content, as explained in the following equations:

$$c_{v,AN} = \frac{\rho_{m,dry}}{M_{m,dry}}\lambda_{AN} \tag{2.61}$$

$$c_{v,CA} = \frac{\rho_{m,dry}}{M_{m,dry}}\lambda_{CA} \tag{2.62}$$

$$c_v = c_{v,CA} - c_{v,AN} \tag{2.63}$$

2.2.1.2 Others Approaches

Different approaches from the reference work of Springer et al. are presented by Dutta et al. [26], Nguyen and White [24], Kulikovsky [29], Ge et al. [32], Pukrushpan et al. [2] and Vetter and Schumacher [50]. The equations presented in these works and related to the membrane water content λ, electro-osmotic drag coefficient n_d and water back-diffusion D_w are reported in Table 2.1. This table summarizes and compares these main literature approaches: many other publications base their work on these equations.

Table 2.1 – Membrane hydration models comparison

Ref	***Equations***
Springer et al. [23]	$\lambda = \begin{cases} 0.043 + 17.81 \cdot a - 39.85 \cdot a^2 + 36 \cdot a^3 & 0 < a \leq 1 \\ 14 + 1.4 \cdot (a - 1) & 1 < a \leq 3 \end{cases}$ $n_d = \frac{2.5}{22}\lambda$ $D_\lambda = \begin{cases} 0.89 \cdot 10^{-6} & \lambda < 2 \\ (-3.25 + 2.05 \cdot \lambda) \cdot 10^{-6} & 2 \leq \lambda < 3 \\ (6.65 + 1.25 \cdot \lambda) \cdot 10^{-6} & 3 \leq \lambda < 4 \\ (2.563 \cdot \lambda + 0.0264 \cdot \lambda^2 - 0.00067 \cdot \lambda^3) \cdot 10^{-6} & \lambda \geq 4 \end{cases}$ $D_w = D_\lambda \cdot exp\left[2416\left(\frac{1}{303} - \frac{1}{T_{st}}\right)\right]$
Dutta et al. [26]	$\lambda =$ *Springer et al.* [23] $n_d = 0.0029 \cdot \lambda^2 + 0.05 \cdot \lambda - 3.4 \cdot 10^{-19}$ $D_\lambda = \begin{cases} 1 \cdot 10^{-6} & \lambda < 2 \\ (1 + 2 \cdot (\lambda - 2)) \cdot 10^{-6} & 2 \leq \lambda < 3 \\ (3 - 1.67 \cdot (\lambda - 3)) \cdot 10^{-6} & 3 \leq \lambda < 4 \\ 1.25 \cdot 10^{-6} & \lambda \geq 4 \end{cases}$ $D_w = D_\lambda \cdot exp\left[2416\left(\frac{1}{303} - \frac{1}{T_{st}}\right)\right]$
Nguyen, White [24]	$\lambda =$ *Springer et al.* [23] $n_d = \begin{cases} 0.0049 + 2.024 \cdot a - 4.53 \cdot a^2 + 4.09 \cdot a^3 & 0 < a \leq 1 \\ 1.59 + 0.159 \cdot (a - 1) & 1 < a \leq 3 \end{cases}$ $D_w = n_d \cdot 5.5 \cdot 10^{-7} \cdot exp\left[2416\left(\frac{1}{303} - \frac{1}{T_{st}}\right)\right]$
Kulikovsky [29]	$\lambda = 0.3 + 6 \cdot a[1 - tanh(a - 0.5)] + 3.9\sqrt{a}\left[1 + tanh\left(\frac{a - 0.89}{0.23}\right)\right]$ $n_d = \begin{cases} 1 & \lambda < 9 \\ 0.117 \cdot \lambda - 0.0544 & \lambda \geq 9 \end{cases}$ $D_w = 4.1 \cdot 10^{-6}\left(\frac{\lambda}{25}\right)^{0.15}\left[1 + tanh\left(\frac{\lambda - 2.5}{1.4}\right)\right]$

Ge et al. [32]	$\lambda_{30°C} =$ *Springer et al.* [23] $\lambda_{80°C} = \begin{cases} 0.3 + 10.8 \cdot a - 16 \cdot a^2 + 14.1 \cdot a^3 & 0 < a \leq 1 \\ 9.2 + 1.4 \cdot (a - 1) & 1 < a \leq 3 \end{cases}$ $\lambda = \lambda_{30°C} + \left(\frac{\lambda_{80°C} - \lambda_{30°C}}{50}\right)(T_{st} - 303)$ $n_{d,30°C} = 0.011 + 0.1949\lambda - 0.0139\lambda^2 + 4.06 \cdot 10^{-4}\lambda^3 \quad \lambda \leq 14$ $n_{d,50°C} = 0.017 + 0.1803\lambda - 0.0091\lambda^2 + 1.12 \cdot 10^{-4}\lambda^3 \quad \lambda \leq 12.08$ $n_{d,80°C} = 0.106 + 0.1191\lambda + 0.0049\lambda^2 - 7.046 \cdot 10^{-4}\lambda^3 \quad \lambda \leq 9.20$ $n_d = \begin{cases} n_{d,30°C} + \left(\frac{n_{d,50°C} - n_{d,30°C}}{20}\right)(T_{st} - 303) & T_{st} < 323 \\ n_{d,50°C} + \left(\frac{n_{d,80°C} - n_{d,50°C}}{30}\right)(T_{st} - 323) & T_{st} \geq 323 \end{cases}$
Pukrushpan et al. [2]	$\lambda =$ *Springer et al.* [23] $n_d =$ *Dutta et al.* [26] $D_w =$ *Dutta et al.* [26]
Vetter, Schumacher [50]	$\lambda =$ *Springer et al.* [23] $n_d =$ *Springer et al.* [23] $D_w = \frac{3.842\lambda^3 - 32.03\lambda^2 + 67.74\lambda}{\lambda^3 - 2.115\lambda^2 - 33.013\lambda + 103.37} \cdot 10^{-6} \cdot exp\left[\frac{20}{R}\left(\frac{1}{303} - \frac{1}{T_{st}}\right)\right]$

Figure 2.6 shows the principal equations of the membrane water content λ, as function of the membrane water activity a, present in literature. In particular, the equation presented by Springer et al. in [23] is obtained at 30°C and it is not depending on stack temperature. A similar equation is obtained by Kulikovsky in [29] at 80°C, always independent on the stack temperature. A slightly different approach is proposed by Ge et al. in [32] and consists of linear interpolation in function of the stack temperature between two equations, obtained at 30°C and 80°C (see Table 2.1). Anyway, Springer et al. overcome this problem introducing the temperature correction factor of Equation (2.59).

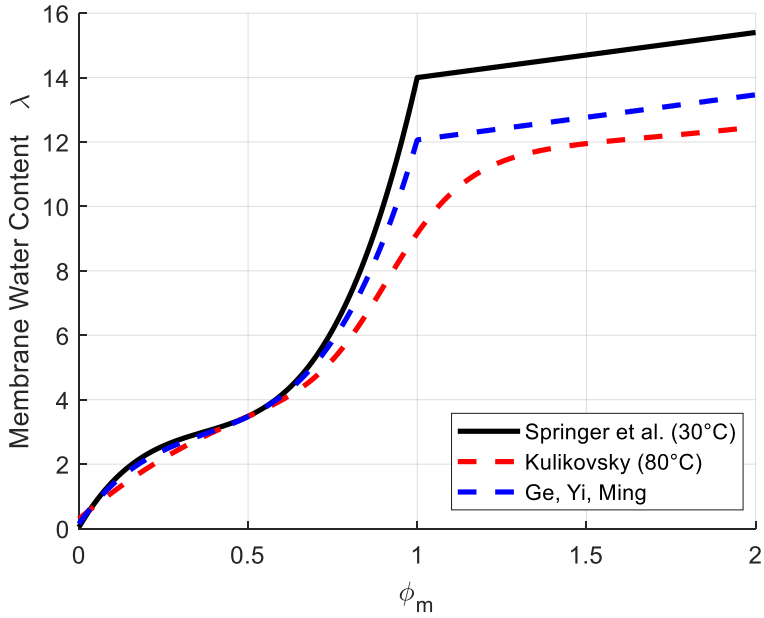

Figure 2.6 – Different membrane water contents as functions of membrane water activity at 50°C

Figure 2.7 presents the comparison of the water back-diffusion drag coefficients reported in Table 2.1. These formulations are quite different from each other. Therefore, it is impossible to identify the absolute best solution.

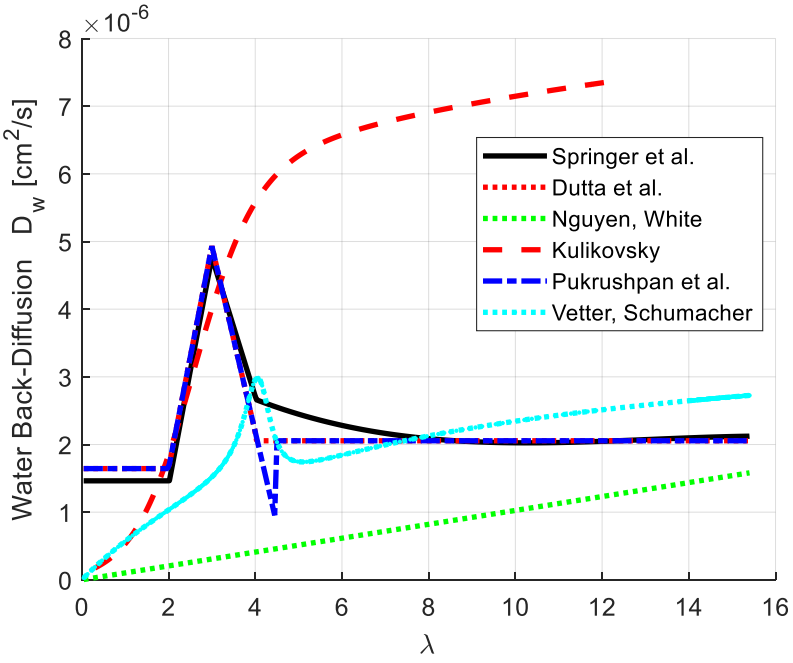

Figure 2.7 – Different water back-diffusion drag coefficients at 50°C

Figure 2.8 shows the comparison between different formulations of the electro-osmotic drag coefficient n_d. The linear dependence with membrane water content, provided by Springer et al. [23] and by Nguyen and White [24], results a good compromise between the approaches proposed by Dutta et al. in [26] and by Ge et al. in [32] at 50°C, while the

equation provided by Kulikovsky in [29] is quite different from all the others. The electro-osmotic drag coefficient is normally not dependent on the stack temperature, as visible in Table 2.1, except for the formulation of Ge et al. [32] that perform a linear interpolation between different equations of n_d, obtained at different temperatures.
In conclusion, the model chosen is the reference model proposed by Springer et al in [23] due to its simplicity, completeness and wide use in literature and leaving the possibility to implement any other of the models presented if necessary.

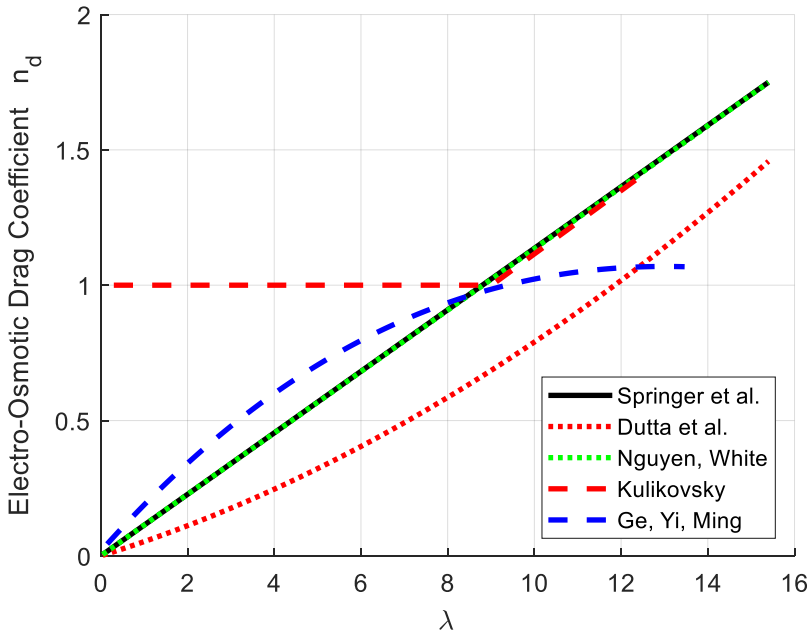

Figure 2.8 – Different electro-osmotic drag coefficients at 50°C

2.3 Anode Flow Model

The anode mass flow model represents hydrogen and water flows behaviour inside the anode of the fuel cell stack. The model is developed, on the basis of the approach presented in [2], using the mass conservation principle and according to following assumptions:

- All gases are assumed to behave like ideal gas.
- The temperature of the flows inside channels is uniformly over the whole stack and equal to the stack temperature, controlled by cooling system.
- The conditions of pressure, temperature and humidity in outlet flows are the same of those of gases in the anode flow channels. Additionally, these quantities are considered uniform along flow channels.
- The anode flow channels of all cells are lumped into one volume.

In this model, hydrogen is supplied to the anode of the fuel cell stack by a hydrogen supply valve fed by a high-pressure hydrogen tank.
Figure 2.9 illustrates mass flows inside the anode. This model considers a dead-end PEM fuel cell, without outlet mass flow, but has been improved with a tool able to simulate a

timed purge, not activated during our simulations, but already implemented for future expansion of the model to take into account the nitrogen diffusion through the membrane.

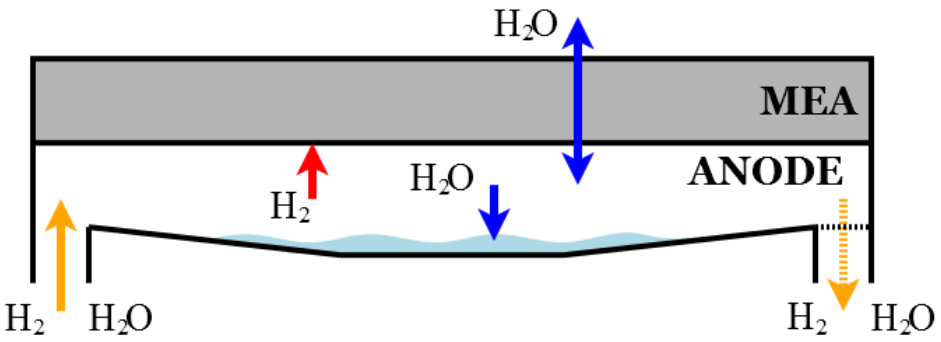

Figure 2.9 – Anode mass flows

Figure 2.10 shows block diagram of the anode model, with required inputs and outputs calculated. Considering a dead-end fuel cell total mass flow out from anode $W_{out,AN}$ is zero.

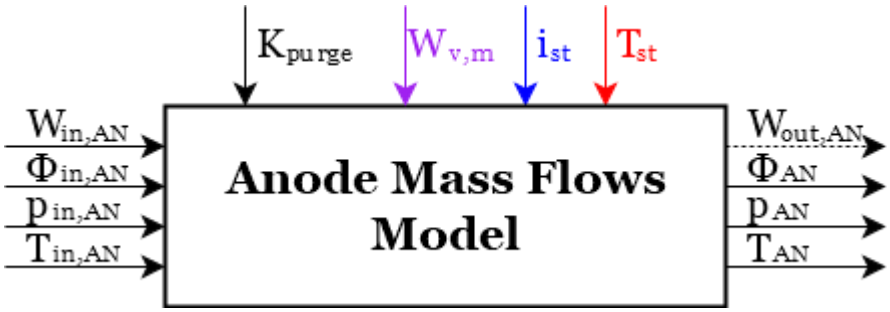

Figure 2.10 – Block diagram of the anode flow model

Anode model is based on mass hydrogen balance, Equation (2.64), mass vapor balance, Equation (2.65) and mass liquid water balance, Equation (2.67).

$$\frac{dm_{H_2,AN}}{dt} = W_{H_2,in,AN} - W_{H_2,out,AN} - W_{H_2,react} \tag{2.64}$$

$$\frac{dm_{v,AN}}{dt} = W_{v,in,AN} - W_{v,out,AN} - W_{v,membr} \tag{2.65}$$

$$\frac{dm_{l,AN}}{dt} = W_{phase,AN} - W_{l,out,AN} \tag{2.66}$$

The water mass flow across the membrane $W_{v,membr}$ is calculated in the membrane hydration model explained in Section 2.2.

Inlet dry hydrogen mass flow $W_{H_2,in,AN}$ and inlet vapor mass flow $W_{v,in,AN}$ are calculated, using equations below, from the total inlet mass flow $W_{in,AN}$, inlet humidity $\Phi_{in,AN}$ and inlet pressure $p_{in,AN}$, resulting from anode inlet manifold model.

$$p_{v,in,AN} = \Phi_{in,AN} \cdot p_{sat}(T_{st}) \tag{2.67}$$

$$p_{H_2,in,AN} = p_{in,AN} - p_{v,in,AN} \tag{2.68}$$

$$\omega_{in,AN} = \frac{M_v}{M_{H_2}} \frac{p_{v,in,AN}}{p_{H_2,in,AN}} \tag{2.69}$$

$$W_{H_2,in,AN} = \frac{1}{1 + \omega_{in,AN}} W_{in,AN} \tag{2.70}$$

$$W_{v,in,AN} = W_{in,AN} - W_{H_2,in,AN} \tag{2.71}$$

Mass flow of hydrogen consumed in the reaction $W_{H_2,react}$ is a function of stack current, according to the following electrochemical principles:

$$W_{H_2,react} = M_{H_2} \cdot \frac{n_{FC} i_{st}}{2F} \tag{2.72}$$

The water inside the anode is supposed to be produced in vapor form but both the forms, vapor and liquid, are present, depending on the saturation state of the anode.
Using the approach proposed in [51] and recently used in [52] and [53], a finite-phase model is used to describe the water condensation and vaporization. When the vapor partial pressure is higher than the saturation pressure, condensation occurs:

$$W_{phase,AN} = \frac{k_c V_{AN}}{R_v T_{st}} x_{v,AN} \left(p_{AN} x_{v,AN} - p_{sat}\right) M_{H_2O} \tag{2.73}$$

where k_c is the condensation rate and $x_{vap,AN}$ the molar fraction of vapor.
When the vapor partial pressure is lower than the saturation pressure, water evaporates:

$$W_{phase,AN} = k_e m_{l,AN} \left(p_{AN} x_{v,AN} - p_{sat}\right) \tag{2.74}$$

where k_e is the evaporation rate. The molar fraction of vapor can be obtained by:

$$x_{v,AN} = \frac{m_{v,AN}}{M_{H_2O}} \frac{R_v T_{st}}{p_{AN} V_{AN}} \tag{2.75}$$

This phenomenon of condensation, even if implemented both in anode and cathode flow models, would not usually occurs at the anode, where normally there isn't liquid water production and where, on the contrary, the problem consists in a not perfect hydration of the membrane.
The mass of hydrogen and vapor calculated in Equations (2.64) and (2.65) are used to determine hydrogen partial pressure $p_{H_2,AN}$, vapor partial pressure $p_{v,AN}$, anode pressure p_{AN} and relative humidity Φ_{AN} of the gas inside the anode using the following equations.

$$p_{H_2,AN} = \frac{m_{H_2,AN} R_{H_2} T_{st}}{V_{AN}} \tag{2.76}$$

$$p_{v,AN} = \frac{m_{v,AN} R_v T_{st}}{V_{AN}} \tag{2.77}$$

$$p_{AN} = p_{H_2,AN} + p_{v,AN} \tag{2.78}$$

$$\Phi_{AN} = \frac{p_{v,AN}}{p_{sat}(T_{st})} \tag{2.79}$$

Considering dead-end fuel cell without purge, all mass flows outgoing from the anode are zero, in particular outlet hydrogen mass flow $W_{H_2,out,AN}$, outlet vapor mass flow $W_{v,out,AN}$ and outlet liquid water mass flow $W_{l,out,AN}$. To simulate this operating condition just set the purge coefficient K_{purge} equal to zero.

Considering timed purge, instead, the total mass flow rate at anode exit is determined using the orifice equations discussed in Section 1.2. Since the pressure drop between the anode and the atmosphere is normally quite significant, the Equations (2.80) and (2.81) are used to represent the anode outlet in subcritical and supercritical conditions. The critical condition is reported in Equation (2.82).

$$\begin{aligned} W_{\substack{out,AN,\\ subcr}} = K_{purge} \frac{C_{D,out,AN} A_{T,out,AN} p_{AN}}{\sqrt{R T_{AN}}} \left(\frac{p_{atm}}{p_{AN}}\right)^{\frac{1}{\gamma_{H_2}}} \\ \cdot \left\{ \frac{2\gamma_{H_2}}{\gamma_{H_2} - 1} \left[1 - \left(\frac{p_{atm}}{p_{AN}}\right)^{\frac{\gamma_{H_2}-1}{\gamma_{H_2}}} \right] \right\}^{\frac{1}{2}} \end{aligned} \tag{2.80}$$

$$W_{\substack{out,AN,\\ supercr}} = K_{purge} \frac{C_{D,out,AN} A_{T,out,AN} p_{AN}}{\sqrt{R T_{AN}}} \gamma_{H_2}^{\frac{1}{2}} \left(\frac{2}{\gamma_{H_2} + 1}\right)^{\frac{\gamma_{H_2}+1}{2(\gamma_{H_2}-1)}} \tag{2.81}$$

$$\left(\frac{p_{atm}}{p_{AN}}\right)_{cr} = \left(\frac{2}{\gamma_{H_2} + 1}\right)^{\frac{\gamma_{H_2}}{\gamma_{H_2}-1}} \tag{2.82}$$

The outlet hydrogen mass flow $W_{H_2,out,AN}$ and outlet vapor mass flow $W_{v,out,AN}$ are calculated in Equations (2.84) and (2.85), according to the approach proposed in [16].

$$m_{TOT,AN} = m_{H_2,AN} + m_{v,AN} \tag{2.83}$$

$$W_{H_2,out,AN} = \frac{m_{H_2,AN}}{m_{TOT,AN}} W_{out,AN} \tag{2.84}$$

$$W_{v,out,AN} = \frac{m_{v,AN}}{m_{TOT,AN}} W_{out,AN} \tag{2.85}$$

Not considering the capillary pressure between the gas phase and the liquid phase in the anode flow channel, two phases share the common velocity and the liquid water outflow mass flow rate can be obtained by [52]:

$$W_{l,out,AN} = \frac{m_{l,AN}}{V_{AN}} \frac{W_{out,AN}}{\rho_{AN}} = \frac{m_{l,AN}}{m_{H_2,AN} + m_{v,AN}} W_{out,AN} \tag{2.86}$$

K_{purge} is a coefficient that can be always zero (purge always off) or a step time signal that varies between zero and one (purge on), according to the real functioning of purge valve. Figure 2.11 shows a time trend example of K_{purge} achievable in the Matlab-Simulink model.

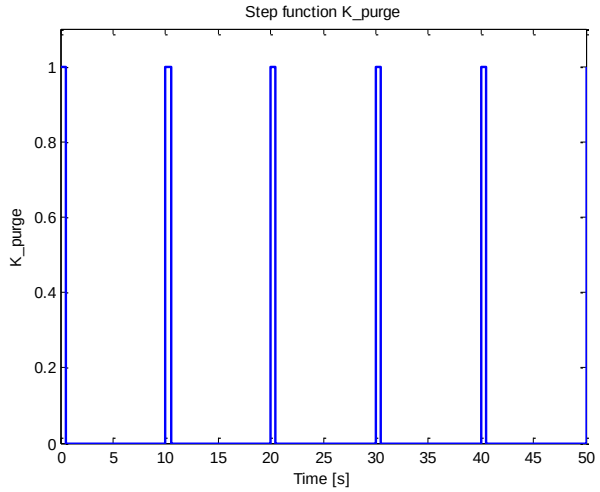

Figure 2.11 – Example of the time trend of K_{purge}

2.4 Cathode Flow Model

The cathode mass flow model represents air and water flows behaviour inside the cathode of the fuel cell stack. The model is developed, on the basis of the approach presented in [2], using the mass conservation principle and thermodynamic and psychometric properties of air, reviewed in Section 1.1.

The assumptions made for cathode flow model are totally similar to those made for the anode flow model in Section 2.3.

Figure 2.12 illustrates all flows inside the cathode channel.

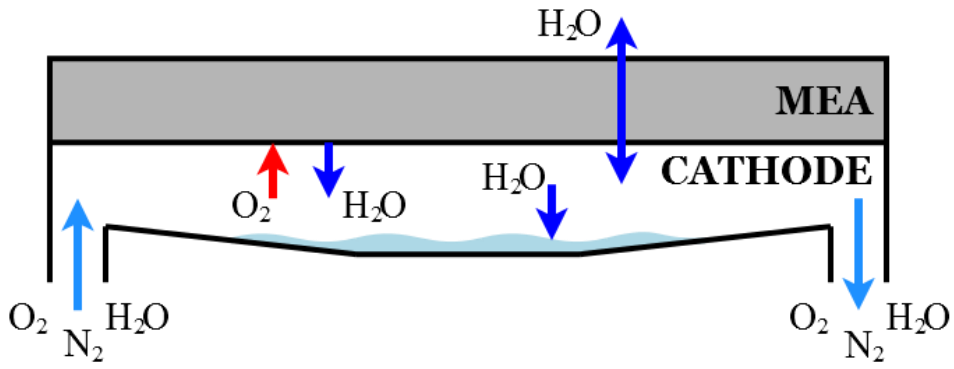

Figure 2.12 – Cathode Mass Flows

Figure 2.13 shows block diagram of the cathode model, with required inputs and outputs calculated. The cathode outlet manifold pressure p_{rm} is calculated in the corresponding model, described in Section 3.3.

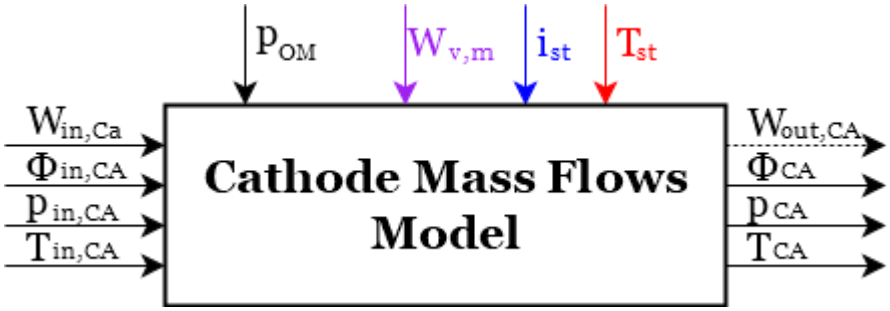

Figure 2.13 – Block diagram of the cathode flow model

Cathode model is based on the following oxygen, nitrogen, vapor and liquid water balances.

$$\frac{dm_{O_2,CA}}{dt} = W_{O_2,in,CA} - W_{O_2,out,CA} - W_{O_2,react} \tag{2.87}$$

$$\frac{dm_{N_2,CA}}{dt} = W_{N_2,in,CA} - W_{N_2,out,CA} \tag{2.88}$$

$$\frac{dm_{w,CA}}{dt} = W_{v,in,CA} - W_{v,out,CA} + W_{v,gen,CA} + W_{v,membr} - W_{v,out,CA} \tag{2.89}$$

$$\frac{dm_{l,CA}}{dt} = W_{phase,CA} - W_{l,out,CA} \tag{2.90}$$

The water mass flow across the membrane $W_{v,membr}$ is calculated in the membrane hydration model explained in Section 2.2.

Inlet mass flow rate of dry air $W_{dry\ air,in,CA}$ and vapor $W_{v,in,CA}$ are calculated, using equations below, from the (total) inlet mass flow $W_{in,CA}$, inlet humidity $\Phi_{in,CA}$ and inlet pressure $p_{in,CA}$, resulting from cathode inlet manifold model.

$$p_{v,in,CA} = \Phi_{in,CA} \cdot p_{sat}(T_{st}) \tag{2.91}$$

$$p_{dry\ air,in,CA} = p_{in,CA} - p_{v,in,CA} \tag{2.92}$$

$$\omega_{in,CA} = \frac{M_v}{M_{dry\ air,in,CA}} \frac{p_{v,in,CA}}{p_{dry\ air,in,CA}} \tag{2.93}$$

$$W_{dry\ air,in,CA} = \frac{1}{1 + \omega_{in,CA}} W_{in,CA} \tag{2.94}$$

$$W_{v,in,CA} = W_{in,CA} - W_{dry\ air,in,CA} \tag{2.95}$$

Furthermore, the equations below are used to calculate oxygen inlet mass flow $W_{O_2,in,CA}$ and nitrogen inlet mass flow $W_{N_2,in,CA}$.

$$M_{dry\ air,in,CA} = x_{O_2,in,CAT} \cdot M_{O_2} + \left(1 - x_{O_2,in,CAT}\right) M_{N_2} \tag{2.96}$$

$$y_{O_2,in,CA} = x_{O_2,in,CAT} \frac{M_{O_2}}{M_{dry\ air,in,CA}} \tag{2.97}$$

$$y_{N_2,in,CA} = \left(1 - x_{O_2,in,CAT}\right) \frac{M_{N_2}}{M_{dry\ air,in,CA}} \tag{2.98}$$

$$W_{O_2,in,CA} = y_{O_2,in,CA} \cdot W_{dry\ air,in,CA} \tag{2.99}$$

$$W_{N_2,in,CA} = y_{N_2,in,CA} \cdot W_{dry\ air,in,CA} \tag{2.100}$$

Where $x_{O_2,in,CAT}$ is oxygen mole fraction, about 0.21 for ambient air, $y_{O_2,in,CA}$ is oxygen mass fraction and $y_{N_2,in,CA}$ is nitrogen mass fraction. Electrochemistry principles are used to calculate the rate of oxygen consumption $W_{O_2,react}$ and water production $W_{v,gen,CA}$ in the fuel cell reaction, both depending of stack current.

$$W_{O_2,react} = M_{O_2} \cdot \frac{n_{FC} i_{st}}{4F} \tag{2.101}$$

$$W_{v,gen,CA} = M_v \cdot \frac{n_{FC} i_{st}}{2F} \tag{2.102}$$

The water inside the cathode can be in two forms, vapor and liquid, depending on the vapor saturation state of the cathode.

Using the approach proposed in [51] and recently used in [52] and [53], a finite-phase model is used to describe the water condensation and vaporization. When the vapor partial pressure is higher than the saturation pressure, condensation occurs:

$$W_{phase,CA} = \frac{k_c V_{CA}}{R_v T_{st}} x_{v,CA} \left(p_{CA} x_{v,CA} - p_{sat}\right) M_{H_2O} \tag{2.103}$$

where k_c is the condensation rate and $x_{vap,AN}$ the molar fraction of vapor.

When the vapor partial pressure is lower than the saturation pressure, water evaporates:

$$W_{phase,CA} = k_e m_{l,CA} \left(p_{CA} x_{v,CA} - p_{sat}\right) \tag{2.104}$$

where k_e is the evaporation rate. The molar fraction of vapor can be obtained by:

$$x_{v,CA} = \frac{m_{v,CA}}{M_{H_2O}} \frac{R_v T_{st}}{p_{CA} V_{CA}} \tag{2.105}$$

The mass of oxygen, nitrogen and vapor calculated in Equations (2.87), (2.88) and (2.89) are used to determine oxygen partial pressure $p_{O_2,CA}$, nitrogen partial pressure $p_{N_2,CA}$, vapor partial pressure $p_{v,CA}$, cathode pressure p_{CA} and relative humidity Φ_{CA} of the gas inside the cathode using the following equations.

$$p_{O_2,CA} = \frac{m_{O_2,CA} R_{O_2} T_{st}}{V_{CA}} \tag{2.106}$$

$$p_{N_2,CA} = \frac{m_{N_2,CA} R_{N_2} T_{st}}{V_{CA}} \tag{2.107}$$

$$p_{v,CA} = \frac{m_{v,CA} R_v T_{st}}{V_{CA}} \tag{2.108}$$

$$p_{dry\ air,CA} = p_{O_2,CA} + p_{N_2,CA} \tag{2.109}$$

$$p_{CA} = p_{dry\ air,CA} + p_{v,CA} \tag{2.110}$$

$$x_{O_2,CAT} = \frac{p_{O_2,CA}}{p_{sat}(T_{st})} \tag{2.111}$$

$$\Phi_{CA} = \frac{p_{v,CA}}{p_{sat}(T_{st})} \tag{2.112}$$

where $x_{O_2,CAT}$ is the oxygen mole fraction.

Since the pressure drop between the cathode and the cathode outlet manifold is normally quite low, the total mass flow rate at cathode exit is determined using the simplified orifice equation discussed in Section 1.2, as reported in Equation (1.21). The outlet oxygen mass flow $W_{O_2,out,CA}$, outlet nitrogen mass flow $W_{N_2,out,CA}$ and outlet vapor mass flow $W_{v,out,CA}$ are calculated in equations below, according to the approach proposed in [16].

$$W_{out,CA} = K_{out,CA}(p_{CA} - p_{OM}) \tag{2.113}$$

$$m_{TOT,CA} = m_{O_2,CA} + m_{N_2,CA} + m_{v,CA} \tag{2.114}$$

$$W_{O_2,out,CA} = \frac{m_{O_2,CA}}{m_{TOT,CA}} W_{out,CA} \tag{2.115}$$

$$W_{N_2,out,CA} = \frac{m_{N_2,CA}}{m_{TOT,CA}} W_{out,CA} \tag{2.116}$$

$$W_{v,out,CA} = \frac{m_{v,CA}}{m_{TOT,CA}} W_{out,CA} \tag{2.117}$$

Not considering the capillary pressure between the gas phase and the liquid phase in the cathode flow channel, two phases share the common velocity and the liquid water outflow mass flow rate can be obtained by [52]:

$$W_{l,out,CA} = \frac{m_{l,CA}}{V_{CA}} \frac{W_{out,CA}}{\rho_{CA}} = \frac{m_{l,CA}}{m_{O_2,CA} + m_{N_2,CA} + m_{v,CA}} W_{out,CA} \tag{2.118}$$

2.5 Stack Thermal Balance

The stack thermal balance comes from the energy balance of the PEM fuel cell and is used to simulate the thermal transient of the PEM fuel cell. The energy balance reported in Equation (2.119) is obtained considering:

- the average heat capacity of the fuel cell,
- the energy produced in the chemical reaction of water formation (which is supposed to be formed in the chemical water steam),
- the energy produced in the form of electricity,
- the amount of heat supplied and evacuated by the mass flows,
- the heat removed by the cooling system.

$$m_{FC}c_{FC}\frac{dT_{st}}{dt} = \Delta H_c W_{H_2,react} - P_{el} - Q_{amb} + Q_i - Q_{cool} \tag{2.119}$$

where:

- $m_{FC} \cdot c_{FC}$ [J/K] represents the average heat capacity of the fuel cell,
- ΔH_c [J/kg] is the hydrogen lower heating value and is equal to $1.1996 \cdot 10^8$ J/kg,
- $W_{H_2,react}$ [kg/s] is the mass flow of hydrogen consumed in the chemical reaction, calculated in Equation (2.72),
- P_{el} [W] is the electric power generated by the fuel cell, calculated in Equation (2.50),
- Q_{amb} [W] is the heat released into the environment,
- Q_i [W] is the heat supplied or removed from the mass flows entering and leaving the fuel cell,
- Q_{cool} [W] is the heat removed by the cooling system (see Section 3.5).

The heat released into the environment Q_{amb}, due to convection, is calculated by the following equation, where the product $h_{FC}A_{ext,FC}$ is the average heat exchange coefficient related to the external surface of the fuel cell.

$$Q_{amb} = h_{FC}A_{ext,FC}(T_{st} - T_{amb}) \tag{2.120}$$

All the mass flows enter and leave the fuel cell carrying heat with them. The mass flows have been previously calculated in the respective models, hence it is possible to execute the following balance, implementing only the heat capacity change with temperature of each element.

$$Q_i = \sum_j m_{in,j}c_{p,in,j}T_{in,j} - \sum_k m_{out,k}c_{p,out,k}T_{st} \tag{2.121}$$

In general, the inlet anode mass flow is composed by hydrogen and vapor while the outlet anode (if the purge is active) can be composed by hydrogen, vapor, liquid water (very rarely) and not considering nitrogen. The inlet cathode mass flow is composed by oxygen, nitrogen and vapor while the outlet cathode mass flow is composed by oxygen, nitrogen, vapor and liquid water, when the saturation condition is reached into the cathode channels.

The heat capacities $c_{p,i}$ of hydrogen, oxygen and nitrogen are calculated by the Equations (2.122) as functions of temperature. This approach is suggested by NIST in [54] and in Table 2.2 are reported the parameters for the examined species.

$$c_{p,i} = A + Bt + Ct^2 + Dt^3 + \frac{E}{t^2} \tag{2.122}$$

where

$$t = \frac{T}{1000} \tag{2.123}$$

Table 2.2 – Hydrogen, oxygen and nitrogen parameters for heat capacity calculation

	H_2	O_2	N_2
A	33.066178	31.32234	28.98641
B	-11.363417	-20.23531	1.853978
C	11.432816	57.86644	-9.647459
D	-2.772874	-36.50624	16.63537
E	-0.158558	-0.007374	0.000117
T [K]	*298 – 1000*	*100 – 700*	*100 – 500*

The heat capacity $c_{p,w}$ of water, both in vapor and in liquid form, is calculated by the Equation (2.124), always as function of temperature. This equation is obtained by a regression of the vapor and liquid water data presented by NIST in [54]. The values of the coefficients, obtained with the regression of vapor and liquid water data, are reported in Table 2.3.

$$c_{p,w} = A_w + B_w T + C_w T^2 + D_w T^3 + E_w T^4 \tag{2.124}$$

Table 2.3 – Vapor and liquid water parameters for heat capacity calculation between 273 K and 450 K

	Vapor	***Liquid water***
A_w	-22.5914542031468	259.193648482918
B_w	0.525206762826457	-1.98736183503556
C_w	-0.00158385779744722	0.00807329055630358
D_w	1.26841858283208e-06	-1.47108405843869e-05
E_w	9.65636406481091e-10	1.02418118481342e-08

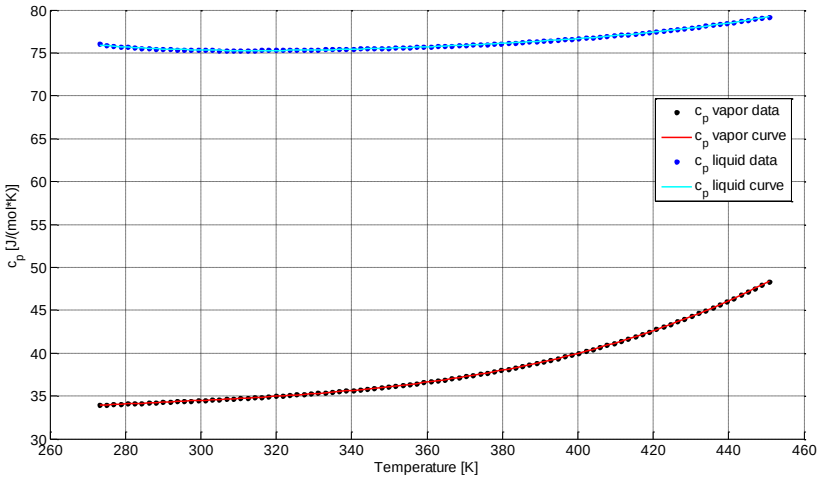

Figure 2.14 – Heat capacities of vapor and liquid water

3 PEM-FC Model: Auxiliary Components

In the previous section, the development of the fuel cell stack model, which consists of stack voltage, anode flow, cathode flow, membrane hydration and stack thermal models, is presented. In this section, the focus has been set on the reactant supply subsystems of a typical PEM-FC system and thus the models of the components related to these subsystems are developed.

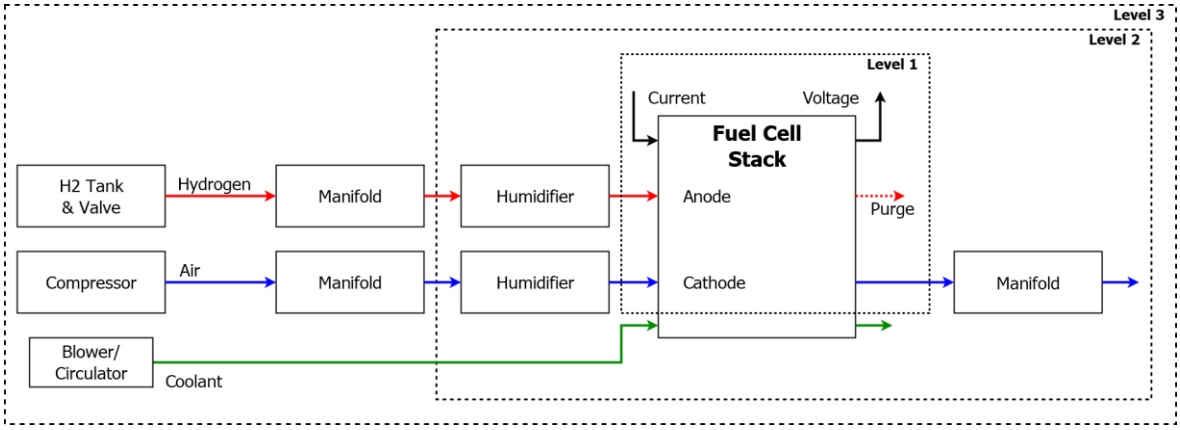

Figure 3.1 – Block diagram of the PEM-FC system model

The block diagram of Figure 3.1 illustrates the components of the PEM fuel cell system model and the proposed subdivision into distinct levels:

- Level 1: Fuel Cell Module (or Fuel Cell Stack) comprising the models of stack voltage, membrane hydration, anode and cathode fluxes and anode purge, described in previous section.
- Level 2: Auxiliary components of the system including the humidifiers and the cathode return manifold.
- Level 3: Complete system with hydrogen storage model, anode pressure regulation valve, air compressor, inlet manifolds and cooling system.

In the following sections, the models belonging to levels 2 and 3 will be described in detail.

3.1 Hydrogen Supply Valve Model

Usually the fuel used to supply a PEM fuel cell system is stored into a hydrogen tank in gaseous form, normally compressed at 200 bar or less. Therefore, the model considers a high-pressure hydrogen supply. The pressure in the tank can vary depending on the hydrogen tank load, but in any case the pressure must be reduced using a pressure reducing valve, also called Joule-Thomson valve. This valve guarantees, by an isenthalpic process, a constant pressure at the downstream flow and hence at the anode channel, independently from the variable mass flow rate consumed by the fuel cell. For this reason, the simplified hydrogen supply model valve calculates, directly and instantly, the hydrogen mass flow required by the fuel cell stack, according to the current generated by the PEM-FC. Thus, the inlet

hydrogen mass flow to the anode supply manifold $W_{in,sm,AN}$, calculated in the Equation (3.1), is assumed to be equal to the hydrogen which reacts into the fuel cell, calculated in Equation (2.72).

$$W_{in,sm,AN} = \frac{i_{st} n_{FC} M_{H_2}}{2F} \tag{3.1}$$

The outlet pressure of the valve corresponds to the anode supply manifold pressure calculated by the Equation (3.20).

In general, during the process of expansion from the pressurized tank to the desired pressure, hydrogen increase its temperature proportionally to the pressure drop. Figure 3.2 shows the T-S diagram for equilibrium hydrogen for interested temperatures. Considering a pressurized PEM fuel cell that usually operates in the range of 1÷3 bar, and the hydrogen tank at the ambient temperature of about 295 K, the hydrogen temperature increases according to the storage pressure. For drop pressure lower than 50 bar the hydrogen temperature increase is negligible, considering the expansion process at constant enthalpy performed by the pressure reducing valve. For higher drop pressure the temperature increase is greater but however limited to 10÷15 K. For this reason, in this model the temperature of hydrogen output from the pressure reducing valve and along the supply model is assumed to be constant and equal to the ambient temperature.

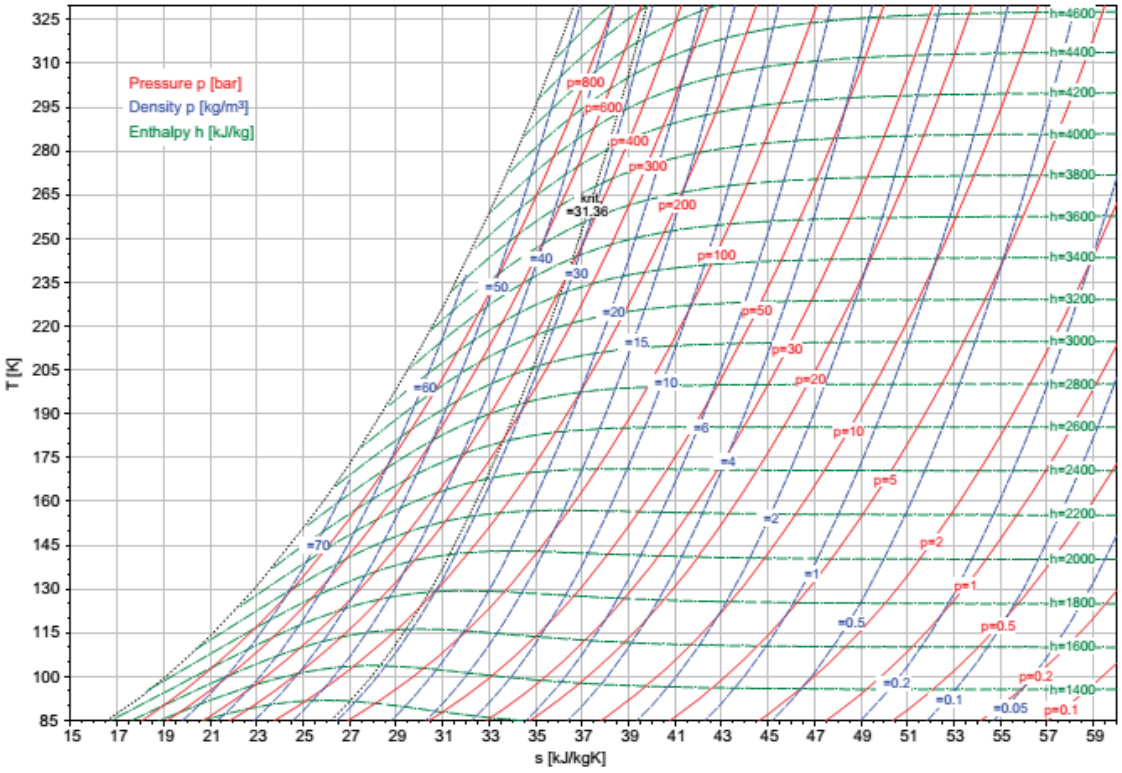

Figure 3.2 – T-S diagram for equilibrium hydrogen for temperatures from 85 to 330 K [55]

3.2 Air Compressor Model

The air compressor model is developed on the basis of the work presented in [2] and modified to easily reproduce the performances of different compressors, especially in terms of air mass flow, starting from the reference compressor tested in [56] and analysed in [2]. Therefore, is possible to simulate the right compressor for the PEM fuel cell under investigation, only by adjusting the scale parameter.

The air compressor model consists of two sub-models, as shown in Figure 3.3. The first static sub-model allows calculating the air mass flow processed W_{cp} by means of the interpolation of the characteristic curves of the compressor and the outlet air temperature $T_{cp,out}$ and the absorbed power P_{cp} using the thermodynamic equations. The second dynamic sub-model represents the inertia of the compressor and its electric motor and allow to calculate the rotational speed ω_{cp} starting from the absorbed power P_{cp} and the voltage supply to the electric motor V_{cm}, the only control parameter of the compressor model. Therefore, the rotational speed ω_{cp} is the only dynamic variable of this model.

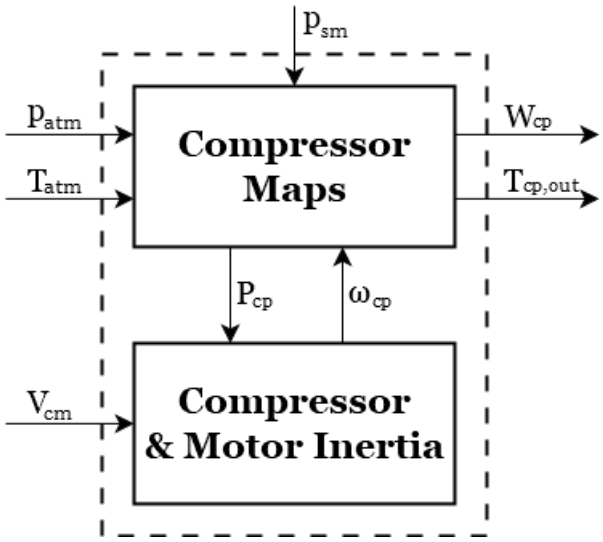

Figure 3.3 – Block diagram of air compressor model [2]

The Jensen & Kristensen method, presented in [57], is adopted to digitalize and interpolate the compressor maps. This is a not linear method for the regression of generic characteristic curves.

The following equations are used to calculate the corrected values of temperature, pressure, rotational speed and air mass flow with the aim of correctly considering the effect of possible variations on the input quantities to the compressor:

$$\theta = T_{cp,in}/288\ K \tag{3.2}$$

$$\delta = p_{cp,in}/1\ atm \tag{3.3}$$

$$N_{cp,corr} = N_{cp}/\sqrt{\theta} \tag{3.4}$$

$$W_{cp,corr} = W_{cp}\sqrt{\theta}/\delta \tag{3.5}$$

Using the Jensen & Kristensen method, the dimensionless head parameter Ψ is initially defined as follows:

$$\Psi = c_p T_{cp,in}\left[\left(\frac{p_{cp,out}}{p_{cp,in}}\right)^{\frac{\gamma-1}{\gamma}} - 1\right] \Bigg/ \left(\frac{U_c^2}{2}\right) \tag{3.6}$$

where γ is ratio of the specific heats of the gas at constant pressure, equal to 1.4 in the case of air, and the U_c is the compressor blade tip speed, calculated as follows:

$$U_c = \frac{\pi}{60} d_c N_{cp,corr} \tag{3.7}$$

where d_c is the diameter of the assumed reference compressor and $N_{cp,corr}$ is calculated by the Equation (3.4). The normalized compressor air flow rate Φ is defined by the following equation:

$$\Phi = \frac{W_{cp,corr}}{\rho_a \frac{\pi}{4} d_c^2 U_c} \tag{3.8}$$

where ρ_a is the air density. The normalized compressor air flow rate Φ is then related to the dimensionless head parameter Ψ as follows:

$$\Phi = \Phi_{max}\left[1 - exp\left(\beta\left(\frac{\Psi}{\Psi_{max}} - 1\right)\right)\right] \tag{3.9}$$

where Φ_{max}, β and Ψ_{max} are polynomial functions of the Mach number M, defined by the following equations:

$$\Phi_{max} = K_{scale}(a_4 M^4 + a_3 M^3 + a_2 M^2 + a_1 M + a_0) \tag{3.10}$$

$$\beta = b_2 M^2 + b_1 M + b_0 \tag{3.11}$$

$$\Psi_{max} = c_5 M^5 + c_4 M^4 + c_3 M^3 + c_2 M^2 + c_1 M + c_0 \tag{3.12}$$

The coefficient K_{scale} allows the scalability of the compressor maps based on the maximum air mass flow required by the PEM fuel cell system. In fact, it is possible to scale the compressor maps with relative accuracy with regard to the mass flow rate. This procedure is equivalent to considering the same type of compressor by varying the geometric dimensions: the performance in terms of pressure ratio will be comparable while in terms of mass flow will be very different. Further details regarding the setting of the coefficient K_{scale} on the basis of the selected PEM fuel cell system are reported in Section 4.3.
The compressor inlet Mach number, used in Equations (3.10)-(3.12), is defined by:

$$M = \frac{U_c}{\sqrt{\gamma R_a T_{cp,in}}} \tag{3.13}$$

where R_a is the air gas constant. In Table 3.1 are visible the values of the parameters used in the static air compressor sub-model.

Table 3.1 – Parameters for the static air compressor sub-model [2]

Parameter	*Description*	*Value*	*Unit*
$\boldsymbol{R_a}$	Air gas constant	286.9	J/(kg·K)
$\boldsymbol{\rho_a}$	Air density	1.23	kg/m^3
$\boldsymbol{d_c}$	Reference compressor diameter	0.2286	m

In Equations (3.10)-(3.12), a_i, b_i and c_i are the characteristic coefficients of the reference compressor, obtained by the regression process that allows to fit the Jensen & Kristensen equations to the experimental data available.
Given the limited availability on the market and in literature of complete compressors maps, especially for applications in PEM fuel cells, the results presented in [2] were used as reference data. These results are obtained in [2] by digitizing the experimental compressor map presented in [57]. The regression coefficients are reported in Table 3.2 and the Figure 3.4 shows that the Jensen & Kristensen method with these coefficients is able to represents the experimental data very well.

Table 3.2 – Compressor map regression coefficients [2]

Parameter	*Value*
$\boldsymbol{a_4}$	-3.69906×10^{-5}
$\boldsymbol{a_3}$	$+2.70399 \times 10^{-4}$
$\boldsymbol{a_2}$	-5.36235×10^{-4}
$\boldsymbol{a_1}$	-4.63685×10^{-5}
$\boldsymbol{a_0}$	$+2.21195 \times 10^{-3}$
$\boldsymbol{b_2}$	$+1.76567$
$\boldsymbol{b_1}$	-1.34837
$\boldsymbol{b_0}$	$+2.44419$
$\boldsymbol{c_5}$	-9.78755×10^{-3}
$\boldsymbol{c_4}$	$+0.10581$
$\boldsymbol{c_3}$	-0.42937
$\boldsymbol{c_2}$	$+0.80121$
$\boldsymbol{c_1}$	-0.68344
$\boldsymbol{c_0}$	$+0.43331$

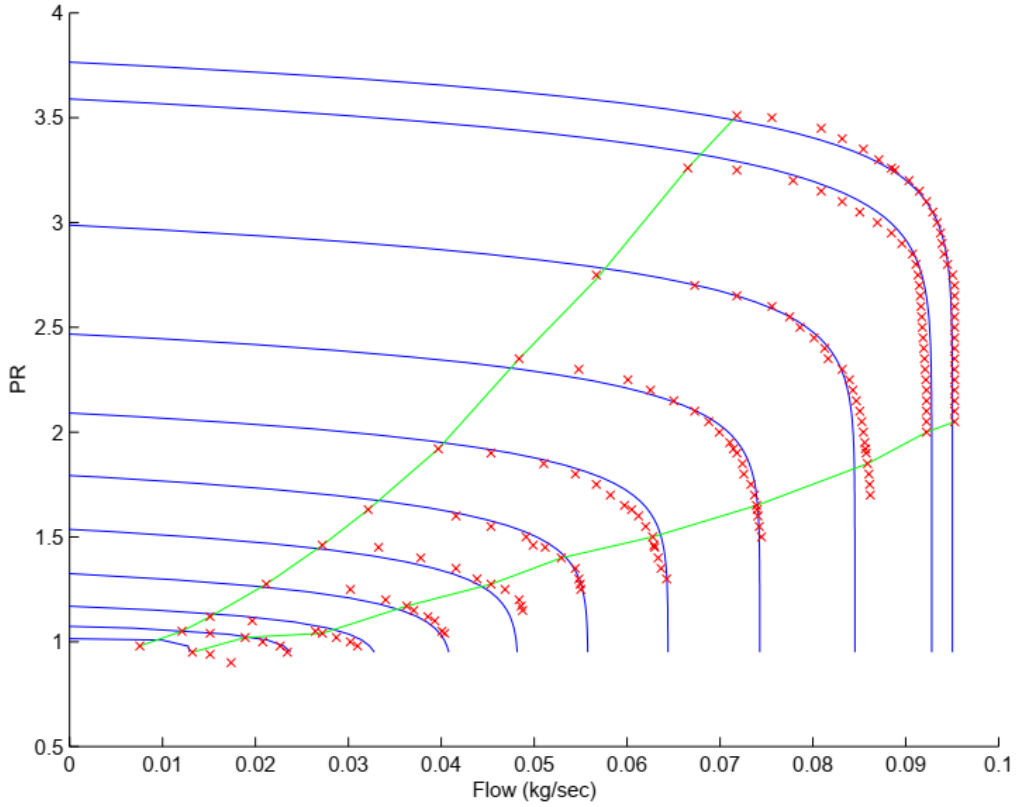

Figure 3.4 – Validation of the compressor map model with the experimental data [2]

A matrix of compressor efficiency experimental data is used in a Matlab©-Simulink© look-up table able to interpolate the data as a function of the air mass flow and the pressure ratio across the compressor, with maximum efficiency values of about 80%.
The compressor outlet air temperature is calculated by the following traditional thermodynamic equation [58], [59]:

$$T_{cp,out} = T_{cp,in} + \frac{T_{cp,in}}{\eta_{cp}}\left[\left(\frac{p_{cp,out}}{p_{cp,in}}\right)^{\frac{\gamma-1}{\gamma}} - 1\right] = T_{atm} + \frac{T_{atm}}{\eta_{cp}}\left[\left(\frac{p_{sm}}{p_{atm}}\right)^{\frac{\gamma-1}{\gamma}} - 1\right] \tag{3.14}$$

The torque τ_{cp} required to drive the compressor is calculated in the standard way [58], [59]:

$$\tau_{cp} = \frac{c_p}{\omega_{cp}}\frac{T_{atm}}{\eta_{cp}}\left[\left(\frac{p_{sm}}{p_{atm}}\right)^{\frac{\gamma-1}{\gamma}} - 1\right] W_{cp} \tag{3.15}$$

To better represent the dynamic behaviour of the compressor, in terms of rotational speed, the following lumped rotational parameter approach is adopted.

$$J_{cp}\frac{d\omega_{cp}}{dt} = \left(\tau_{cm} - \tau_{cp}\right) \tag{3.16}$$

where:

- J_{cp} is the combined inertia of compressor and electric motor (kg·m^2);
- ω_{cp} is the rotational compressor speed (rad/s);
- τ_{cm} is the compressor motor torque (N·m);
- τ_{cp} is the torque required to drive the compressor (N·m), calculated in Equation (3.15).

The inertia of the rotating elements is calculated in [60] based on the compressor diameter as follows:

$$J_{cp} = K_{scale} \cdot 0.092 \cdot \frac{d_c^2}{4} \tag{3.17}$$

The compressor motor torque is calculated from the electric motor voltage V_{cm} by means of the following static motor equation:

$$\tau_{cm} = \eta_{cm} \frac{k_t}{R_{cm}} \left(V_{cm} - k_v \omega_{cp}\right) \tag{3.18}$$

where k_t, R_{cm} and k_v are characteristic electric motor constants and η_{cm} is the motor mechanical efficiency. The values used for these parameters are reported in Table 3.3.

Table 3.3 – Parameters for the dynamic air compressor sub-model [2]

Parameter	*Value*	*Unit*
$\boldsymbol{c_p}$	1004	J/(kg·K)
$\boldsymbol{k_v}$	0.0153	V/(rad/s)
$\boldsymbol{k_t}$	0.0225	N·m/A
$\boldsymbol{R_{cm}}$	$1.2/K_{scale}$	Ω
$\boldsymbol{\eta_{cm}}$	98	%

For the application of this adaptable air compressor model is sufficient to fit the necessary maximum air mass flow for the PEM-FC analysed with the air compressor performances, changing the coefficient K_{scale} in an appropriate way. An example of this procedure is reported in Section 4.3.

3.3 Manifold Models

The manifold's models are necessary to represents the dynamic delays related to the volumes of the pipes or components that make up the complete PEM fuel cell system under investigation. For example, referring to the PEM-FC system in Figure 1.12, three different manifolds are reported:

- the anode supply manifold model that represents the lumped volume associated with the volume of the pipes between the pressure reducing valve of the hydrogen tank and the fuel cell stack, including the volume of the humidifier;
- the cathode supply manifold model that represents the lumped volume associated with the volume of the pipes between the compressor and the fuel cell stack, including the volume of the humidifier;
- the cathode return manifold that represents the pipeline at the cathode fuel cell stack exhaust.

1. Mass conservation principle

Different equations are necessary to develop the manifold model. The first equation is the following mass conservation principle:

$$\frac{dm_{man}}{dt} = W_{in,man} - W_{out,man} \tag{3.19}$$

where m_{man} is the mass of the gases accumulated into the manifold volume and $W_{in,man}$ and $W_{out,man}$ are the manifold inlet and outlet mass flows.

2. Energy conservation principle

In general, if it is expected that the flow temperature changes inside the manifold, the following pressure dynamic equation, derived from the energy conservation principle and the ideal gas law, is used with the mass balance equation (3.19) [2].

$$\frac{dp_{man}}{dt} = \frac{\gamma_{gas} R_{gas}}{V_{man}} \left(W_{in,man} T_{in,man} - W_{out,man} T_{out,man} \right) \tag{3.20}$$

where γ_{gas} is the ratio of the specific heat capacities of the gas considered, R_{gas} is the gas constant and V_{man} is the volume of the manifold. The outlet temperature $T_{out,man}$ in Equation (3.29) is calculated with the ideal gas law as follows:

$$T_{out,man} = \frac{p_{man} V_{man}}{m_{man} R_{gas}} \tag{3.21}$$

Otherwise, if the manifold inlet temperature is almost equal to ambient temperature or it is expected no change in flow temperature inside the manifold, the manifold filling dynamics follow the isothermal relation [2]:

$$\frac{dp_{man}}{dt} = \frac{R_{\text{gas}} T_{man}}{V_{man}} \left(W_{in,man} - W_{out,man}\right) \tag{3.22}$$

Therefore, if the temperature is constant along the manifold:

$$T_{in,man} = T_{out,man} = T_{man} \tag{3.23}$$

3. Nozzle flow equation

In general, the outlet mass flow of the manifold is governed by nozzle (throttle) equations (1.19) and (1.20) [2]. The outlet mass flow is a function of the manifold pressure p_{man} and the pressure downstream from the manifold, which is normally assumed to be fixed. Since the pressure drop between the manifold and the downstream is normally quite large, the Equations (3.24) and (3.25) are used to represent the manifold respectively in subcritical and supercritical conditions [2]. The critical condition is reported in Equation (3.26).

$$W_{out,man,subcr} = \frac{C_D A_T p_{man}}{\sqrt{R T_{man}}} \left(\frac{p_{ds}}{p_{man}}\right)^{\frac{1}{\gamma}} \left\{ \frac{2\gamma}{\gamma - 1} \left[1 - \left(\frac{p_{ds}}{p_{man}}\right)^{\frac{\gamma-1}{\gamma}} \right] \right\}^{\frac{1}{2}} \tag{3.24}$$

$$W_{out,man,supercr} = \frac{C_D A_T p_{man}}{\sqrt{R T_{man}}} \gamma^{\frac{1}{2}} \left(\frac{2}{\gamma + 1}\right)^{\frac{\gamma+1}{2(\gamma-1)}} \tag{3.25}$$

$$\left(\frac{p_{ds}}{p_{man}}\right)_{cr} = \left(\frac{2}{\gamma + 1}\right)^{\frac{\gamma}{\gamma-1}} \tag{3.26}$$

where γ is the ratio of the specific heat capacities of the gas flowing through the manifold. The throttle opening area A_T can be set constant or can be used as an extra control variable to regulate the manifold pressure, and thus all the upstream volumes or components [2].

If the pressure difference between the manifold and the downstream volume is small and always fall into the sub-critical flow region, the mass flow can be calculated by the linearized form of the sub-critical nozzle flow equation explained in Section 1.2.

$$W_{out,man} = K_{man}(p_{man} - p_{ds}) \tag{3.27}$$

where K_{man} is the inlet anode nozzle constant, which strongly depends from the manifold geometry as explained in Section 4.2.

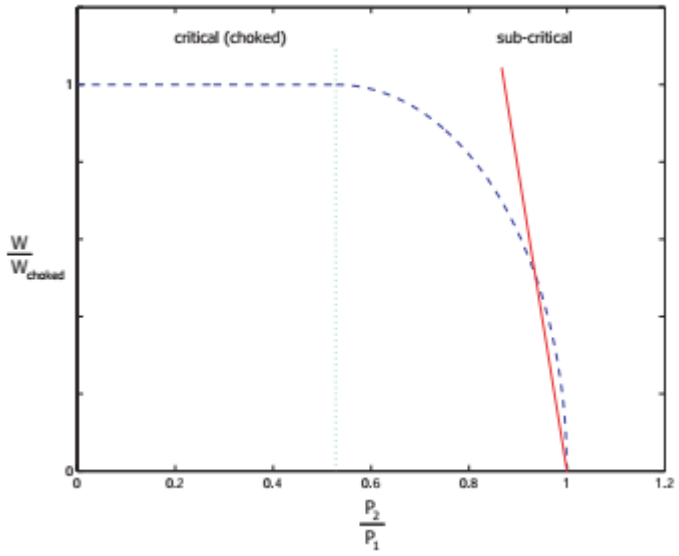

Figure 3.5 – Relative (dashed line) and linearized (solid line) mass flow as functions of pressure ratio [2]

3.4 Humidifier Models

Air flow from the air compressor and hydrogen flow from the hydrogen supply valve are humidified before entering the stack by injecting water into the streams in theirs humidifiers. Usually the volume of the humidifier is small and hence it can be considered as part of the supply manifold volume [2]. A static model of the humidifier is used to calculate the change in the flow humidity due to the additional injected water [2]. The temperature of the flow is assumed to be constant, thus $T_{in} = T_{out}$ [2]. The water injected is assumed to be in the form of vapor or the latent heat of vaporization is assumed to be taken into account in the flow cooler [2].

The vapor saturation pressure is calculated from the inlet flow temperature using the set of equations reported in Section 1.1. Then, the inlet vapor pressure is determined using Equation (1.6):

$$p_{v,in} = \Phi_{in} \cdot p_{sat}(T_{in}) \tag{3.28}$$

Since humid flow is a mixture of dry flow and vapor, the dry gas partial pressure is the difference between the total pressure and the vapor pressure as follows:

$$p_{dry,in} = p_{in} - p_{v,in} \tag{3.29}$$

where dry represents dry air for the cathode circuit and dry hydrogen for the anode circuit. The inlet humidity ratio can then be calculated from:

$$\omega_{in} = \frac{M_v}{M_{dry}} \frac{p_{v,in}}{p_{dry,in}} \tag{3.30}$$

where M_{dry} is the molar mass of the dry gas considered. The inlet mass flow rate of dry gas and the inlet mass flow rate of the vapor are:

$$W_{dry,in} = \frac{1}{(1+\omega_{in})} W_{in} \tag{3.31}$$

$$W_{v,in} = W_{in} - W_{dry,in} \tag{3.32}$$

The mass flow rate of dry gas remains the same for inlet and outlet of the humidifier, $W_{dry,in} = W_{dry,out}$. Now it is possible to calculate, knowing the desired humidity, the vapour partial pressure of the outgoing flow from the static humidifier model as follows:

$$p_{v,out} = \Phi_{des} \cdot p_{sat}(T_{out}) \tag{3.33}$$

The outlet desired humidity ratio can then be calculated from following equation, with the hypothesis of $p_{dry,in} = p_{dry,out}$.

$$\omega_{des} = \frac{M_v}{M_{dry}} \frac{p_{v,out}}{p_{dry,out}} = \frac{M_v}{M_{dry}} \frac{p_{v,out}}{p_{dry,in}} \tag{3.34}$$

Thus, the outlet mass flow of the vapour and the mass flow of vapour injected are:

$$W_{v,out} = \omega_{des} \cdot W_{dry,out} \tag{3.35}$$

$$W_{v,inj} = W_{v,out} - W_{v,in} \tag{3.36}$$

Finally, the total outlet mass flow and total outlet pressure are:

$$W_{out} = W_{in} + W_{v,inj} \tag{3.37}$$

$$p_{out} = p_{v,out} + p_{dry,in} \tag{3.38}$$

3.5 Cooling System Model

Figure 3.6 shows schematically the cooling system considered. The aim of the cooling system model is to calculate the heat removed by the coolant Q_{cool}, necessary into the stack thermal balance of Equation (2.119) to control the stack temperature. The cooling system model considers the fuel cell temperature T_{st} uniform all over the stack and can simulate air or water cooling. The cooling system is assumed to be composed of a stack temperature sensor, a PI controller and a cooling fan/circulator. The purpose of the cooling system is to monitor and maintain constant the stack temperature, modifying the coolant mass flow through the fuel cell stack.

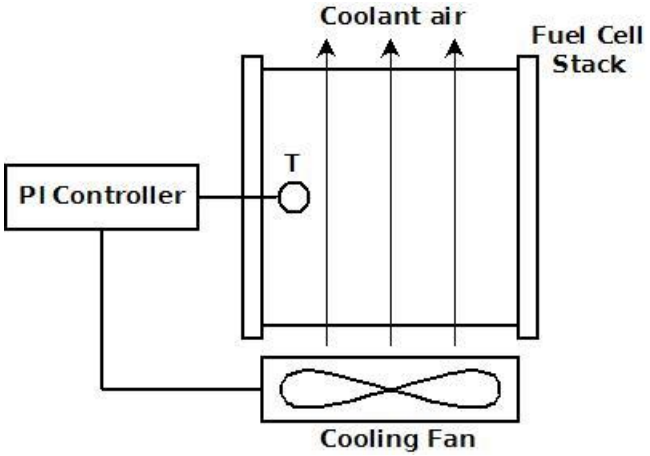

Figure 3.6 – Block diagram of the cooling system

The stack temperature T_{st} is measured by the temperature sensor, usually thermoresistance or thermocouple, modeled by a first order delay equal to 1 second. In general, the thermoresistance sends the information of the stack temperature to the PI controller.
This controller, during the start-up, is able to maintain the cooling fan/circulator disable until the stack temperature has not reached the set-point temperature. During the switch-off, the controller allows to maintain constant the coolant flow even after turning off the FC, to simulate the forced cooling phase performed for safety reasons. In all other operative conditions, the PI controller calculates the difference between the stack temperature and the set-point temperature and, based on this difference, controls the cooling fan/circulator to maintain the stack temperature as close as possible to the set-point value.
Usually, is quite difficult to obtain the characteristic curves of the cooling fan or the circulator. Therefore, the PI controller generates directly the coolant mass flow W_{cool}. Downstream, a dead time of 0.1 s and a first order delay of 0.2 s were inserted to simulate the dynamic delays of the cooling fan/circulator.
The heat removed by the cooling system Q_{cool} and the flow rate of cooling fluid W_{cool} generated by the fan/circulator are used in the following thermal balance, assuming as temperature of the cooling fluid inlet $T_{cool,in}$ the ambient temperature T_{amb} in case of air cooling of the system, in order to calculate the fluid outlet temperature $T_{cool,out}$.

$$\left(m_{cool}^{0} c_{p,cool}\right) \frac{dT_{cool,out}}{dt} = W_{cool} c_{p,cool}\left(T_{cool,in} - T_{cool,out}\right) - Q_{cool} \tag{3.39}$$

By varying the specific heat related to the fluid $c_{p,cool}$ it is easy to modify the type of the cooling system considered, whether air or water based. The product $m_{cool}^{0} c_{p,cool}$ represents the average heat capacity of the coolant inside the cooling system, while the average heat capacity of the fuel cell was already been considered into Equation (2.119).
The convective heat exchange between the cooling fluid and the fuel cell module Q_{cool} is modeled through the following equation with the temperature T_{FC} calculated using the Equation (2.119).

$$Q_{cool} = (hA)_{cool}\left(T_{FC} - T_{cool,avg}\right) \tag{3.40}$$

The product $(hA)_{cool}$ represents the average surface convection coefficient of the heat exchange between stack and cooling fluid and the temperature $T_{cool,avg}$ is the average between the inlet and the outlet cooling temperatures. This approach is commonly used and presented in [27] and also allows to obtain, if necessary, the convection coefficient by means of experimental tests.

4 PEM-FC Model: Validations

In this section the validation of the model of the PEM fuel cell system is presented. Due to lack of experimental data, it was necessary to validate and analyse the 4 kW Ballard MK5-E system, studied extensively in literature by Laurencelle et al. in [12] and by Lee, Yang in [61]. The experimental data used to validate the model are therefore derived from literature: this approach does not affect the goodness and generality of the results since the PEM fuel cells are scalable and modular. In fact, the individual cells are stacked to generate the total power required, generally up to a maximum of 35-45 kW per stack. To achieve this result around 200-300 cells are stacked, with criticalities related to the correct distribution of flows and removal of liquid water, but with performance of the single cell very similar to those of the stack of smaller sizes. Even the tests that the manufacturers make on their systems are usually carried out on modules of reduced power, cheaper and easily managed. For these reasons the results that are presented for the 4 kW Ballard MK5-E system are completely scalable even for larger systems.

4.1 Stack Voltage Model Validation

In this section is explained the validation of the stack voltage model developed in Section 2.1 and summarized in Section 2.1.5. This validation consists initially in the fitting process of the stack voltage model parameters in order to adapt the polarization curves resulting from the model to the experimental data available. For this purpose, a Matlab® code algorithm has been developed and deeply explained in Appendix A. After the fitting process, it has been necessary to compare resulting parameters against the parameters available in literature.
Therefore, the algorithm developed for this purpose was made as general and adaptable as possible, to be applied to different types of PEM fuel cells. In general, this algorithm can calculate, if they are not known, all the desired stack voltage model parameters: in this case ξ_1, ξ_2, ξ_3 and ξ_4 for activation loss, λ_m for Ohmic loss, m_{conc} and n_{conc} for concentration loss. In fact, for the validation process presented in this section, the stack voltage model used is the Amphlett-Springer one (see Section 2.1.5) due to the availability of some stack voltage parameters related to the indicated model.
Clearly, if more polarization curves are available, the results of the algorithm will be more accurate. Thus, for a perfect fitting process with the algorithm, different polarization curves at different stack temperature and operative pressure should be available. However, it will be demonstrated that even with a limited number of polarization curves (at least one) the stack voltage parameters, resulting from the adaptation process with the algorithm, will show a good degree of precision.

The stack voltage model validation is presented considering the experimental data of a PGS-105B prototype from Ballard Power Systems, reported by Laurencelle et al. in [12] and also named MK5-E. It is based on a Ballard 4 kW PEM-FC fuel cell stack model Mark V. Table

4.1 reports the fuel cell parameters and the experimental operative parameters given in [12]. Figure 4.1 shows the polarization curves at different stack temperatures resulting in [12].
Normally, the polarization curves are obtained by varying the required current to the fuel cell, maintaining constant all other parameters as the anode and cathode pressures and the membrane humidity. Since in [12] is not explicitly mentioned the behaviour of the membrane hydration, a specific test was conducted to deduce control and behaviour of the membrane water content. The membrane hydration model, exposed in Section 2.2, allows to calculate the membrane water content λ_m knowing only anode and cathode humidity. Therefore, Matlab-Simulink simulations with the complete model and the operative data exposed in Table 4.1 was conducted at variable and constant membrane water content and the results of these two simulations were compared with the polarization curve at 345 K and the load switching points at the same temperature available in [12]. This study clearly confirmed that the Ballard MK5-E PEM fuel cell operates at almost constant membrane water content, probably by means of the control of inlet air and hydrogen humidification levels based on the requested current. Therefore, the membrane water content is an unknown and constant parameter for all the polarization curves and it is calculated by the algorithm during the fitting process.
In [12] Laurencelle et al. developed a concentration model similar to that exposed in Section 2.1.4, providing the values of the parameters m_{conc} and n_{conc} for the MK5-E fuel cell, reported in Table 4.1. Since in the polarization curves of Figure 4.1 there are no experimental points in the concentration loss area, it was decided to integrate Laurencelle parameters for concentration loss and calculate only the activation and Ohmic parameters by the algorithm.

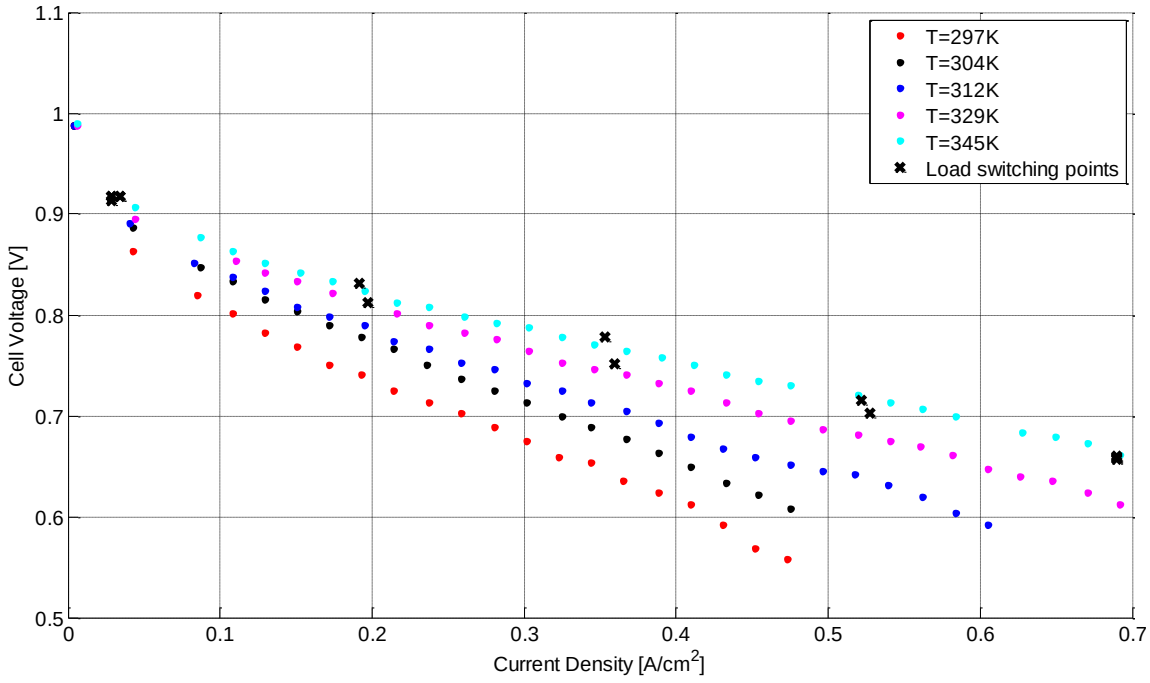

Figure 4.1 – Polarization curves of Ballard MK5-E [12]

Table 4.1 – Ballard MK5-E characteristics and operational parameters [12]

Symbol	*Value*	*Unit*	*Description*
n_{FC}	36	-	Number of cells
A_{FC}	232	cm^2	Cell active area
t_m	0.0178	cm	Membrane thickness
p_{AN}	$3 \cdot 10^5$	Pa	Operative anode pressure
p_{CA}	$3 \cdot 10^5$	Pa	Operative cathode pressure
j_{lim}	0.7	A/cm^2	Limit current density
P_{nom}	4	kW	Nominal power
m_{conc}	$1.1 \cdot 10^{-4} - 1.2 \cdot 10^{-6} \cdot T$ if $T \geq 39°C$ $3.3 \cdot 10^{-3} - 8.2 \cdot 10^{-5} \cdot T$ if $T < 39°C$	V	Parameter for concentration loss
n_{conc}	8	cm^2/A	Parameter for concentration loss

In Figure 4.1 are also visible the black x-marks that represent the fuel cell stack voltages at different loads during a real operation of the fuel cell at the nominal stack temperature of 72°C (345 K), reported in Figure 4.2. Since these points are close to the polarization curve shown in Figure 4.1, it follows that, during the fuel cell operation, the membrane water content λ_m remains almost constant. This difference of stack voltages at different loads are due to the dynamic effects of the fuel cell, in particular to the direction of current variations. This phenomenon is called hysteretic effect and is clearly shown in Figure 4.3. When the current increases, the water is drained mainly from the anode to the cathode side of the membrane by electro-osmotic drag, lowering temporarily the humidification level of the membrane, directly related to the stack voltage [12]. Inversely, as the water production at the cathode increases with current, the membrane humidity increases temporarily due to back diffusion of water from the cathode to the anode side of the membrane, until equilibrium is reached [12]. Another contributing factor to the hysteresis could be the load sweep rate, which is faster than the response time of the mass flow controller [12].

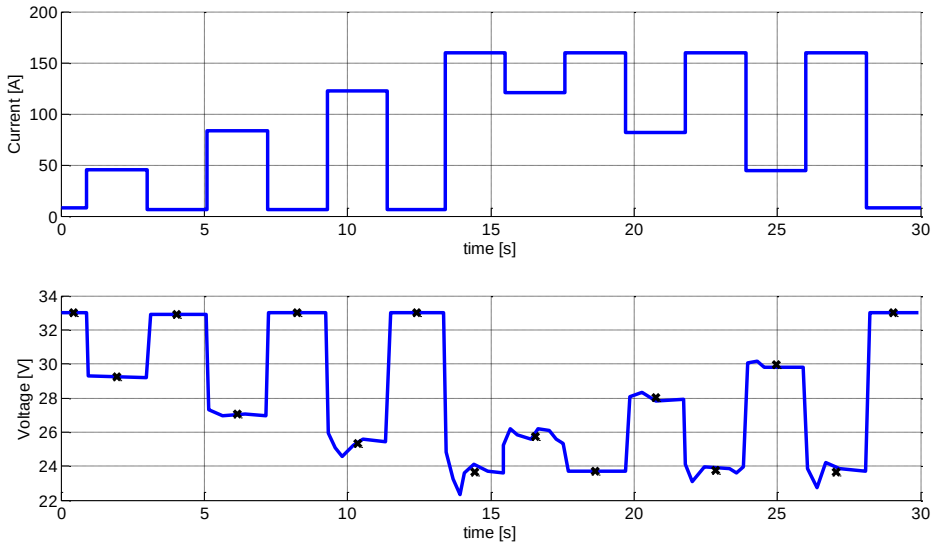

Figure 4.2 – Current and voltage under a series of load switching [12]

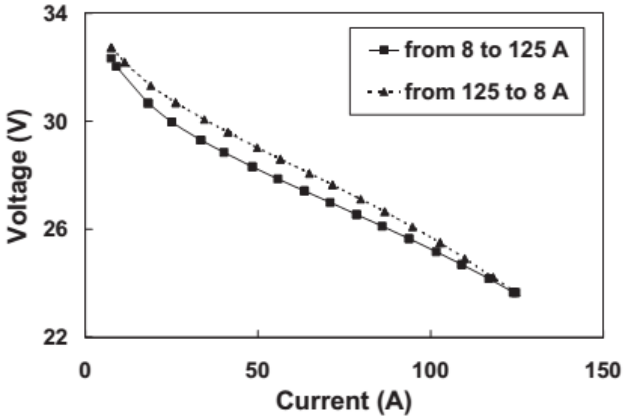

Figure 4.3 – Hysteresis of the polarization curve measurements presented in [12]

The results of the fitting process for the activation and Ohmic parameters by the algorithm, exposed in Appendix A, using all five polarization curves available from [12], are:

- ξ_1 = 0.9123
- ξ_2 = $3 \cdot 10^{-3}$
- ξ_3 = $6.8789 \cdot 10^{-5}$
- ξ_4 = $1.0041 \cdot 10^{-4}$
- λ_m = 9.8174

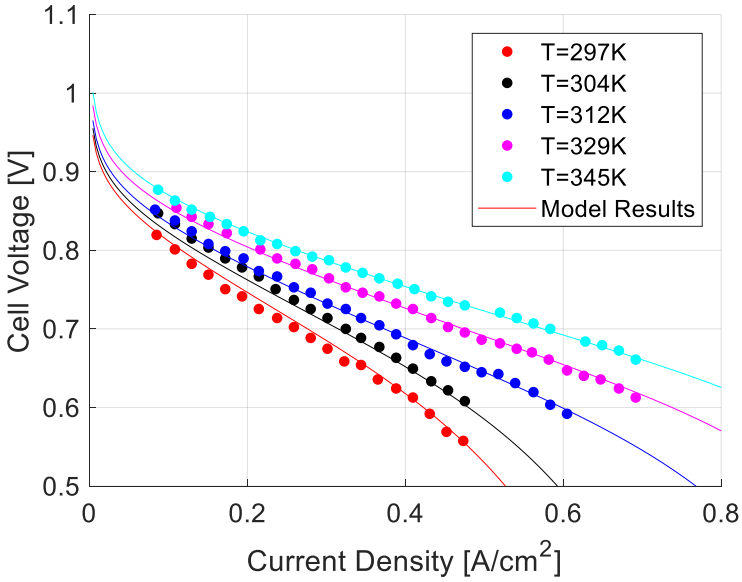

Figure 4.4 – Stack voltage model validation using all the polarization curves

With this set of parameters the Amphlett-Springer model exposed in Section 2.1.5.1 gives the polarization curves presented in Figure 4.4 with maximum error under 2%, as visible in the parity plot of Figure 4.5.

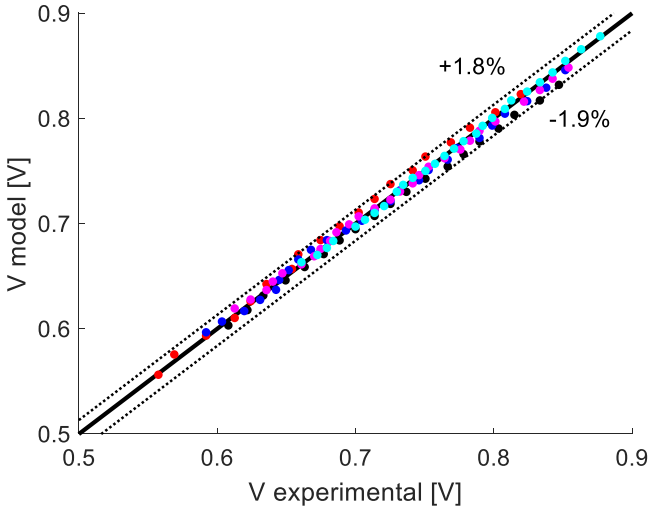

Figure 4.5 – Parity plot of stack voltages using all the polarization curves

As shown by the average errors and in Figure 4.4, the approximation degree of the stack voltage model results very good, especially for the polarization curves at higher temperature. This agrees with the assignment, inside the Matlab algorithm, of a greater weight to the average errors of polarization curves at 329 K and 345 K (see Appendix A).

The results of the fitting process of the activation and Ohmic parameters by the algorithm, exposed in Appendix A, using only the polarization curve at 329 K, are:

- ξ_1 = 1.1118
- ξ_2 = $3.8 \cdot 10^{-3}$
- ξ_3 = $8.3020 \cdot 10^{-5}$
- ξ_4 = $1.2006 \cdot 10^{-4}$
- λ_m = 9.8262

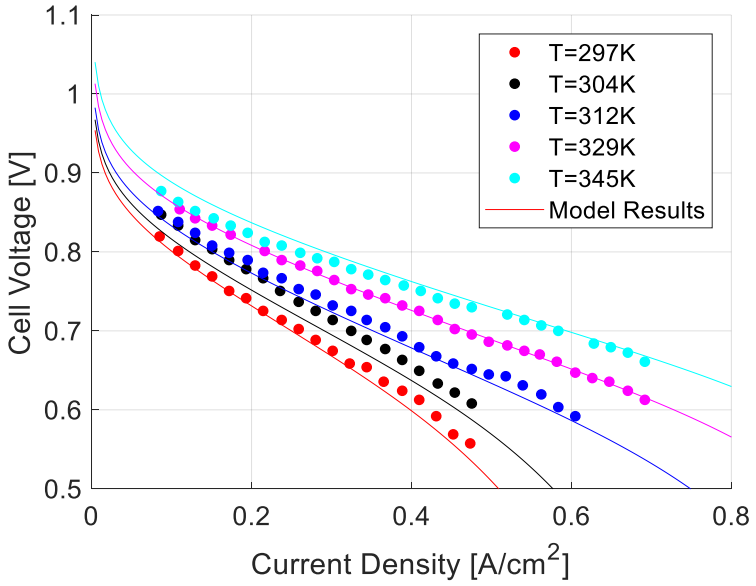

Figure 4.6 – Stack voltage model validation using one polarization curve at 329 K

With this set of parameters the Amphlett-Springer model exposed in Section 2.1.5.1 gives the polarization curves presented in Figure 4.6 with maximum error of about 3%, as visible in the parity plot of Figure 4.7.

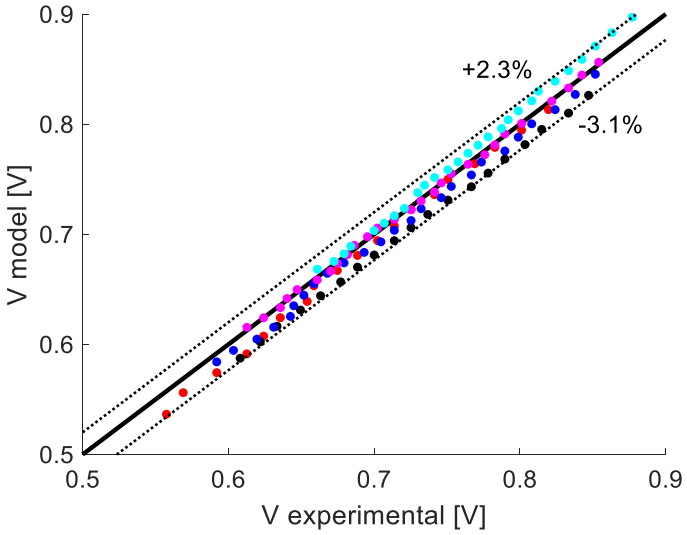

Figure 4.7 – Parity plot of stack voltages using one polarization curve at 329 K

As explained in Section 2.1.5, the polarization curve is the sum of:

- Nernst potential, constant at different current density;
- activation loss, acting mainly at low current density;
- Ohmic loss, which varies the slope of the polarization curve affecting the central field;
- concentration loss, acting at high current density.

Since this validation process regards the calculation of activation and Ohmic losses, the good approximation of the model is visible at low and medium values of current density. Taking this into account, even if the average errors of this second fitting process, using only one polarization curve, seems to be comparable with the errors of the first fitting process considering all the polarization curves, it is clearly that the second fitting process is much less accurate with respect to the first one. However, the result obtainable with only one polarization curve is good enough to justify and allow the use of this fitting process also if only a polarization curve is available.

4.2 PEM-FC System Model Validation

Following the validation of the stack voltage model, presented in the previous paragraph, in this section is explained the validation of the PEM-FC system model developed in Section 2 and 3. This validation process consists in a comparison of the performances of the PEM-FC system model, during a variable request of current, against the experimental data provided by Laurencelle et al. in [12] and obtained using a Ballard MK5-E 4 kW PEM-FC system. All the fuel cell and operative experimental parameters are shown in Table 4.1 in Section 4.1.

Laurencelle et al in [12], during an experimental test at variable load, measured the stack voltage generated by the MK5-E fuel cell. Based on these results, reported in Figure 4.8, the validation is considered successful if the model of the complete PEM-FC system provides the same results in terms of stack voltage of the experimental test.

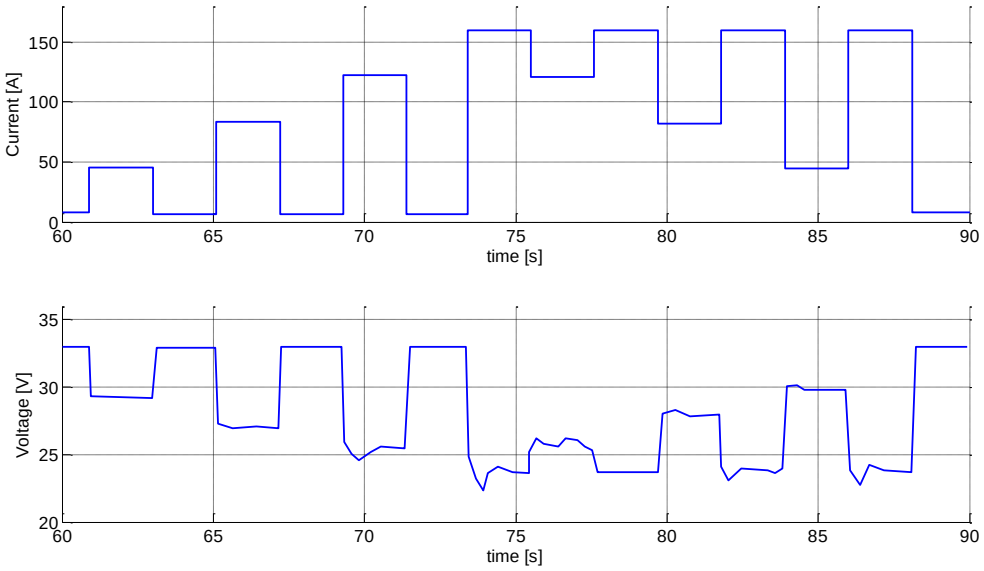

Figure 4.8 – Current and voltage under a series of load switching [12]

Table 4.2 shows all the parameters necessary to set the Matlab-Simulink model on the performance of the Ballard MK5-E fuel cell. The stack voltage model parameters obtained with the related validation presented in the previous section are also present in Table 4.2. For this validation process, the only excluded model was the air compressor model, since the experimental results [12] were obtained by feeding the fuel cell by means of a compressed air line, therefore without a dedicated compressor for the Ballard MK5-E system. The simulations were carried out with both the cooling model and the membrane humidification models active, resulting both sub-models validated at the end of the procedure. This is an important result to obtain information on the effective operative condition of the fuel cell in terms of membrane humidity, which greatly affects the performance, and about the goodness of the thermal balance and the control system of the stack temperature.

Table 4.2 – Parameters for the Ballard MK5-E PEM-FC system model

Symbol	Value	Unit	Description
T_{amb}	296	K	Ambient temperature
p_{amb}	$1.01325 \cdot 10^5$	Pa	Ambient pressure
ω_{amb}	0.5	-	Ambient relative humidity
$T_{setpoint,FC}$	345	K	FC set-point temperature [12]
dt	0.1	s	Time constant of integration
n_{FC}	36	-	Number of cells [12]
A_{FC}	232	cm^2	Cell active area [12]
t_m	0.0178	cm	Membrane thickness [61]
$\rho_{m,dry}$	0.002	kg/cm^3	Membrane dry density [61]
$M_{m,dry}$	1.1	kg/mol	Membrane dry equivalent weight [61]
p_{AN}	$3 \cdot 10^5$	Pa	Operative anode pressure [12]
p_{CA}	$3 \cdot 10^5$	Pa	Operative cathode pressure [12]
i_{max}	160	A	Maximum current [12]
P_{max}	4	kW	Maximum power [12]
ξ_1	0.9123	-	Parameter for activation loss
ξ_2	0.003	-	Parameter for activation loss
ξ_3	6.8789e-5	-	Parameter for activation loss
ξ_4	1.0041e-4	-	Parameter for activation loss
λ_m	9.8174	-	Membrane water content
m_{conc}	$1.1 \cdot 10^{-4} - 1.2 \cdot 10^{-6} \cdot T$ T≥39°C $3.3 \cdot 10^{-3} - 8.2 \cdot 10^{-}5 \cdot T$ T<39°C	V	Parameter for concentration loss [12]
n_{conc}	8	cm^2/A	Parameter for concentration loss [12]
p_{tank,H_2}	$10 \cdot 10^5$	Pa	Hydrogen pressure tank [12]
V_{AN}	$5 \cdot 10^{-3}$	m^3	Anode volume [61]
V_{CA}	$1 \cdot 10^{-2}$	m^3	Cathode volume [61]
$\omega_{des,AN}$	0.3	-	Inlet anode relative humidity desired
$\omega_{des,CA}$	1	-	Inlet cathode relative humidity desired
$V_{sm,AN}$	$2.5 \cdot 10^{-3}$	m^3	Anode supply manifold volume
$V_{sm,CA}$	$5 \cdot 10^{-3}$	m^3	Cathode supply manifold volume
$V_{rm,CA}$	$5 \cdot 10^{-3}$	m^3	Cathode return manifold volume
$C_{D,rm,CA}$	0.00124	-	Cathode return manifold throttle discharge coefficient [13]
K_{purge}	0	-	Purge coefficient
$K_{sm,AN}$	$3 \cdot 10^{-9}$	kg/(s·Pa)	Inlet anode nozzle constant
$K_{sm,CA}$	$2.05 \cdot 10^{-7}$	kg/(s·Pa)	Inlet cathode nozzle constant
$K_{out,CA}$	$2.05 \cdot 10^{-7}$	kg/(s·Pa)	Outlet cathode nozzle constant
$m_{FC}c_{FC}$	35	kJ/K	Average heat capacity of the stack
ΔH_c	$1.1996 \cdot 10^8$	J/kg	Hydrogen lower heating value
$h_{FC}A_{ext,FC}$	5	W/K	External convective heat transfer coefficient
$(hA)_{cool}$	50	W/K	Heat transfer coefficient of the cooling system [27]
m_{cool}^0	0.5	kg	Cooling fluid mass inside the stack
$c_{p,cool}$	1004	J/(kg·K)	Heat capacity of cooling fluid (air)
i_{nom}	60	A	Nominal stack current
i_{max}	160	A	Maximum stack current

The initial conditions are necessary for all the derivative terms and, for this validation process, they are assumed equal to the nominal operative conditions. The simulation has been conducted starting from the nominal conditions and, from these conditions, variable loads have been applied. To simulate the start-up, it is needed to set up different initial conditions, in general all relating to the environmental conditions. The pressure information available are only the anode and cathode nominal pressure, hence it has been assumed that the pressure drops between the anode inlet manifold and the anode channel, between the cathode inlet manifold and the cathode channel and between the cathode channel and the cathode return manifold are always equal to 0.2 bar. Therefore, the initial pressure conditions are presented in

Table 4.1, while the anode and cathode initial partial pressures are calculated by following equations:

$$p_{v,AN}^0 = \omega_{des,AN} \cdot p_{sat}(T_{setpoint,FC}) \tag{4.1}$$

$$p_{H_2,AN}^0 = p_{AN}^0 - p_{v,AN}^0 \tag{4.2}$$

$$p_{v,CA}^0 = \omega_{des,CA} \cdot p_{sat}(T_{setpoint,FC}) \tag{4.3}$$

$$p_{O_2,CA}^0 = y_{O_2,amb}\left(p_{CA}^0 - p_{v,CA}^0\right) \tag{4.4}$$

$$p_{N_2,CA}^0 = \left(1 - y_{O_2,amb}\right)\left(p_{CA}^0 - p_{v,CA}^0\right) \tag{4.5}$$

Table 4.1 – Initial conditions for validation of the Ballard MK5-E PEM-FC system model

Symbol	***Value***	***Unit***	***Description***
$p_{sm,AN}^0$	$3.2 \cdot 10^5$	Pa	Anode supply manifold initial pressure
$p_{sm,CA}^0$	$3.2 \cdot 10^5$	Pa	Cathode supply manifold initial pressure
p_{AN}^0	$3 \cdot 10^5$	Pa	Anode initial pressure
p_{CA}^0	$3 \cdot 10^5$	Pa	Cathode initial pressure
$p_{rm,CA}^0$	$2.8 \cdot 10^5$	Pa	Cathode return manifold initial pressure

The initial masses of vapour, hydrogen, oxygen and nitrogen are calculated from the pressure initial condition as follows:

$$m_{H_2,sm,AN}^0 = \frac{p_{sm,AN}^0 V_{sm,AN}}{M_{H_2} T_{amb}} \tag{4.6}$$

$$m_{a,sm,CA}^0 = \frac{p_{sm,CA}^0 V_{sm,CA}}{M_a T_{setpoint,FC}} \tag{4.7}$$

$$m_{v,AN}^0 = \frac{p_{v,AN}^0 V_{AN}}{M_v T_{setpoint,FC}} \tag{4.8}$$

$$m^0_{H_2,AN} = \frac{p^0_{H_2,AN} V_{AN}}{M_{H_2} T_{setpoint,FC}} \tag{4.9}$$

$$m^0_{v,CA} = \frac{p^0_{v,CA} V_{CA}}{M_v T_{setpoint,FC}} \tag{4.10}$$

$$m^0_{O_2,CA} = \frac{p^0_{O_2,CA} V_{CA}}{M_{O_2} T_{setpoint,FC}} \tag{4.11}$$

$$m^0_{N_2,CA} = \frac{p^0_{N_2,CA} V_{CA}}{M_{N_2} T_{setpoint,FC}} \tag{4.12}$$

The nozzle constants of the anode and cathode supply manifolds and of the cathode outlet can be calculated, in a first approximation, based on the initial conditions and on the maximum mass flows required by the fuel cell. In the following analysis the vapor mass flow will not be considered, simplification hypothesis justified by the reduced impact on the results.

Therefore, the maximum hydrogen mass flow is calculated in Equation (4.13) on the basis of the Equation (3.1) of hydrogen supply valve model, using the maximum current i_{max} drained by the fuel cell.

$$W_{H_2,max} = \frac{i_{max} n_{FC} M_{H_2}}{2F} \tag{4.13}$$

The inlet anode nozzle constant $K_{sm,AN}$ can now be calculated from the maximum hydrogen mass flow, in order to be sure that the linear nozzle model is valid for any operative conditions.

$$K_{sm,AN} = W_{H_2,max}\left(p^0_{sm,AN} - p^0_{AN}\right) \tag{4.14}$$

The calculation of the inlet cathode nozzle constant $K_{sm,CA}$ is similar to the inlet anode nozzle constant calculation. In this case, the maximum flow rate of the supplied dry air to the fuel cell $W_{a,max}$ is calculated as follows:

$$W_{O_2,max} = \frac{n_{FC} i_{max}}{4F} M_{O_2} \tag{4.15}$$

$$W_{a,max} = W_{O_2,max} \frac{\lambda_{O_2,min}}{y_{O_2,amb}} \tag{4.16}$$

where:

- $y_{O_2,amb}$ is the oxygen mass fraction in ambient air, equal to 0.233 considering the oxygen molar fraction equal to 0.21.
- $\lambda_{O_2,min}$ is the oxygen excess ratio at the maximum stack current, assumed to be 2.

Starting from the calculation of the maximum dry air flow rate necessary to the PEM fuel cell, the inlet cathode nozzle constant can be derived from the following equation.

$$K_{sm,CA} = W_{a,max}\left(p^0_{sm,CA} - p^0_{CA}\right) \quad (4.17)$$

Also, the outlet cathode nozzle constant $K_{out,CA}$ is calculated using the maximum flow rate of the supplied dry air to the fuel cell $W_{a,max}$, according to the hypothesis to not consider the vapor mass flow.

$$K_{out,CA} = W_{a,max}\left(p^0_{CA} - p^0_{rm,CA}\right) \quad (4.18)$$

As described at the beginning of this section, the validation process is realized without the compressor model described in Section 3.2, but a specific model of the cathode flow controller, used in the reference tests [12], is developed and used as an air compressor. For the modeling of this mass flow controller the Equations (4.15) and (4.16) are applied, but using the instantaneous current required on the stack and not the maximum one. In this way, this component can vary the air mass flow rate in order to keep constant the excess air in the cell and equal to $\lambda_{O_2,min}$. The dynamic delay of this mass flow controller is simulated by means of a dead time of 0.8 seconds and a first order delay of 0.4 seconds.
Furthermore, to better reproduce the test-rig used in [12], the model of the cathode return manifold has been slightly modified in order to represent the pressure regulation valve.
This component can automatically vary the outlet air mass flow from the cathode in order to maintain constant the operative pressure inside the stack. In detail, a pure proportional control has been implemented, with a time constant equal to 1e-7, able to vary the value of the nozzle section $A_{T,rm,CA}$ of the cathode return manifold starting from the difference between the instantaneous cathode pressure p_{CA} and the related set-point p^0_{CA}. The dynamic delay of the pressure regulation valve is simulated by means of a dead time of 0.4 seconds and a first order delay of 0.2 seconds.

The results of the simulations performed for the validation process of the PEM-FC system are shown in the following figures. Figure 4.9 shows the cornerstone of model validation: a variable current is imposed to the cell model, detecting the voltage generated by the system. The model is validated because it is able to approximate quite well the experimental results, obtaining a stack voltage very close to that obtained in [12], with a maximum error of less than 7% and only during some load transients. The peaks at load variations are not simulated by our model due to the type of approach adopted. In fact, the dynamic model is 0D, i.e. there are no parameter changes along the main spatial direction and the individual stack cells all operate under the same conditions, which is why the electrochemical performance of all the cells is the same. This approach is correct for a global and mediated view of the system, which is the main purpose of this study, while not simulating some phenomena related to the different conditions of singular cells. For example, during current variations, the last cells in the direction of the flows could be in the absence of hydrogen at the anode and/or oxygen at the cathode. Furthermore, the hydration of the membrane may undergo variations along the stack due to the temperature and pressure differences, going to provoke flooding or dryness

of the cells. Despite this, the model can well predict stack performance, which is why the validation can be considered complete.

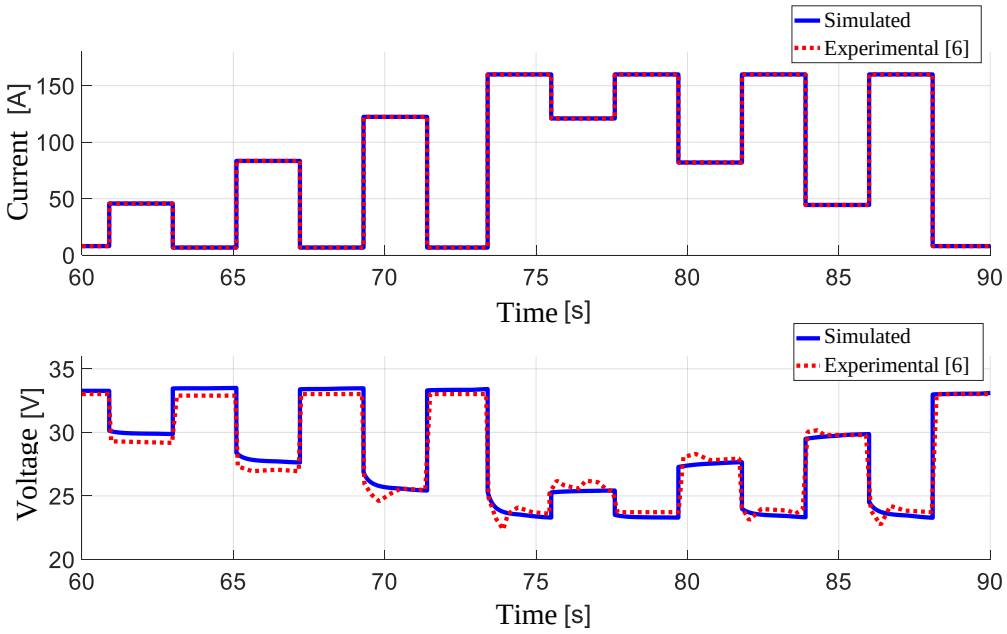

Figure 4.9 – Ballard MK5-E PEM-FC system model versus experimental data from [12]

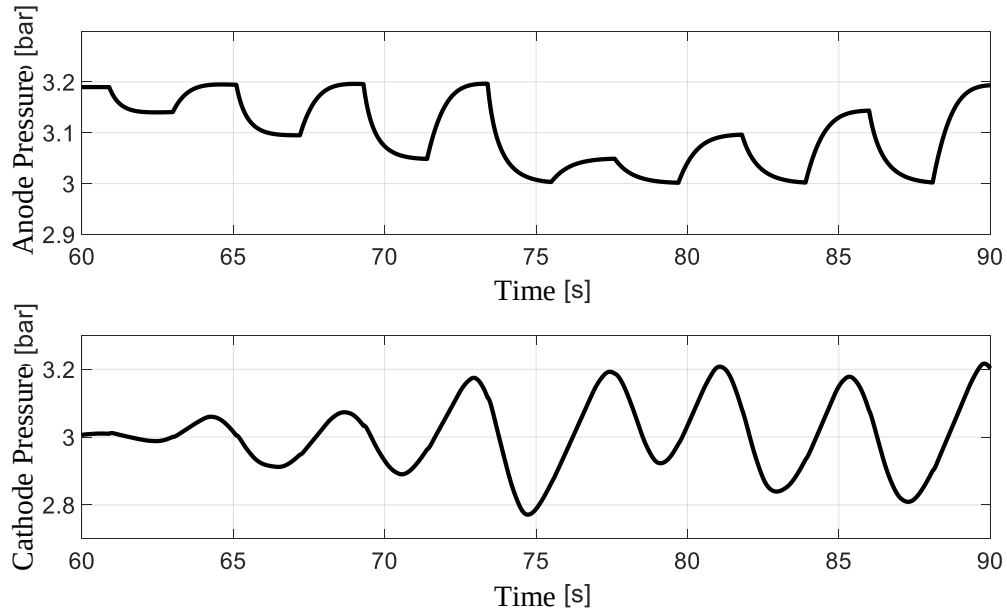

Figure 4.10 – Simulated anode and cathode pressures

Figure 4.10 and Figure 4.11 show the trends of the anode and the cathode pressures and the related mass flow rates of hydrogen and air supplied by the feeding systems. The two mass flow rates follow the load variations with a characteristic delay of the two systems. In particular, the valve that regulates the hydrogen flow has a faster dynamic than the air flow

controller that manages the cathode adduction. This difference in the dynamics of the two valves causes the different trends of the anode and cathode pressures. The cathode pressure, in fact, has a more "smoothed" trend and an oscillation amplitude greater than the anode pressure.

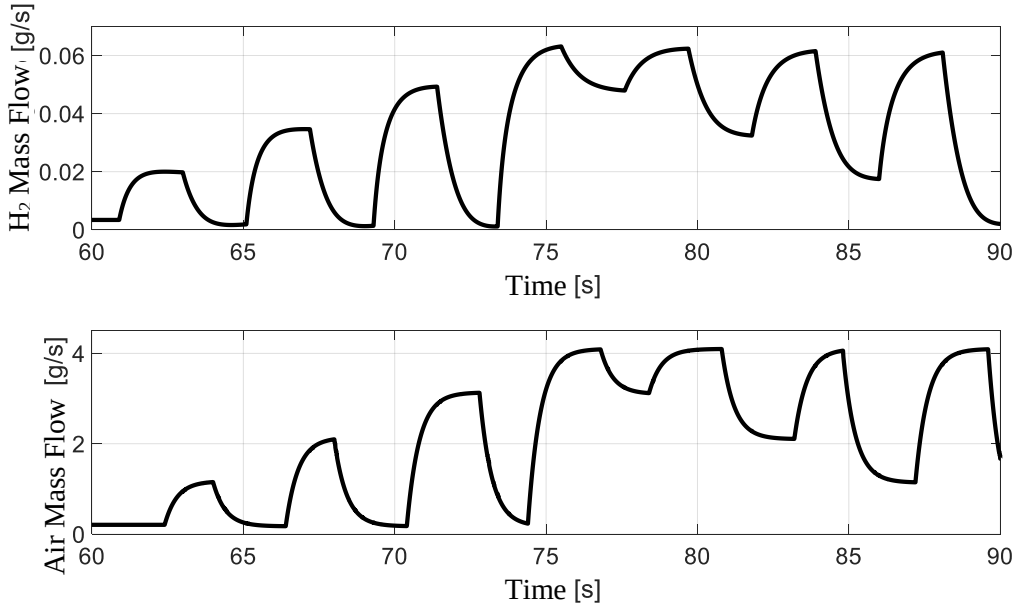

Figure 4.11 – Simulated hydrogen and air mass flows

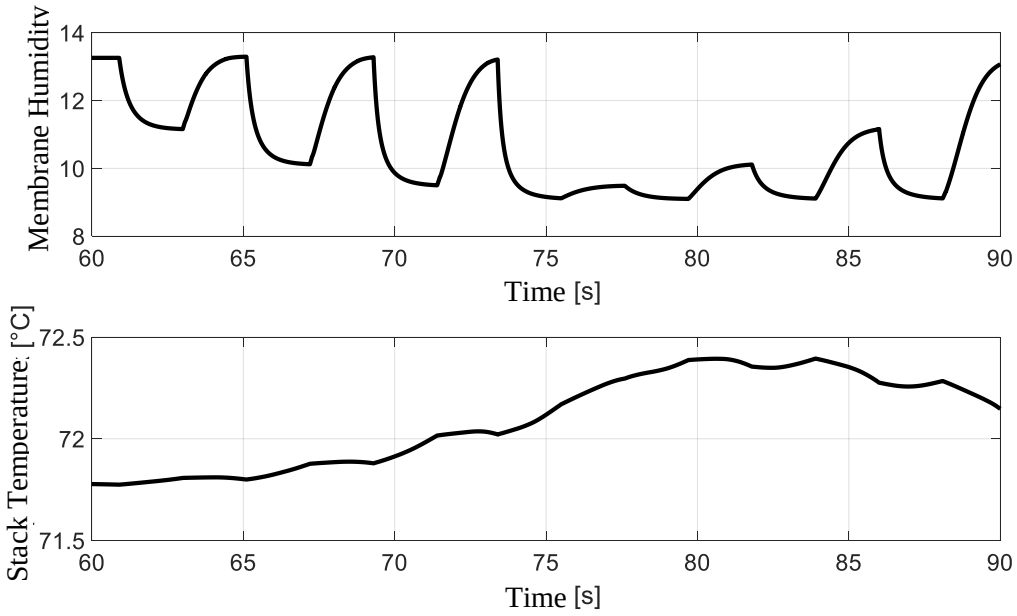

Figure 4.12 – Simulated membrane humidity and stack temperature

Figure 4.12 shows the trends of the membrane water content and the stack temperature. The membrane water content is inversely proportional to the load request, in fact, by increasing the current to the fuel cell, the membrane tends to dry out, reducing the voltage. This phenomenon directly affects the overall performance of the fuel cell, strongly influencing the ohmic polarization losses according to Equation (2.47). Another parameter that greatly influences the performance of the stack is the operating temperature, which in this case is rather stable over time. The load variations, in fact, end after 30 seconds and they are quite fast, which is why the cell temperature does not have the time necessary to undergo strong variations, considering the thermal inertia and the cooling circuit that are able to control the temperature at about 72°C.

4.3 Transient Simulations

Downstream of the validating process for the complete model of the PEM fuel cell system, in this section the results of the simulations performed with the insertion of the air compressor are shown. As introduced in Section 3, the slowest dynamics of the system are related to gas flows, to changes in membrane humidity and stack temperature and, when present, to the air compressor. Normally, in fact, it is the dynamics of this component that limits the overall performance of the PEM fuel cell: the compressor has an inertia that prevents strong transients in reduced time instants.
The results of this analysis will provide important information to support this thesis and highlight the most relevant physical phenomena involved. In this way the possibilities and the limits of a complete PEM fuel cell system will be clear.
At this stage, the use of the air compressor was considered by scaling, in terms of flow rate, the performance of the reference component in order to perfectly couple with the PEM-FC model, set and validated on the Ballard MK5-E system. Based on the maximum air flow to be supplied to the system, calculated using Equations (4.16), the following coefficient was used to adapt the compressor maps to the system under examination:

$$K_{scaling} = 0.05 \tag{4.19}$$

In this analysis, also the start-up of the system is simulated, which is why it was necessary to change the initial conditions of the model, related to the conditions of ambient temperature and pressure.

Table 4.3 – Initial conditions of Ballard MK5-E PEM-FC system for transient simulations

Symbol	*Value*	*Unit*	*Description*
$p^0_{sm,AN}$	$2.1 \cdot 10^5$	Pa	Anode supply manifold initial pressure
$p^0_{sm,CA}$	$1.2 \cdot 10^5$	Pa	Cathode supply manifold initial pressure
p^0_{AN}	$2 \cdot 10^5$	Pa	Anode initial pressure
p^0_{CA}	$1.1 \cdot 10^5$	Pa	Cathode initial pressure
$p^0_{rm,CA}$	$1 \cdot 10^5$	Pa	Cathode return manifold initial pressure

Although the same set of equations used in the previous validation was used, i.e. the equations from (4.1) to (4.18), the initial conditions are different and have been reported in Table 4.3.

Due to the addition of the air compressor model, which consumes a part of the electrical power generated by the stack, and to better represent the real behaviour of the system a power control loop has been added capable of modifying the current required to the fuel cell to obtain in output exactly the net power desired by the user. For this purpose, a PI controller (Kp = 0.4 and Tr = 1) is used, able to manage the current demand to the fuel cell based on the difference between the current net power produced by the system and the requested power by the user. The set-point temperature of the fuel cell was set at 70°C, close to the maximum temperature of 72°C [12], adopting 2°C as safety margin.

The system start-up is analysed by means of the power loading ramp shown in Figure 4.13. First, 10 seconds of zero load are imposed, corresponding to the phase of purging of the anode and cathode channels, necessary for safety reasons.
Subsequently, during the actual start-up phase, since the system must reach the nominal temperature and is more sensitive to sudden changes in load, an upward ramp of 0.2% of the maximum net power per second is imposed. The ramp ends when the net power is equal to 75% of the maximum net power, which corresponds to the limit imposed during the starting phase, with the stack at a lower temperature than the steady state. In this way, the power of 75% is reached after about 6 minutes.
The 75% power is maintained for a further 14 minutes, to ensure that the system reaches a steady-state temperature of 70°C. As can be seen from Figure 4.17, after about 17 minutes from the start-up the stack reaches the nominal temperature and the cooling system starts working to maintain the temperature on the set-point.

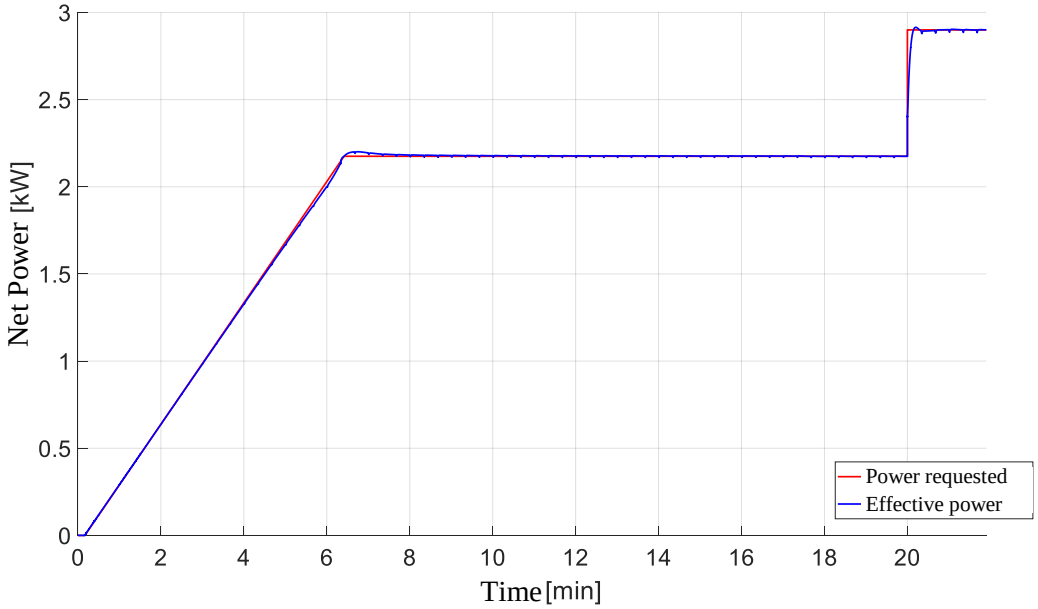

Figure 4.13 – Comparison between net power requested and effective during the start-up

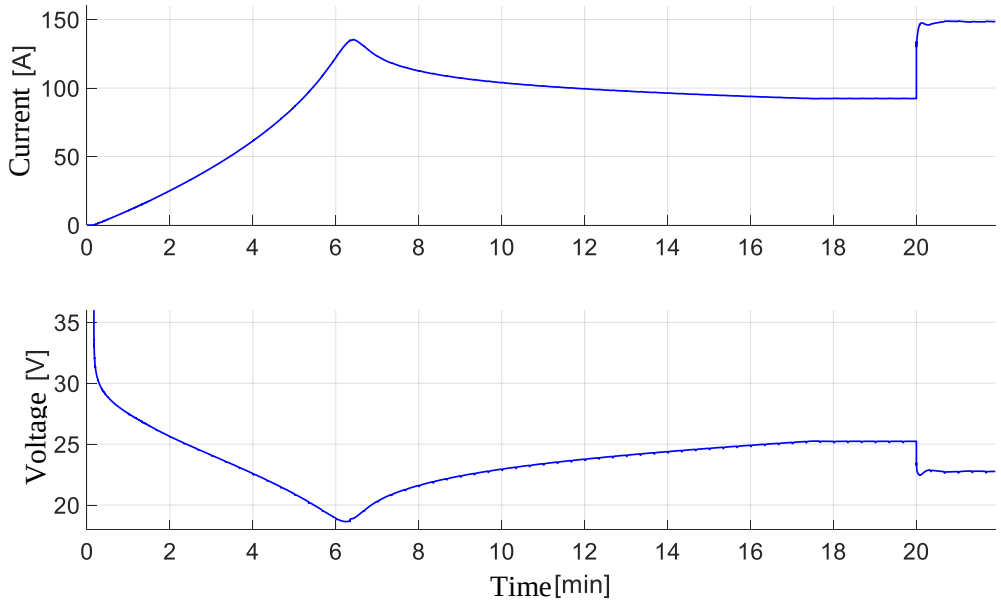

Figure 4.14 – Stack current and voltage during the start-up

Figure 4.14 shows the current and voltage trends of the PEM fuel cell system. In particular, it can be observed that there is a current peak around the sixth minute when 75% of the power is reached: this peak is due to the control system which tries to obtain the required power by increasing the current and causing a sharp decrease voltage, compensated subsequently by the progressive increase in stack temperature and humidity of the membrane, visible in Figure 4.17.

Once the set-point temperature is reached, it is possible to increase the net power of the system up to 100%. With the system at nominal temperature, it is possible to request power steps, the only limitation becomes the dynamic of the compressor. In fact, too high power steps cause instability and excessive overshoots and for this reason they are limited. Operating with power ramps is certainly favourable, but in this analysis we want to investigate the limits of the system and it is for this reason that load steps are used where possible and within operational limits given by the air compressor.

Figure 4.15 shows the anode and cathode pressures during the whole start-up phase of the system. The anode pressure has regular peaks due to the temporized purge which expels the gases from the anode, where the nitrogen which counter-diffuses from the cathode tends to accumulate and slightly reduce the cell performance during time. Although this phenomenon is not simulated, it is important to implement the purge model to better represent the real operating conditions and to consider the amount of hydrogen lost. The imposed purge time is equal to 1 second every 20 seconds of normal operation of the system. This time step is deducted from the existing commercial systems. The anode pressure is kept approximately constant at the value of 2 bar from the pressure regulating valve which feeds the anode line. The cathode pressure on the other hand is strictly related to the performance of the air compressor and varies according to the power required up to a maximum of about 3 bar. For this reason, an anode pressure of 2 bar was chosen, corresponding to the average value

between the minimum and maximum cathode pressure. The approach is commonly used on commercial PEM fuel cell systems available on the market.

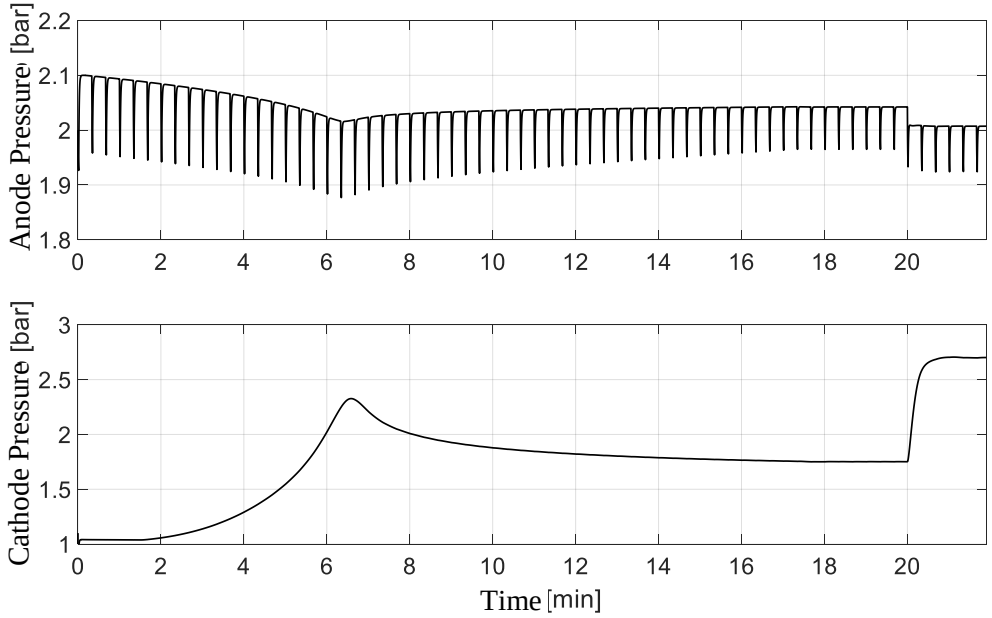

Figure 4.15 – Anode and cathode pressures during the start-up

Figure 4.16 shows the anode and cathode flow rates of hydrogen and air. Mass flow rates are completely related to pressure. The hydrogen flow rate has peaks due to temporized purge and the cathode air flow is determined by the performance of the compressor.

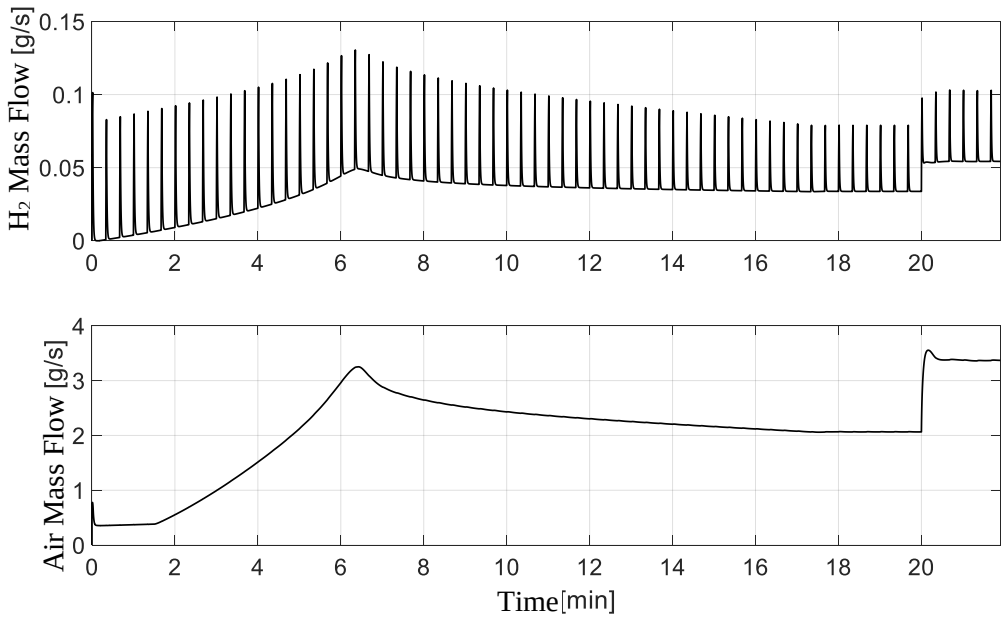

Figure 4.16 – Hydrogen and air mass flows during the start-up

Figure 4.17 shows the stack temperature and the water content of the membrane. Recalling that the maximum value of this parameter is 14 (see Section 2.2), it can be observed that it tends to decrease proportionally to the load request. Once the start-up ramp is over, there is

a recovery linked to the reduction in pressure and mass flow rate of the anode and cathode flows. The temperature of the fuel cell increases gradually from the ambient temperature depending on the load demand and the thermal capacity of the stack, shown in Table 4.2. Once the nominal temperature has been reached, it can be observed how the cooling system correctly controls the temperature of the PEM fuel cell.

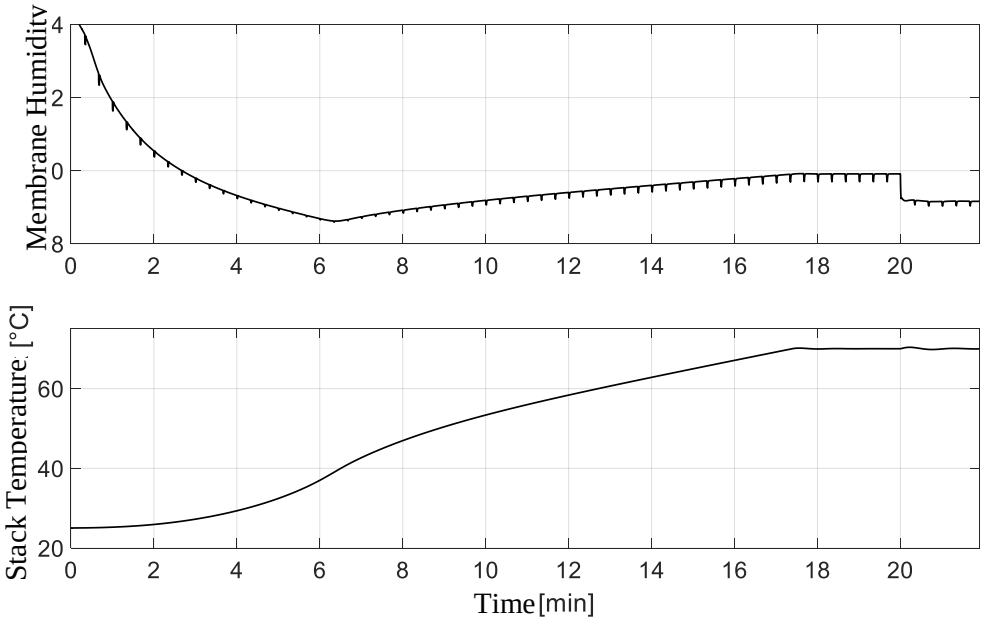

Figure 4.17 – Membrane humidity and stack temperature during the start-up

Once the start-up phase is completed, the load variations shown in Figure 4.18 are simulated. It can be seen that, for power steps of different width, the response time of the system is comparable, about 20 seconds to realign the actual power with the required power, while the peaks due to the transient increase, with ever-increasing overshoots.

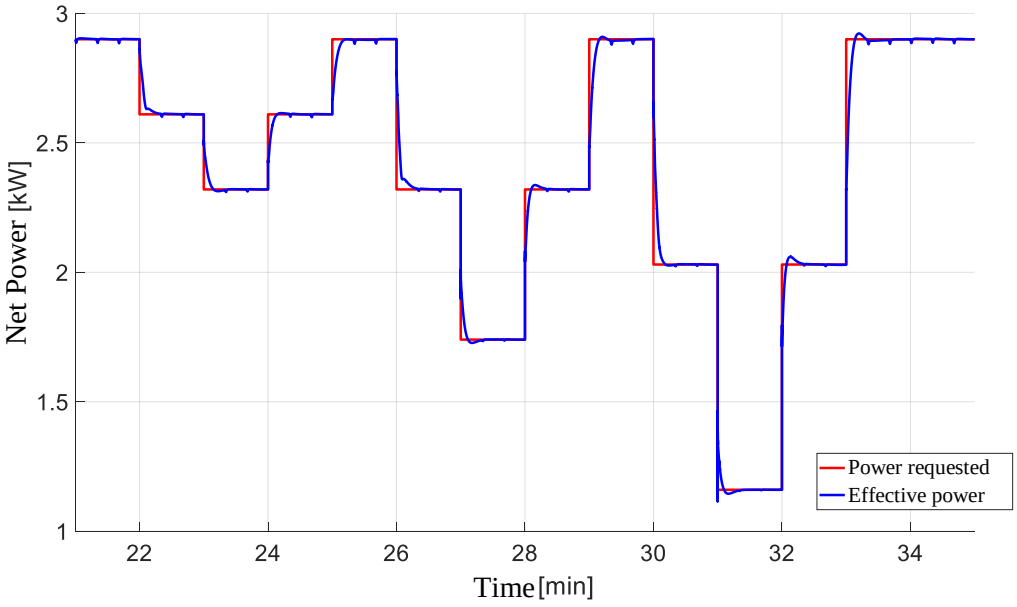

Figure 4.18 – Comparison between net power requested and effective

The stack current and voltage trends related to the power demand are shown in Figure 4.19.

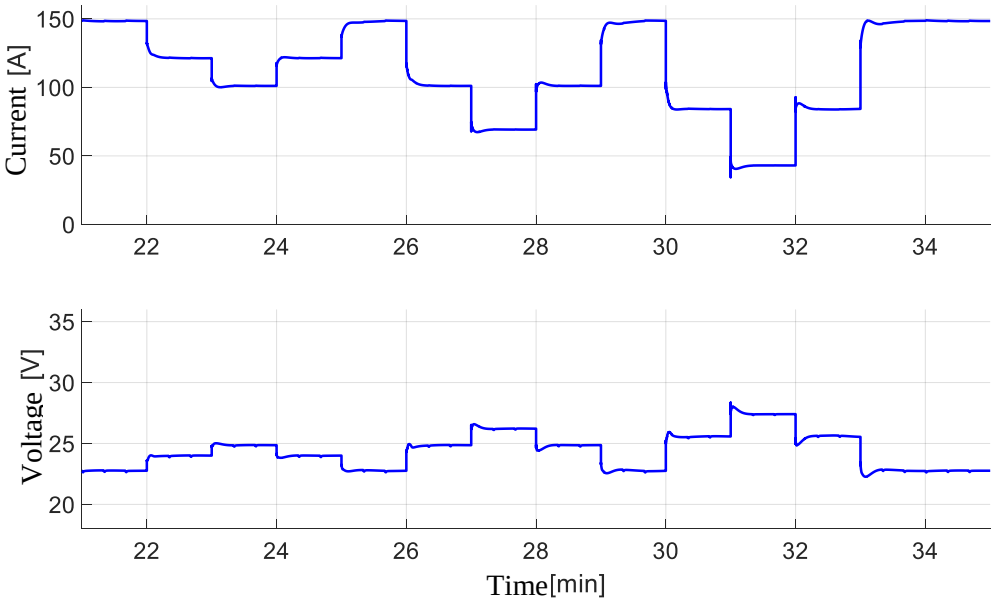

Figure 4.19 – Stack current and voltage

Figure 4.20 shows the pressure trends at the anode and cathode channels. The anode pressure remains approximately constant around 2 bar, a value imposed to limit the differences in pressure between anode and cathode side in any operative condition to a maximum of 1 bar, an approach motivated by the actual behaviour of the PEM-FC systems available on the market. The cathode pressure in fact varies from about 1.2 bar up to a maximum of about 2.7 bar, depending on the operating point of the compressor, which in turn depends on the power required by the fuel cell. The pressure peaks at the anode are always caused by timed purges imposed on the system.

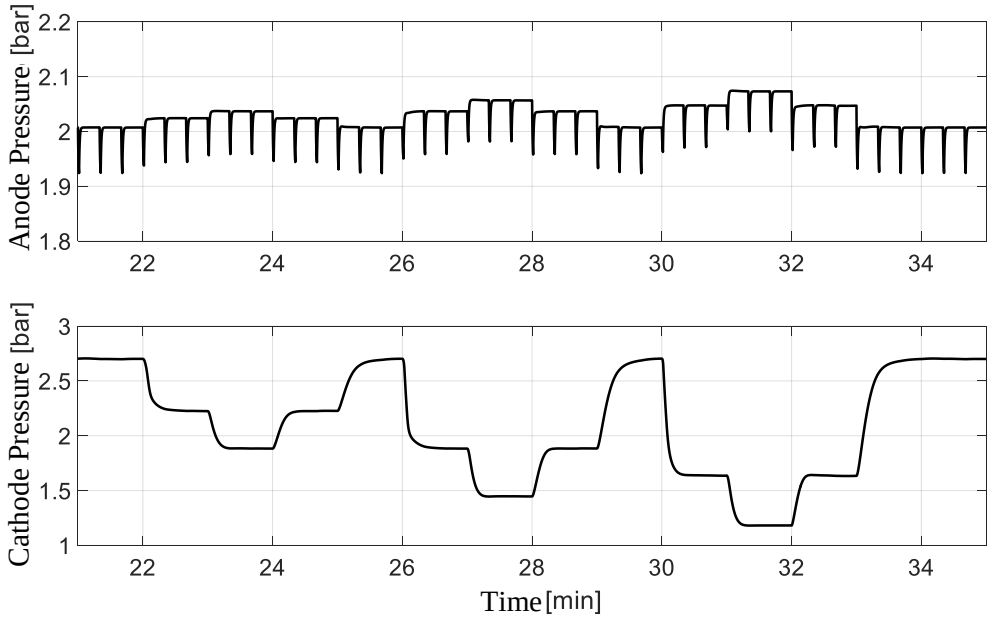

Figure 4.20 – Anode and cathode pressures

Figure 4.21 shows the hydrogen mass flow rate at the anode and air mass flow rate at the cathode. The hydrogen flow peaks are due to timed purges, while the air flow peaks at the load changes are due to transients of the air compressor.

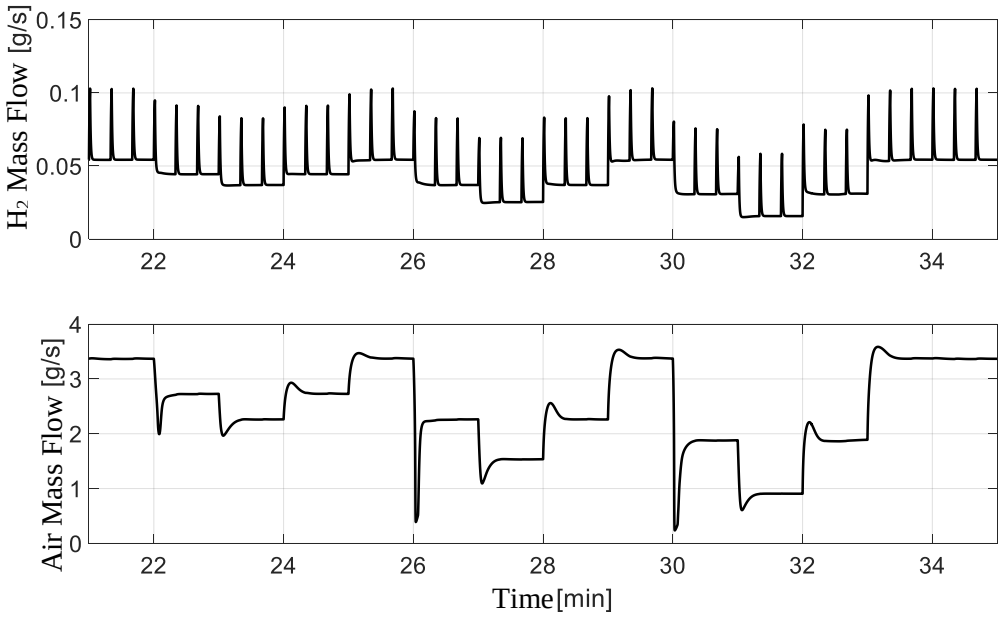

Figure 4.21 – Hydrogen and air mass flows

Figure 4.22 highlights how the membrane humidity remains on good levels, higher than 9, able to guarantee good electrochemical performance of the stack. The lower values correspond to the higher load values. In addition, the cooling system adequately controls the stack temperature around the steady-state temperature of 70°C.

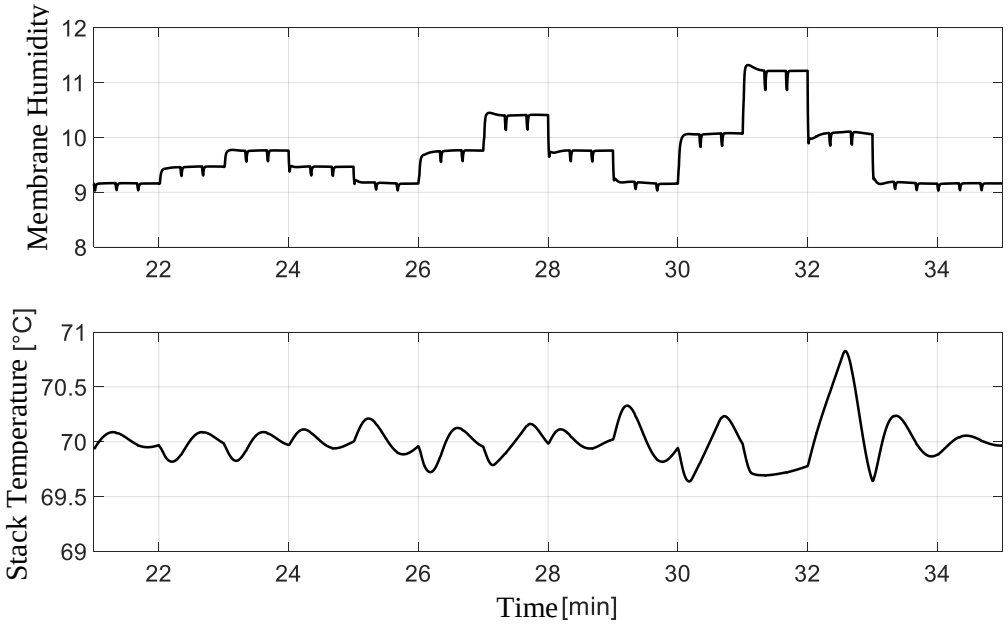

Figure 4.22 – Membrane humidity and stack temperature

5 HI-SEA Joint Laboratory

Regulations are setting to change common practice in marine power generation under the pressure of pollutant emissions reduction. The International Maritime Organization (IMO) is already imposing tight emission limits on Particulate Matter, SO_x and NO_x that for emission control areas (ECAs) are difficult if not impossible to be meet with traditional diesel engines and bunker fuels [62]. Fuel cell systems (FCS) are considered among the most promisign technologies able to reduce pollutants emissions and increase efficiencies [63]. The shipping fuel cell (FC) propulsion technology state of the art (SOA) is poor due to variuous reasons, among which the absence of prescriptive rules for the installation of alternative systems and lack of regulations on ships environmental impact, in particular on greeenhouse gasses (GHGs) [64], [65] and [66].

A recent review of fuel cell systems for marine applications [67] showed the potentials of this technology coupled with different fuels while the European Maritime Safety Agency (EMSA) commissioned to DNV-GL a study [68] on the use of fuel cell in shipping that further distinguished the most suitable fuel cell technology for marine applications among which PEM-FC result to be the most mature one. In parallel, the TESEO project “High Efficiency Technologies For On-Board Energy And Environmental Sustainability” [69] investigated among all the use of PEM-FC for the development and demonstration of an electrical generator of 260 kW output power for marine application, that has been designed and built by Fincantieri with the technical support of the University of Genoa. Due to the relevance of the topic, the prototype has been designed inside a container with a high flexible electric architecture to permit the future continuation of the studies. The exploitaion of the system research potential required the outfitting of a dedicated laboratory that has been modeled considering past experiences, technology SOA, ships and rule requirements.

Figure 5.1 – The HI-SEA Joint Laboratory of Fincantieri and Unige in the Savona Campus.

At the end of the project, Fincantieri decided to carry on the study integrating the FCS inside the laboratory of UNIGE in order to assess the potentiality in terms of cogeneration and trigeneration and to complete the analysis of battery hybridization of the system. The HI-SEA Joint Laboratory has been developed in the frame of a long time signed agreement between Fincantieri S.p.A. and the University of Genoa: it integrates a Hybrid PEM power generator system with the Innovative Energy Systems (IES) Laboratory of the Thermochemical Power Group (TPG) of the University of Genova in the Savona Campus (Figure 5.1). The HI-SEA Joint Laboratory represents the first and largest effort to solve key challenges in the energy sector and to generate solutions for the low-emission ships and enhance the innovation capacity of a new business sector. The goal of the laboratory is to define the best design for a modular FC system for ship application able to guarantee the maximum life span of FC stacks without omit performance.

5.1 HI-SEA Laboratory Description

The plant layout of the HI-SEA Joint Laboratory of Fincantieri and University of Genova in the Savona Campus is visible in Figure 5.2.

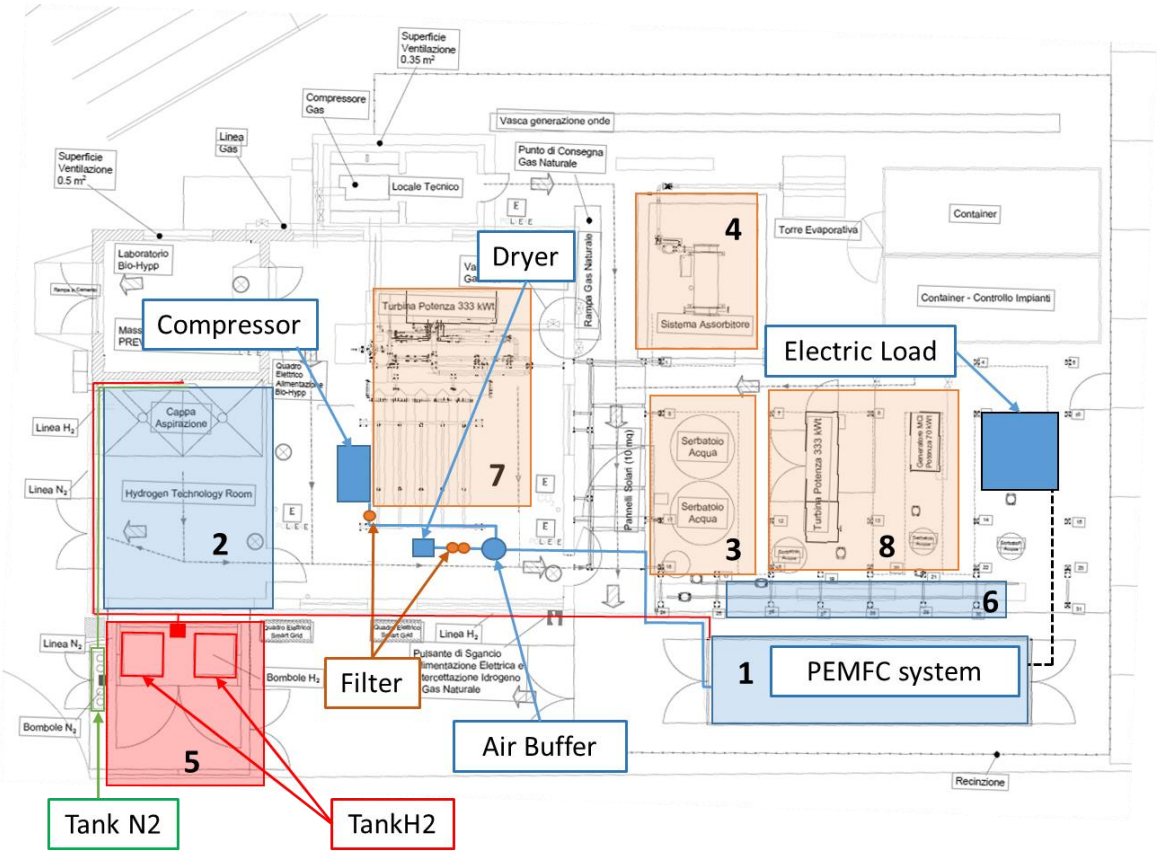

Figure 5.2 – Plant Layout of the HI-SEA Lab inside the IES Lab in Savona Campus.

The HI-SEA Laboratory is composed by:

1. A fuel cell system of 8 stacks of PEM fuel cells sized 33 kW each for a total maximum power of 260 kW, fuelled by compressed hydrogen and air and installed into a 30 ft container. This plant is provided of all auxiliary systems: a hydrogen and compressed air distribution system; a water based primary cooling system that has as well a heat exchanger to interact with an external secondary cooling circuit; a conditioning system for the DC current produced by the stacks composed by two DC/DC converters; a system for the simulation of a battery box composed by an AC/DC converter sized 66 kWe;
2. An 8.5 bar air compressor, 130 Nm^3/h, not oil-free, provided with a dryer and filters;
3. A group of tanks to feed the PEM fuel cell system, made up of 2 groups of 25 tanks at 200 bar, for a global maximum capacity of 400 Nm^3 of hydrogen;
4. A hydrogen distribution line linking the tanks group to the PEM-FC system, provided with safety systems, operating at a nominal pressure of 20 bar and with a maximum flow of 40 Nm^3/h;
5. An electric load made up of modular resistive banks, which can be inserted with 1 kWe steps, to dissipate the electrical DC current produced into heat form;
6. A DAQ system able to acquire all the signals of the sensors and control all the components according to the operational procedures of the system.

The following subdivision into working levels has been adopted to schematize and best capture all the components of the system. In particular it is possible to distinguish 3 different working levels (levels 1 and 2 are to be considered 8 times, one for each stack):

- Level 1 is the stack subsystem: it refers to the single cell that composes the stack. The stack (the set of cells) is combined with interface manifolds, hydrogen management, and cell voltage monitoring. The process fluid inputs and outputs of the Level 1 sub-system are depicted as arrows on the outside of the shaded box:

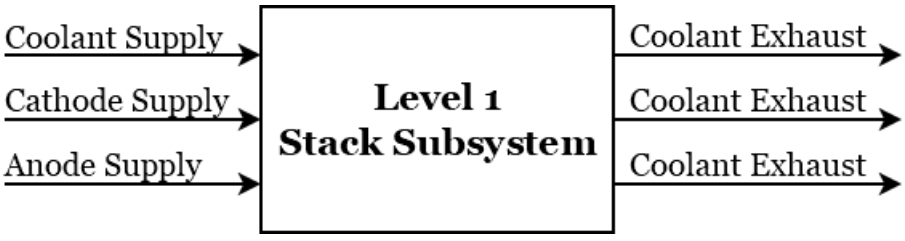

Figure 5.3 – HI-SEA Level 1 block diagram

- Level 2 represents the stack itself: the auxiliaries and the cells that compose the entity able to generate power. With respect to Level 1, it adds the cathode air management, the stack cooling management, and the engine controls which enable Level 2 to produce unregulated DC power;

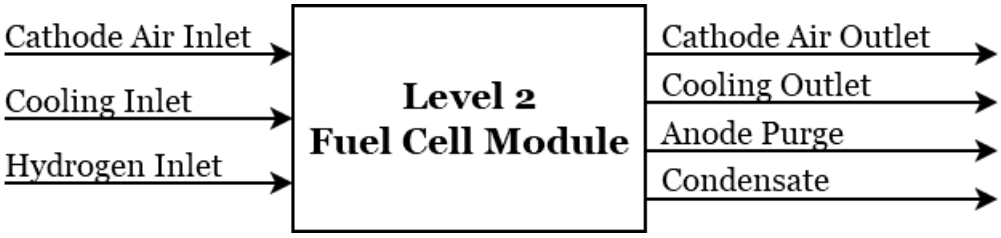

Figure 5.4 – HI-SEA Level 2 block diagram

- Level 3 involves the fuel cell system interconnections: it integrates the fuel cell engine within the target application and includes power electronics, hybridization, hydrogen storage/supply, and the application load.

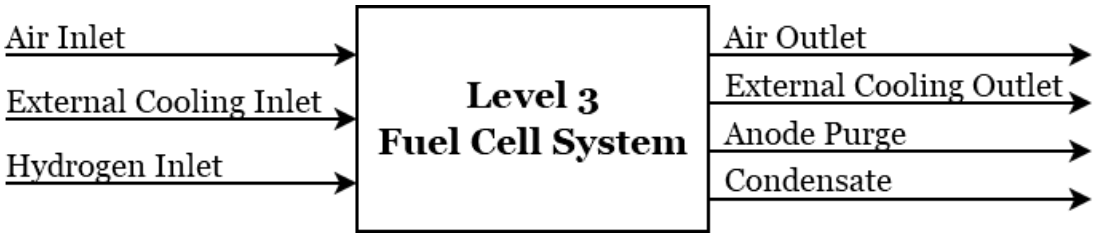

Figure 5.5 – HI-SEA Level 3 block diagram

5.1.1 PEM-FC Stacks

The first and main objective of the FCS test rig, developed during the TESEO Project [69] was the definition of the best design and size of a modular PEM-FC system for ship application. The goal was achieved towards the development of a high flexible system able to demonstrate the feasibility of the technology in a simulated relevant environment, namely a ship fuel cell room. Moreover, the test rig has been designed in order to be easily transported (inside a 30 ft container, Figure 5.1) and integrated into a laboratory able to simulate a ship infrastructure (Figure 5.2).

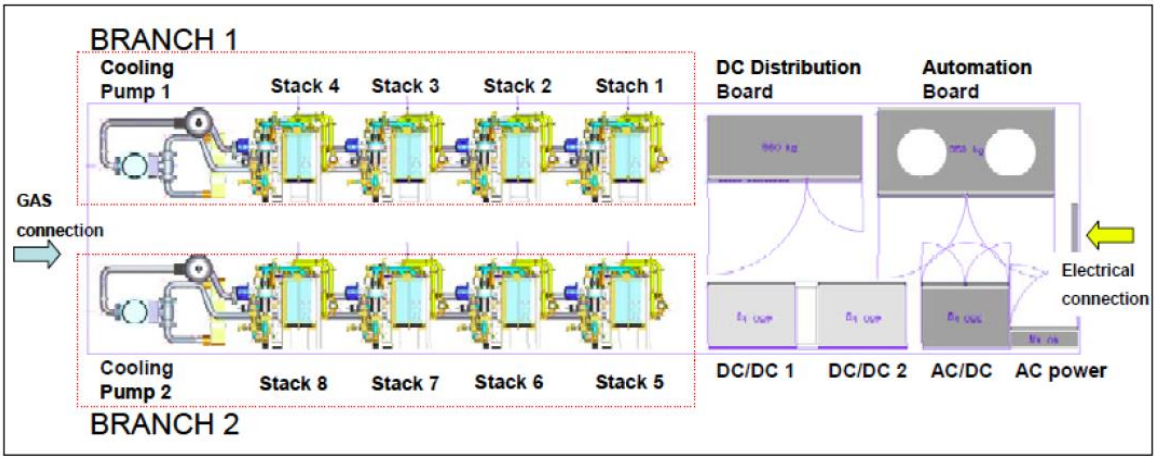

Figure 5.6 – Plant layout of the PEM-FC system inside the container

In order to permit the investigation of the best electric and fluid architecture, a mixed configuration has been adopted connecting two symmetrical branches composed by 4 stacks in series, as visible in Figure 5.6. Each stack (L1) has been integrated with BoP components that integrate also an air Mass Flow Controller (MFC) able to control the cathode air flow in order to simulate the behaviour of different blowers specification (L2). Each branch is autonomous, with dedicated DC/DC converter and cooling system (L3). The chosen technology for the test rig is the commercial PEM-FC Nuvera Orion Stack, characterized by metallic bipolar plates, anode passive recirculation and cathode open flow with 30 kW of nominal power at 1 A/cm^2.

Figure 5.7 – Nuvera Orion Stack.

The Nuvera module Orion 30 kW, visible in Figure 5.7, is a self-humidified module able to work without an external humidification unit. The main characteristic data are reported in the following table.

Table 5.1 – Nuvera Orion Stack Parameters

Parameter	*Value*	*Unit*
P	32.6	kW
Vtot	130.3	V
#cel	184	-
Vcel	0.708	V
ETA LHV	57	%
ETA HHV	48	%

5.1.2 Cooling Lines

During the operation, the plant produces a total thermal power that ranges from 0 to 260 kW$_t$ dissipated by a suitable cooling system comprising two circuits:

- Primary circuit, visible in Figure 5.6;
- Secondary circuit, visible in Figure 5.8.

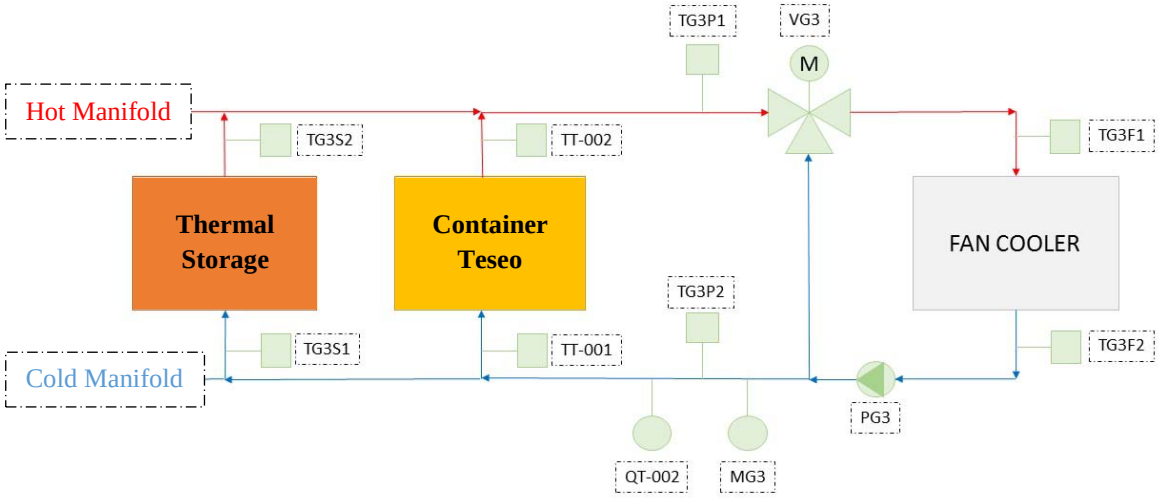

Figure 5.8 – Scheme of the secondary cooling circuit

The heat released by the 8 fuel cell stacks is removed by the primary cooling system, that is totally integrated in the container. It is made up of two circuits, one for each of the two branches of the PEM-FC system, thus each one cools down 4 PEM fuel cell stacks.
The cooling fluid of the primary circuits, as recommended by the fuel cell producer, must have precise values of conductivity for the security of the stacks. For this reason, two conductivity sensors have been added to have a real time monitoring of this important safety parameter. In each branch, there is a plate heat exchanger that allows the heat exchange between primary and secondary circuits, thus at least the heat is dissipated with the external fan-cooler of 300 kW.
Each primary circuit includes also a three-way valve that allows to regulate the cooling flow rate inside the heat exchanger and, consequently, to control the temperature of the related primary cooling circuit.
Also the secondary circuit has a three-way valve that allows regulation of secondary water flow rate and, consequently, the control of the water temperature and the regulation of fan-cooler rotor (managed by the inverter). This configuration can support also cogenerative layouts of the plant, coupled with thermal storages or connected to the thermal grid of the Campus. The secondary circuit is equipped with 8 RTD type PT100 with 4 wires and 2 flowmeters.

5.1.3 Air Compressor and Air Line

The air compressor selected to supply the PEM stacks is the Ceccato model DRE 100 8,5 CE 400 5, visible in Figure 5.9. The choice of the compressor was related to the minimum requirements in terms of performances and air quality. In addition, for this stationary application, the compressor's dynamic response can be more limited than the target requested for mobile applications. Therefore, the compressor's operative pressure was chosen equal to the maximal working pressure (8.5 bar) and the operative compressor's flow rate equal to the maximum flow rate requested by the 8 PEM stack at the maximum power

(13 m^3/min). The rapid dynamic response of compressors for mobile applications can be emulated by the air mass flow controllers installed at the cathode inlet of each stack, able to reproduce the behaviour of different blowers.

Figure 5.9 – HI-SEA Air Compressor

The compressed air line includes three filters, a dryer and a storage vessel, as visible in Figure 5.10. This system is able to provide the 8 stacks with compressed air at the necessary flow rate and pressure, depending on the operative conditions of the fuel cells.

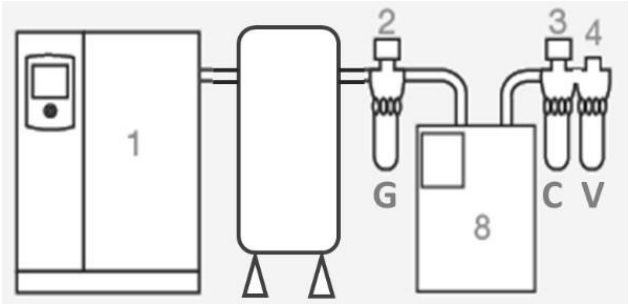

Figure 5.10 – Compressed air scheme

All the components of the compressed air line are installed in the IES Laboratory, to ensure a greater protection against atmospheric agents and consequently a longer useful life.

Pipeline material is aluminium to guarantee a high quality of air, in terms of purity. The three filters installed for air purification are designed to filter moisture, particles, oils and hydrocarbons and should be able to reduce pollutants under the safety limits suggested by Nuvera. A remote sensor and an analogic pressure sensor have been installed on the cathode line. The dryer eliminates water from the air circuit avoiding condensation inside the mass flow controllers that can be leads to a malfunction of the MFCs. Compressed air is stored into the accumulation volume, then it passes through the dryer and finally through shut-off valve at the container inlet.

Figure 5.11 – Compressed air line inside the IES Laboratory

5.1.4 Hydrogen Line

Hydrogen is stored in high-pressure tanks, and because of its high flammability and explosiveness, the safety issues are an important aspect (see Section 1.3). The system requires a high amount of hydrogen to feed the plant that requires at maximum 14.4 kg/h of hydrogen. As visible in Figure 5.12, risks are minimized using a box, in which two groups of tanks (25 or 16 units, 40 l each one) are safety stored and naturally aired and it can contain an eventual explosion.

Pipelines exiting from the box (see Figure 5.2) are made by inox steel 316L and provide hydrogen to the HI-SEA Lab and to the H2-LAB for test with metal hydrides and stacks up to 30 kW. There is a control panel for a first pressure reduction from 200 bar to 30 bar and a second one that allows to vary the pressure in the interval 0-30 bar. The HI-SEA inlet pressure can vary in range 7-12 bar and the inlet pressure of the H2-LAB is quite similar. Close to the H_2 box, there is the inert box that contains pressurized nitrogen. This gas is used to guarantee safety work conditions and to pressurize the system in case of maintenance or long periods of inactivity. After closing the H_2 valves that control the distribution from the

box, system is ventilated for about two minutes before N_2 is pressurized inside pipes and H_2 is totally removed from system.

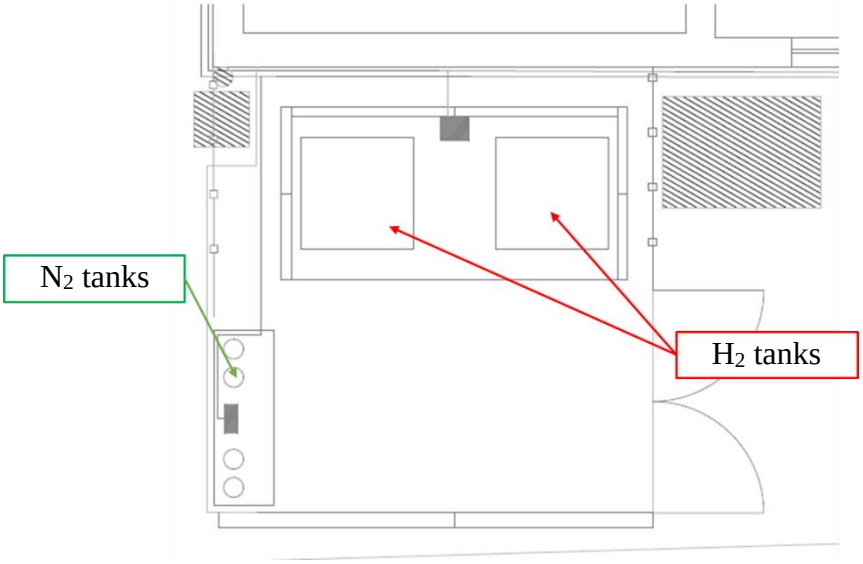

Figure 5.12 – Plant layout of the gas boxes

5.1.5 Electrical Load and AC and DC Lines

The HI-SEA Joint Laboratory produces a DC current in an operative range between 0 and 600 V_{DC} at a maximum current of 1000 A, corresponding to a maximum power of 260 kW. The DC/DC converter is able to work with the tension of 3 or 4 connected stacks enabling the simulation of a single stack fault on each branch permitting the control of the output tension and current. The DC/DC can also be bypassed to directly connect the FC to the electric load. Moreover, the 60 kW AC/DC rectifier together with the controllable electric load permit the simulation of any kind of battery packs, enabling the assessment of the optimum balance between FC and battery dimension as a function of the operational profile and the optimal integration of PEM-FCs in a DC grid. Different operational profiles can be tested to investigate the possibility to utilizing PEM-FC system to power only auxiliaries or propulsion.

To dissipate such electrical power, two paths have been evaluated: its injection on the electrical network or its dissipation through resistances. To follow the first path, a DC/DC converter and then a DC/AC one to transform continuous in alternate current at 50 Hz are to be installed in order to inject current on the network. This is an interesting but complex solution in terms of both safety and bureaucracy. Then the second option was chosen, and commutable resistor banks are installed to modulate the load. The heat generated in this way is dissipated through air or water. The absence of any external connection makes the whole system easier to be transported if it was necessary. Table 5.2 shows the technical data necessary for the electrical load.

Table 5.2 – HI-SEA electrical data

Parameter	*Value*	*Units*
Max Current	1000	A
Max Power	260	kW
Power step	1	kW
Max power step	60	kW
Max current step	100	A

Due to economic and technical aspects, the chosen supplier is SAE, the same that supplied all electronics components from the power side for the TESEO project [69]. To reduce the noise deriving from the operation, a water cooling system has been evaluated but with poor results; thus, air cooling was chosen due to the simpler installation procedure. The resulting electrical load in visible in Figure 5.13.

Figure 5.13 – SAE electrical load

The electrical load is provided with remote and on-site control systems that allow the accomplishment of different trial schemes. To register the electrical load data on the same software file log, some output signals are directed to the Programmable Logical Controller (PLC) referred to the HI-SEA container, in particular:

- Voltage measure;

- Current measure;
- Resistance setpoint.

In addition, an input signal from the PLC to the load provides the settings for the desired load level. In this way, it is possible to manage the load even from the control software of the container HI-SEA. Through the load control software, instead, it is possible to set both the manual control, to set the desired power value, and the programmed control, depending on a defined load profile. The load control software allows to set the value of power to be dissipated, then the PLC automatically commutates resistivity to answer the required power setpoint. The insertion of single resistivity can be controlled.

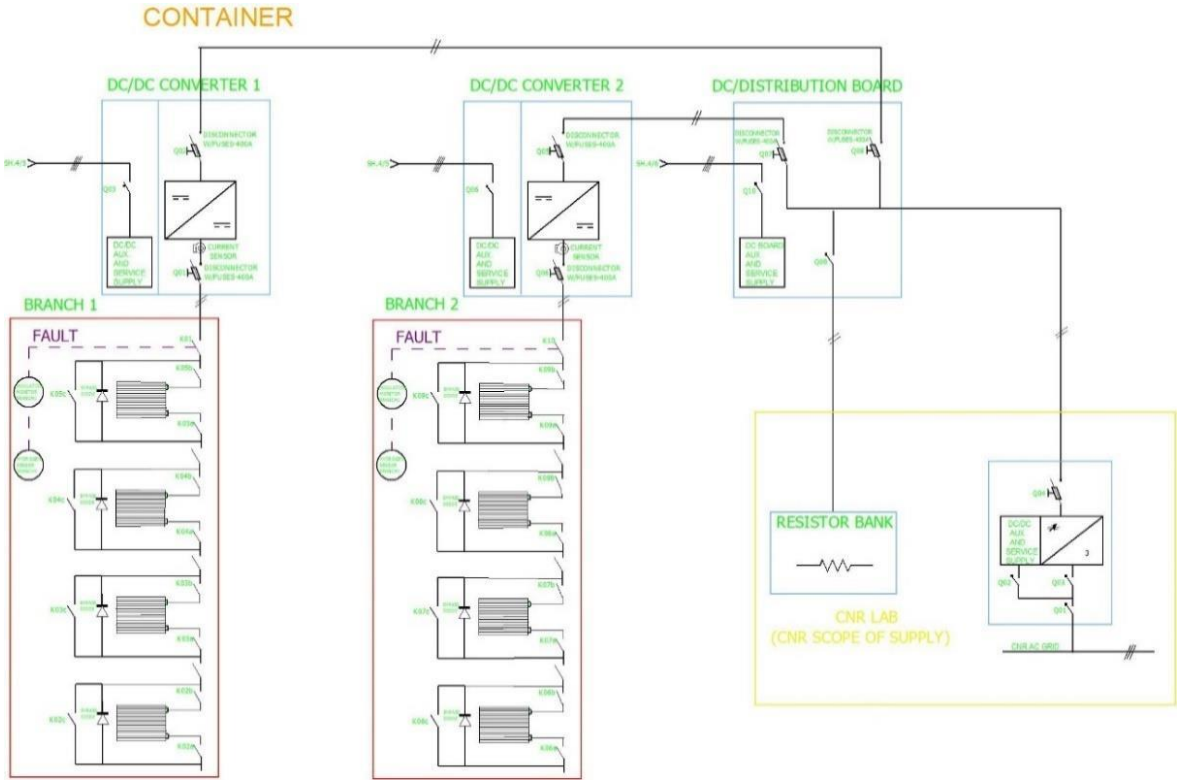

Figure 5.14 – Scheme of the DC lines of the PEM-FC System

Single and triphasic electrical connections were already available in the TPG IES Laboratory in Savona. Therefore, it was just necessary to create the internal connections to feed the HI-SEA laboratory, without changing the existing infrastructures. The main system in the DC line, visible in Figure 5.14, consists in the electrical dissipation plant, which has a switch, the electrical load, a power supply line for the load's PLC, a line connecting the electrical resistors to the container HI-SEA and finally an Ethernet connection for remote control of the load's PLC from the container.

The supply line of the HI-SEA container is fed by three different lines at 380 V that start from the laboratory and reach the electrical panel inside the container. The first line is the non-preferential one and it starts from a switch located inside the container. The second line

is connected to an Uninterruptible Power Supply (UPS) to ensure current supply in any conditions. The third line is the AC/DC one, with a different supply.

5.1.6 DAQ & Control system

The data acquisition system (DAQ) is able to control the whole PEM fuel cell plant of the HI-SEA Laboratory and consists in a supervisor computer and a local panel that contains a PLC model GE IP Rx3i, field I/O, power suppliers and all the auxiliary components for the communication lines management. Figure 5.15 shows the system's architecture.

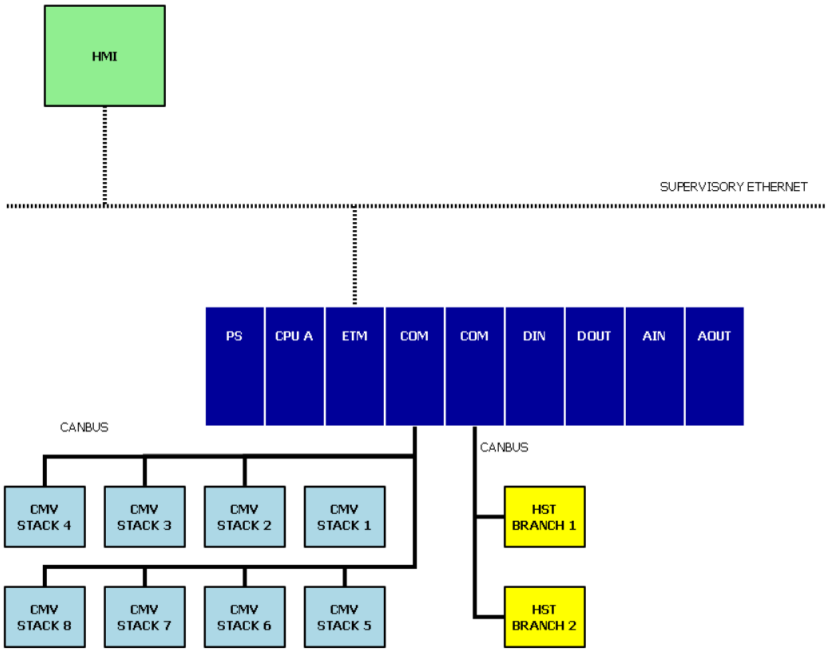

Figure 5.15 – HMI system architecture

Referring to this architecture, the supervisor computer communicates with the PLC and performs the monitoring and historicizing of all the process variables, beyond handling the HMI (Human Machine Interface) and implementing the procedures for the standard safety levels to access the information.

The HMI interface is homogeneous and intuitive; it identifies the plant section in object, gives different information about it and about its main components, reveals any alarms in the plant and let easily access to the other sections, by means of the bottom menu visible in Figure 5.16.

The main window of the HMI appears through the *Home* button and allows to monitor the main parameters of the plant. In the same screen it is possible to check out the correct functioning of the main components, to verify any anomaly and interact with the control system, including start and stop any of the 8 stacks. On the left side of the window are grouped information about the electric components and the cooling circuits.

Figure 5.16 – HMI Home window

The *Equipment MOS* (Manual Override Switch) window is visible for each stack and shows the status of all the level 2 components. By this window the cooling water heater, valves and contactors can be controlled.

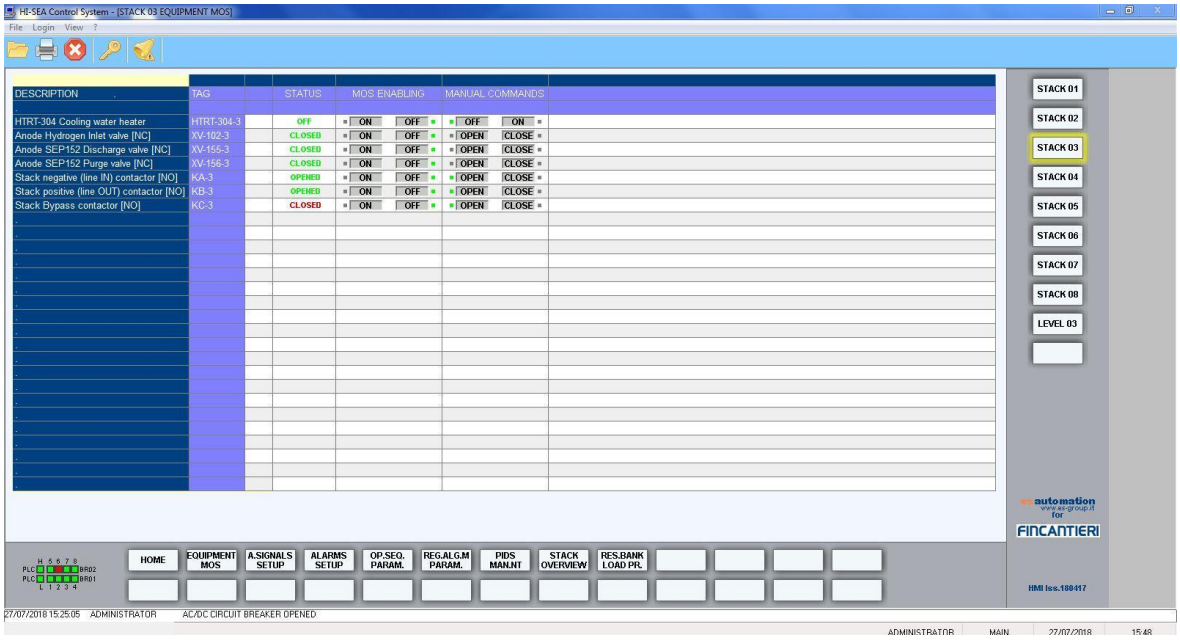

Figure 5.17 – HMI Equipment MOS window

The *Analog Signals Setup* window is available for each stack to set the parameters of the analog transmitters of the working level 3.

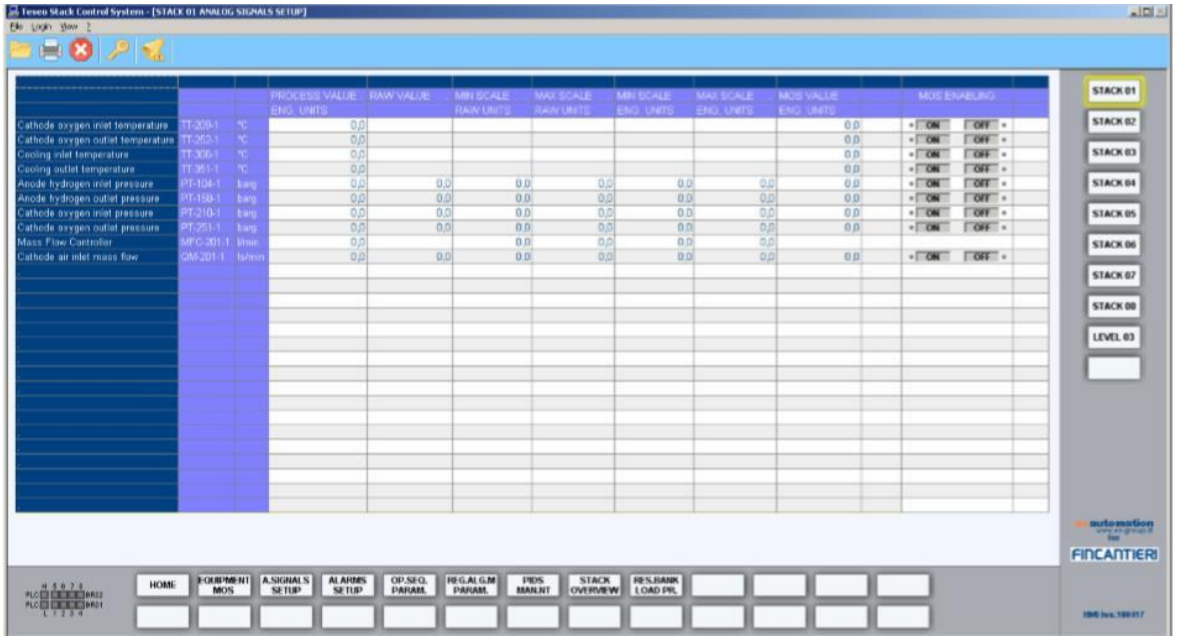

Figure 5.18 – HMI Analogue Signals Setup window

The *Analog Alarms Setup* window allows to set the alarm threshold for the analog transmitters of the level 3.

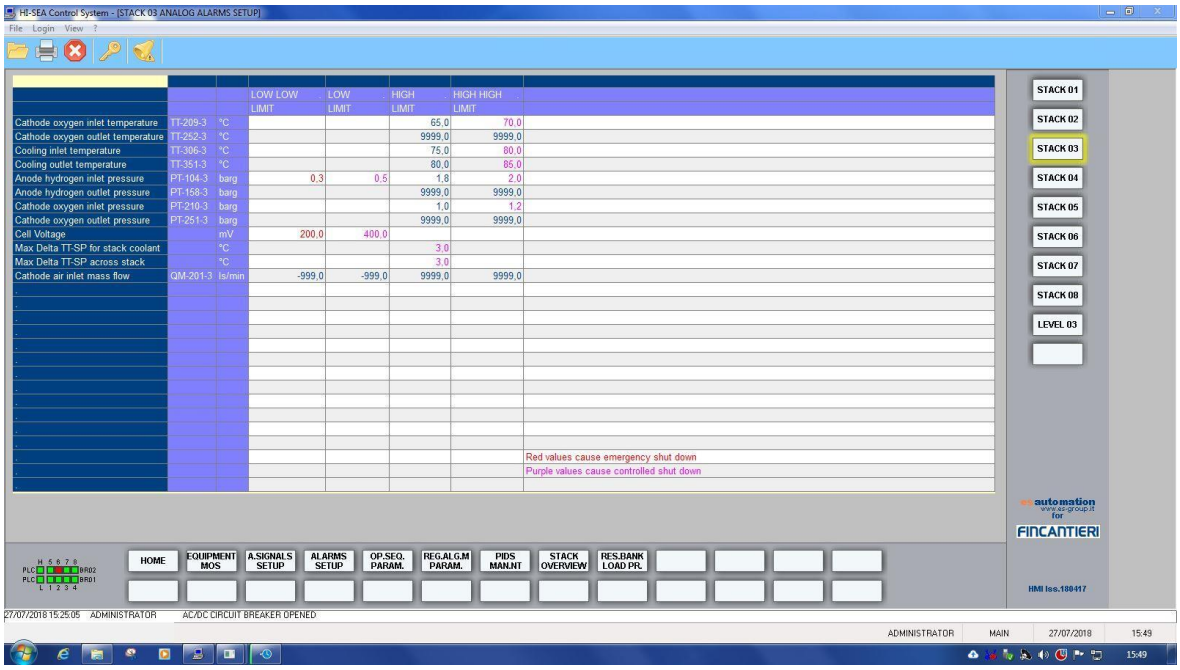

Figure 5.19 – HMI Analog Alarms Setup window

The *Operative Sequence Parameters* panel groups all times and setpoints that allow to parameterize the automatic working algorithm of each stack.

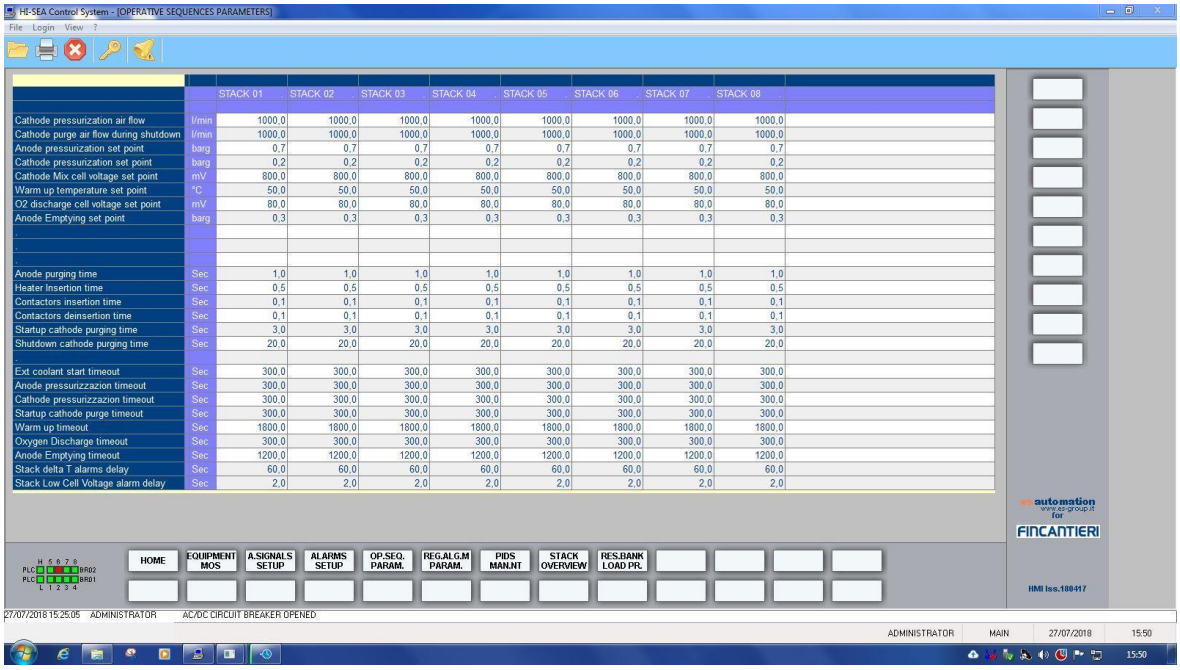

Figure 5.20 – HMI Operative Sequence Parameters window

The *Regulation Algorithm Parameters* groups all the curves that allow to calculate the automatic setpoints for the working algorithm of the stacks and of level 3 components.

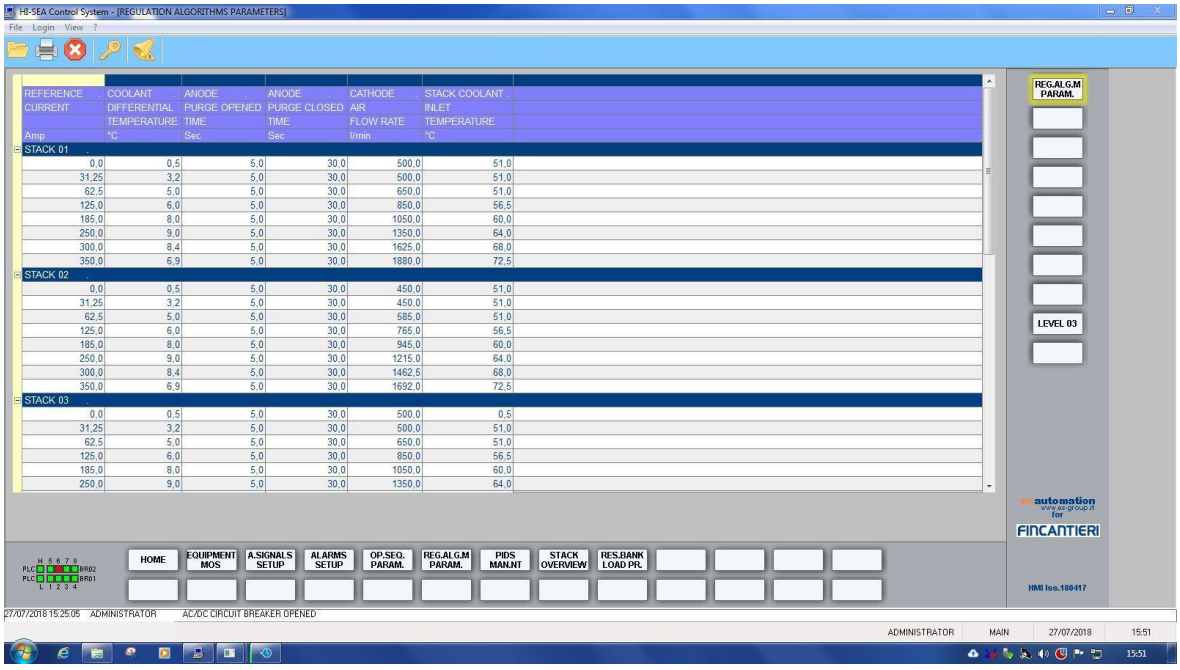

Figure 5.21 – HMI Regulation Algorithm Parameters window

The *PIDS Management* window shows the Proportional-Integral-Derivative regulators present in the system and let them to be controlled.

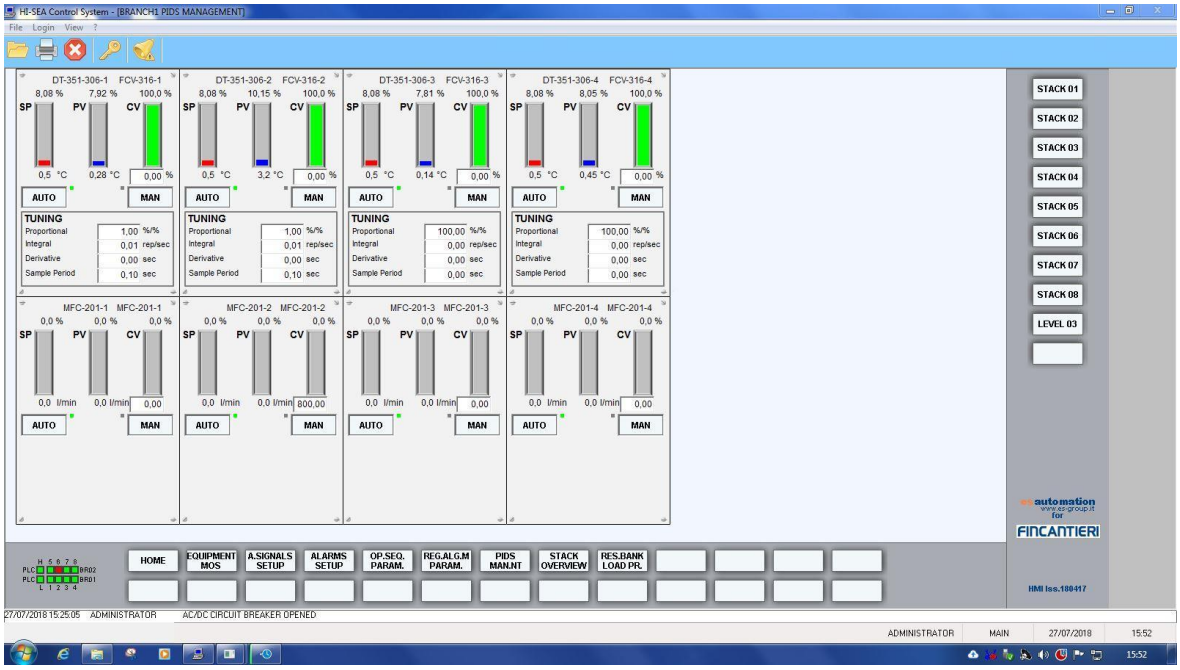

Figure 5.22 – HMI PIDS Management window

The *Stack Overview* window is available for each stack and shows in detail the status of all the components, the analog transmitters, valves and auxiliaries of levels 1 and 2.

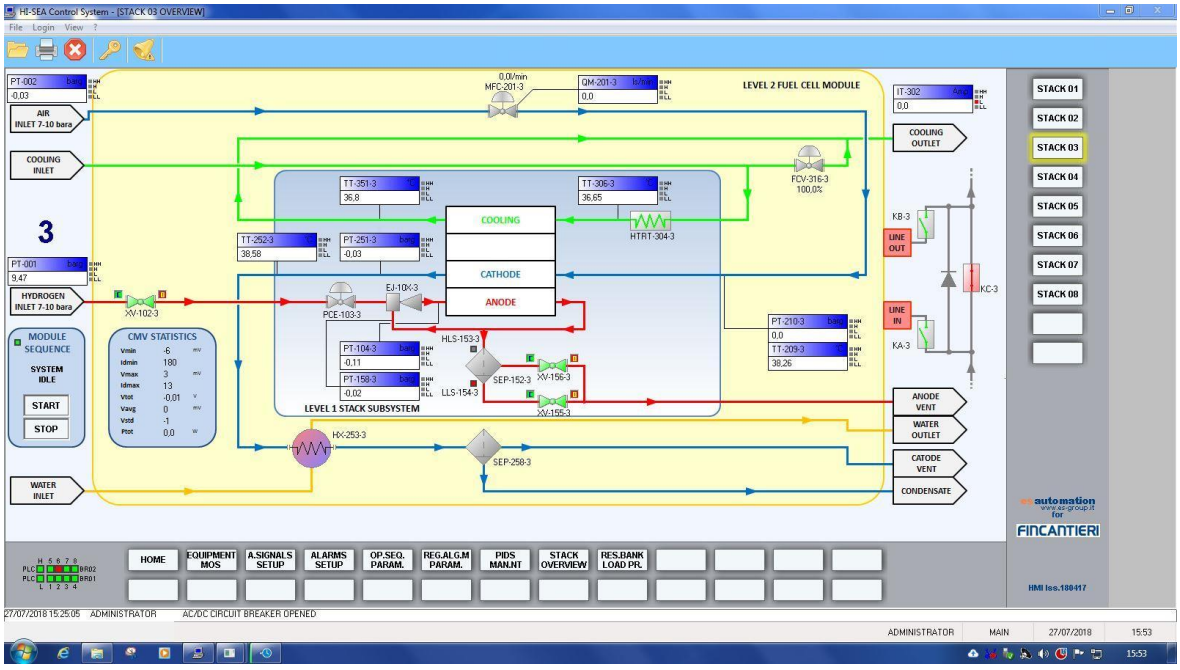

Figure 5.23 – HMI Stack Overview window

The panel *Resistor Bank Load Profile* allows to import and use the load profiles, called "recipes", defined by the user and that the electric load is able to automatically reproduce by selecting an active combination of its resistances.

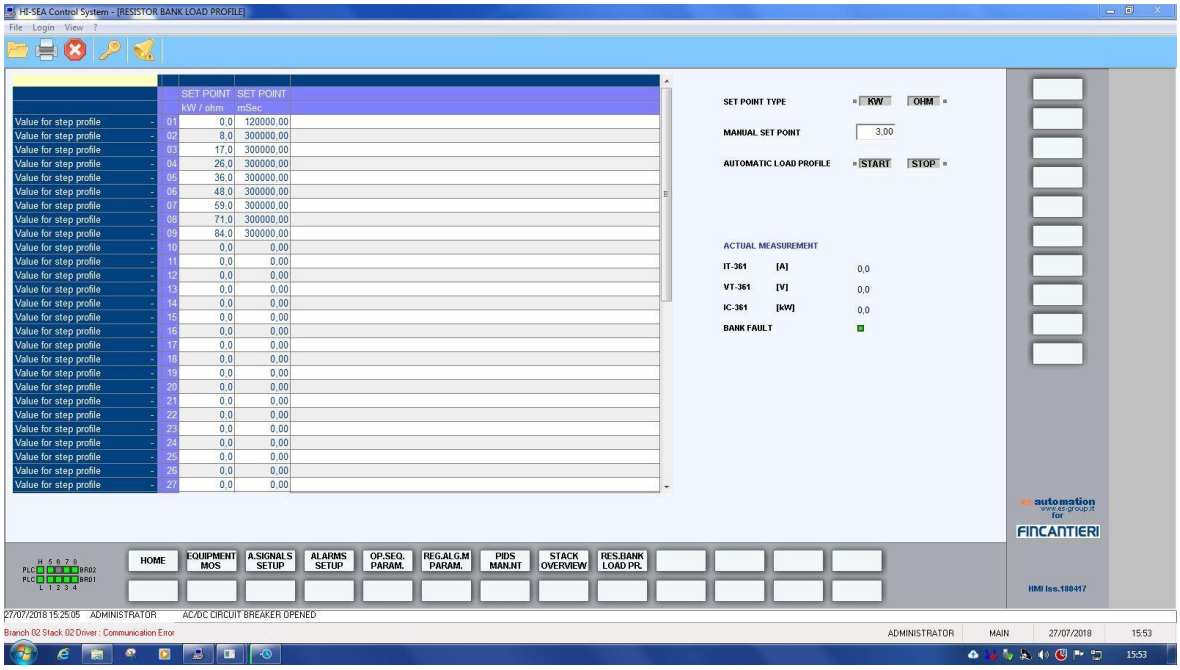

Figure 5.24 – HMI Resistor Bank Load Profile window

A recipe is made up of 50 pairs of values that can be called back and loaded in the supervisor computer to automatically generate a load profile. A pair of value consists in a power or resistive set point and a time value, which has a minimum value equal to 100 milliseconds. The setpoint corresponds to a value, measured in kilowatts or ohm, that the system communicates to the resistor bank via the controlled signal XT-361. As the load profile is being performed, it is possible at any time to stop the procedure.

5.1.7 Control Procedures & Alarms

The HMI allows the user to start up and shut down the PEM fuel cells individually by means of the start and stop buttons visible in Figure 5.16. The system starts FCs in a sequential way, operating on one at a time; if the start or stop button is selected on more than one stack, the system automatically creates a starter queue and shows *Wt (Wait)* on the stack that will be started/stopped in a second moment. Moreover, the system does not enter the *warm-up* phase unless all minimum cell voltages have reached a proper value. At that point, the system keeps in the *warm-up* phase until the coolant inlet temperature reaches the setpoint. During this period, the cooling water heater is on and stack's performance is limited to a percentage of the maximum power. When the necessary conditions are verified, the system turn in *running* state and can perform at its best.

Start-up

Here below are listed the conditions to be verified, as the system is off, to switch from a step to the next on the start-up procedure:

- Pump start up;
- Anode pressurization;

- Anode initial purge;
- Cathode pressurization;
- Heater connection;
- Cathode initial purge;
- Contactor closed;
- Warm-up: system is started and can produce power;
- Running: coolant inlet temperature measured reaches the setpoint.

Shutdown

Here below are listed the conditions to be verified, as the system is running, to switch from a step to the next on the shutdown procedure:

- Stack disconnection: the supervisor computer receives the command of shutdown the system;
- Stack by-pass closes;
- Cathode purge;
- Oxygen consume;
- Cathode emptying;
- Module shutdown;
- System shutdown.

The shutdown of the stack can be caused by one of the following alarms:

- Anode and cathode inlet pressures are out of the limits;
- Cathode air inlet temperature is higher than the limit for 3 seconds;
- The branch current is lower than the minimum value for 15 minutes or higher than the maximum;
- The coolant inlet and outlet temperatures are higher than the maximum value for 10 seconds;
- The coolant inlet temperature is lower than the setpoint for 60 seconds, this means that is not reached the running state of the stack;
- The difference between the coolant inlet and outlet temperature is higher than the setpoint for 60 seconds;
- The minimum cell voltage is lower than 400mV.

5.2 Matlab GUI for Test Data Analysis

In order to perform easily the post processing of the data acquired during tests with the PEM-FC system of the HI-SEA Joint Laboratory, a Matlab GUI named Data Viewer has been developed. Figure 5.25 shows the interface of this tool that can realize the following tasks:

- Conversion of the test file from the .xslm extension generated by the HMI control software to .mat data file and saving the file in the database folder, optimizing the data storage and usage;
- Loading of the .mat test file to be analysed, necessary to upload the test data inside the Data Viewer before any other operation;
- Creation of temporal charts selecting the desired variables (for example Figure 5.25) by means of the check box matrix, in which are reported the main parameters of the individual stacks, or the three lines of popup menus, in which all the registered variables are selectable, grouped by level and area of belonging;
- By means of the selection of the related check box, plotting of the polarization curves of the stack, which are the voltage-current curves, comprising the factory data, the stable voltages reached in each step of power and the voltages predicted by the stack voltage model developed and set on the reference factory data for each stack (for example Figure 5.26);
- By means of the Calc button, the calculation of the parameters necessary for the stack usage history, i.e. the number of start-up occurred during the test, the overall operating hours and those limited to certain powers, in particular below 3 kW, between 3 and 10 kW, between 10 and 20 kW and above 30 kW;
- By means of the Save Img button, the saving of the current graph composed by the user inside the appropriate Figures folder.

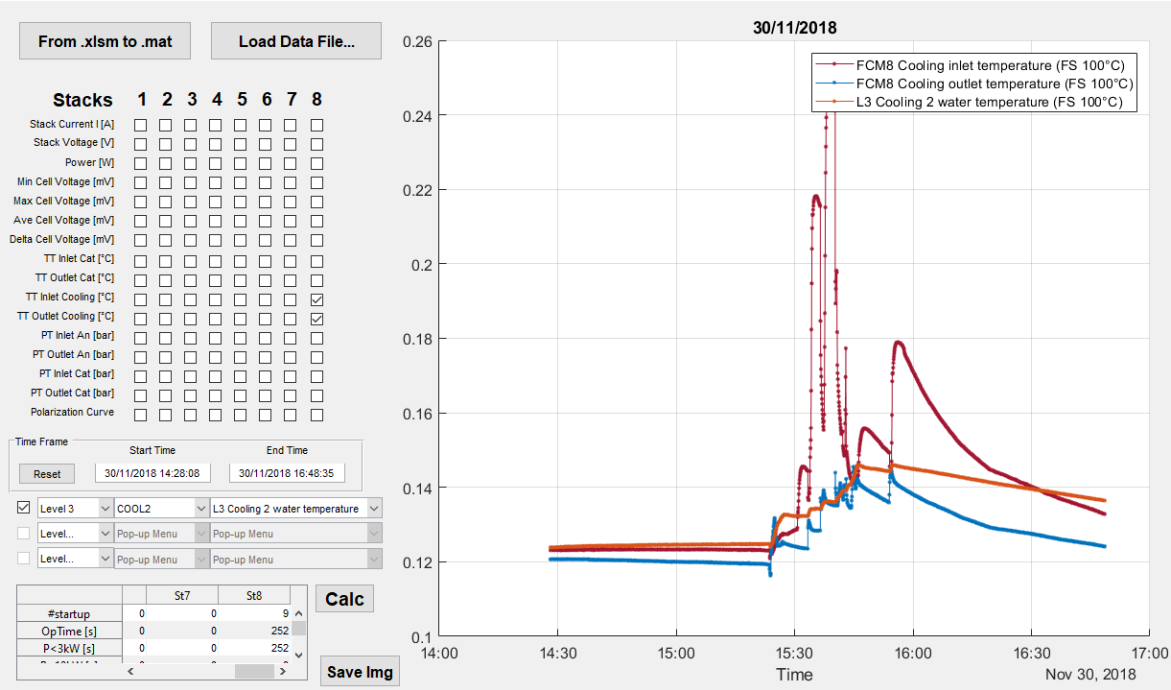

Figure 5.25 – HI-SEA Data Viewer: example of temporal charts

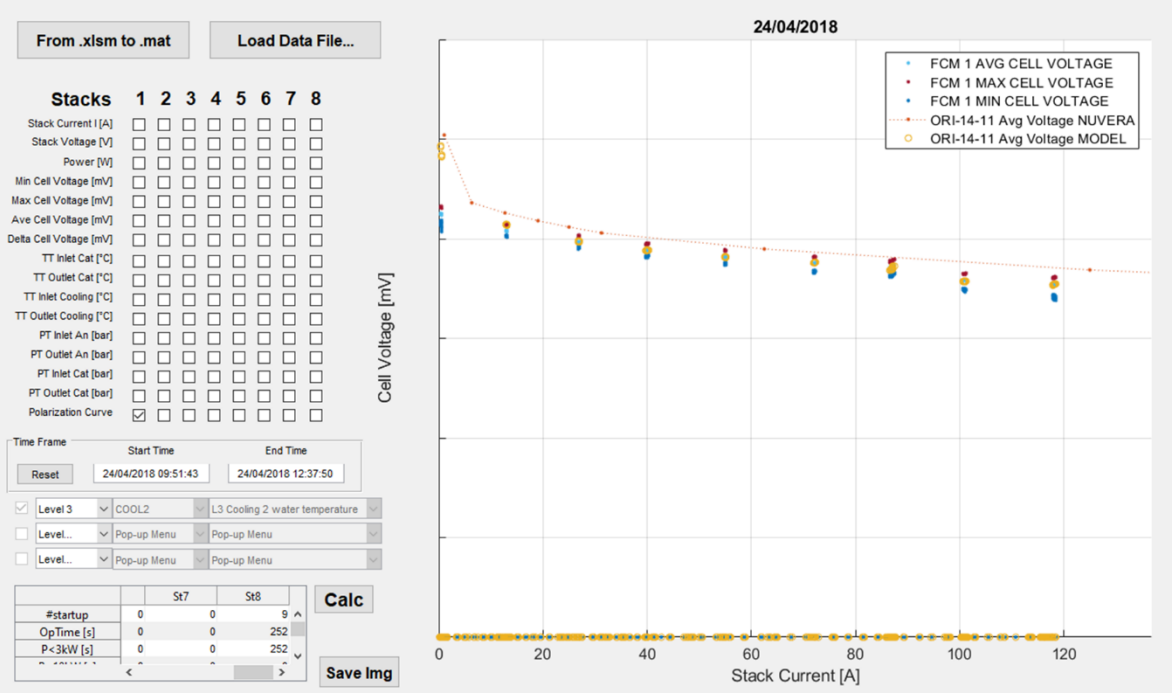

Figure 5.26 – HI-SEA Data Viewer: example of polarization curve

5.3 High speed DAQ

The data acquisition system of the HI-SEA laboratory presented in Section 5.1.6 is not fast enough to record all the phenomena of the PEM fuel cell system. Therefore, a LabView High Speed DAQ is developed to acquire sensible signals with fast dynamics composed by electrical and pressure parameters, listed in Table 5.3.

Table 5.3 – Signals acquired by the high speed DAQ

INSTRUMENT TAG NAME	*EQUIPMENT*	*SERVICE (DESCRIPTION)*	*UNIT*
IT-302	BRANCH1	Current sensor	A
IT-303	BRANCH1	LEM3 Current sensor	A
VT-301	BRANCH1	Voltage sensor	V
ICV-331	BRANCH1	DC/DC conv.1 current set point	A
ICV-332	BRANCH1	DC/DC conv.1 Volt set point	V
IT-322	BRANCH2	Current sensor	A
IT-323	BRANCH2	LEM3 Current sensor	A
VT-321	BRANCH2	Voltage sensor	V
ICV-341	BRANCH2	DC/DC conv.2 current set point	A
ICV-342	BRANCH2	DC/DC conv.2 Volt set point	V
IT-351	RECTIFIER	Output current sensor	A
VT-351	RECTIFIER	Output voltage sensor	V
ICV-352	RECTIFIER	Remote current adj.	A
ICV-351	RECTIFIER	Remote voltage adj.	V
IT-361	RES. BANK	Load current	A
VT-361	RES. BANK	Load voltage	V
IC-361	RES. BANK	Power/Resistance set point feedback	kW/Ohm

XT-361	RES. BANK	Power/Resistance set point	kW/Ohm
XC-361	RES. BANK	Power/Resistance set point selection	-
QM-001	L3	Hydrogen Inlet Mass Flow	kg/h
PT-104-1	FCM1	Anode hydrogen inlet pressure	barg
PT-158-1	FCM1	Anode hydrogen outlet pressure	barg
PT-251-1	FCM1	Cathode oxygen outlet pressure	barg
VTOT-01	FCM1	Cell total voltage	V
QM-201-1	FCM1	Cathode air inlet mass flow	ls/min
PT-210-1	FCM1	Cathode oxygen inlet pressure	barg
PT-104-2	FCM2	Anode hydrogen inlet pressure	barg
PT-158-2	FCM2	Anode hydrogen outlet pressure	barg
PT-251-2	FCM2	Cathode oxygen outlet pressure	barg
VTOT-02	FCM2	Cell total voltage	V
QM-201-2	FCM2	Cathode air inlet mass flow	ls/min
PT-210-2	FCM2	Cathode oxygen inlet pressure	barg
PT-104-3	FCM3	Anode hydrogen inlet pressure	barg
PT-158-3	FCM3	Anode hydrogen outlet pressure	barg
PT-251-3	FCM3	Cathode oxygen outlet pressure	barg
VTOT-03	FCM3	Cell total voltage	V
QM-201-3	FCM3	Cathode air inlet mass flow	ls/min
PT-210-3	FCM3	Cathode oxygen inlet pressure	barg
PT-104-4	FCM4	Anode hydrogen inlet pressure	barg
PT-158-4	FCM4	Anode hydrogen outlet pressure	barg
PT-251-4	FCM4	Cathode oxygen outlet pressure	barg
VTOT-04	FCM4	Cell total voltage	V
QM-201-4	FCM4	Cathode air inlet mass flow	ls/min
PT-210-4	FCM4	Cathode oxygen inlet pressure	barg
PT-104-5	FCM5	Anode hydrogen inlet pressure	barg
PT-158-5	FCM5	Anode hydrogen outlet pressure	barg
PT-251-5	FCM5	Cathode oxygen outlet pressure	barg
VTOT-05	FCM5	Cell total voltage	V
QM-201-5	FCM5	Cathode air inlet mass flow	ls/min
PT-210-5	FCM5	Cathode oxygen inlet pressure	barg
PT-104-6	FCM6	Anode hydrogen inlet pressure	barg
PT-158-6	FCM6	Anode hydrogen outlet pressure	barg
PT-251-6	FCM6	Cathode oxygen outlet pressure	barg
VTOT-06	FCM6	Cell total voltage	V
QM-201-6	FCM6	Cathode air inlet mass flow	ls/min
PT-210-6	FCM6	Cathode oxygen inlet pressure	barg
PT-104-7	FCM7	Anode hydrogen inlet pressure	barg
PT-158-7	FCM7	Anode hydrogen outlet pressure	barg
PT-251-7	FCM7	Cathode oxygen outlet pressure	barg
VTOT-07	FCM7	Cell total voltage	V
QM-201-7	FCM7	Cathode air inlet mass flow	ls/min
PT-210-7	FCM7	Cathode oxygen inlet pressure	barg
PT-104-8	FCM8	Anode hydrogen inlet pressure	barg
PT-158-8	FCM8	Anode hydrogen outlet pressure	barg
PT-251-8	FCM8	Cathode oxygen outlet pressure	barg
VTOT-08	FCM8	Cell total voltage	V
QM-201-8	FCM8	Cathode air inlet mass flow	ls/min
PT-210-8	FCM8	Cathode oxygen inlet pressure	barg

The maximum sample time achievable with the combination of the PLC available and the LabView software is 200 milliseconds: a good improvements respect to the 4-5 seconds realized by the original DAQ system, although all the data are saved every second by the HMI.

The homepage of the high speed DAQ system is the *Plant* window (Figure 5.27) that shows the plant layout of the external cooling system and allows to define the fan-cooler control type, to set the fan-cooler speed in percentage and to control the opening of the three-way valve visible in figure.

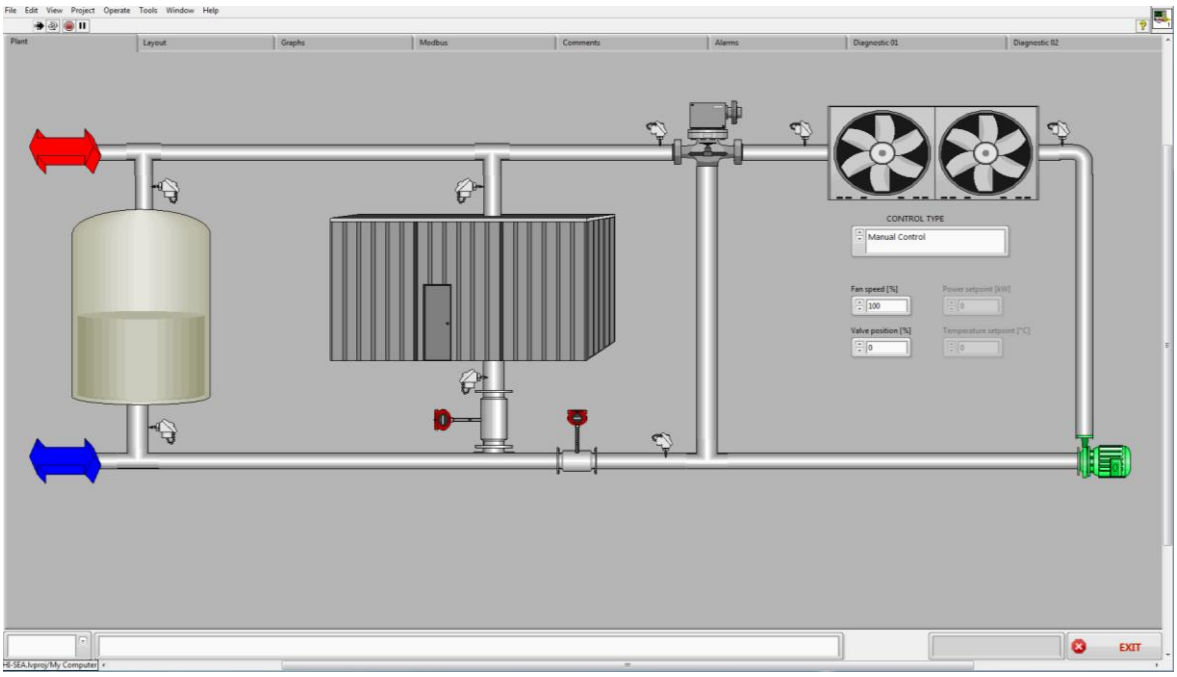

Figure 5.27 – High Speed DAQ Plant window

The *Layout* window represents the P&I diagram of the external cooling system and shows all the data acquired by the system, in particular temperature and water mass flow, useful to control the correct operation of the system. Therefore, is also possible to start-up or shutdown the water pump by the PG3 button.

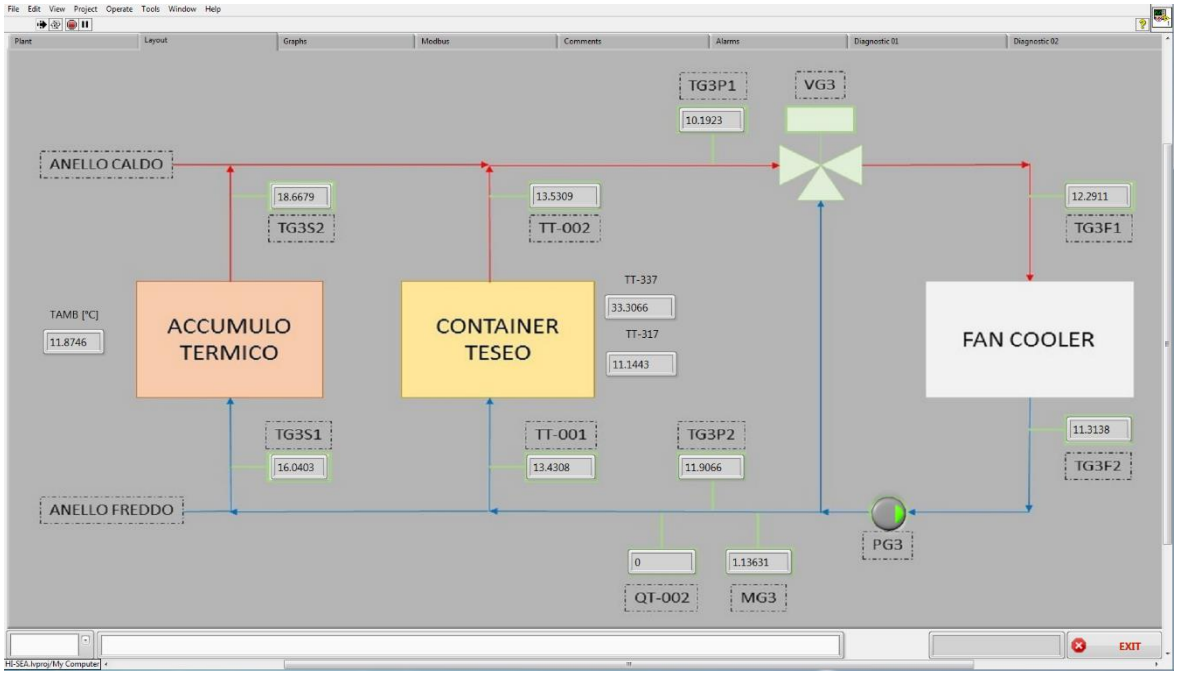

Figure 5.28 – High Speed DAQ Layout window

The *Graphics* window allows to graph over time all the acquired signals along with the calculated parameters, such as the thermal cooling power extracted from the HI-SEA laboratory by means of the heat exchangers of the two branches.

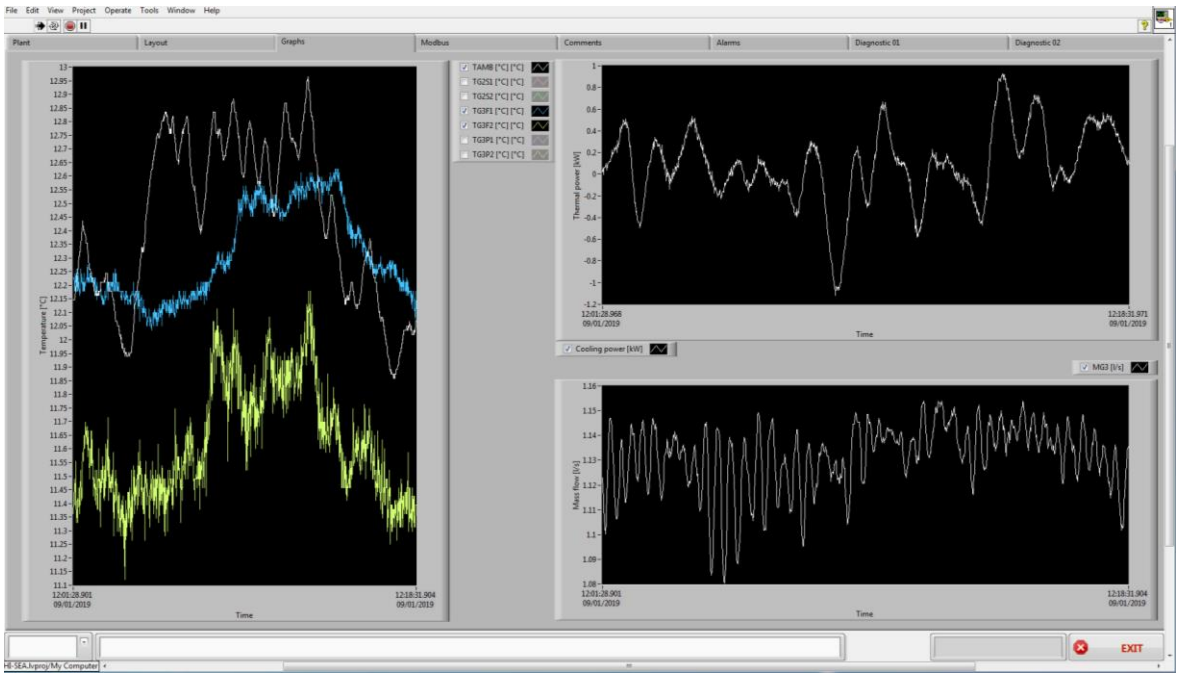

Figure 5.29 – High Speed DAQ Graphics window

The *first Diagnostic* window shows the FAT polarization curves of the 8 Nuvera stack together with the actual value of current density and voltage performed by the stacks. This representation is useful to immediately understand the performance of the stack, in particular

if it is near to the factory performance or not, even if probably the external conditions like pressures and temperature are different. As described below, a more valid approach involves setting a stack voltage model that best predicts stack performance on the basis of the actual external conditions of the PEM fuel cell considered.

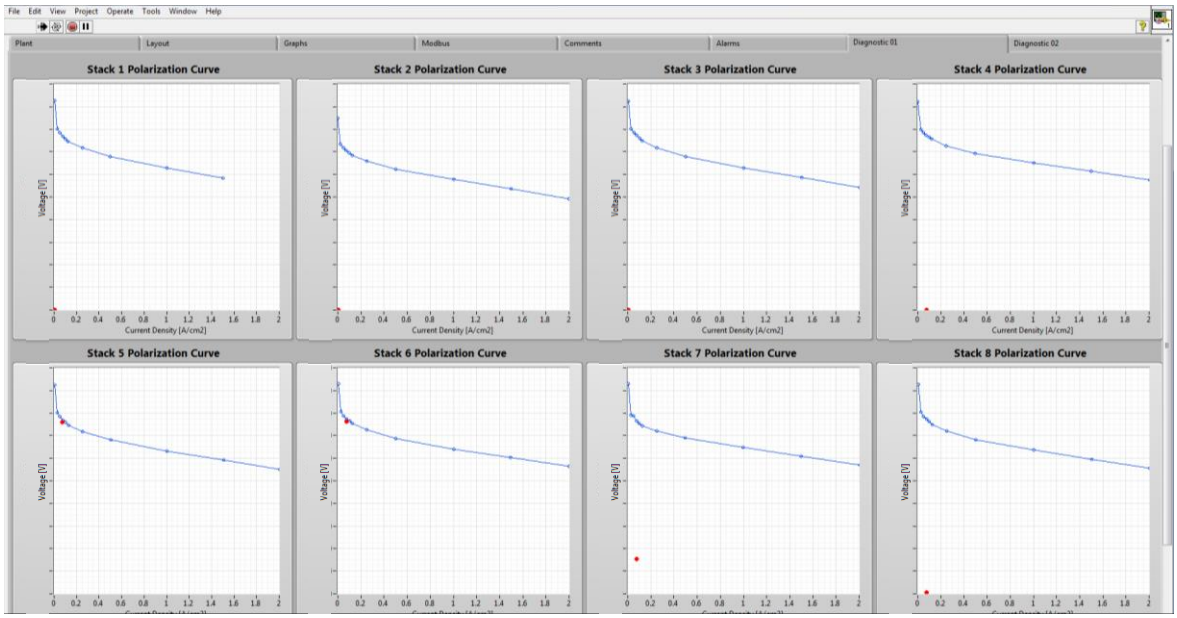

Figure 5.30 – High Speed DAQ first Diagnostic window

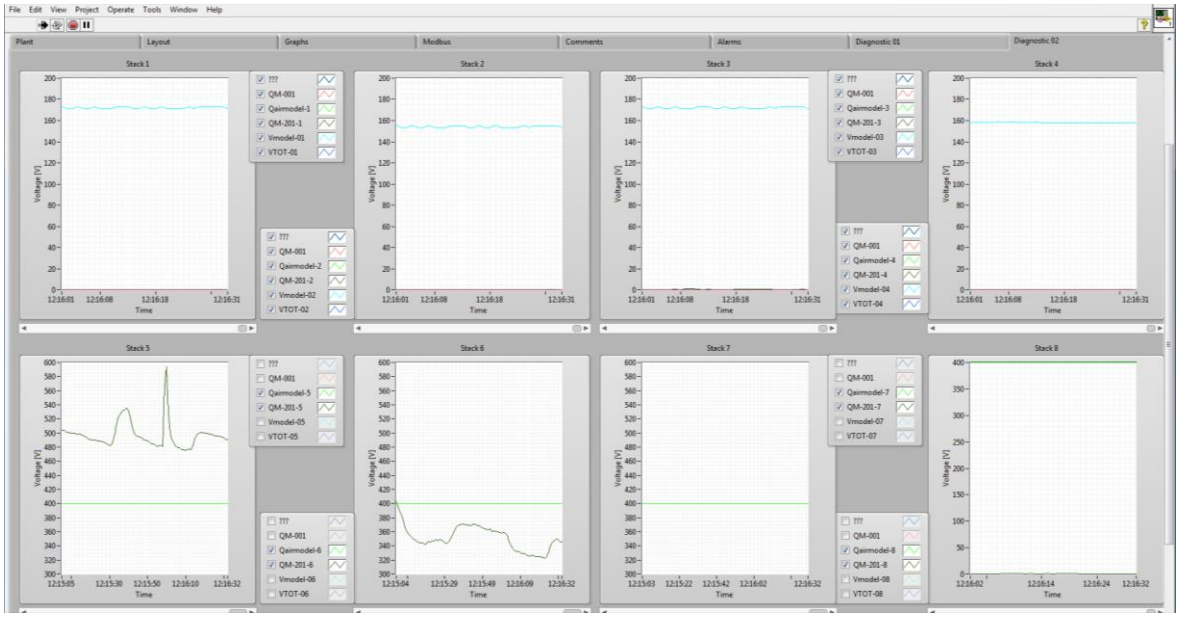

Figure 5.31 – High Speed DAQ second Diagnostic window

The *second Diagnostic* window graphs some interesting acquired signals and the related set-points values or model results. This panel allows for example to compare:

- the instantaneous cathode air mass flow rate with the setpoint value imposed to the stack, variable with the current request;

- the instantaneous hydrogen mass flow consumed by the stack with the stoichiometric quantity, which depends on the stack current, to evaluate the hydrogen losses due to timed purges;
- the instantaneous stack voltage to the value resulting from the stack voltage model exposed in next Sections, to evaluated if the operating point of the stack is expected or is far from stable and secure operating conditions.

Figure 5.32 and Figure 5.33 present the comparison between the original low speed DAQ system of the HI-SEA laboratory in comparison with the high speed DAQ system developed in LabView and dedicated to acquire sensible signals with fast dynamics composed by electrical and pressure parameters. For simplicity, only the current density signal of the branch 2 is considered. Figure 5.32 verifies the correct operation and comparable results of the two DAQ systems. The HMI and LabView systems do not significantly differ in how they acquire data except for rare peaks in high speed DAQ that do not affect the goodness of this acquisition system. The curves in Figure 5.32 overlap quite well most of the time. Therefore, data from the low speed DAQ can be employed during the analysis of static regime behaviour of the system, with no significant loss of information.

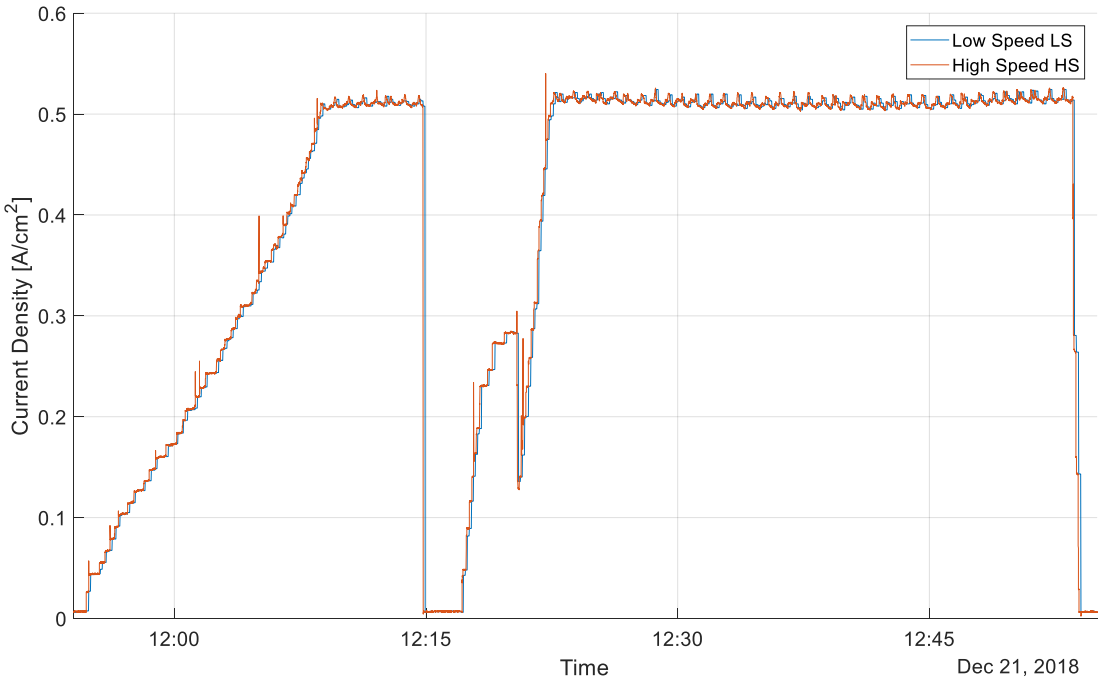

Figure 5.32 – Signals' comparison between original low speed DAQ and the new LabView high speed DAQ

Figure 5.33 shows a detailed comparison of the two systems: is visible the same trend of the current density signals acquired with a time shift equal to about 4-5 seconds. As reported before, the original low speed DAQ save all the data once a second but, for the great amount of data that it has to manage, is able to actually update the signals with a minimum delay of

about 4-5 seconds. Anyway, taking into account this limitation, the acquired signals are comparable with the two DAQ system available.

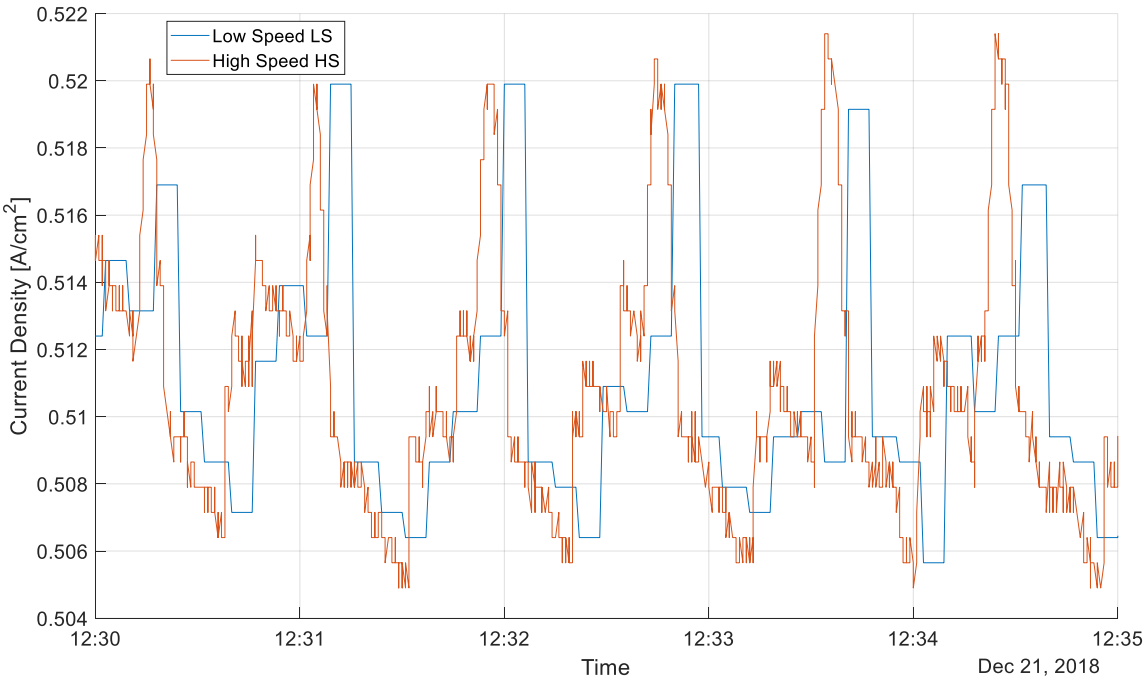

Figure 5.33 – Zoom of the signals' comparison between low speed DAQ and high speed DAQ

5.4 Lessons Learned from Test Data Analysis

Thanks to the data acquisition systems developed, both the HMI low speed and LabView high speed systems, it is possible to analyse different tests to better understand the characteristic behaviour of the HI-SEA laboratory and of its components, with the aim of improve the performance of the stacks and the safety of the system. In particular, different test during the last four years will be analysed, starting from the first tests performed not in the HI-SEA laboratory: these preliminary tests highlighted some problems and weakness of the system, then resolved with the adoption of various precautions and plant modifications. After some years, the PEM-FC system is again operating into the HI-SEA laboratory, but obviously with different difficulties to restore the original performance of the stacks that have not worked for a long time. Therefore, a membrane rehydration process is developed with the help of the stacks supplied Nuvera and an upgrade is performed to stabilize the cathode air mass flow controllers that, in the original configuration, cause high oscillations in the performance of the stacks.

5.4.1 TESEO First Tests & System Upgrades

In this section are analysed the first tests on the PEM-FC System realized during the TESEO project and thus not into the HI-SEA laboratory in Savona Campus, therefore with a different balance of plant (different compressed air line, hydrogen line and electronic load). This tests

analysis was important to understand the basic problems of the system and foresee some important changes for the safety of the systems.
The most important test day of this series was the 21th October 2015. Figure 5.34 shows in detail the behaviour of current, minimum, maximum and average cell voltage and power output of the stack number 2 between 12:52 and 13:13.

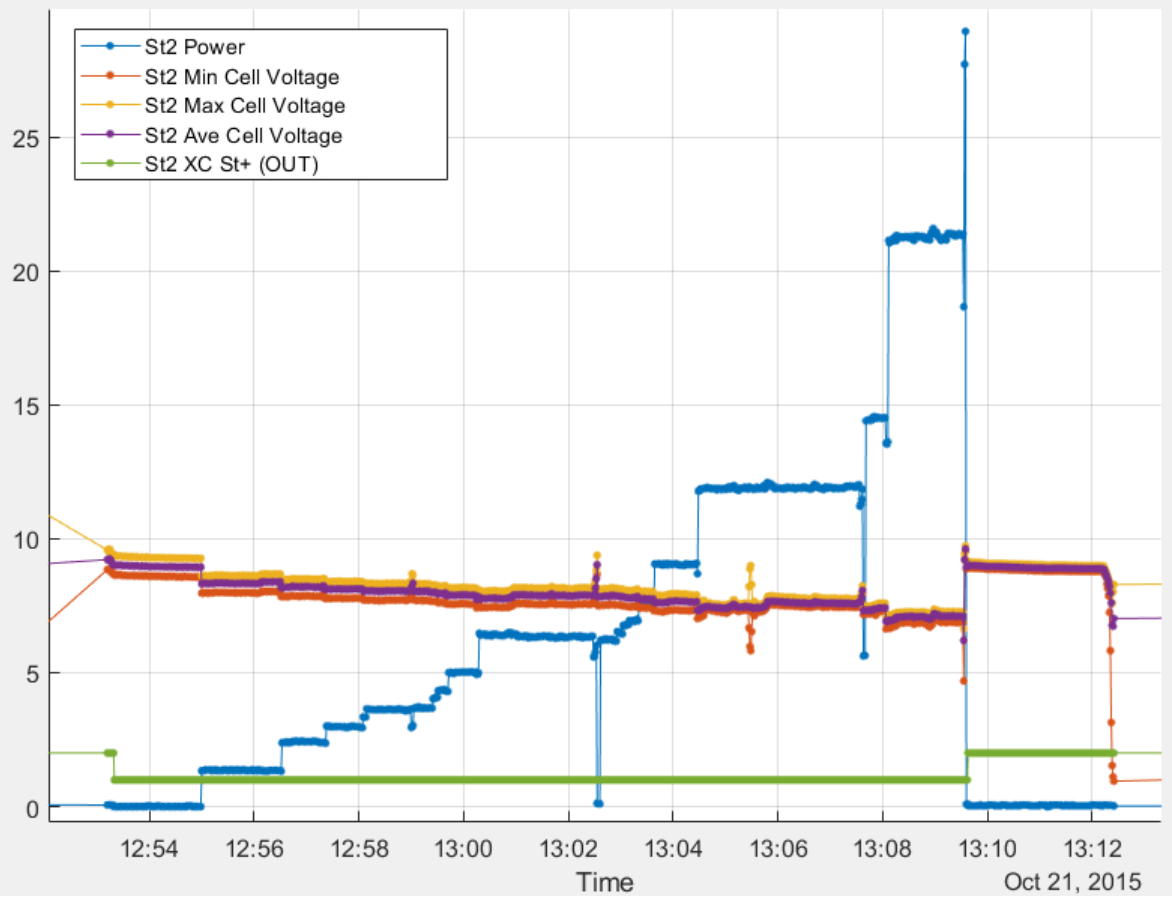

Figure 5.34 – 21/10/2015 test day: morning test

The test starts around at 12:53: stack bypass is closed, current remains 0 for some minutes and then power is set starting from 2 kW and increasing up to 28 kW in less than 15 minutes. The test runs for almost 20 minutes and meanwhile stack 1, 3 and 4 are working together with stack 2. Despite the high load steps, the four stacks responded very well and always provided the required power in the correct way: observing the minimum and maximum voltage of the stack 2, the difference tends to decrease and to stabilize. This is an important factor that indicates the correct operation of the fuel cell. At 13:09 bypass of stack 2 closes, the device is shut down and data are no longer collected by the HMI until the afternoon. It is important to clarify that unfortunately the data acquired during these tests are incomplete: in fact, only the data relating to the stacks are available, i.e. the level 1 data (see Section 5.1). Furthermore, for these first tests, data was recorded only when the stack went into operation. Unfortunately, this approach is completely inappropriate to better understand the conditions of the system before and after the start of the single stack and to reconstruct any malfunctions.

However, tests restarted in the afternoon, as visible in Figure 5.35. For 6 minutes, bypass of stack 2 is left open, the stack is ready to work but no current is circulating. This means that air is flowing but it makes cells membranes drier as there is no power production to compensate the effect of the air flow with water production by the electrochemical reactions. As soon as 2 kW are requested to stack 2, minimum and maximum cell voltage behave strangely but the resulting average cell voltage seems normal, shadowing to the operator the bad functioning of the system.

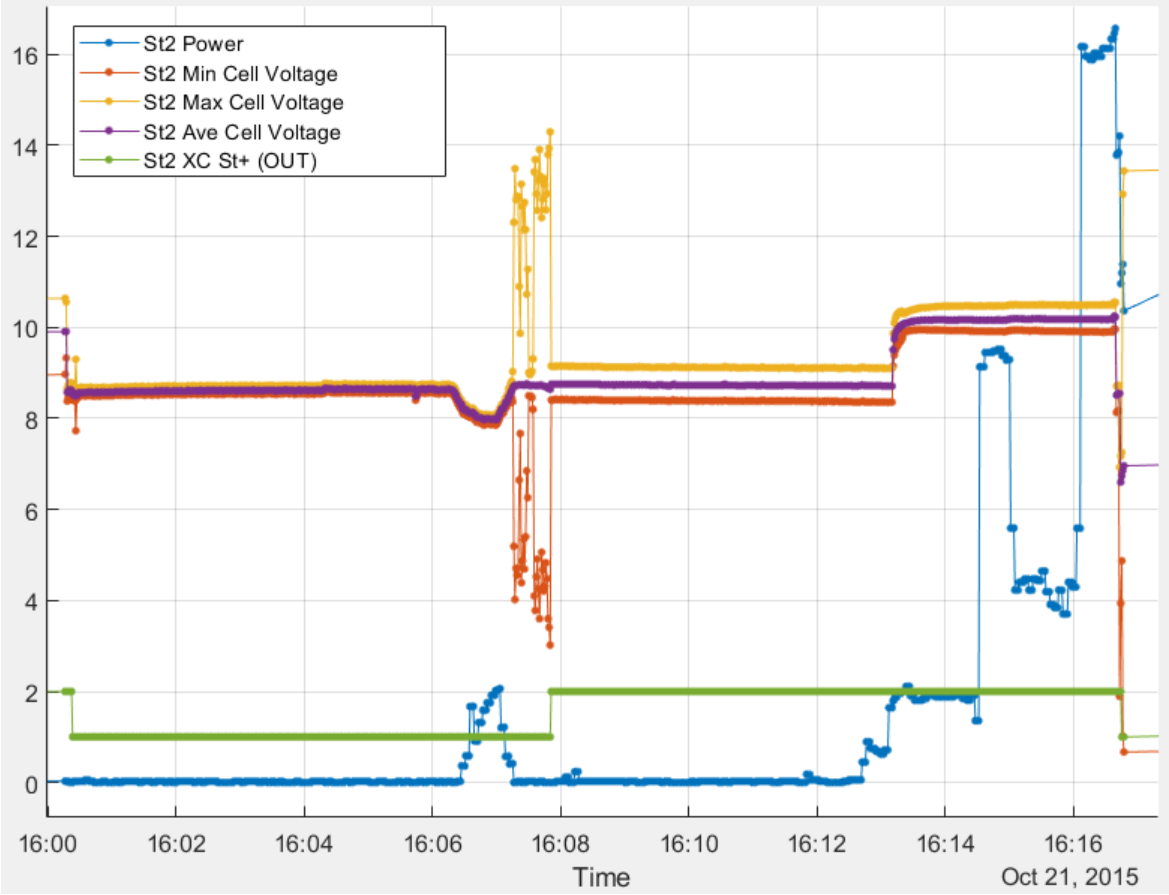

Figure 5.35 – 21/10/2015 test day: first part of the afternoon test

It is presumable that this load request of 2 kW, together with particular membrane humidity conditions, probably dictated by incorrect manual settings of the system between morning and afternoon tests, caused some membrane damages that made cell voltages vary so strongly. In fact, after this event, the maximum and minimum cell voltages are very far apart and most importantly the voltages are no longer related to the load request. This strange behaviour is highlighted at 16:13 when the power request increase and the stack voltages also increase, contrary to the normal operation shown in Figure 5.34. After that, the voltages are quite constant despite the variable load profile until the moment when the minimum cell voltage collapses at 16:16:45 and the safety procedures shutted-down this stack.
After that, as visible in Figure 5.36, the operators tried to reconnect the stack 2 to the branch 1 but was no possible: the stack was already damaged and moreover they tried to reconnect

the stack directly at high current level, causing further damages. As explained above, the system saves data only when the stack is running, thus in this case is no possible to correctly reconstruct the system behaviour due to lack of data. In fact, only few points are saved starting to the point when the operator decided to try to reconnect the stack. The system acquired few points as long as the procedures intervened to stop the operation of the stack.

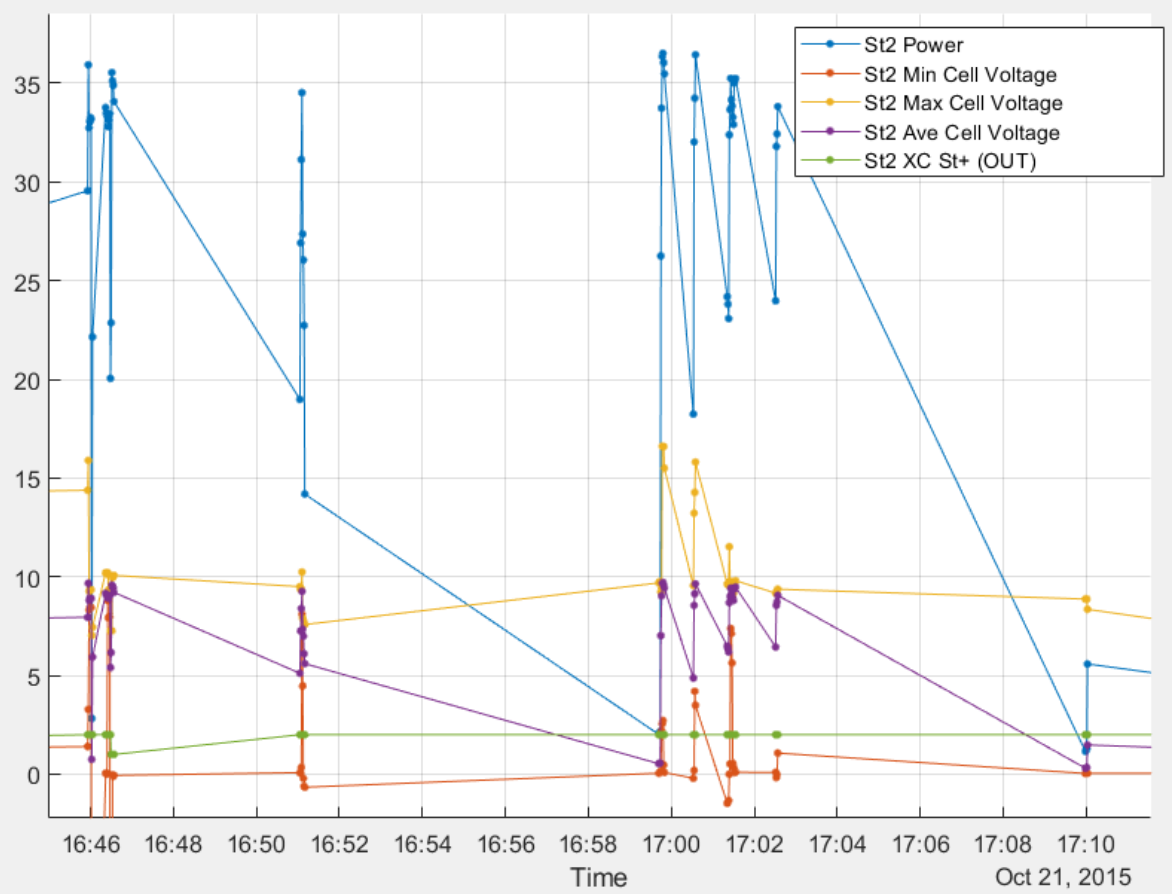

Figure 5.36 – 21/10/2015 test day: second part of the afternoon test

After the conclusion of this test, operators noticed that some of the cells composing stack 2 were broken, which could have caused a short circuit. The most likely causes for cells rupture are linked to:

- The incorrect membrane humidity conditions of the stack when at the 16:07 the power request start to increase. Membrane humidity is a determining factor and the stack may have dried out as a result of incorrect manual settings perpetuated between morning and afternoon tests.
- The high conductivity of coolant: it could have acted as a bridge for the current among cells, causing hot spots with high temperature. In fact, after the test the non-presence of deionizing cartridges in the filters was detected. Having to use a specific coolant with low conductivity, the presence of deionizing filters is essential to guarantee this specification over time. An increase in the coolant conductivity it may have been a determining contributor that led to the rupture of some cells in the stack.

As explained, test data were originally collected only when the stack was running, so it is not clear what happened, but excessive drying of membranes is normally due to a high air flow rate. When membranes have not enough humidity, current can only pass through some specific parts of them, where there is still some humidity; temperature in those sites strongly increases, up to the creation of hot spots. If temperature overcomes a limit value, the membrane burns and breaks up. Meanwhile, where the membrane is dry and not able to conduct current, the reaction between ions H^+ and OH^- is no longer verified even if the ions continue to flow. This implies an accumulation of H^+ and OH^- on the two different sides of the membrane, which can be damaged by the acid pH of OH^- ions. Mass flow valves are thus controlled to verify if this is what happened to stack 2. Therefore, the procedure for control of the air flow regulator, MFC-201, has been reviewed.
To avoid further similar problems, the following measures are adopted:

- MFC-201 air mass flow measurement is acquired at each stack. A modification of the system hardware is made necessary for this action: the data measured by MFC-201 was in fact not acquired but just controlled previously. In this way, it is possible to check the air mass flow in any condition and to prevent the system from a bad control or a bad functioning of the instrument;
- The acquisition of coolant conductibility measurements is enabled. This will set up an alarm when the conductibility is too high;
- Acquisition of hydrogen mass flow measurement is enabled for total stacks in the hydrogen line level;
- Data acquisition of all the signals every second for the whole period in which the HMI is open;
- Manual settings and operations are strongly discouraged and should always be avoided. Not possible to delete due to their fundamental utility in same conditions and specific tests on singular components;
- Finally, the three-way valves, originally present in the project, have been installed. These components allow the accurate regulation of the coolant temperature and therefore of the stacks during the operation.

These measurements aim to avoid faults in the future, but performance of stack 2 is lower than the other 7 stacks due to removal of 16 cells from the stack.

5.4.2 Membrane Rehydration Process

First tests described in previous Section and not performed into the HI-SEA laboratory allow to highlight the problems and the necessary upgrades of the system, especially in terms of security measures, alarms and operational procedures. The HI-SEA laboratory collects this experience and involves the updates previously described.
Due to the period of about 2 years between the first tests on the system and the new stat-up of the stacks, it became necessary to perform a membrane rehydration process on the stacks, as suggested by the manufacturer Nuvera.

Figure 5.37 shows the process on the Stack 6 of the branch 2. A slow load ramp is supplied to the stack, in order to reach the nominal conditions as quickly as possible but gradually, avoiding supplying too high fluctuations on the stack in terms of current, temperature or gasses mass flows. The major difficulties are related, on one side, to rapidly increase the current to avoid both the time-out alarm of the minimum branch current and of the nominal stack temperature and, on the other side, to increase slowly and gently the current to avoid system failure caused by the membrane dryness that makes the system very sensitive and unstable. Moreover, the difficult of work with all the stacks of one branch, due to different reasons, makes it even more difficult to avoid current and temperature time-outs.
As visible in Figure 5.37, during the first ramp, the minim cell voltage approaches the average cell voltage, and both tend to stabilize before incurring instabilities that generally precede the collapse of the minimum cell voltage and the emergency shutdown of the system. In this case, the emergency shut-down is avoided thanks to a timely switch-off of the stack. These instabilities are also probably due to the incorrect regulation of the coolant temperature, in turn probably due to wrong settings of the external cooling circuit. In fact, during the others load ramp, the coolant temperature is well controlled around the local set-point of 51°C.

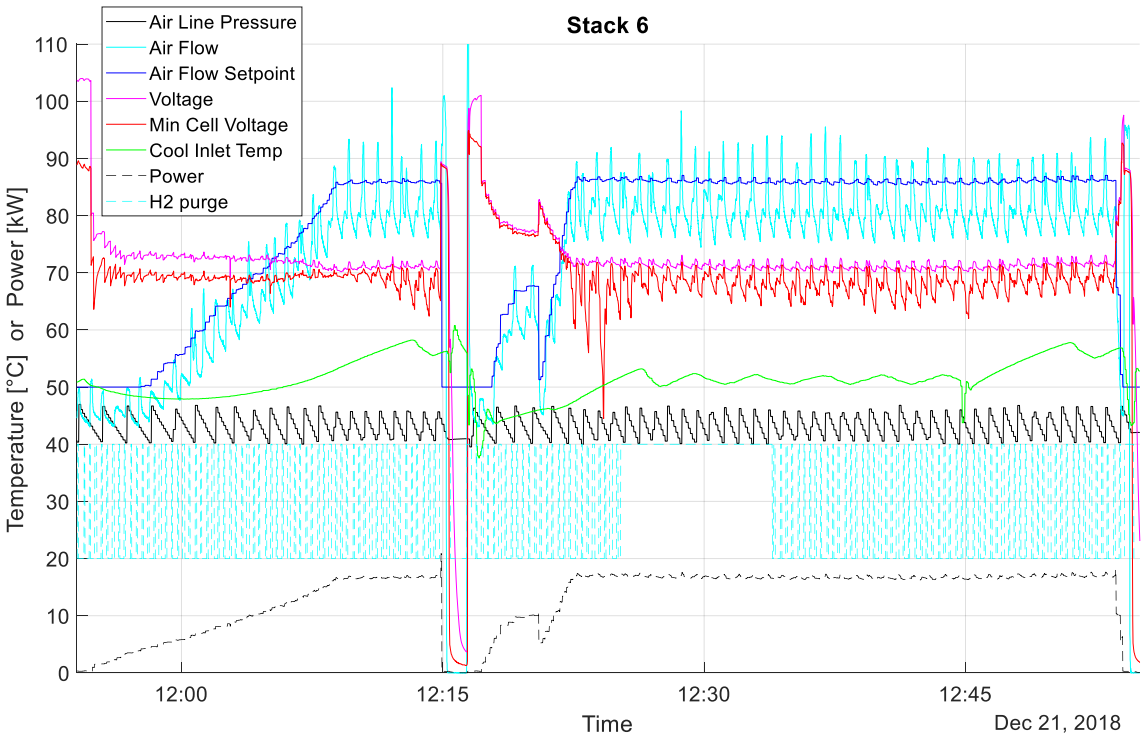

Figure 5.37 – 21/12/2018 test day: rehydration process

During the second small load ramp the system already responds in a much better way, as visible from the minimum and average cell voltages that are very stable, close and of greater absolute value. This behaviour is a proof that the process is leading to the desired results.

The last and third load ramp is quickly, thanks to the improved performances of the stacks, and reaches the same maximum power of the first ramp, which in that case had led to increasing instabilities. Immediately the minimum cell voltage starts to oscillate strongly but luckily after a few minutes it stabilizes; to avoid further problems it has decided to operate for about 10 minutes with the anode purge valve always open. After that, the timed purged has been re-established and the stack operates well until the end of the rehydration process.

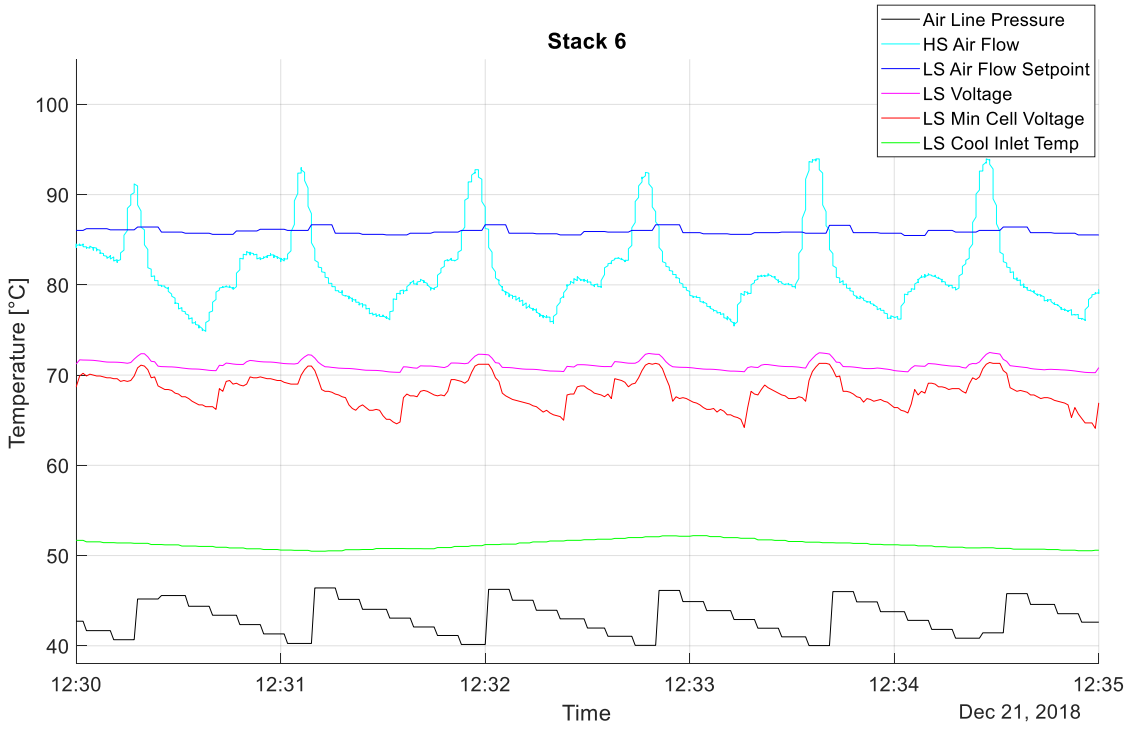

Figure 5.38 – 21/12/2018 test day: rehydration process (zoom)

During all the operation the most evident factor is the cathode air mass flow oscillations. As better visible in Figure 5.38, the air flow guarantee by the mass flow controller oscillates and never reaches a constant operation near the setpoint value. This trend highly influences the performances of the fuel cell, in particular is clear from the figure that this trend is strongly correlated to the minimum cell voltage. If the air mass flow decreases, also the minimum cell voltage decreases, with a strong impact on the stability operation of the stack: the minimum cell voltage oscillation, together with a dehydrated membrane, can causes a collapse of the cell voltage below the safety limits, causing an emergency shutdown of the system. This behaviour has been very frequent during the preliminary tests performed into the HI-SEA laboratory and also during the first load ramp visible in Figure 5.37. The oscillation of the air mass flow controller seems to be directly related to the air pressure, controlled by the air compressor and not regulated by a pressure reduction valve into the air line: for this reason, in the following section, the benefits of installation of dedicated air pressure regulators in line, able to stabilize the pressure before the air mass flow controllers and thus the air mass flow flowing inside the stacks, are explained.

5.4.3 Cathode Air Mass Flow Controllers Stabilization

On the 23th of January 2019, the following tests are performed for the stabilization of the cathode air mass flow controller. As described in the previous section, the solution adopted to reduce the oscillations of the air mass flow controllers is the installation of pressure regulator before these components. During this test day, the comparison between stack 7 equipped with the new pressure regulator, and the stack 6 in the old configuration is realized. Figure 5.39 shows the principal electrical signals, branch current and maximum and minimum cell voltages of the two stacks while in Figure 5.40 air flow signals, cathode inlet pressure and air mass flow, are visible. Three ramps of branch current are performed with the two stacks 6 and 7 connected.

These fast ramps allow the correct utilization of the stacks and partly follow the membrane humidification process described in previous section, in order to rehydrate increasingly the membranes and thus improve the stack performances during the test. In fact, as highlighted by the green arrows in Figure 5.39 the cell voltages increase from the fist ramp to the last one in the same current condition. Moreover, the maximum and minimum cell voltages are closer and more stable during the last ramp, index of a performances' improvement and a better operational condition.

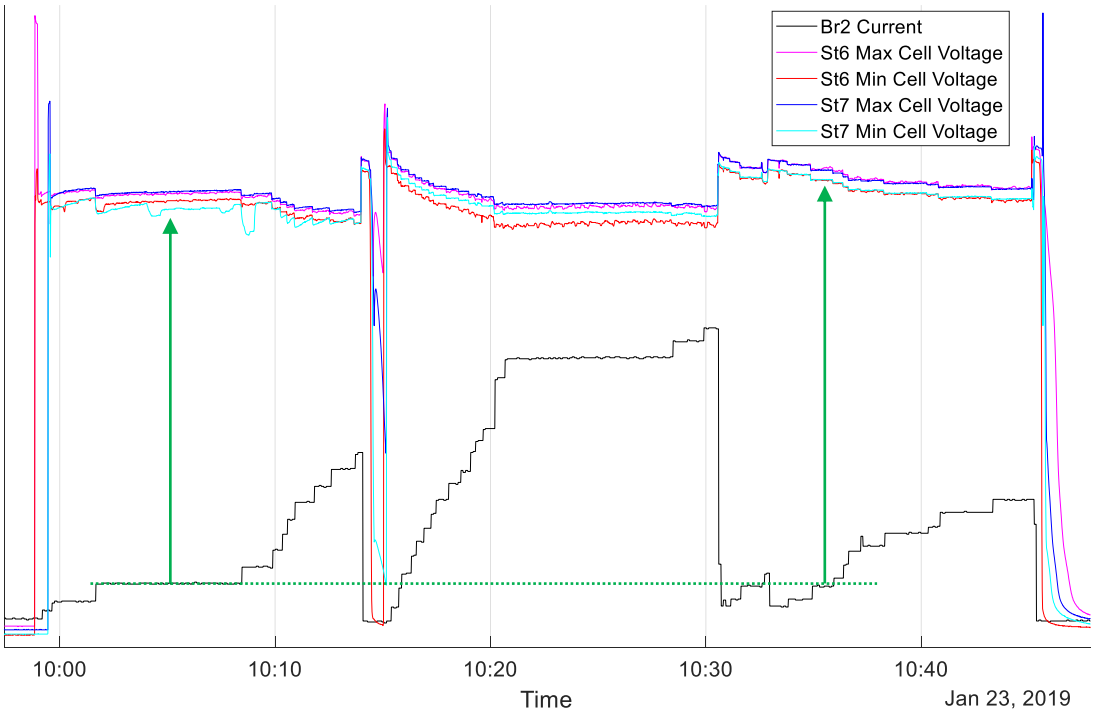

Figure 5.39 – 23/01//2019 test day: mass flow controllers' stabilization, electrical signals

In the first ramp is visible as the cell voltages of the stack 6, already rehydrated on the 21th December 2018, are higher while the cell voltages of the stack 7 are more stable due to the upgrade allowed by the pressure regulator valve. Figure 5.40 highlights this phenomenon showing a more stable cathode air mass flow of the stack 7 with an increase of the cathode

air inlet pressure, beneficial for the stack operation and able to improve the cell voltages, as clear from the Equation (2.11).

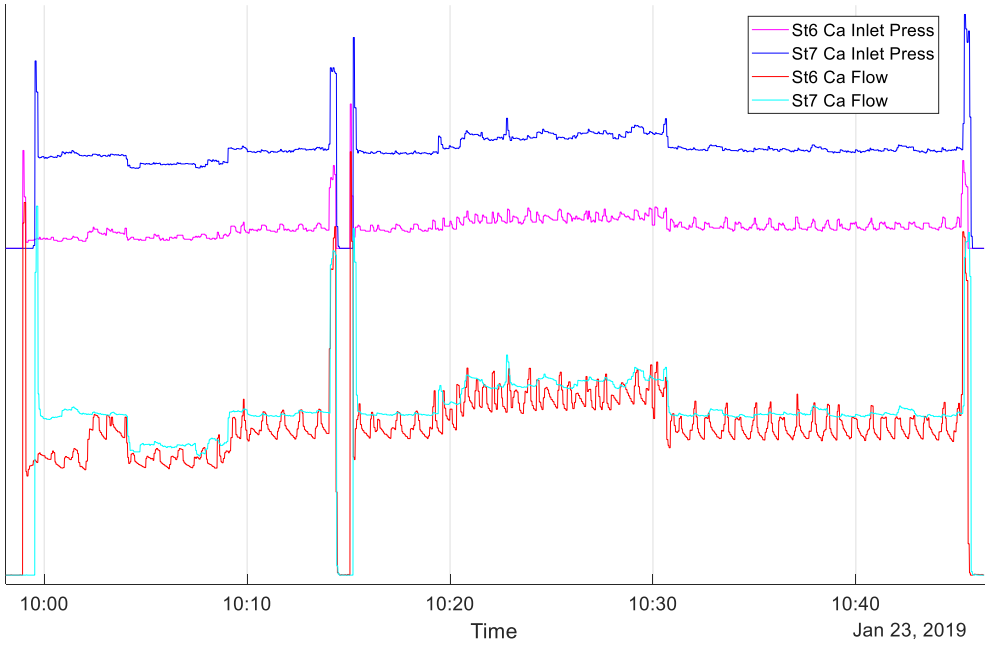

Figure 5.40 – 23/01//2019 test day: mass flow controllers' stabilization, air flow signals

Despite the probably less hydrated membrane initial conditions and thanks to the stabilization improvement by the pressure regulator, the stack 7 is able to perform better than 6 as visible between 10:20 and 10:30 at high current level. However, after this period of stable and beneficial operation, the cell voltages in the last ramps are almost the same for the two stacks, with a more stable trend for the stack 7 equipped with the pressure regulator. Therefore, the installation of these components for all the stacks is certainly beneficial for the stack operation and will be implemented as soon as possible, allowing a stabilization of the stack performance and a correct functioning of the cathode air flow controllers.

6 HI-SEA Model

In the previous section, the HI-SEA laboratory is presented and analysed in its entirety: a review of each components of the plant, the original data acquisition system, the high-speed system developed in LabView for the electrical and pressure signals and the Matlab GUI realized for post processing and to easily plot the data of a test day under investigation. In the end of the previous section, also, some lessons learned by the test data analysis are presented. From the first tests performed during the TESEO project, useful to improve and upgrade the system in terms of security and performance, to the membrane rehydration process developed in collaboration with Nuvera, the manufacturer of the PEM fuel cell stacks, for restoring stacks turned off for a long time, to the stabilization of the cathode air mass flow controllers thanks to the regulation of their inlet pressure. These are some important lessons learned that allowed to acquire an ever-increasing knowledge of the plant and to improve it in different parts.

Another important tool able to help the investigation of this system is the static and dynamic modeling, i.e. the equations able to describe the polarization curves of the stacks and the larger set of equations able to describe the dynamic behaviour of the whole system.

In this section, the stack voltage model is presented first, with the details about the model used and the process adopted to set the equation's constants to each stack of the plant. After that, a comparison between the results calculated by this model with the experimental data performed in the HI-SEA laboratory is described.

Finally, the simplified dynamic model of the whole PEM-FC system is reported and, also for this model, a comparison with the experimental data is discussed. The dynamic model is a simplified version of the detailed model developed in Section 2 and 3 and validated in Section 4, due to the necessity to set the model only with the commercially available data, usually limited to the datasheet information. This huge limitation makes the dynamic model less accurate but, at the same time, simpler and able to provide some important results starting from few easily obtainable data.

These two models are able to predict well the experimental data, considering the uncertainties due to the intrinsic errors of the approximations realized by the models and to the measurement errors of the plant often not negligible.

6.1 Stack Voltage Model Setting

As introduced in Section 5.1.1, Nuvera provided the reference polarization curves of the 8 fuel cell stacks installed in the HI-SEA laboratory, as reported in Figure 6.1. As the Factory Acceptance Tests (FAT) are carried out on a pilot scale, their results are expected to show the best performance obtainable: the pilot plant is smaller, and the tests run over controlled environmental conditions (temperature, air humidity, etc.), thus limiting losses and ensuring the best performance. The polarization curves are obtained imposing an increasing power output to the stacks, individually. Each set point for the power output is kept constant during a period and meanwhile voltage and current density are monitored. As the power increases, current density becomes higher while voltage lowers. Voltage is observed in its maximum, average and minimum values detected among the cells of the stack.

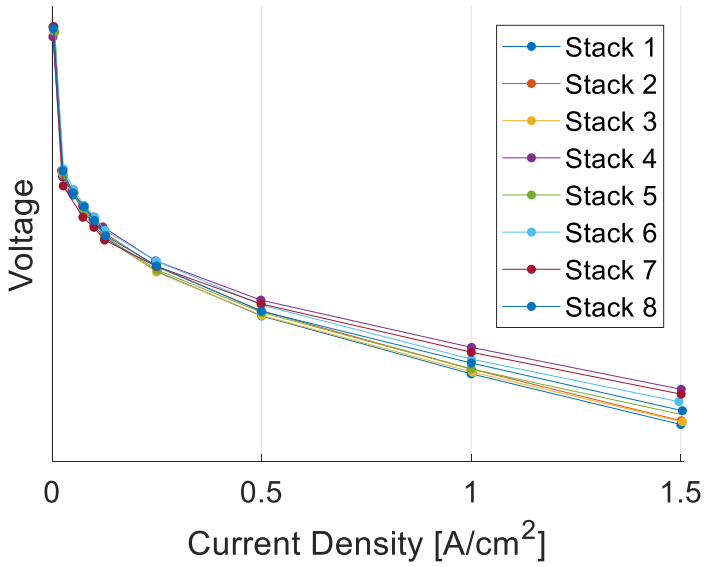

Figure 6.1 – Nuvera FAT stack polarization curves comparison

Figure 6.1 reports only the average cell voltage of the stacks; the FAT polarization curves are slightly different from each other probably due to small constructive differences inside the stack, considering that these results are obtained by Nuvera using the same test bench and in the same external conditions. This hypothesis is further supported by the graphs of the anode and cathode pressures shown in Figure 6.2. From the FAT pressure curves supplied by Nuvera, the operating pressures as function of the current density are slightly different for the 8 stacks, especially the anode pressures greatly influenced by very small geometric variations of the anode ejector. These variations certainly explain in part the slight differences between the stack polarization curves. The cathode pressure is quite similar for the 8 stacks as it is mainly influenced by the external air supply system, which is always the same test bench during the factory tests.

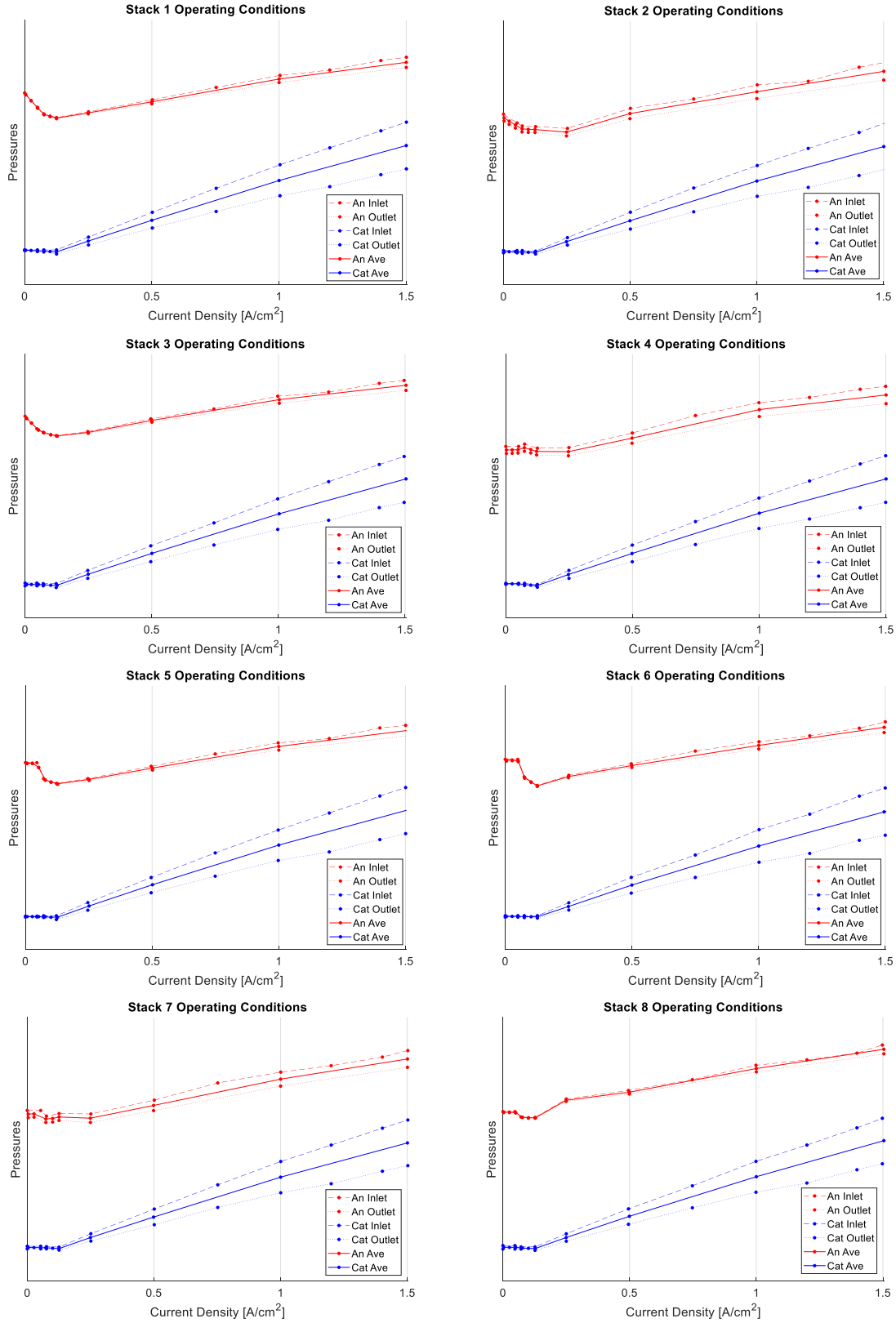

Figure 6.2 – Nuvera FAT operating pressure curves.

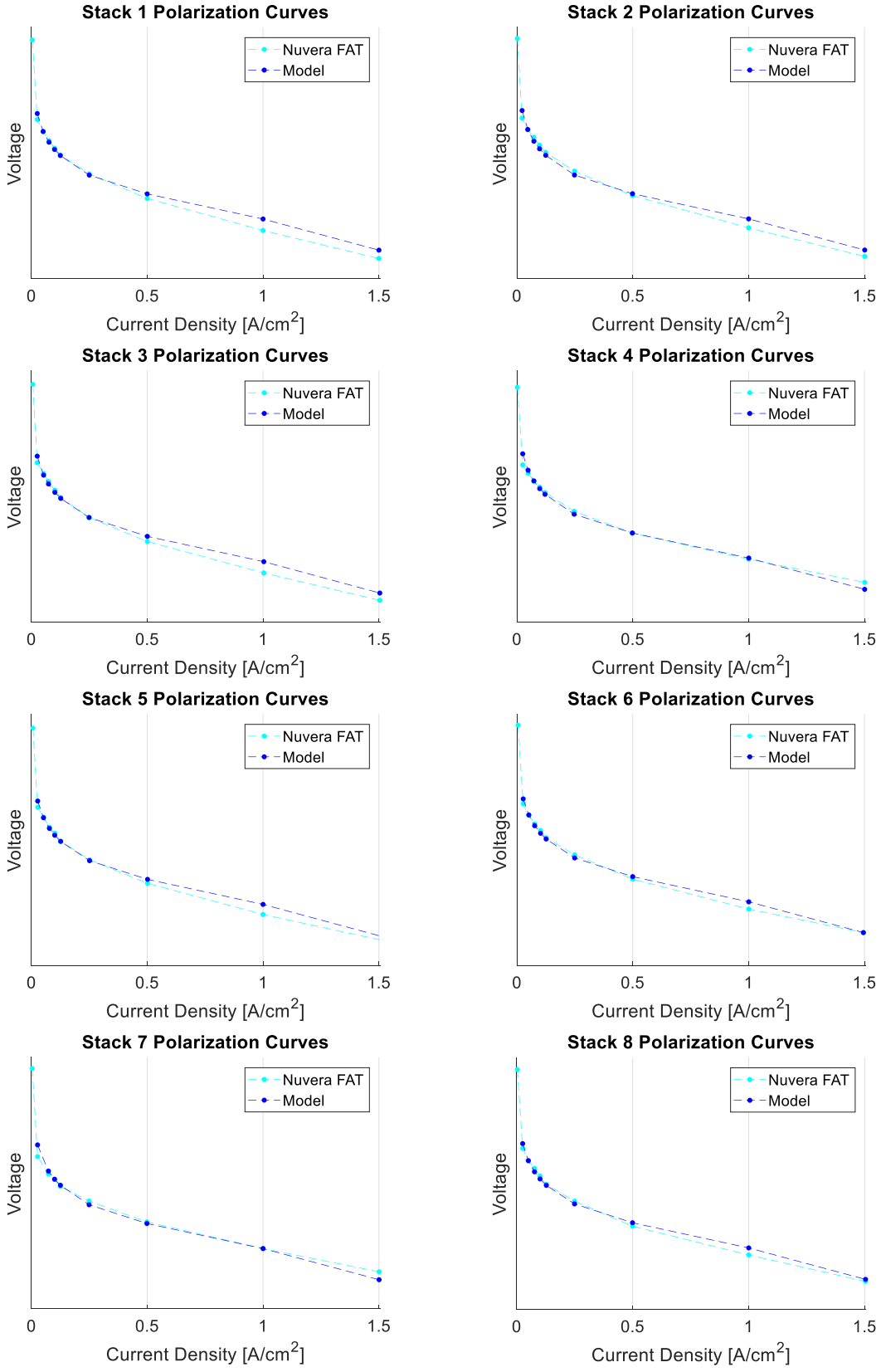

Figure 6.3 – Adaptation of the stack voltage models on the FAT data.

The Mert-Mann stack voltage model summarized in Section 2.1.5.2 is used to represents the Nuvera FAT polarization curve, due to its better adaptability to the factory data available. The assumptions made are:

- Perfect membrane hydration ($\lambda = 14$) for all the points of the polarization curves;
- Operating pressures from Figure 6.2;
- Stack temperature not uniform at various current density but in line with the Nuvera factory data expressed in Table 6.1. This temperature trend is the one used during the factory test to obtain the polarization curves of the stacks compared in Figure 6.1.

Table 6.1 – Nuvera FAT operating temperature

Current Density [A/cm²]	*Stack Temperature [°C]*
0	51.5
0.125	54.2
0.25	56
0.5	62.5
0.74	68
1	73
1.2	76.4
1.4	79.4

Whit these hypothesis, the differential evolution algorithm developed specifically for this purpose (see Appendix A) allows to obtain all the necessary constant parameters to fit the stack voltage model with the real performances represented by the FAT polarization curves, as clearly visible in Figure 6.3. Using the Mert-Mann approach, the membrane thickness t_m and the anode charge transfer coefficient α_{AN} are sufficient to adapt the model. Figure 6.3 shows the graphical results obtained by the application of the differential evolution algorithm.

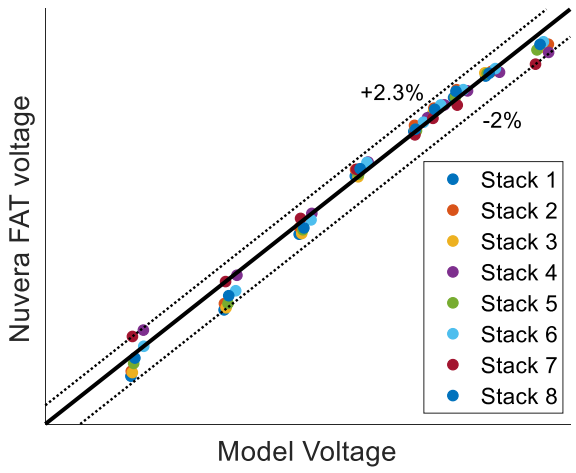

Figure 6.4 – Parity plot of the Nuvera stack voltage

Figure 6.4 summarizes the results of the fitting process of the stack voltage model developed against the experimental data available from the Nuvera FAT of the 8 stacks. As visible, using the Mert-Mann formulation and the differential evolution algorithm to find the model constants, the maximum error resulting by the process is about 2%, more than satisfactory result.

6.2 Stack Voltage Model vs Experimental Data

From the setting process of the stack voltage model exposed in the previous section, is possible to create the stack voltage Matlab function described in Appendix B, useful to easily and rapidly compare the model results with the experimental data also inside the Matlab Data Viewer. In particular, the performance depends strongly on the operating temperature and also on the anode and cathode pressures. Therefore, is important to compare the model results and not the FAT polarization curves with the experimental data, in order to compare the expected performance of the stack in the same temperature and pressure conditions of the tests realized in the HI-SEA laboratory.
To obtain the polarization curve of a stack is usually necessary establish a stepped load ramp to be imposed on the stack under examination. By definition of the characteristic curve, in addition, the temperature and pressure conditions of the stack should be constants at the equilibrium points assumed for the reconstruction of the polarization curve. In fact, a load step is imposed to the fuel cell and the time required for stabilizing the performance must have elapsed before defining the stable conditions and thus acquiring the current and voltage pair to be used for the polarization curve.
An important and general input for the definition of the correct load ramp comes from the Joint Research Centre (JRC) of the European Commission. The JRC defines many protocols for PEM-FC tests [70]. As reported in [70], the objective of performing polarisation curve measurements is to determine the MEA performance in terms of cell voltage and power density against current density at specified operating conditions. The dwell time of each set point should be sufficient long enough to ensure that stabilisation criteria of cell voltage of ±5 mV within 2 min but not longer than 15 min, except for the OCV which shall not exceed 1 min dwell time [70]. The proposed set points are summarised in Table 6.2 and Figure 6.5.

Table 6.2 – JRC polarization curve set-points [70]

Set Point No.	*Current Density [A/cm^2]*	*Recommended dwell time [s]*	*Recommended Data acquisition time [s]*
1	0.00	≤60	≥30
2	0.02	≤60	≥30
3	0.04	≤60	≥30
4	0.06	≤60	≥30
5	0.08	≤60	≥30
6	0.10	≤60	≥30

7	0.20	≥120	≥30
8	0.30	≥120	≥30
9	0.40	≥120	≥30
10	0.60	≥120	≥30
11	0.80	≥120	≥30
12	1.00	≥120	≥30
13	1.20	≥120	≥30
14	1.40	≥120	≥30
15	1.60	≥120	≥30
16	1.80	≥120	≥30
17	2.00	≥120	≥30
18	1.80	≥120	≥30
19	1.60	≥120	≥30
20	1.40	≥120	≥30
21	1.20	≥120	≥30
22	1.00	≥120	≥30
23	0.80	≥120	≥30
24	0.60	≥120	≥30
25	0.40	≥120	≥30
26	0.30	≥120	≥30
27	0.20	≥120	≥30
28	0.10	≤60	≥30
29	0.08	≤60	≥30
30	0.06	≤60	≥30
31	0.04	≤60	≥30
32	0.02	≤60	≥30
33	0.00	≤60	≥30

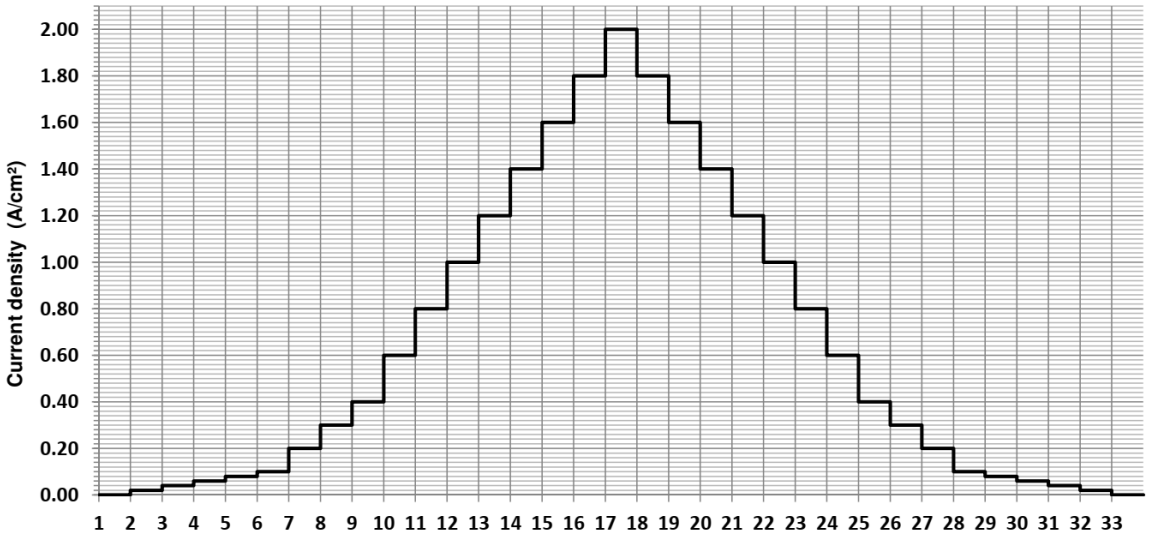

Figure 6.5 – JRC Schematic of current density steps [70]

If the maximum current density of 2.0 A/cm^2 cannot be reached, the end point of the polarisation curve will be at the closest current setting giving a cell voltage of 0.4 V [70]. If higher current density settings than 2.0 A/cm^2 are possible it is recommended to continue recording in 0.2 A/cm^2 steps until a cell voltage of 0.4 V is obtained [70]. The measurements should be conducted in galvanostatic operation.

Similar to the JRC protocols, the Orion stacks manufacturer, Nuvera, performs the polarization curves with the following request of current density, summarized in Table 6.3 and visible in Figure 6.6.

Table 6.3 – Nuvera polarization curve set-points

Current Density [A/cm^2]	*Power [kW]*	*Time Step [min]*
0	0	2
0.017	0.70	1
0.035	1.38	1
0.046	1.83	1
0.069	2.69	1
0.092	3.53	1
0.121	4.58	17
0.242	8.80	15
0.496	17.05	15
0.998	31.73	15
1.5	44.30	15

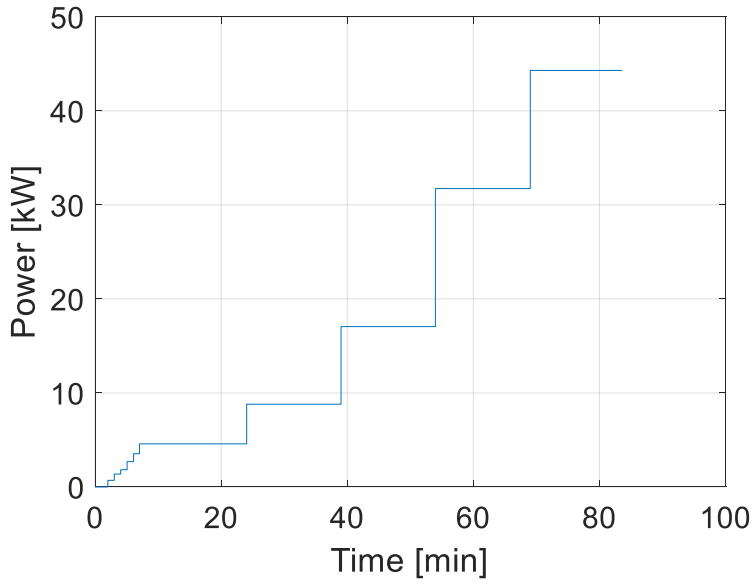

Figure 6.6 – Nuvera Schematic of current density steps

The major difference between JRC procedure and Nuvera procedure is due to the stack temperature utilized by Nuvera: during the load variations a variation in temperature, function of the current, is imposed on the stack. Moreover, Nuvera does not divulge the precise set of temperatures utilized during the factory test to obtain FAT data. Therefore, the temperatures set assumed during the setting procedure of the stack voltage model, exposed in the previous section, refers to the set available in the HI-SEA laboratory, but not necessary the same of the FAT due to different application and experimental configuration of the system.
Thanks to the Nuvera procedures, it is possible to reproduce the characteristic curves of each stack using the HI-SEA laboratory. However, the unfavourable conditions of the stacks and the whole system prevented the exact reproduction of the procedure during the test days considered, namely on 27 and 28 September 2018. Therefore, the characteristic curves obtainable experimentally in the HI-SEA laboratory have a tighter range than Nuvera FAT. In fact, in the test days considered was not possible to reach the nominal potentiality of the system due to different reasons, among which some difficulties in controlling the FCM temperature at increasing current densities and the discontinuity in operativity by the plant: this makes the membrane uneasy to keep to the right humidity conditions. In these days, on average, 7 power steps are set for the tests. They all are set up when the system is in running and each step is kept for 5 minutes.
Figure 6.7 summarizes the stepped load imposed to the stacks of the branch 1, in sequence, to obtain some stable points (in red) to compare with the FAT polarization curves.

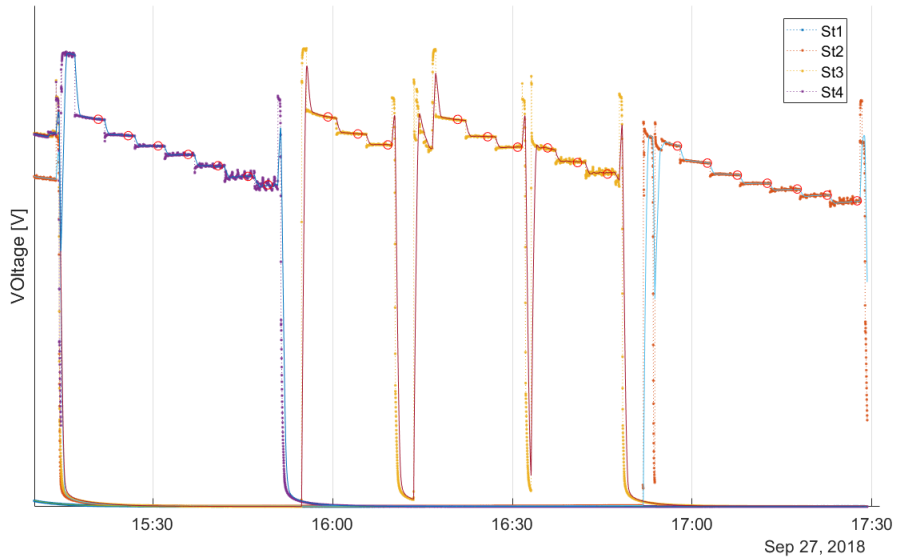

Figure 6.7 – 27/09/2018 test day: branch 1 voltages

Figure 6.8 shows the plot of polarization curves experimentally obtained with the stack 2, compared with its polarization curves supplied by Nuvera. As visible, all the experimental voltages are lower than FAT values and the spread between the maximum and minimum voltages is bigger, symptom of a non-ideal operating condition. The simulated points are obtained with the static model, set in the previous section, and suggests a greater

performance than the experimental one. In fact, the model has been set on the factory curves and the fuel cell, to get closer to those performances, should be in conditions similar to when the FAT tests were carried out. For stack 2 it is very unlikely, especially as a result of the severe damage suffered and described in the Section 5.4.1.

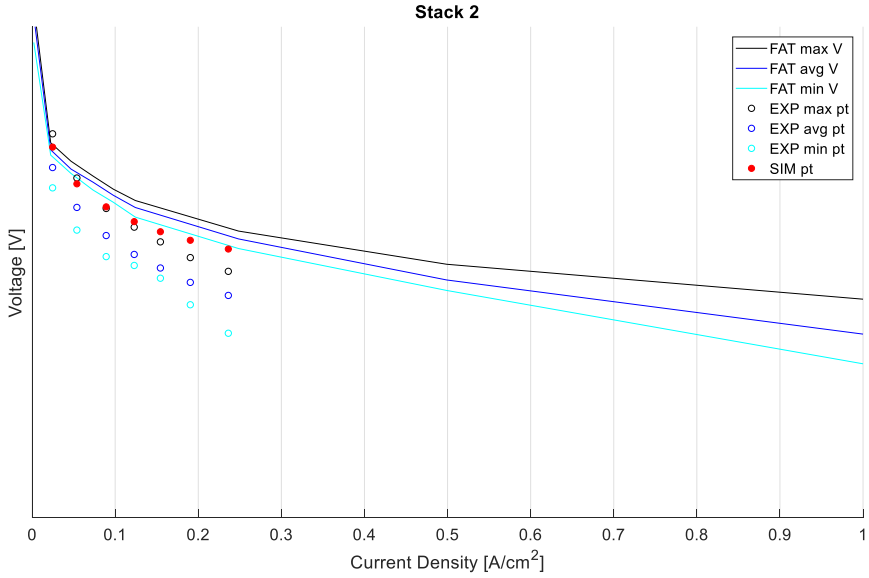

Figure 6.8 – 27/09/2018 test day: stack 2 voltages

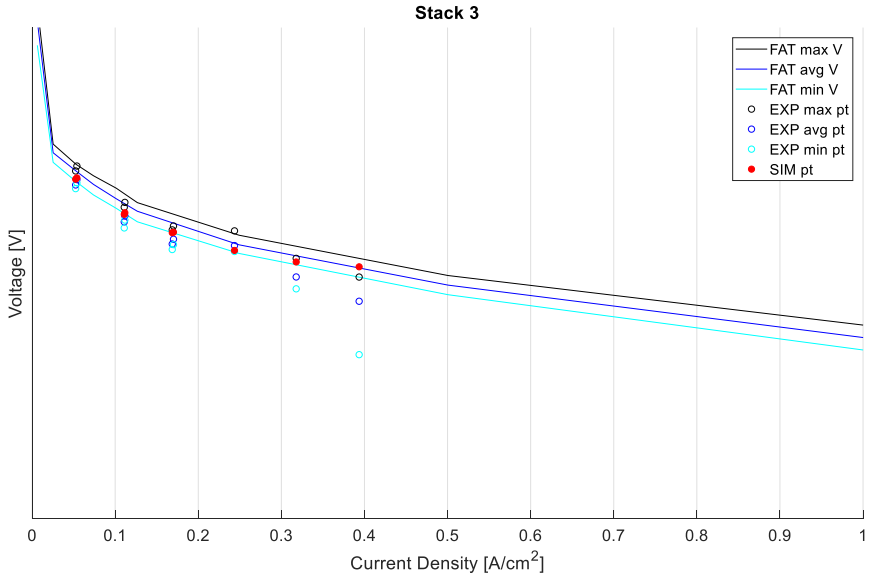

Figure 6.9 – 27/09/2018 test day: stack 3 voltages

Figure 6.9 shows the polarization curves of the stack 3. In this case, the experimental results are closer to the FAT values and the model is able to predict very well the performance of the stack. The problems are evident for current densities higher than 0.3 A/cm^2 when the minimum cell voltage collapses due, most likely, to adverse conditions of membrane humidity and cathode air mass flow oscillations resolved after this day of testing (see Section 5.4.3).

The same considerations apply to the stack 4, whose polarization curves are visible in the Figure 6.10 with the only difference that for this stack the experimental performances are slightly lower than those expected based on the factory data test FAT.

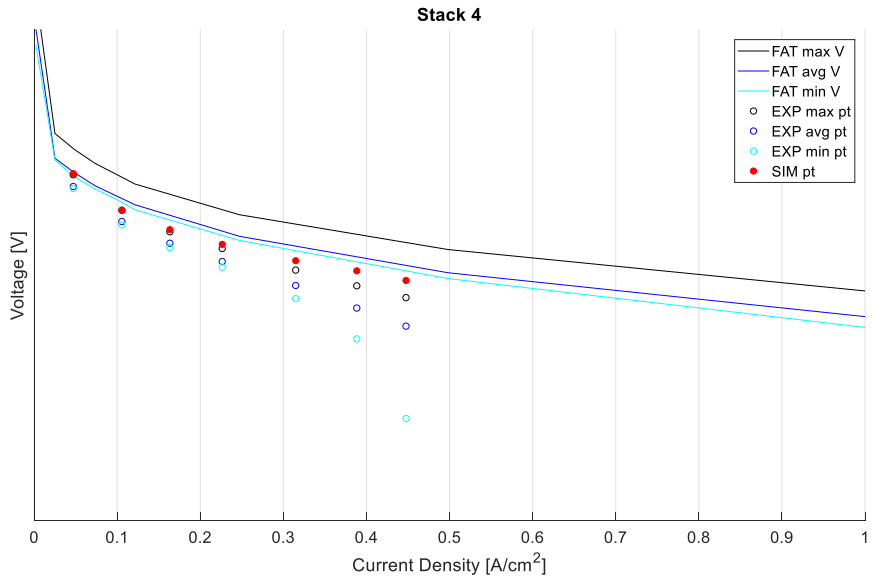

Figure 6.10 – 27/09/2018 test day: stack 4 voltages

Figure 6.11 summarizes the stepped load imposed, the day after, to the stacks of the branch 2, in sequence, to obtain some stable points (in red) to compare with the FAT polarization curves.

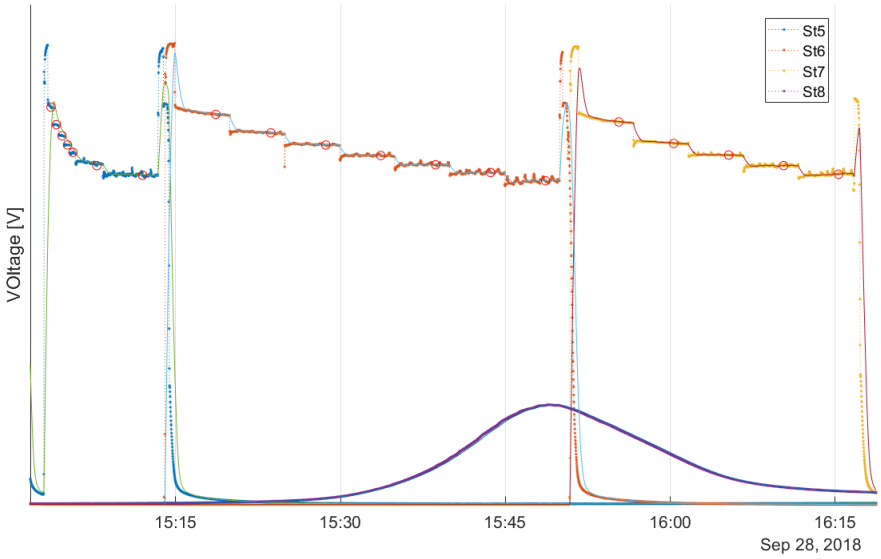

Figure 6.11 – 28/09/2018 test day: branch 2 voltages

Figure 6.12 shows the polarization curves of the stack 5. The experimental results are closer to the FAT values and the model is able to predict pretty well the performance of the stack,

even if the cell voltages suddenly decrease above 0.3 A/cm^2 for the reasons already explained for stacks 3 and 4. However, for stack 5 this phenomenon is less evident.

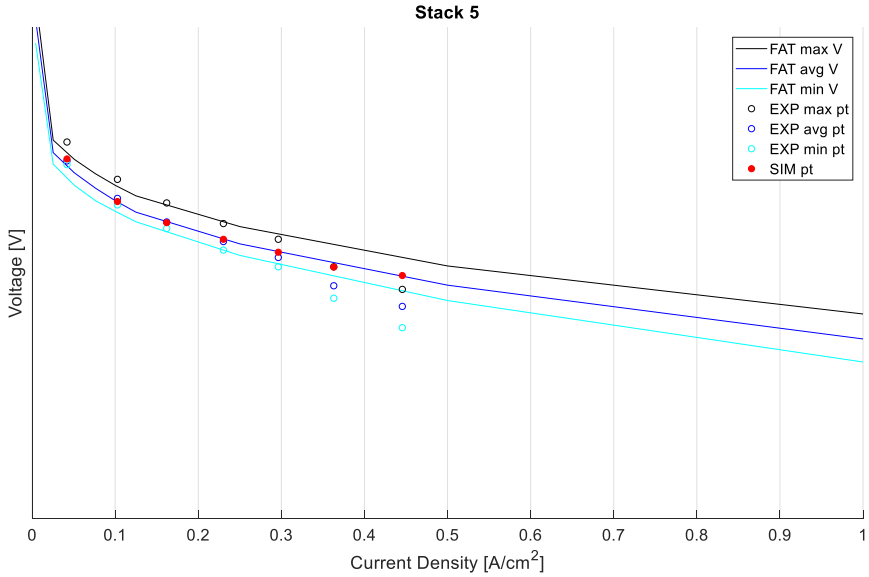

Figure 6.12 – 28/09/2018 test day: stack 5 voltages

In Figure 6.13 the experimental results are lower than the voltages of the polarization curve of the stack 6. The model predicts performance higher than the real one even if the stack does not seem to suffer from the now classic problem of the spread at higher current densities.

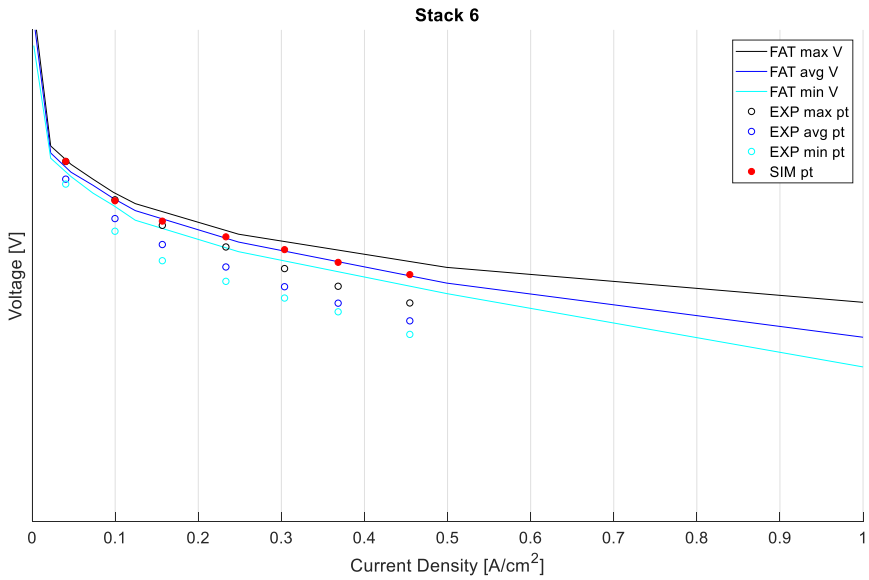

Figure 6.13 – 28/09/2018 test day: stack 6 voltages

At last, Figure 6.14 reports the experimental data of the stack 7, the worst of the branch 2, similar and comparable, in terms of performance, to the stack 2. Also for this stack, the voltage model results are closer to the FAT data than to the experimental values.

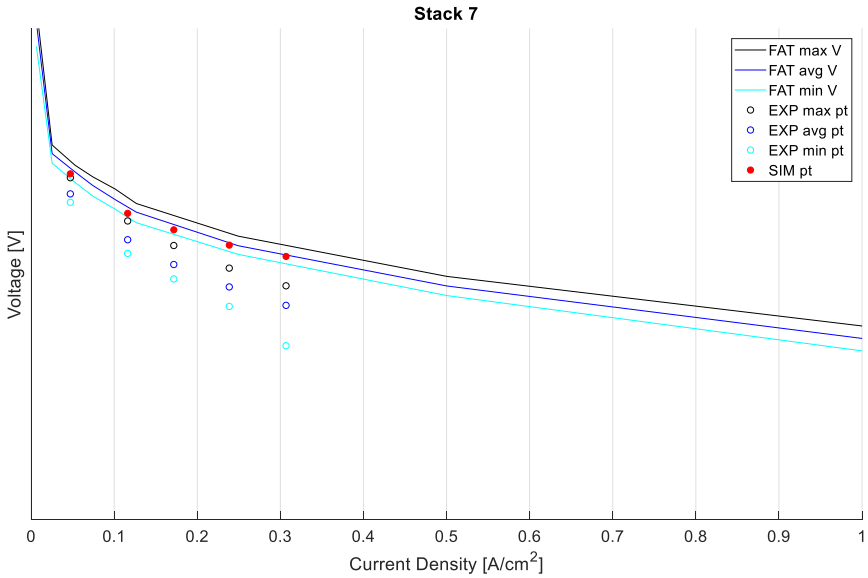

Figure 6.14 – 28/09/2018 test day: stack 7 voltages

6.3 Dynamic Model Development

In this section the HI-SEA dynamic model is presented and described in detail. The HI-SEA model is realized starting from the Matlab-Simulink dynamic sub-models developed in Section 2 and 3. These sub-models are developed to be more detailed and flexible as possible, to better adapt to different PEM-FC stacks and different system configurations.

Nevertheless, the purpose of the HI-SEA dynamic model is quite different as it aims to represent, as better as possible, the performance of the whole PEM-FC system, using the available data concerning the PEM fuel cells and the other BoP components. In particular, the available data coincide with the commercial data usually and easily available on the datasheets of the components and, usually, they are not sufficient for the development of detailed models such as those described in Section 2 and 3. For example, are very difficult to know the dimensions of the anode and cathode channels, the fuel cell active area, details on the polymer membrane used and details on the anode recirculation system. Therefore, if all the necessary geometrical end electrochemical parameters are known is possible to develop a detailed model using the sub-models presented in previous sections, otherwise the approach described below can be used to predict the stack performance with good approximation and using much less parameters.

Figure 6.15 shows the dynamic model developed in Matlab-Simulink environment for the branch 1 (for branch 2 it is completely the same) and allows to understand the system configuration: a cooling circuit with four stacks connected in parallel.

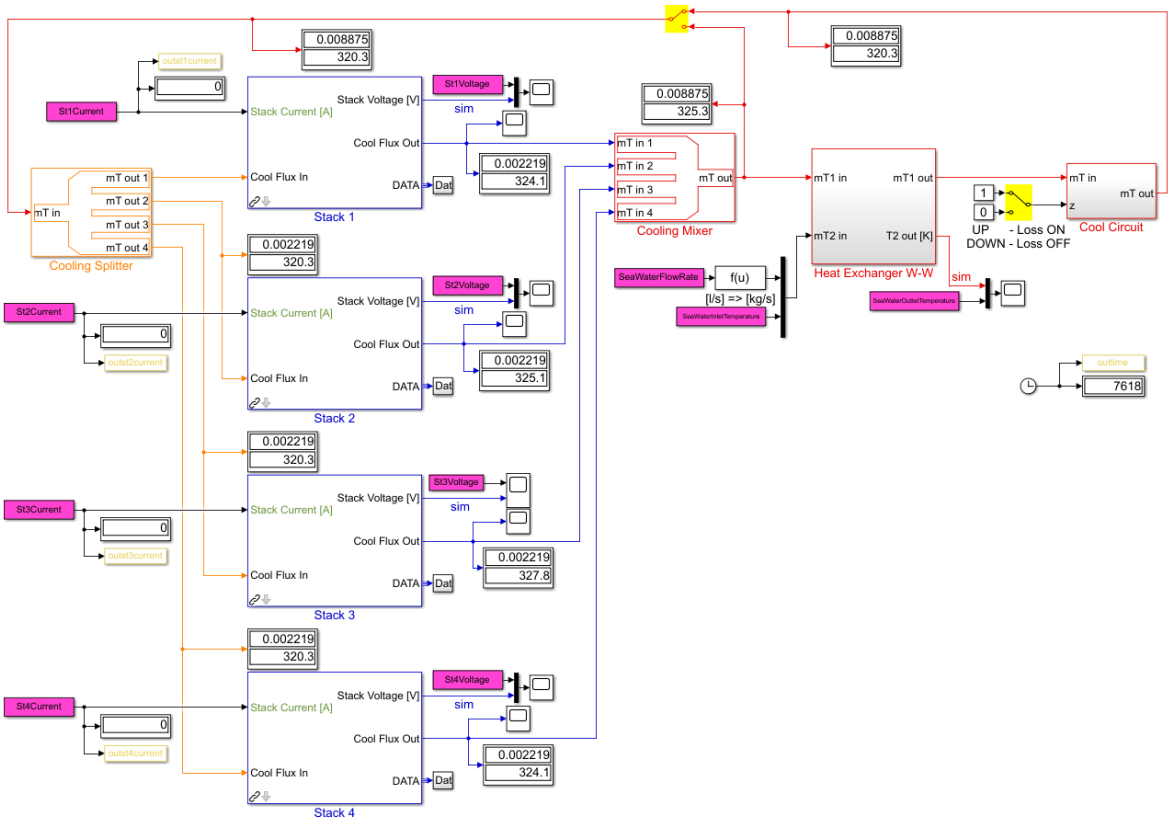

Figure 6.15 – HI-SEA Matlab-Simulink dynamic model

As explained, the lack of data regarding different components like PEM-FC stacks makes some hypotheses necessary. To compensate this lack of detailed information, the use of experimental data has been adopted in the following components:

- Branch current is used instead of a detailed model of the electronic load, not so interesting in the analysis of the system and not so representative of the operation with real loads;
- Branch coolant mass flow instead of a detailed model of the coolant pump, complicated and not of great interest for this first approach;
- External cooling mass flow and temperatures across the heat exchanger as it is not interesting to simulate the external cooling circuit;
- Anode pressure inside each stack due to the difficult to simulate the anode recirculation with no data available (the anode pressure is assumed to be the average of inlet and outlet pressure);
- Cathode inlet pressure, temperature and mass flow instead of a detailed model of the cathode air mass flow controller, used in turn to simulate the performance of different air supply systems and for this reason the modeling of these components by itself is not interesting;

6.3.1 Cooling Pipes Thermal Balance

The cooling circuit of a branch is able to remove the heat produced by the four stacks and dissipate it into the heat exchanger, transferring the heat to the external cooling circuit. To better represent and simulate the real configuration, the cooling circuit is divided into different pipes: the cooling manifold, the heat exchanger, the four small pipes with the heaters placed immediately before the cooling inlet of the stacks and the four cooling circuits inside the stacks. All these pipes are simulated in the same manner using the follow equation with concentrated parameters:

$$\left(m_{cool}^{0} c_{p,cool}\right) \frac{dT_{cool,out}}{dt} = W_{cool} c_{p,cool} \left(T_{cool,in} - T_{cool,out}\right) + Q_{exc} \tag{6.1}$$

$$Q_{exc} = hA\left(T_{ext} - T_{cool,avg}\right) \tag{6.2}$$

where T_{ext} usually corresponds to the ambient temperature and only for the cooling circuit inside the stacks is equal to the stack temperature. For this specific sub-model, the hypothesis is that the coolant can exchange heat only with the solid parts of the stack, and then the ambient dissipation is emulated in the stack thermal balance.
The product hA represents the average surface coefficient of convection related to the heat exchange between the pipes and the ambient air or between the stack and coolant. The approach used is the same as presented in [27] that allows to obtain the convection coefficient by means of experimental tests.

6.3.2 Splitter and Mixer

The splitter is a simple model necessary to divide the coolant mass flow of the collector to the four mass flows of the individual PEM fuel cells. For this simple model the assumption is that the global coolant mass flow is equally divided between the stacks. No direct experimental data are available to demonstrate this hypothesis, but it is reasonable due to the different pipe diameters of the collector and the smaller pipes dedicated to supply coolant to the stacks and to the results of simulations that approximate well the experimental results in terms of stacks coolant temperature. The temperature of the coolant inside this model is constant.
The mixer model, on the other hand, is slightly more complicated. The mass flow at the exit of the mixer is equal to the sum of the inlet mass flows. The outlet temperature of the coolant is calculated by the following equation:

$$T_{cool,out} = \frac{\sum_k \left(W_{k,cool,in} \cdot T_{k,cool,in}\right)}{\sum_k W_{k,cool,in}} \tag{6.3}$$

To make the model more robust and reliable, if the coolant mass flow is equal to zero in some period of the test, a switch allows to calculate the outlet temperature by the average of the inlet temperatures.

6.3.3 Heat Exchanger

To dissipate the excess heat generated by the PEM fuel cell stacks the cooling circuit is equipped with a heat exchanger. This component is able to exchange heat with an external cooling circuit not involved in this model because not interesting.
For the development of the counter-flow exchanger model, the ε-NTU method described by the following equations is used. Note the two coolant mass flows entering the heat exchanger and their c_p it is possible to obtain the performance of the heat exchanger over time.

$$C_1 = W_1 c_{p,1} \ , \ C_2 = \mathrm{W}_2 c_{p,2} \tag{6.4}$$

$$C_{min} = min(C_1 , C_2) \ , \ C_{max} = max(C_1 , C_2) \tag{6.5}$$

$$NTU = UA/C_{min} \tag{6.6}$$

$$C_r = C_{min}/C_{max} \tag{6.7}$$

$$\varepsilon_{HE} = \frac{1 - e^{-NTU(1-C_r)}}{1 - C_r e^{-NTU(1-C_r)}} \tag{6.8}$$

This method assumes the knowledge of the exchange surface A and of the transmittance of the exchanger U. If these parameters are not known, in the Matlab-Simulink model, the possibility of changing the method has been included, in particular providing a fixed and known value of ε_{HE} based on the datasheet of the component or calculated by the experimental data.
The dynamic behaviour of the heat exchanger and the influence of the thermal capacities of the coolant were simulated using the following equations that represent the energy balances of the two sides of the heat exchanger:

$$\left(m_1^0 c_{p,1}\right) \frac{dT_{1,out}}{dt} = \mathrm{W}_1 c_{p,1}\left(T_{1,in} - T_{1,out}\right) - Q_{exc} \tag{6.9}$$

$$\left(m_2^0 c_{p,2}\right) \frac{dT_{2,out}}{dt} = \mathrm{W}_2 c_{p,2}\left(T_{2,in} - T_{2,out}\right) + Q_{exc} \tag{6.10}$$

$$Q_{exc} = C_{min}\left(T_{1,in} - T_{2,in}\right)\varepsilon_{HE} \tag{6.11}$$

Thanks to these equations, known the input quantities such as flow rates and temperatures, it is possible to obtain the two outlet temperatures. The hypotheses inside these equations are to neglect the thermal inertia of the metal of the heat exchanger, small compared to that of the liquid, and also the convective heat exchange towards the ambient, concentrated inside the cooling manifold model (see Section 6.3.1).

6.3.4 PEM-FC Model

The PEM-FC stack model is developed based on the model explained in Section 2 with some important simplifications. The stack voltage model uses the Mert-Mann approach (Section

2.1.5.2) and has been set on the factory data test as explained in Section 6.1. This sub-model represents the static performance of the fuel cell in terms of the polarization curve of the stacks.
The anode flow model is unused due to the unknown parameters of the anode recirculation system. In particular the ejector geometry, the anode channels volume and the orifice dimension of the anode purge are not known and impossible to obtain. For this reason, the experimental anode pressure, calculated as the average of the inlet and outlet pressures, has been decided to use as input value for the stack voltage model that requires the partial pressure of the hydrogen. In details, the formula used to calculate the hydrogen partial pressure is:

$$p_{H_2} = \left(\frac{p_{AN,in} + p_{AN,out}}{2}\right) - p_{sat} \tag{6.12}$$

The assumption is to consider water vapor at the saturation condition inside the stack. Although the hydrogen humidification is absent, the anode recirculation and the presence of water in liquid phase in the anode purge, found during the tests, justify the adoption of this hypothesis. Furthermore, the impossibility of calculating the correct humidity value in the anode channels renders the membrane humidity model unusable.
Also for the cathode flow model is impossible to obtain the cathode volume and the orifice dimension of the cathode outlet manifold. For these reasons, the cathode flow model uses the experimental data regarding the air mass flow and the inlet pressure and temperature. These data are necessary to use a more detailed approach, respect to the anode Equation (6.12), proposed in [71] [72] and summarized by the following equations:

$$U_{f,O_2} = \frac{6000 \cdot R \cdot T_{st} \cdot n_{FC} \cdot i_{st}}{4 \cdot F \cdot p_{CA,in} \cdot W_{CA,in}} \tag{6.13}$$

$$p_{O_2} = \left(1 - U_{f,O_2}\right) \cdot p_{CA,in} \cdot 0.21 \tag{6.14}$$

The PEM fuel cell thermal model used is composed by the stack thermal balance described in Section 2.5 and by the cooling system model presented in Section 3.5.
Finally, the heater model was added to the cooling inlet to better represents the real configuration and obtain precise inlet coolant temperature. The heater model is developed following the approach of the cooling pipes described in Section 6.3.1.

6.4 Dynamic Model Analysis and Results

In this section the HI-SEA dynamic model is set on the characteristic and geometrical parameters of the plant and the model results are compared to the experimental acquired data to validated and analyse the system model.
Referring to the plant layout of the PEM-FC system of Figure 5.6, better comprehensible in the Matlab-Simulink model of Figure 6.15, all the necessary parameters for the dynamic model developed are reported in the following table. As explained in Section 6.3, the dynamic model follows a simplified approach to reduce the number of necessary parameters, especially the geometrical and chemical constants of the PEM-FC components.

Table 6.4 – Parameters for the HI-SEA dynamic model

Symbol	Value	Unit	Description
dt	0.2	s	Time constant of integration
t_m	0.00508	cm	Membrane thickness
λ_m	14	-	Membrane water content
c_{FC}	814	J/(kg·K)	Average heat capacity of the stack
m_{FC}	65	kg	Stack mass
ΔH_c	1.1996·108	J/kg	Hydrogen lower heating value
$h_{FC}A_{ext,FC}$	20	W/K	External convective heat transfer coefficient of the stack
$(hA)_{st,cool}$	1000	W/K	Heat transfer coefficient of the cooling system inside the stack
$h_{ext,pipe}$	10	W/(m^2·K)	External convective heat transfer coefficient of the pipes
$D_{ext,pipe}$	0.1	m	Pipes external diameter
L_{pipe}	6	m	Pipes length
$m_{cool,br}$	32	kg	Total coolant mass inside the branch
$m_{cool,st}$	2	kg	Coolant mass inside the stack
$m_{cool,ht}$	0.5	kg	Coolant mass inside the stack heater
$m_{cool,HE}$	2	kg	Coolant mass inside the heat exchanger
$c_{p,cool}$	4192	J/(kg·K)	Heat capacity of the coolant
ρ_{cool}	1065	kg/m^3	Coolant density
ε_{HE}	0.5	-	Effectiveness of the heat exchanger

The initial conditions for the integrative blocks correspond to the ambient conditions of the test day considered and obtained based on the experimental data.
In the following sub-sections are reported the experimental and model predicted results of the test days 24th April 2018 and 27th September 2018.

6.4.1 Test Day: 24/04/2018

The test performed on 24th April 2018 is summarized in Figure 6.16 where the cooling mass flow, the average temperature of the cooling circuit and the imposed branch current are visible. Three ramps of current are required to different PEM-FC stacks, in order stack 3, 1 and 2. The cooling mass flow in the model is assumed to be the same of the experimental value acquired as the branch current that is the principal input for the stack voltage model. From Figure 6.16 is also visible as the average temperature of the branch cooling circuit is quite well predicted by the Matlab-Simulink model. The major difference is between 4000 and 5000 seconds, due to the shutdown of the cooling pump. In this condition the model suffers more in accuracy due to the change in the physical problem and its representation by the adopted equations.

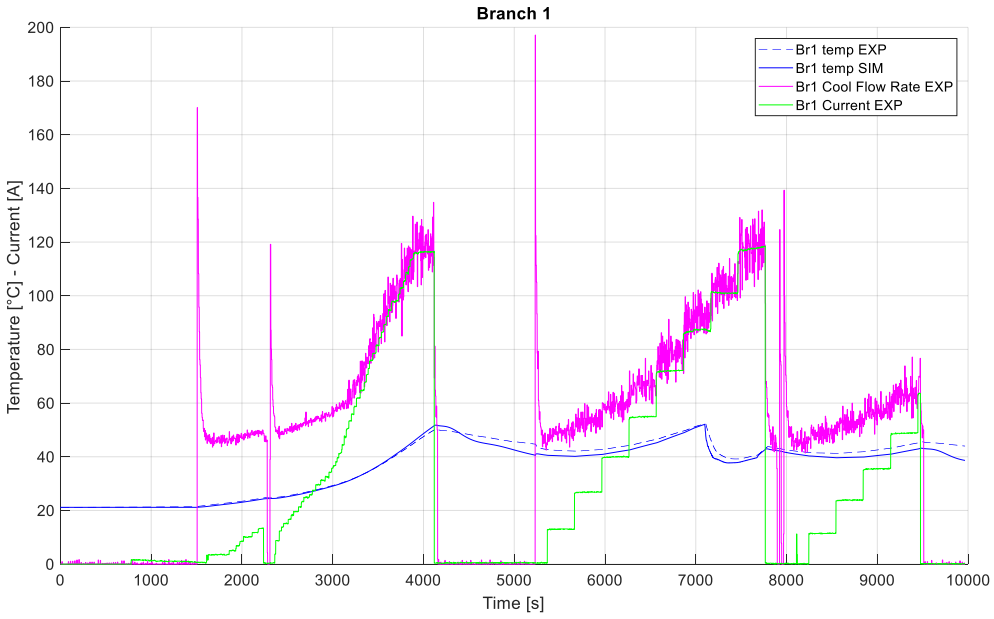

Figure 6.16 – 24/04/2018 test day: Branch 1 data

Figure 6.17 shows the cooling details of the stack 3: the required current and the inlet and outlet cooling temperature that well approximate the experimental data (dotted lines). Moreover, this dynamic model is able to predict the stack temperature, associated with metallic and solid parts of the stack, i.e. the inlet and outlet collectors, the bipolar plates and the MEA, and characterized by a dynamic delay due to the thermal capacity of the stack. As anticipated, when the stack 3 is off the developed model is not able to predict sufficiently well the experimental data, even if the average value of temperature is sufficient for the purposes of these simulations.

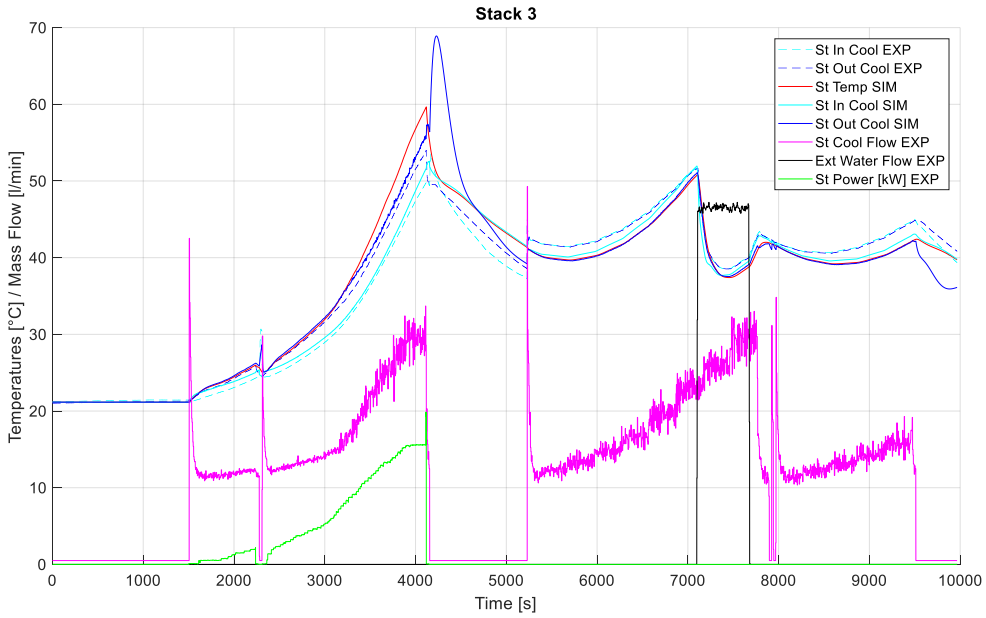

Figure 6.17 – 24/04/2018 test day: Stack 3 cooling data

After the stack 2, the stack 1 starts with a stepped current ramp less linear than the first one, as reported by the green line of the Figure 6.18. Also in this case, the dynamic model is able to correctly predict the inlet and outlet cooling temperature to the stack, reproducing the outlet temperature steps experimentally found. Moreover, after the 7000 seconds, the external cooling circuit is activated, as visible by the black line, and the model approximates very well the heat exchange that reduce the temperatures of the cooling inside the branch.

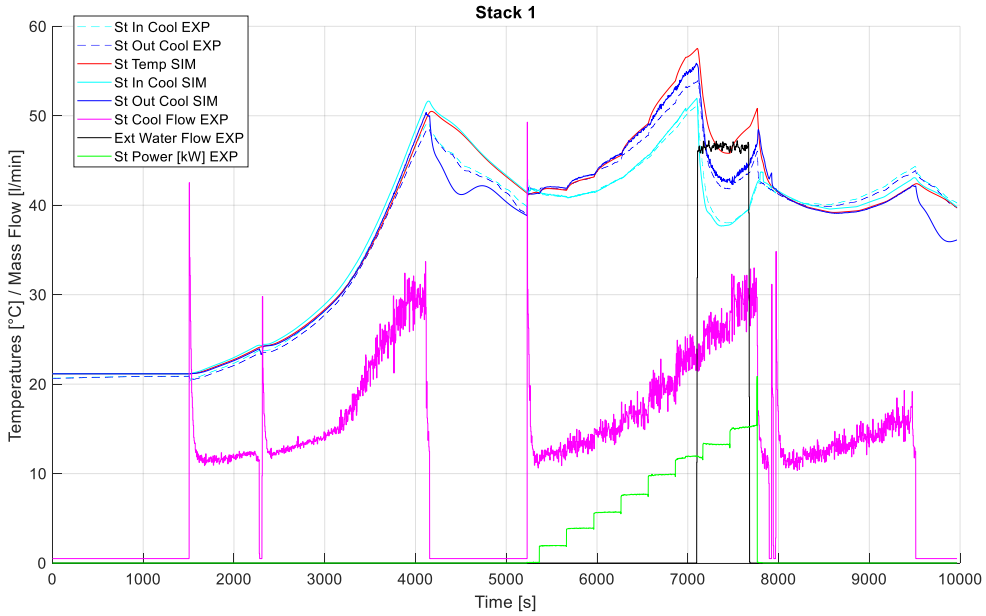

Figure 6.18 – 24/04/2018 test day: Stack 3 cooling data

At the last, the stack 2 starts and realizes a little stepped current ramp, visible in Figure 6.19. In this case the inlet and outlet cooling temperatures, calculated by the dynamic model, do not approximate very well the experimental data, probably due to the accumulation of errors during the simulation time. However, the differences are limited and are part of the measurement error of the two-wire PT100 sensors, unfortunately very inaccurate (about ± 4°C) due to the incorrect adoption of this wiring that does not guarantee good performance for long distances between sensors and PLC, and i.e. for the HI-SEA laboratory.

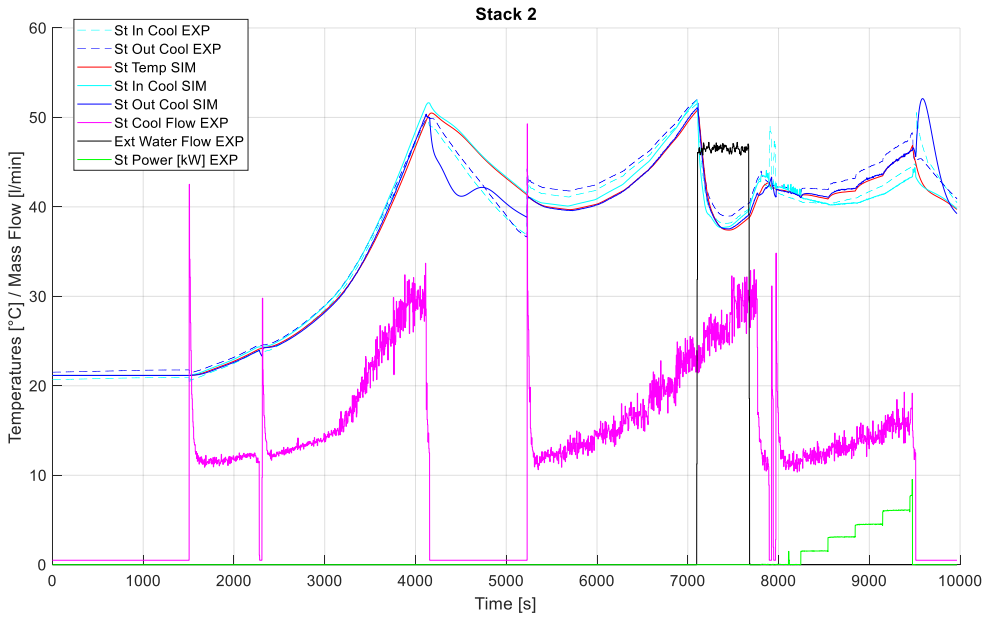

Figure 6.19 – 24/04/2018 test day: Stack 2 cooling data

In Figure 6.20 the electrical data of the stack 3 are reported. In particular, the branch current and the related stack current and above all the stack voltage. These parameters are the most important results of the simulation and it includes all the ability of the Matlab-Simulink model to predict the performances provided by the PEM fuel cell in static and dynamic conditions, especially linked to temperature and pressure transients. The stack voltage, and thus the stack power directly related by Equation (2.50), is well predicted by the model, even if in some transients it differs a little from the experimental data. This deviation is probably due to the not perfect fitting of the stack voltage model to the experimental data, as visible in Figure 6.3, and the sum of the signal errors related to the experimental values utilized inside the model, as the anode and cathode pressures and the cooling mass flow.

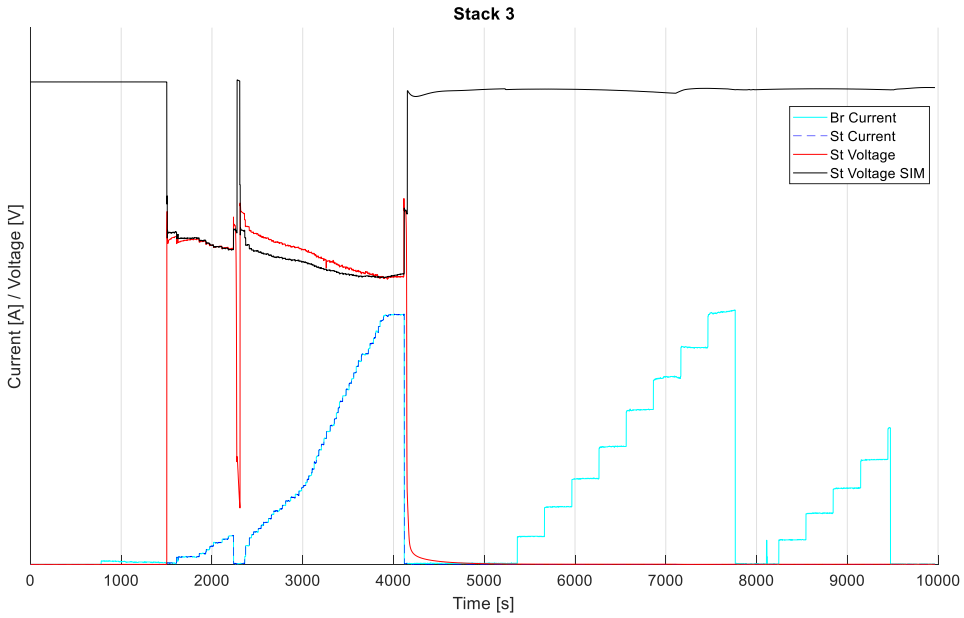

Figure 6.20 – 24/04/2018 test day: Stack 3 electrical data

Figure 6.21 shows the electrical model results of the stack 2: for this load ramp the model predicts very well the voltage provided by the fuel cell and acquired during the experimental test. Note that the biggest difference in terms of stack voltage is when the current to the PEM fuel cell is zero: in these conditions the stack voltage model provides the open circuit voltage while the real system discharge the tension with a dedicated shut-down procedure not implemented in the model at this stage.

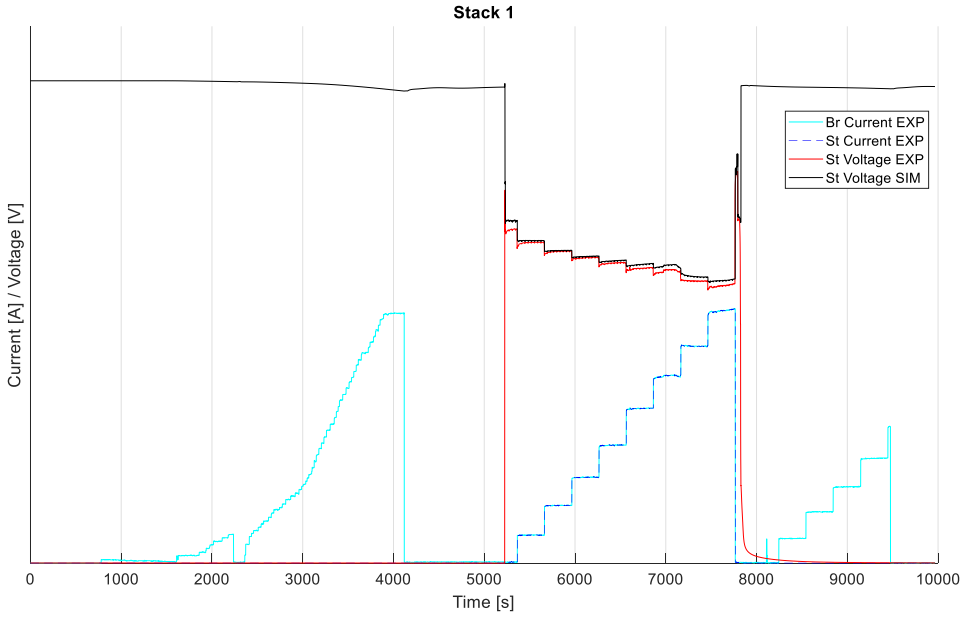

Figure 6.21 – 24/04/2018 test day: Stack 1 electrical data

At last, Figure 6.22 illustrates the performances of the stack 2 during the last load ramp of this test day. The model predicted well the voltage produced by the fuel cell, with some peaks due to real problems occurred during the start-up of this stack. Moreover, the voltage model little differs by the experimental data probably also due to the different condition of this stack respect to the FAT data. In fact, the stack voltage model is set on factory data, as explained in section 6.1 even if this particular system suffered a serious damage, explained in Section 5.4.1, followed by the removal of 16 cells from the stack. The stack voltage model includes this cells reduction in the calculation of the stack voltage, but probably the system performs slightly worse due to a precocious and general deterioration of all the cells due to the serious damage mentioned.

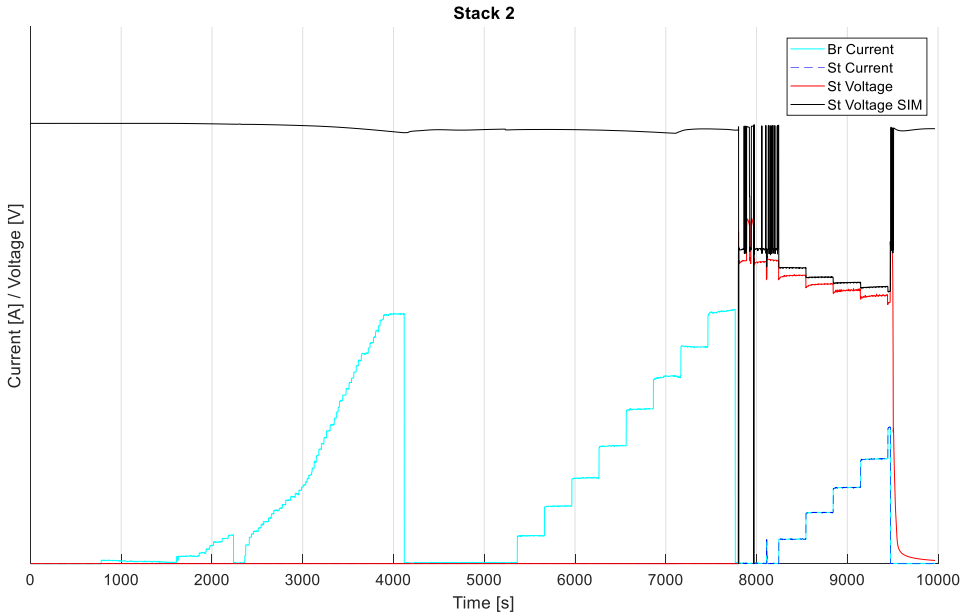

Figure 6.22 – 24/04/2018 test day: Stack 2 electrical data

6.4.2 Test Day: 27/09/2018

Another interesting test day to analyse with the support of the dynamic model developed is on the 27th of September 2018. In this test day the stacks used are the numbers 2, 3 and 4. Figure 6.23 summarized the whole test: different load ramps are imposed to the stacks, with a maximum current in the medium range of what the fuel cells can provide. The average temperature of the branch cooling circuit is well predicted by the Matlab-Simulink model, except in the last phases of the test, where it deviates a little from the experimental data, probably due to the accumulation of the errors during the simulation.

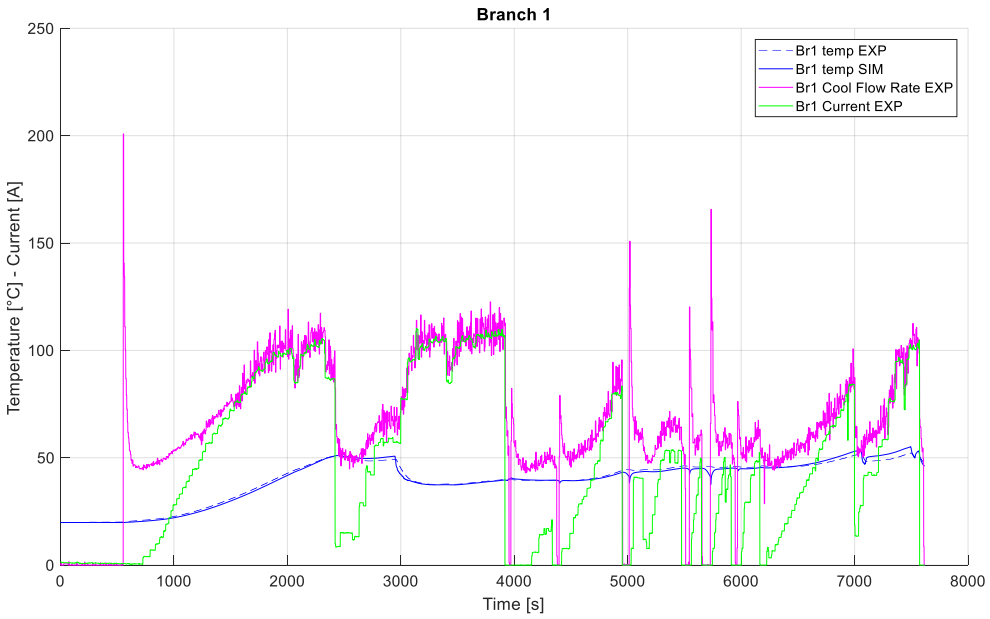

Figure 6.23 – 27/09/2018 test day: Branch 1 data

Figure 6.24 shows the cooling details of the stack 4, the first stack used in the test day. The inlet and outlet cooling temperatures approximate very well the experimental data (dotted lines), also when the external cooling is activated to remove the excess of heat produced by the stack.

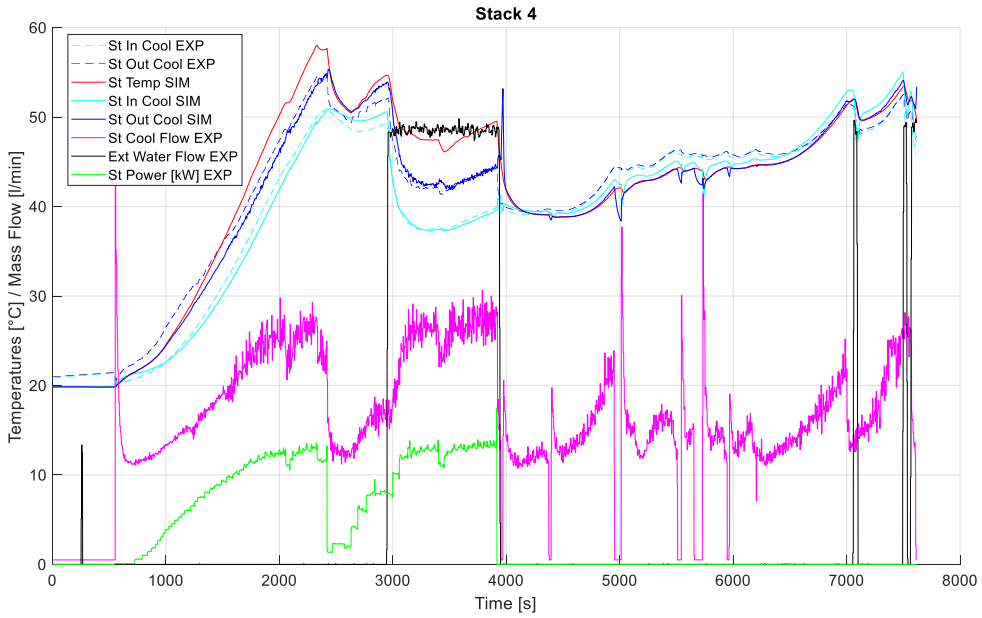

Figure 6.24 – 27/09/2018 test day: Stack 4 cooling data

Figure 6.25 show the cooling parameters of the stack 2, the second system used with many little consecutive load ramps. Many cooling pumps stops are present during these phases of the test, causing mass flow peaks inside the cooling circuit due to the starts of the pump. This phenomenon causes positive peaks in the stack inlet cooling temperature and negative peaks in the outlet cooling temperature. The model predicts these behaviours with an excessive absolute value of the peaks. However, the cooling temperatures are well predicted by the model during the tests related to the stack 2.

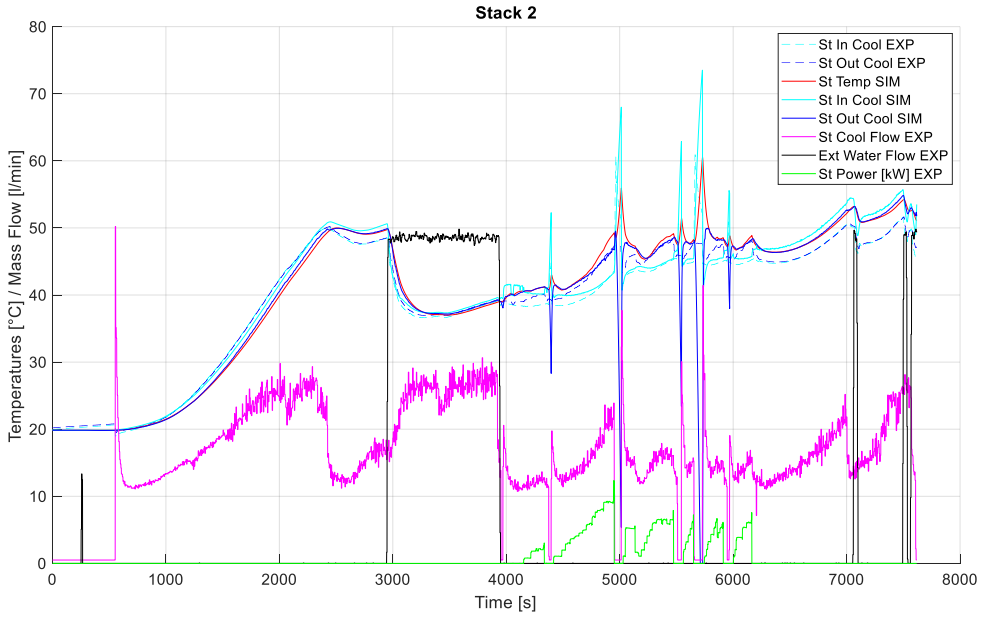

Figure 6.25 – 27/09/2018 test day: Stack 2 cooling data

Figure 6.26 shows the cooling details of the stack 3, the last stack used. This time, the coolant temperatures are not quite well approximate by the dynamic model, as anticipated, due to different starting condition at about 6200 second of the cooling temperature. The differences between model and experimental data increase during the test simulation due to the accumulation of the errors.

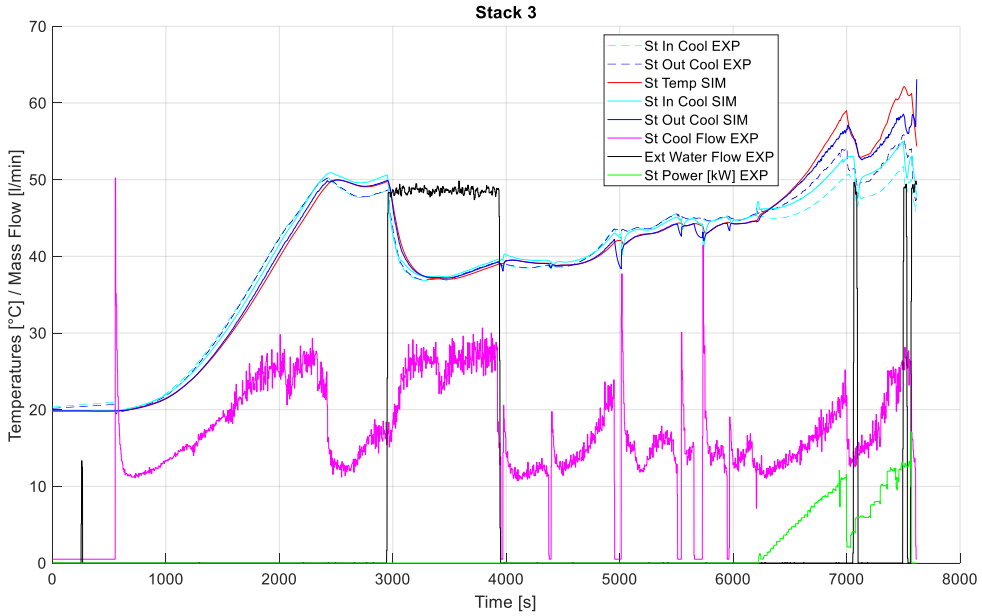

Figure 6.26 – 27/09/2018 test day: Stack 3 cooling data

In Figure 6.27 the electrical data of the stack 4 are reported. The stack voltage, and thus the stack power, is quite well predicted by the dynamic model, even if it progressively moves away with the increase in the current required by the load. This deviation is probably due to the not perfect fitting of the stack voltage model to the experimental data, as visible in Figure 6.3, and the sum of the signal errors related to the experimental values utilized inside the model, as the anode and cathode pressures and the cooling mass flows

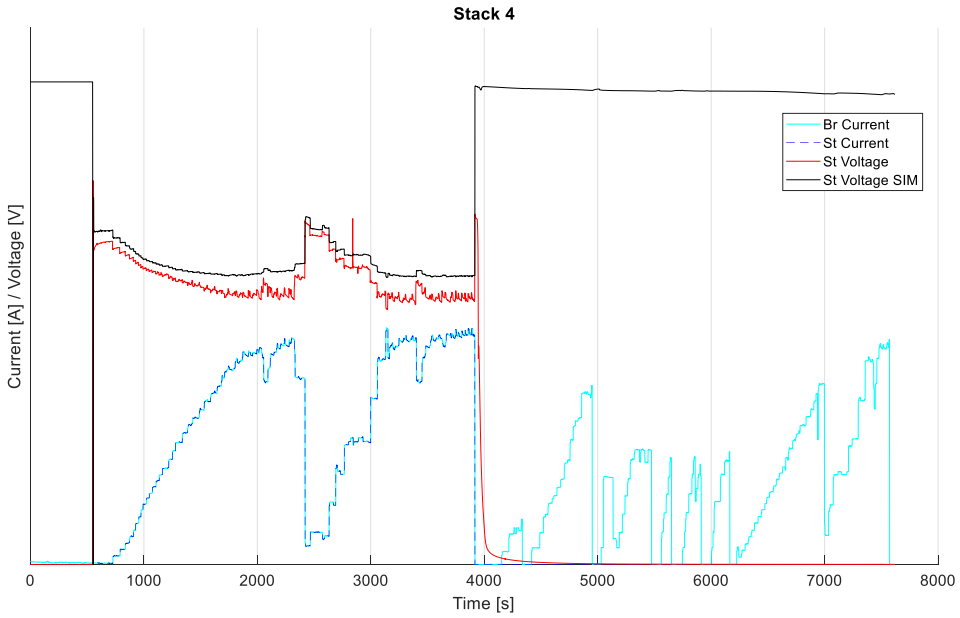

Figure 6.27 – 27/09/2018 test day: Stack 4 electrical data

Figure 6.28 shows the electrical model results of the stack 2: for this series of limited load ramps the model predicts quite well the voltage provided by the fuel cell and acquired during the experimental test. As always, the big difference in terms of stack voltage is when the current to the PEM fuel cell is zero due to the absence of the shut-down procedure in the dynamic model. Moreover, the voltage model little differs by the experimental data probably also due to the different condition of this stack respect to the FAT data, as explained in the previous section.

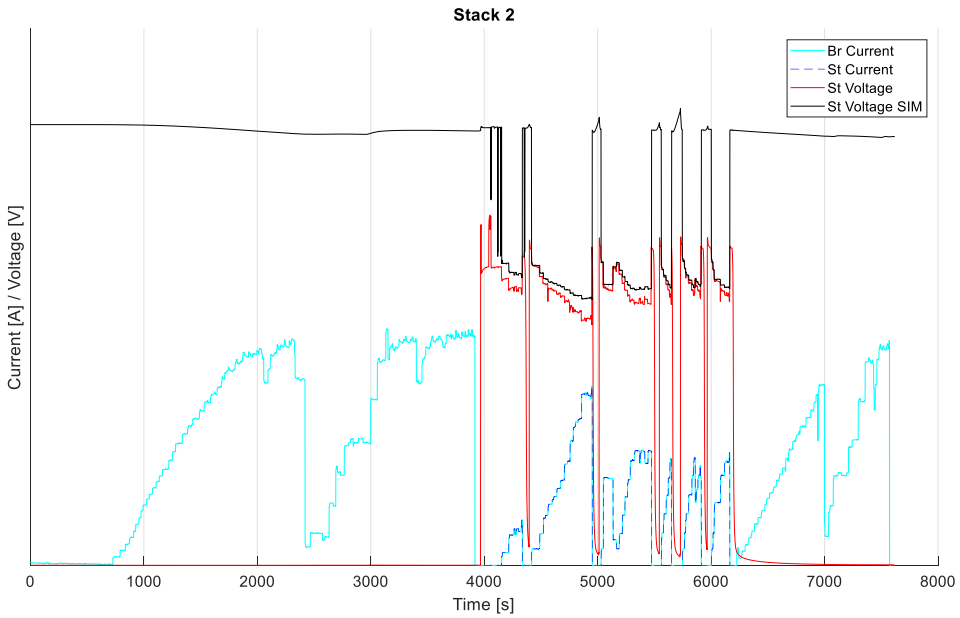

Figure 6.28 – 27/09/2018 test day: Stack 2 electrical data

At last, Figure 6.29 illustrates the performances of the stack 3 during the last two load ramps of this test day. The stack voltage calculated by the dynamic model little differs by the experimental data due to the different temperatures of the coolant calculated by the model during these last load ramps.

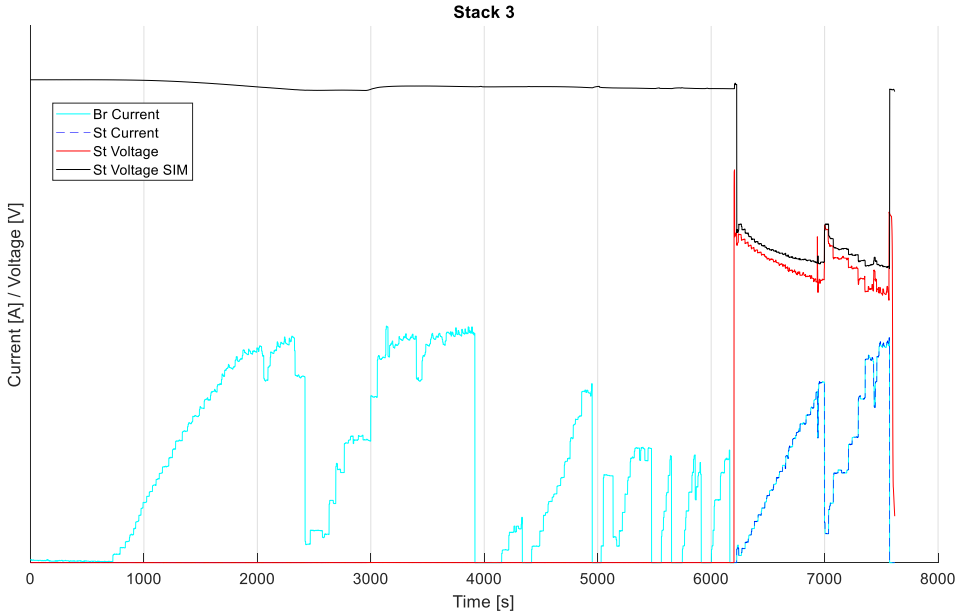

Figure 6.29 – 27/09/2018 test day: Stack 3 electrical data

7 Conclusions

In this thesis a semi-empirical dynamic model of PEM-FC system has been developed, explained and validated against literature and experimental data. The aim to create a generic, flexible and easily adaptable model was achieved mainly thanks to the development of the algorithm which solves the polarization curve fitting problem and considering the development of an easily adaptable air compressor model. A theoretical stack thermal model has been developed and tested and, in general, the approach to realize sub-models allow to easily change the configuration of the system model to better adapt to real PEM-Fc system under investigation. With this approach, in the thesis, two different PEM-FC system models have been developed, studied and validated: a more general and detailed model representing a low power system, validated with experimental literature data, and a more specific and less detailed model representing a large power application, validated with the experimental results obtained in the HI-SEA Joint Laboratory of Fincantieri S.p.A. and the University of Genoa. The first application allows to analyze in particular the membrane hydration model and the stack thermal model, two parts usually modeled in many different ways in literature and difficult to validate. The second application allows to better understand the peculiarities and the problems of a large power PEM-FC application and to validate a simplified system model, quite easy to set-up and able to well predict the electrical and thermal behavior of the stacks.

In general, the major work concerned the development of the fuel cell stack model, with detailed analysis of different theories for the best representation of the polarization curve, the membrane hydration and the stack thermal balance. The electrical results of the PEM-FC system models appear to be good for both the system analyzed, as well as the behavior of air compressor model, the membrane hydration model and the thermal models.

Future developments will concern the realization of sub-models able to simulate the nitrogen diffusion through the membrane and also its diffusion into the gas diffusion layer. Future applications of the model will also consider different PEM fuel cell applications, from mobile to stationary, as well as fuel cell hybrid systems, from FC and batteries systems to metal hydrides thermal coupling.

8 Bibliography

[1] J. B. Heywood, *Internal Combustion Engine Fundamentals*. 1998.

[2] J. T. Pukrushpan, A. G. Stefanopoulou, and H. Peng, *Control of Fuel Cell Power Systems*, vol. 150, no. 1. London: Springer London, 2004.

[3] A. Züttel, "Materials for hydrogen storage," *Mater. Today*, vol. 6, no. 9, pp. 24–33, Sep. 2003.

[4] A. Züttel, "Hydrogen storage methods," *Naturwissenschaften*. 2004.

[5] Förster, "Handbook of Chemistry and Physics," *Zeitschrift fur Phys. Chemie*, 1956.

[6] E. Tzimas, C. Filiou, S. D. Peteves, and J. B. Veyret, "Hydrogen storage: state of the art and future technologies," 2003.

[7] College of the Desert, "Hydrogen Fuel Cell Engines MODULE 1: Hydrogen Properties," 2001.

[8] NETL, "Seventh Edition Fuel Cell Handbook," Pittsburgh, PA, and Morgantown, WV, Nov. 2004.

[9] "Types of Fuel Cells." [Online]. Available: http://www.jobsinfuelcells.com/fctypes.htm.

[10] "PEM Fuel Cells." [Online]. Available: https://physics.nist.gov/MajResFac/NIF/pemFuelCells.html.

[11] J.-H. Jung and S. Ahmed, "Dynamic Model of PEM Fuel Cell Using Real-time Simulation Techniques," *J. Power Electron.*, vol. 10, no. 6, pp. 739–748, 2010.

[12] F. Laurencelle *et al.*, "Characterization of a Ballard MK5-E Proton Exchange Membrane Fuel Cell Stack," *Fuel Cells*, vol. 1, no. 1, pp. 66–71, 2001.

[13] J. T. Pukrushpan, A. G. Stefanopoulou, and H. Peng, "Modeling and control for PEM fuel cell stack system," *American Control Conference, 2002. Proceedings of the 2002*. pp. 3117–3122 vol.4, 2002.

[14] J. C. Amphlett, R. M. Baumert, R. F. Mann, B. A. Peppley, and P. R. Roberge, "Performance Modeling of the Ballard Mark IV Solid Polymer Electrolyte Fuel Cell I. Mechanistic Model Development," *J. Electrochem. Soc.*, vol. 142, no. 1, p. 1, 1995.

[15] J. C. Amphlett, R. M. Baumert, R. F. Mann, B. A. Peppley, and P. R. Roberge, "Performance Modeling of the Ballard Mark IV Solid Polymer Electrolyte Fuel Cell II. Empirical Model Development," *J. Electrochem. Soc.*, vol. 142, no. 1, p. 9, 1995.

[16] A. J. del Real, A. Arce, and C. Bordons, "Development and experimental validation of a PEM fuel cell dynamic model," *J. Power Sources*, vol. 173, no. 1, pp. 310–324, 2007.

[17] C. A. Ramos-Paja, R. Giral, L. Martinez-Salamero, J. Romano, A. Romero, and G. Spagnuolo, "A PEM fuel-cell model featuring oxygen-excess-ratio estimation and power-electronics interaction," *IEEE Trans. Ind. Electron.*, vol. 57, no. 6, pp. 1914–1924, 2010.

[18] J. M. Corrêa, F. A. Farret, L. N. Canha, and M. G. Simoes, "An electrochemical-based fuel-cell model suitable for electrical engineering automation approach," *IEEE Trans. Ind. Electron.*, vol. 51, no. 5, pp. 1103–1112, 2004.

[19] R. Talj, T. Azib, O. Béthoux, G. Remy, C. Marchand, and E. Berthelot, "Parameter analysis of PEM fuel cell hysteresis effects for transient load use," *Eur. Phys. J. Appl. Phys.*, vol. 54, no. 2, p. 23410, 2011.

[20] H. J. Avelar, E. a. a. Coelho, J. R. Camacho, J. B. V. Junior, L. C. Freitas, and M. Wu, "PEM fuel cell dynamic model for electronic circuit simulator," *2009 IEEE Electr. Power Energy Conf.*, pp. 1–6, 2009.

[21] R. F. Mann, J. C. Amphlett, M. a. I. Hooper, H. M. Jensen, B. a. Peppley, and P. R. Roberge, "Development and application of a generalised steady-state electrochemical model for a PEM fuel cell," *J. Power Sources*, vol. 86, no. 1–2, pp. 173–180, 2000.
[22] S. O. Mert, I. Dincer, and Z. Ozcelik, "Exergoeconomic analysis of a vehicular PEM fuel cell system," *J. Power Sources*, vol. 165, no. 1, pp. 244–252, 2007.
[23] T. Springer, T. Zawodzinski, and S. Gottesfeld, "Polymer electrolyte fuel cell model," *J. Electrochem. Soc*, vol. 138, no. 8, pp. 2334–2341, 1991.
[24] T. V. Nguyen and R. E. White, "A Water and Heat Management Model for Proton-Exchange-Membrane Fuel Cells," *J. Electrochem. Soc.*, vol. 140, no. 8, p. 2178, 1993.
[25] T. F. Fuller, "Water and Thermal Management in Solid-Polymer-Electrolyte Fuel Cells," *J. Electrochem. Soc.*, vol. 140, no. 5, p. 1218, 1993.
[26] S. Dutta, S. Shimpalee, and J. W. Van Zee, "Numerical prediction of mass-exchange between cathode and anode channels in a PEM fuel cell," *Int. J. Heat Mass Transf.*, vol. 44, no. 11, pp. 2029–2042, 2001.
[27] J. C. Amphlett, R. F. Mann, B. A. Peppley, P. R. Roberge, and A. Rodrigues, "A model predicting transient responses of proton exchange membrane fuel cells," *Journal of Power Sources*, vol. 61, no. 1–2. pp. 183–188, 1996.
[28] S. Motupally, A. J. Becker, and J. W. Weidner, "Diffusion of Water in Nafion 115 Membranes," *J. Electrochem. Soc.*, vol. 147, no. 9, p. 3171, 2000.
[29] A. A. Kulikovsky, "Quasi-3D Modeling of Water Transport in Polymer Electrolyte Fuel Cells," *J. Electrochem. Soc.*, vol. 150, no. 11, p. A1432, 2003.
[30] H. Wu, P. Berg, and X. Li, "Non-isothermal transient modeling of water transport in PEM fuel cells," *J. Power Sources*, vol. 165, no. 1, pp. 232–243, 2007.
[31] S. Ge, X. Li, B. Yi, and I.-M. Hsing, "Absorption, Desorption, and Transport of Water in Polymer Electrolyte Membranes for Fuel Cells," *J. Electrochem. Soc.*, vol. 152, no. 6, p. A1149, 2005.
[32] S. Ge, B. Yi, and P. Ming, "Experimental Determination of Electro-Osmotic Drag Coefficient in Nafion Membrane for Fuel Cells," *J. Electrochem. Soc.*, vol. 153, no. 8, p. A1443, 2006.
[33] R. Storn and K. V. Price, "Differential Evolution - A Simple and Efficient Heuristic for Global Optimization over Continuous Spaces," *J. Glob. Optim.*, vol. 11, no. 4, pp. 341–359, 1997.
[34] W. Gong, Á. Fialho, and Z. Cai, "Adaptive strategy selection in differential evolution," *Proc. 12th Annu. Conf. Genet. Evol. Comput. - GECCO '10*, no. 1, p. 409, 2010.
[35] W. Gong and Z. Cai, "Parameter optimization of PEMFC model with improved multi-strategy adaptive differential evolution," *Eng. Appl. Artif. Intell.*, vol. 27, pp. 28–40, 2014.
[36] N. Benchouia, A. E. Hadjadj, A. Derghal, L. Khochemane, and B. Mahmah, "Modeling and validation of fuel cell PEMFC," *Rev. des Energies Renouvelables*, vol. 16, pp. 2–365, 2013.
[37] H. Radmanesh, S. Saeid, H. Yazdi, G. B. Gharehpetian, and S. H. Fathi, "Modelling and Simulation of Fuel Cell Dynamics for Electrical Energy Usage of Hercules Airplanes," vol. 2014, 2014.
[38] I. M. M. Saleh, R. Ali, and H. Zhang, "Simplified mathematical model of proton exchange membrane fuel cell based on horizon fuel cell stack," *J. Mod. Power Syst. Clean Energy*, vol. 4, no. 4, pp. 668–679, Oct. 2016.
[39] C. Restrepo, C. Torres, J. Calvente, R. Giral, and R. Leyva, "Simulator of a PEM fuel-cell stack based on a dynamic model," *IECON Proc. (Industrial Electron. Conf.*, pp.

2796–2801, 2009.
[40] F. Musio *et al.*, “PEMFC system simulation in MATLAB-Simulink®environment,” *Int. J. Hydrogen Energy*, vol. 36, no. 13, pp. 8045–8052, 2011.
[41] F. Tiss, R. Chouikh, and A. Guizani, “Dynamic modeling of a PEM fuel cell with temperature effects,” *Int. J. Hydrogen Energy*, vol. 38, no. 20, pp. 8532–8541, 2013.
[42] I. S. Martín, A. Ursúa, and P. Sanchis, “Modelling of PEM fuel cell performance: Steady-state and dynamic experimental validation,” *Energies*, vol. 7, no. 2, pp. 670–700, 2014.
[43] A. L. Dicks and D. A. J. Rand, *Fuel Cell Systems Explained*, Second Ed. Chichester, UK: John Wiley & Sons, Ltd, 2018.
[44] T. Berning, “Three-dimensional computational analysis of transport phenomena in a PEM fuel cell,” University of Victoria, 2002.
[45] “Nafion NR211 and NR212 datasheet.” [Online]. Available: https://www.fuelcellstore.com/spec-sheets/chemours-nafion-211-212-spec-sheet.pdf. [Accessed: 06-Dec-2018].
[46] V. Liso, M. P. Nielsen, S. K. Kær, and H. H. Mortensen, “Thermal modeling and temperature control of a PEM fuel cell system for forklift applications,” *Int. J. Hydrogen Energy*, vol. 39, no. 16, pp. 8410–8420, 2014.
[47] J. Larmine and A. Dicks, *Fuel Cell Systems Explained*. .
[48] J. Kim, “Modeling of Proton Exchange Membrane Fuel Cell Performance with an Empirical Equation,” *J. Electrochem. Soc.*, 1995.
[49] F. Gao, B. Blunier, A. Miraoui, and A. El-Moudni, “Cell layer level generalized dynamic modeling of a PEMFC stack using VHDL-AMS language,” *Int. J. Hydrogen Energy*, vol. 34, no. 13, pp. 5498–5521, 2009.
[50] R. Vetter and J. O. Schumacher, “Free open reference implementation of a two-phase PEM fuel cell,” *Comput. Phys. Commun.*, 2018.
[51] D. Natarajan and T. Van Nguyen, “A Two-Dimensional, Two-Phase, Multicomponent, Transient Model for the Cathode of a Proton Exchange Membrane Fuel Cell Using Conventional Gas Distributors,” *J. Electrochem. Soc.*, vol. 148, no. 12, p. A1324, Dec. 2001.
[52] C. Bao, M. Ouyang, and B. Yi, “Modeling and control of air stream and hydrogen flow with recirculation in a PEM fuel cell system-I. Control-oriented modeling,” *Int. J. Hydrogen Energy*, vol. 31, no. 13, pp. 1879–1896, 2006.
[53] C. Bao, M. Ouyang, and B. Yi, “Modeling and control of air stream and hydrogen flow with recirculation in a PEM fuel cell system-II. Linear and adaptive nonlinear control,” *Int. J. Hydrogen Energy*, vol. 31, no. 13, pp. 1897–1913, 2006.
[54] National Institute of Standards and Technology, “Thermophysical Properties of Fluid Systems.” [Online]. Available: https://webbook.nist.gov/chemistry/fluid/. [Accessed: 30-Oct-2018].
[55] M. Klell, “Storage of Hydrogen in the Pure Form,” in *Handbook of Hydrogen Storage*, Weinheim, Germany: Wiley-VCH Verlag GmbH & Co. KGaA, 2010, pp. 1–37.
[56] J. M. Cunningham, M. A. Hoffman, R. M. Moore, and D. J. Friedman, “Requirements for a Flexible and Realistic Air Supply Model for Incorporation into a Fuel Cell Vehicle (FCV) System Simulation,” *SAE Trans.*, vol. 108, no. 724, pp. 3191–3196, 2011.
[57] P. Moraal and I. Kolmanovsky, “Turbocharger Modeling for Automotive Control Applications,” 1999.
[58] M. P. Boyce, *Gas Turbine Engineering Handbook*. Elsevier, 2012.

[59] J. T. Gravdahl and O. Egeland, *Compressor Surge and Rotating Stall*. London: Springer London, 1999.
[60] J. Panting, K. R. Pullen, and R. F. Martinez-Botas, “Turbocharger motor-generator for improvement of transient performance in an internal combustion engine,” *Proc. Inst. Mech. Eng. Part D J. Automob. Eng.*, vol. 215, no. 3, pp. 369–383, Mar. 2001.
[61] C. H. Lee and J. T. Yang, “Modeling of the Ballard-Mark-V proton exchange membrane fuel cell with power converters for applications in autonomous underwater vehicles,” *J. Power Sources*, 2011.
[62] S. Brynolf, M. Magnusson, E. Fridell, and K. Andersson, “Compliance possibilities for the future ECA regulations through the use of abatement technologies or change of fuels,” *Transp. Res. Part D Transp. Environ.*, vol. 28, pp. 6–18, May 2014.
[63] A. Boudghene Stambouli and E. Traversa, “Fuel cells, an alternative to standard sources of energy,” *Renewable and Sustainable Energy Reviews*, vol. 6, no. 3. Pergamon, pp. 297–306, 01-Sep-2002.
[64] V. Eyring, H. W. Köhler, J. Van Aardenne, and A. Lauer, “Emissions from international shipping: 1. The last 50 years,” *Journal of Geophysical Research D: Atmospheres*, vol. 110, no. 17. pp. 171–182, 2005.
[65] V. Eyring, H. W. Köhler, A. Lauer, and B. Lemper, “Emissions from international shipping: 2. Impact of future technologies on scenarios until 2050,” *Journal of Geophysical Research D: Atmospheres*. 2005.
[66] D. Gerard and L. B. Lave, “Implementing technology-forcing policies: The 1970 Clean Air Act Amendments and the introduction of advanced automotive emissions controls in the United States,” *Technol. Forecast. Soc. Change*, 2005.
[67] L. van Biert, M. Godjevac, K. Visser, and P. V. Aravind, “A review of fuel cell systems for maritime applications,” *Journal of Power Sources*. 2016.
[68] T. Tronstad, H. H. Åstrand, G. P. Haugom, and L. Langfeldt, “Study on the use of Fuel Cells in Shipping,” 2017.
[69] “TESEO Project: High Efficiency Technologies For On-Board Energy And Environmental Sustainability,” 2015.
[70] G. Tsotridis, A. Pilenga, G. De Marco, and T. Malkow, “EU HARMONISED TEST PROTOCOLS FOR PEMFC MEA TESTING IN SINGLE CELL CONFIGURATION FOR AUTOMOTIVE APPLICATIONS,” 2015.
[71] S. M. Njoya, O. Tremblay, and L.-A. Dessaint, “A generic fuel cell model for the simulation of fuel cell vehicles,” in *2009 IEEE Vehicle Power and Propulsion Conference*, 2009, pp. 1722–1729.
[72] S. N. Motapon, O. Tremblay, and L. A. Dessaint, “Development of a generic fuel cell model: application to a fuel cell vehicle simulation,” *Int. J. Power Electron.*, vol. 4, no. 6, p. 505, 2012.

9 Appendix A

In this section is presented the algorithm developed for the fitting process of the stack voltage model parameters against the experimental polarization curves. In order to develop a method more general and flexible as possible, has been chosen to follow the general fitting approach, called Differential Evolution (DE), proposed by Storn and Price in [33]. This is a simple yet powerful, efficient and versatile population-based, direct search algorithm for global numerical optimization.
Recently, several studies [34] [35] have been made to improve and apply this technique to the parameters optimization of proton exchange membrane fuel cell models. Based on these recent studies, the following algorithm is developed and applied to the parameter's optimization process of the Ballard MK5-E PEM fuel cell (see Section 4.1), assuming the Amphlett-Springer approach for the stack voltage model.

The parameters optimization process, as reported in Section 4.1, allows to obtain the activation and ohmic parameters, in particular the four activation parameters ξ_i of Equation (2.20) and the membrane water content λ_m that is the ohmic parameters, considering the assumption explained in Section 4.1.
First, is necessary to implement into the algorithm the PEM fuel cell parameters known, reported in the following Matlab code.

```
%% ====================== Ballard MK5-E parameters ======================
CellActiveArea = 232;       %[cm^2]
MembraneThickness = 0.0178; %[cm]
Faraday = 96485;            %[C/mol] Faraday's constant
R = 8.3145;                 %[J/(mol*K)] Universal gas constant
p_AN = 3*1.01325e5;         %[Pa]
p_H2 = p_AN;                %[Pa]
p_CAT = 3*1.01325e5;        %[Pa]
n = 8;                      %[cm^2/A]
```

Then, is necessary to calculate the saturation pressures at the temperatures of the polarization curves available, using the saturation equations presented in Section 1.1. In the following part of the Matlab code are also reported current, current density and voltage vectors that represent the experimental points of the polarization curves shown in Figure 4.1.

```
%% ======================== Saturation pressures ========================
T_297 = 297;    %[K]
p_sat_H2O_297 = 6.724136297056386e-07*T_297^4-7.275490810279587e-
04*T_297^3+2.969881912941677e-01*T_297^2-
5.416844321033899e+01*T_297+3.722403620916549e+03;
p_sat_H2O_297 = p_sat_H2O_297*1000;     %[kPa] => [pa]
T_304 = 304;    %[K]
p_sat_H2O_304 = ...

%% ==================== Polarization curves from [12]
====================
% ----------------- Polarization curve at 24°C => 297 K -----------------
```

```
J_297 = [85.0242 108.213 129.469 150.725 171.981 193.237 214.493 237.681
258.937 280.193 301.449 322.705 343.961 365.217 388.406 409.662 430.918
452.174 473.43];
J_297 = J_297/1000;
I_297 = J_297.*CellActiveArea;
V_297 = [0.81954 0.801149 0.782759 0.768966 0.750575 0.741379 0.725287
0.713793 0.702299 0.688506 0.674713 0.658621 0.654023 0.635632 0.624138
0.612644 0.591954 0.568966 0.557471];
% ----------------- Polarization curve at 31°C => 304 K -----------------
J_304 = [86.9565 108.213 129.469 150.725 171.981 193.237 214.493 235.749
258.937 280.193 301.449 324.638 343.961 367.15 388.406 409.662 432.85
454.106 475.362];
J_304 = J_304/1000;
I_304 = J_304.*CellActiveArea;
V_304 = [0.847126 0.833333 0.814943 0.803448 0.789655 0.778161 0.766667
0.750575 0.736782 0.725287 0.713793 0.7 0.688506 0.677011 0.663218
0.649425 0.633333 0.621839 0.608046];
% ----------------- Polarization curve at 39°C => 312 K -----------------
J_312 = [83.0918 108.213 129.469 150.725 171.981 195.169 214.493 237.681
258.937 280.193 301.449 324.638 343.961 367.15 388.406 409.662 430.918
452.174 475.362 496.618 517.874 539.13 562.319 583.575 604.831];
J_312 = J_312./1000;
I_312 = J_312.*CellActiveArea;
V_312 = [0.851724 0.837931 0.824138 0.808046 0.798851 0.789655 0.773563
0.766667 0.752874 0.745977 0.732184 0.725287 0.713793 0.704598 0.693103
0.67931 0.667816 0.658621 0.651724 0.644828 0.642529 0.631034 0.61954
0.603448 0.591954];
% ----------------- Polarization curve at 56°C => 329 K -----------------
J_329 = [110.145 129.469 150.725 173.913 216.425 237.681 260.87 282.126
303.382 324.638 345.894 367.15 388.406 409.662 432.85 454.106 475.362
496.618 519.807 541.063 560.386 581.643 604.831 626.087 647.343 670.531
691.787];
J_329 = J_329/1000;
I_329 = J_329.*CellActiveArea;
V_329 = [0.854023 0.842529 0.833333 0.821839 0.801149 0.789655 0.782759
0.775862 0.764368 0.752874 0.745977 0.741379 0.732184 0.725287 0.713793
0.702299 0.695402 0.686207 0.681609 0.674713 0.670115 0.66092 0.647126
0.64023 0.635632 0.624138 0.612644];
% ----------------- Polarization curve at 72°C => 345 K -----------------
J_345 = [86.9565 108.213 129.469 152.657 173.913 195.169 216.425 237.681
260.87 282.126 303.382 324.638 345.894 367.15 390.338 411.594 432.85
454.106 475.362 519.807 541.063 562.319 583.575 628.019 649.275 670.531
691.787];
J_345 = J_345./1000;
I_345 = J_345.*CellActiveArea;
V_345 = [0.877011 0.863218 0.851724 0.842529 0.833333 0.824138 0.812644
0.808046 0.798851 0.791954 0.787356 0.778161 0.771264 0.764368 0.757471
0.750575 0.741379 0.734483 0.729885 0.72069 0.713793 0.706897 0.7
0.683908 0.67931 0.672414 0.66092];
```

Now is important to calculate all the possible parameters before entering in the algorithm loop, to make the code execution as fast as possible. As explained in Section 4.1, for this specific application, the concentration parameters m_{conc} and n_{conc} are known and it is possible to implement them into the algorithm. Therefore, it is possible to calculate for each temperature of the polarization curves available, the concentration loss using Equation (2.45), the oxygen partial pressure at the liquid/gas interface using Equation (2.26) and thus the

oxygen concentration at the interface using Equation (2.25). Furthermore, it is possible to calculate the Nernst potential with the Equation (2.11).

```
%% ================ Preliminary cell voltage calculation ================
% ------- Preliminary calculation for polarization curve at 297 K -------
p_H2O_CAT_297 = p_sat_H2O_297;  %[Pa]
x_H2O_CAT_297 = p_H2O_CAT_297/p_CAT;
p_O2_297= (p_CAT-p_H2O_CAT_297)*0.21;
m_297 = 1.1e-4-(1.2e-6*(T_297-273));
for p=1:length(J_297)
    p_O2_star_297(p) = (p_H2O_CAT_297*1e-
5/1.01325)*((1/(exp(4.192*J_297(p)/(T_297^1.334))*x_H2O_CAT_297))-1);
    c_O2_297(p) = p_O2_star_297(p)/(5.08e6*exp(-498/T_297));
    eta_conc_297(p) = m_297*exp(n*J_297(p));
end
E_297 = 1.229-8.5e-4*(T_297-298.15)+4.308e-5*T_297*(log(p_H2*1e-
5/1.01325)+0.5*log(p_O2_297*1e-5/1.01325));
% ------- Preliminary calculation for polarization curve at 304 K -------
p_H2O_CAT_304 = ...
```

Then, the two parameters characteristic of the logic of the DE algorithm are defined. Gong et al. in [34] recommended to use a crossover rate CR equal to 0.9 and mutation scaling factor F equal to 0.5. Now, before entering in the algorithm, the initial population of the unknown parameters must be defined. In this application, the vectors of the four activation parameters ξ_i and the membrane water content λ_m are the unknown parameters. For a more stable and fast calculation process, a narrow range of variation for the parameters is considered, knowing from literature the possible values for the Ballard MK5-E PEM fuel cell. The parameters vectors length L (recommended by Gong et al. in [34] at maximum equal to 100) and the number of unknown parameters D are also defined. Finally, the matrix of the initial population of the parameters is generated from the parameter's vectors. Even if the concentration parameters are known from [12], the code lines necessary to initialize the calculation of the concentration parameters are visible as note lines.

```
%% ==================== Parameters for DE Algorithm ====================
F = 0.5;
CR = 0.9;
% Generation of the initial population of the parameters: uniform
% distribution and each parameter must have the same number of data.
Csi_1_min = 0.8;  Csi_1_max = 1.2;  Csi_1 = Csi_1_min:4e-3:Csi_1_max;
Csi_2_min = 2e-3; Csi_2_max = 4e-3; Csi_2 = Csi_2_min:2e-5:Csi_2_max;
Csi_3_min = 4e-5; Csi_3_max = 1e-4; Csi_3 = Csi_3_min:6e-7:Csi_3_max;
Csi_4_min = 1e-4; Csi_4_max = 2e-4; Csi_4 = Csi_4_min:1e-6:Csi_4_max;
lambda_min = 4;   lambda_max = 12;  lambda = lambda_min:8e-2:lambda_max;
% m_min = 0;          m_max = 1e-4;       m = m_min:2.5e-7:m_max;
% n_min = 0;          n_max = 0.2;        n = n_min:5e-4:n_max;
L = length(Csi_1);
D = 5;                  % Number of parameters
for i=1:L
    X(i,1)=Csi_1(i);    % i-th vector of the initial population
    X(i,2)=Csi_2(i);
    X(i,3)=Csi_3(i);
    X(i,4)=Csi_4(i);
```

```
    X(i,5)=lambda(i);
%     X(i,6)=m(i);
%     X(i,7)=n(i);
end
```

The reference studies in [33], [34] and [35] provide different logics for random calculation of the trial vector. The trial vector is obtained starting from the calculation of mutant vector V, followed by the control of the parameters range. We use the rand-to-best mutant vector strategy presented in [34].
During an iteration, the results in terms of cell voltage, provided by the trial vector, must be compared to the real cell voltage of the polarization curves. Therefore, the comparison has to be done in correspondence with the experimental values of current density available from each polarization curve. The logic developed to compare the real cell voltage and the trial cell voltage is a kind of standard deviation. The difference between these two values of cell voltage is squared and summed to calculate the DistanceSum for each temperature of the polarization curves. With DistanceSum, the respective values of Sigma are calculated by the square root of DistanceSum divided by the number of the points of the corresponding polarization curve. At last, with a weighted sum of the values of sigma, the average sigma is calculated, to compare with the limit of average sigma. This limit has to be initialized, even if the algorithm replaces its value with the median of the current AverageSigma vector, during each iteration and only if the minimum value of AverageSigma is lower than the limit. The limit of the average sigma is used to replace a trial value into the population when its average sigma is less than the limit. The weights of the sigma values are used to give greater importance, and thus obtain greater precision, to the polarization curves around the nominal polarization curve, normally between 60°C and 80°C.

```
% ------------------ Others initialization parameters -------------------
LimAverageSigma = 0.01;
WeightSigma_345 = 6;
WeighSigma_329 = 3;
WeighSigma_312 = 1;
WeighSigma_304 = 1;
WeighSigma_297 = 1;
count = 1;      %Counter of the generations
stop = 0;       %If stop=1 the algorithm ends
gen_max = 4000; %Maximum number of generations
best = 50;      %First best-value taken in the centre of the param range
a=0; b=0; %Control parameters for the number of trial vector replacements

%% ============================== Algorithm ================================
while stop==0
    for i=1:L-1
        r_1=randi(L-1,1);    %randi provides a random integer between 1
and L-1
        r_2=randi(L-1,1);
        r_3=randi(L-1,1);
        while r_1==i
            r_1=randi(L-1,1);
        end
        while r_2==i || r_2==r_1
```

```
            r_2=randi(L-1,1);
        end
        while r_3==i || r_3==r_2 || r_3==r_1
            r_3=randi(L-1,1);
        end
        V(i,1) = X(r_1,1)+F*(X(best,1)-X(r_1,1))+F*(X(r_2,1)-X(r_3,1));
% Mutant vector V  "rand-to-best" from paper 2010
        V(i,2) = X(r_1,2)+F*(X(best,2)-X(r_1,2))+F*(X(r_2,2)-X(r_3,2));
        V(i,3) = X(r_1,3)+F*(X(best,3)-X(r_1,3))+F*(X(r_2,3)-X(r_3,3));
        V(i,4) = X(r_1,4)+F*(X(best,4)-X(r_1,4))+F*(X(r_2,4)-X(r_3,4));
        V(i,5) = X(r_1,5)+F*(X(best,5)-X(r_1,5))+F*(X(r_2,5)-X(r_3,5));
%         V(i,1) = X(r_1,1)+F*(X(r_2,1)-X(r_3,1));    % Mutant vector V
"rand-to-best" from paper 2010
%         V(i,2) = X(r_1,2)+F*(X(r_2,2)-X(r_3,2));
%         V(i,3) = X(r_1,3)+F*(X(r_2,3)-X(r_3,3));
%         V(i,4) = X(r_1,4)+F*(X(r_2,4)-X(r_3,4));
%         V(i,5) = X(r_1,5)+F*(X(r_2,5)-X(r_3,5));
        j_rand = randi(D,1);
        for j=1:D
            if rand(1)<CR || j==j_rand
                if j==1
                    if V(i,j)>Csi_1_min && V(i,j)<Csi_1_max
                        trial(j)=V(i,j);    %Crossover
                    end
                elseif j==2
                    if V(i,j)>Csi_2_min && V(i,j)<Csi_2_max
                        trial(j)=V(i,j);
                    end
                elseif j==3
                    if V(i,j)>Csi_3_min && V(i,j)<Csi_3_max
                        trial(j)=V(i,j);
                    end
                elseif j==4
                    if V(i,j)>Csi_4_min && V(i,j)<Csi_4_max
                        trial(j)=V(i,j);
                    end
                elseif j==5
                    if V(i,j)>lambda_min && V(i,j)<lambda_max
                        trial(j)=V(i,j);
                    end
%                   elseif k==6
%                       if V(i,k)>m_min && V(i,k)<m_max
%                           trial(k)=V(i,k);
%                       end
%                   elseif k==7
%                       if V(i,k)>n_min && V(i,k)<n_max
%                           trial(k)=V(i,k);
%                       end
%                   else
%                       trial(k)=V(i,k);
                end
            else
                trial(j)=X(i,j);
            end
        end
        DistanceSum_297=0;
        Sigma_m_297 = (0.005139*trial(5)-0.00326)*exp(1268*(1/303-
1/T_297));
        for p=1:length(I_297)
```

```
            eta_act_297(p) = -
trial(1)+(trial(2)*T_297)+(trial(3)*T_297*log(c_O2_297(p)))-
(trial(4)*T_297*log(I_297(p)));
            eta_ohm_297(p) = J_297(p)*MembraneThickness/Sigma_m_297;
%             eta_conc_297(p) = trial(6)*exp(I_297(p)*trial(7));
            CellVoltage_297(p) = E_297+eta_act_297(p)-eta_ohm_297(p)-
eta_conc_297(p);
            DistanceSum_297 = DistanceSum_297+(CellVoltage_297(p)-
V_297(p))^2;
        end
        DistanceSum_304=0;
        Sigma_m_304 = (0.005139*trial(5)-0.00326)*exp(1268*(1/303-
1/T_304));
        for p=1:length(I_304)
            eta_act_304(p) = -
trial(1)+(trial(2)*T_304)+(trial(3)*T_304*log(c_O2_304(p)))-
(trial(4)*T_304*log(I_304(p)));
            eta_ohm_304(p) = J_304(p)*MembraneThickness/Sigma_m_304;
%             eta_conc_304(p) = trial(6)*exp(I_304(p)*trial(7));
            CellVoltage_304(p) = E_304+eta_act_304(p)-eta_ohm_304(p)-
eta_conc_304(p);
            DistanceSum_304 = DistanceSum_304+(CellVoltage_304(p)-
V_304(p))^2;
        end
        DistanceSum_312=0;
        Sigma_m_312 = (0.005139*trial(5)-0.00326)*exp(1268*(1/303-
1/T_312));
        for p=1:length(I_312)
            eta_act_312(p) = -
trial(1)+(trial(2)*T_312)+(trial(3)*T_312*log(c_O2_312(p)))-
(trial(4)*T_312*log(I_312(p)));
            eta_ohm_312(p) = J_312(p)*MembraneThickness/Sigma_m_312;
%             eta_conc_312(p) = trial(6)*exp(I_312(p)*trial(7));
            CellVoltage_312(p) = E_312+eta_act_312(p)-eta_ohm_312(p)-
eta_conc_312(p);
            DistanceSum_312 = DistanceSum_312+(CellVoltage_312(p)-
V_312(p))^2;
        end
        DistanceSum_329=0;
        Sigma_m_329 = (0.005139*trial(5)-0.00326)*exp(1268*(1/303-
1/T_329));
        for p=1:length(I_329)
            eta_act_329(p) = -
trial(1)+(trial(2)*T_329)+(trial(3)*T_329*log(c_O2_329(p)))-
(trial(4)*T_329*log(I_329(p)));
            eta_ohm_329(p) = J_329(p)*MembraneThickness/Sigma_m_329;
%             eta_conc_329(p) = trial(6)*exp(I_329(p)*trial(7));
            CellVoltage_329(p) = E_329+eta_act_329(p)-eta_ohm_329(p)-
eta_conc_329(p);
            DistanceSum_329 = DistanceSum_329+(CellVoltage_329(p)-
V_329(p))^2;
        end
        DistanceSum_345=0;
        Sigma_m_345 = (0.005139*trial(5)-0.00326)*exp(1268*(1/303-
1/T_345));
        for p=1:length(I_345)
            eta_act_345(p) = -
trial(1)+(trial(2)*T_345)+(trial(3)*T_345*log(c_O2_345(p)))-
(trial(4)*T_345*log(I_345(p)));
```

```
            eta_ohm_345(p) = J_345(p)*MembraneThickness/Sigma_m_345;
%             eta_conc_345(p) = trial(6)*exp(I_345(p)*trial(7));
            CellVoltage_345(p) = E_345+eta_act_345(p)-eta_ohm_345(p)-
eta_conc_345(p);
            DistanceSum_345 = DistanceSum_345+(CellVoltage_345(p)-
V_345(p))^2;
        end
        Sigma_297(i) = sqrt(DistanceSum_297/length(I_297));
        Sigma_304(i) = sqrt(DistanceSum_304/length(I_304));
        Sigma_312(i) = sqrt(DistanceSum_312/length(I_312));
        Sigma_329(i) = sqrt(DistanceSum_329/length(I_329));
        Sigma_345(i) = sqrt(DistanceSum_345/length(I_345));
        AverageSigma(i) =
((Sigma_297(i)*WeighSigma_297)+(Sigma_304(i)*WeighSigma_304)+(Sigma_312(i
)*WeighSigma_312)+ ...

(Sigma_329(i)*WeighSigma_329)+(Sigma_345(i)*WeightSigma_345))/ ...

(WeighSigma_297+WeighSigma_304+WeighSigma_312+WeighSigma_329+WeightSigma_
345);
        if AverageSigma(i)<=LimAverageSigma
            X2(i,:)=trial;
            a=a+1;
        else
            X2(i,:)=X(i,:);
            b=b+1;
        end
    end
    for i=1:L-1
        if AverageSigma(i)==min(AverageSigma)
            best = i;   % The best set of parameters for every generation
is the one that has the lowest average Sigma
           break;
        end
    end
    for i=1:L-1
        for j=1:D
            X(i,j)=X2(i,j);
        end
    end
    % If the minimum value of AverageSigma is less than the limit,
    % the limit is recalculated as follow:
    if min(AverageSigma)<LimAverageSigma
        LimAverageSigma = (min(AverageSigma)+max(AverageSigma))/2;
    end
    count=count+1;
    if max(AverageSigma)==min(AverageSigma)
        stop=1;
    elseif count>gen_max
        stop=1;
    else
        stop=0;
    end
end
```

At the end of the algorithm, the set of parameters results is visible into the lines of the matrix X2. If the calculation is not reached the convergence the values of LimAverageSigma may

be too small: in this case parameters a and b help to understand how many times the trial vector provides a value of AverageSigma less than the limit and was replaced into the next generation of the parameters. If the parameters a is equal to zero means that there was not even a replacement during the calculation, thus is necessary to increase the value of LimAverageSigma.

It is important to note that more polarization curves you have (better if the curves are at different operative temperatures and pressures), the greater the precision of the result and the repeatability of the algorithm. If you have few curves, at limit one, the algorithm generates always a result, but it will not be accurate and replicable because normally there are several possible combinations of parameters that provide the result with the same degree of precision.

The results of the algorithm presented in this section are reported visible in Section 4.1.

10 Appendix B

In this Appendix B is explained the stack voltage Matlab function developed to compare experimental stack voltages against the predicted model results inside the Matlab GUI, used for test data analysis and presented in Section 5.2. This stack voltage Matlab function is based on the Mert-Mann approach, summarized in Section 2.1.5.2, with some simplifications regarding the hydrogen and oxygen partial pressures. For more details about these hypotheses, refer to Section 6.3.4. In the follows the Matlab code is reported:

```
function Vstack = stackvoltage(p_Uf,m_Uf,T,p_AN,J,alphaAN,lambda,
membranethickness,cellnumber)

R=8.314472;          %[J/(K*mol)]
Faraday=96485;       %[C/mol]

if T<333.15
    psat = 6.724136297056386e-07.*T.^4-7.275490810279587e-
04.*T.^3+2.969881912941677e-01.*T.^2-
5.416844321033899e+01*T+3.722403620916549e+03;
elseif T<433.15
    psat = 1.495713685503351e-06.*T.^4-1.825218311834390e-
03.*T.^3+8.470901653233313e-01.*T.^2-
1.769873593224579e+02*T+1.402983842744454e+04;
elseif T<533.15
    psat = 1.343667935291511e-06.*T.^4-1.548939938649714e-
03.*T.^3+6.591871124810556e-01.*T.^2-
1.202790615323854e+02*T+7.620604639994208e+03;
else
    psat = 1.006814469908304e-05.*T.^4-2.136003536986599e-
02.*T.^3+1.752662850090859e+01.*T.^2-
6.501866475112054e+03*T+9.128176354446471e+05;
end
psat = psat*1000;

pH2=(p_AN-psat)./101325;
Uf_O2 = (60000.*R.*T.*184.*J*250)./(4*Faraday.*p_Uf.*m_Uf.*0.21);
pO2=(1-Uf_O2).*0.21.*p_Uf./101325;

Vnernst = 1.229-0.85e-3*(T-298.15)+R/2/Faraday*T.*log(pH2.*(pO2.^0.5));

A=R*T/(alphaAN*2*Faraday);
i0berning=1.08e-17.*exp(0.086.*T);
Vact_Tafel=A.*log(J./i0berning);

rm=181.6.*(1+0.03.*J+0.062.*(T./303).^2.*J.^2.5)./(lambda-0.634-
3.*J)./exp(4.18.*((T-303)./T));
Vohm_Mann=J.*membranethickness.*rm;

CellVoltage_TafelMann = Vnernst-Vact_Tafel-Vohm_Mann;
Vstack=CellVoltage_TafelMann*cellnumber;
```

The stack voltage function requires some input to calculate the predicted voltage, in particular the cathode inlet pressure `p_Uf`, the cathode inlet air mass flow `m_Uf`, the stack temperature `T`, the average anode pressure `p_AN`, the stack current density `J`, the anode charge transfer coefficient `alphaAN`, the membrane water content `lambda`, the membrane thickness and the number of cells of the PEM-FC stack. The anode charge transfer coefficient, the membrane thickness and the number of cells are all characteristic constants of the stack analysed, while the membrane water content is assumed to be constant and equal to 14 (perfect membrane humidification conditions) due to the lack of experimental evidence.
After the declaration of the universal gas constant and the Faraday constant, the vapour saturation pressure is calculated using four fourth degree polynomial curves (see Section 1.1) and the hydrogen and oxygen partial pressure are calculated using the Equations (6.12), (6.13) and (6.14) explained in Section 6.3.4. The Nernst voltage is then obtained applying the Equation (2.11), the activation loss by the Mert approach of Equations (2.28) - (2.29), the ohmic loss by the Mann approach of Equations (2.36) - (2.37) and finally the stack voltage using Equations (2.46) and (2.49).